Radiation effects on the structure of chromosomes

By

Archana Bhartiya

Submitted in partial fulfilment of the requirements for the degree of Doctor of Engineering at the University College London

Supervisors
Prof Ian K. Robinson
Prof Stan W. Botchway

Department of Chemistry and London Centre for Nanotechnology
University College London

December 2020

Declaration

I, Archana Bhartiya, confirm that the work presented in this thesis is my own. Where information has been derived from other sources, I confirm that this has been indicated in the thesis.

Archana Bhartiya
December 2020

Abstract

This study aimed to investigate the effect of ionising radiation on the structure of the metaphase (condensed state) chromosomes at doses below 5 Gy. The purpose is to identify the early and the late onset of chromosomal aberrations, eventually to elucidate the damage and processing of territories of the chromosomes via DNA double strand breaks, re-arrangements and re-combinations of DNA sequences within the genome.

In this research the technique to prepare chromosomes has been improved to obtain a set of 46 human chromosomes in one frame commonly known as “spread”. Exponentially growing cells were irradiated with X-ray doses at 0.1 Gy (Gray), 0.5 Gy and 1 Gy followed by extraction of chromosomes from the irradiated as well as non-irradiated cells. DNA specific stain, 4’,6-diamidino-2-phenylindole (DAPI) was used to label the chromosomes during the analysis.

Imaging techniques such as Fluorescence Lifetime Imaging Microscopy (FLIM) and the phase contrast, hard X-ray ptychography have been used to image irradiated chromosomes. FLIM used to record the molecular environment of the metaphase chromosomes upon excitation. Moreover, X-ray ptychography was used to karyotype chromosomes according to their masses.

Using FLIM we observed significant reduction in DAPI lifetime (2.8 ± 0.03 ns) in the excited state at the heterochromatin region of heteromorphic chromosome 1, 9, 15 and 16 relatively to non-heterochromatin regions of chromosomes (2.88 ± 0.02 ns) in the spreads, in a non-irradiated chromosomes. Furthermore, for irradiated chromosomes the heterochromatin regions of above-mentioned chromosomes showed statistically significant reduced lifetime, with the difference ranged between ~260 picoseconds (ps) to ~290 ps, compared to non-irradiated chromosomes. Henceforth, the heterochromatin retains its structure and indicates that the regions are less

susceptible to damage at low-level of radiation doses but probably go through structural re-shuffling.

Key results were obtained from the Diamond Light Source (Harwell), I-13-coherence beamline for imaging of stained and unstained human chromosome spreads at room temperature along with reliable ptychography reconstructions and better resolution. Phase contrast image of chromosomes gave the distribution of electron density which correlates with the mass of the chromosomes. Following, the masses of non-irradiated and irradiated were karyotyped to observe the difference in the masses of the chromosomes. Henceforth, the mass of human genome can be determined using phase-contrast X-ray ptychography.

Acknowledgement

First and foremost, I would to express my sincere gratitude to my academic supervisors Prof Ian K. Robinson, Prof Stanley W. Botchway (Science and Technology Facilities Council) and Dr Mohammed Yusuf (UCL) for their continuous guidance throughout PhD research and thesis writing, for their motivations, enthusiasm and immense knowledge which I will apply in future life.

I would like to acknowledge the UCL's industrial training centre in Molecular Modelling and Material's Science and the PhD sponsor ERC. It also gives me a great pleasure to thank Dr Zhimei Du (UCL) for her administrative guidance throughout the academic year.

I would also like to thank Research Complex at Harwell, Octopus group of Central Laser Facility and I-13-coherence beamline, Diamond Light Source, UK. for giving me an opportunity to perform all the research experiments. I also appreciate support of Dr Darren Batey and Dr Xiaowen Shi for helping during the beamtime and ptychographic reconstructions. My heartiest thanks to Dr Ken Raj and Dr Sylwia Kabacik from Public Health England for offering T-lymphocytes cells for the experiments, group discussions and support.

My efforts will remain incomplete if I don't express my love and deep gratitude to my parents Mrs Anarkali Bhartiya and Mr Phul Chandra Bhartiya and my siblings Arpana and Akhilesh Bhartiya for their never-ending affection and untiring efforts for bringing my dreams and ambitions to a proper shape. I would also like to thank my husband Mr Pankaj Kumar for his immense support, inspiration and love throughout my PhD research.

Publications and conferences

- **A. Bhartiya**, M.Yusuf, S.W. Botchway and I.K. Robinson. "**Application of Fluorescence lifetime Imaging Microscopy for assessment of chromosomal aberrations in X-ray induced chromosomes**". (*In preparation*).

- **A. Bhartiya**, D. Batey, S. Cipiccia, X. Shi, C. Rau, S.W. Botchway, M. Yusuf, and I.K. Robinson. "**X-ray Ptychography Imaging of Human Chromosomes after Low-dose Irradiation**". Chromosome Research, 2020. *(Submitted)*.

- **A. Bhartiya,** M.Yusuf and S.W. Botchway**. "Combining Multicolor FISH (M-FISH) with Fluorescence lifetime imaging (FLIM) for chromosomal identification and chromosomal sub structure investigation".** Frontiers in Molecular Bioscience, 2020. (Submitted).

- **A. Bhartiya**, K. Madi, C. M. Disney, L. Courtois, A. Jupe, F. Zhang, A. Bodey, P. Lee, C. Rau, I.K. Robinson and M. Yusuf, **Phase contrast 3D tomography of HeLa cells grown in PLLA polymer electrospun scaffolds using synchrotron X-ray**, J. Synchrotron Rad, 2020, **27**, 1-6.

- M. Yusuf, F. Zhang, B. Chen, **A. Bhartiya**, K. Cunnea, U. Wagner, F. Cacho-Nerin, J. Schwenke and I. K. Robinson, **Procedures for Cryogenic X-ray Ptychographic Imaging of Biological Samples,** *IUCrJ*, 2017, **4**, 147– 151.

- Presented a **poster** in a Coherence 2018: International workshop on phase retrieval and coherent scattering conference, New York, USA. Poster titled: **"X-ray ptychography on a human chromosome spread".**

- **Talk** in UK-Japan workshop, 2015, Osaka University, Japan. Talk titled: **"Cryo-sample preparation and hard X-ray imaging at I-13-1(Diamond Light Source)".**

Table of Contents

List of Figures

List of Tables

Chapter 1

1. Introduction

1.1. Human Genome

Human Genome project (HGP) was an international collaborative project to sequence DNA of human being towards many applications including cytogenetic analysis in future. Consequently, more than 3 billion DNA sequences and 20,500 human genes were identified after 13 years of successful project (https://www.genome.gov/human-genome-project, accessed on 15 September 2020). Subsequently, human chromosomes contains an exact amount of DNA from 50 million base pairs (Mbp) to 250 (Mbp) and a well-defined amount of accompanying bound proteins which vary during the course of the cell cycle (Gookin *et al.*, 2017).

Human have 22 pairs of autosomes and one pair of sex chromosomes (Wall, 2016). The largest chromosome 1 has 248,956,422 bp and the smallest chromosome 21 has 46,709,983 bp of DNA sequences, Table 1.1 list all 46 human chromosomes for length, DNA bp sequences, GC-content and the weight of bp in picograms (pg) of each individual chromosomes. The high correlation between the sequence length and their masses, used as classifying factor called a chromosome Karyotype, allows each of them to be identified.

Chromosome	Length (bp)	Length (cm)	Weight (pg)	Weight (fg)	GC%
1	*249,250,621*	*8.15 ± 0.08*	*0.25*	*254.87*	41.74
2	243,199,373	7.95 ± 0.08	*0.25*	248.68	40.24
3	198,022,430	6.47 ± 0.06	0.20	202.48	39.69
4	191,154,276	6.25 ± 0.06	0.20	195.45	*38.25*
5	180,915,260	5.91 ± 0.06	0.18	184.99	39.52
6	171,115,067	5.59 ± 0.05	0.17	174.97	39.61
7	159,138,663	5.20 ± 0.05	0.16	162.73	40.75
8	146,364,022	4.78 ± 0.05	0.15	149.66	40.18
9	141,213,431	4.62 ± 0.04	0.14	144.40	41.32
10	135,534,747	4.43 ± 0.04	0.14	138.59	41.58
11	135,006,516	4.41 ± 0.04	0.14	138.05	41.57
12	133,851,895	4.38 ± 0.04	0.14	136.87	40.81

13	115,169,878	3.77 ± 0.04	0.12	117.76	38.53
14	107,349,540	3.51 ± 0.03	0.11	109.77	40.89
15	102,531,392	3.35 ± 0.03	0.10	104.84	42.20
16	90,354,753	2.95 ± 0.03	0.09	92.40	44.79
17	81,195,210	2.65 ± 0.03	0.08	83.03	45.54
18	78,077,248	2.55 ± 0.02	0.08	79.84	39.78
19	59,128,983	1.93 ± 0.02	0.06	60.47	*48.36*
20	63,025,520	2.06 ± 0.02	0.06	64.45	44.13
21	*48,129,895*	1.57 ± 0.02	*0.05*	*49.21*	40.83
22	51,304,566	1.68 ± 0.02	*0.05*	52.47	47.99
X	155,270,560	5.08 ± 0.05	0.16	158.77	39.50
Y	59,373,566	1.94 ± 0.02	0.06	60.71	39.97
Total (1-22, X, Y)	3,095,677,412	101.20 ± 0.97	3.17	3165.45	40.90

Table 1.1: Indicates the length of base pair (bp) and the GC- content of all 46 chromosomes. The length is indicated in bp and in picograms (pg) (Piovesan *et al.*, 2019).

1.2. Chromosome structure

Chromatin is composed of DNA-protein complexes present in nucleated cells. They form a thread-like structure during interphase and becomes condensed at the metaphase stage during cell division. DNA acquires different levels of packaging to fit within the approximately 10 μm nucleus of the cell (Figure 1.2). A 2 meter long DNA is wrapped around octamer histone proteins (H2A, H2B, H3 and H4) to form 11 nm nucleosomes referred to as “beads on a string” (Travers, 2014). Histone H1 proteins are DNA linkers that form complex structures by linking nucleosomes together to maintain chromatin stability (Maeshima and Eltsov, 2008). The nucleosomes are the building blocks of chromosomes.

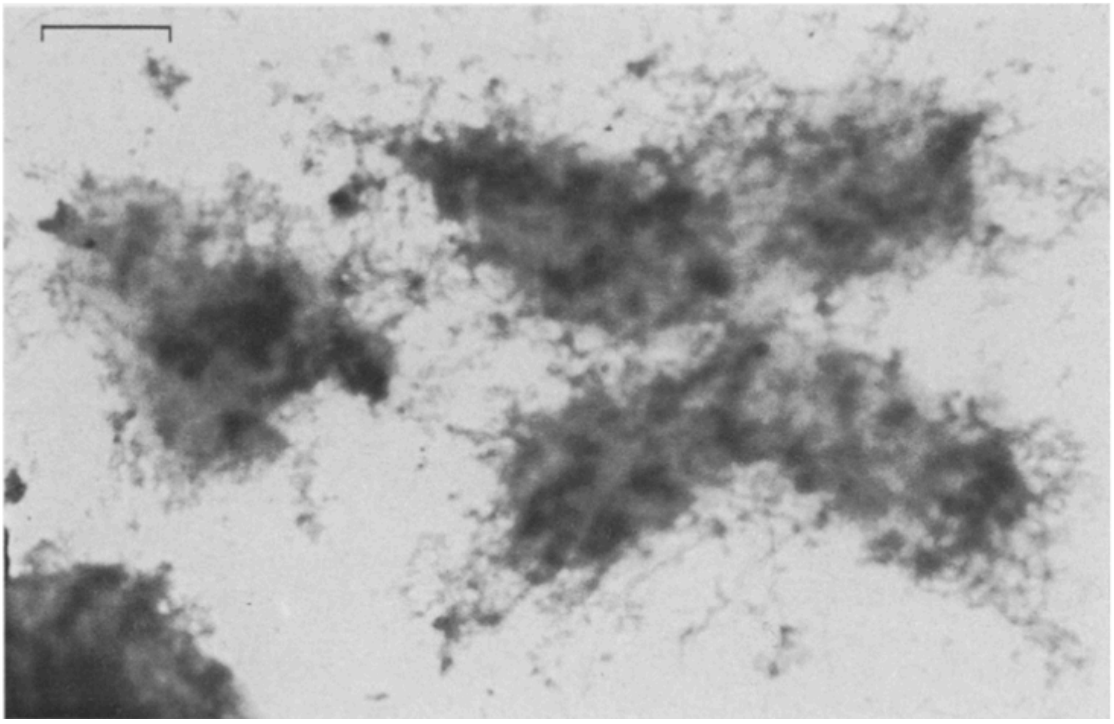

Figure 1.1: Morphology of an unstained metaphase chromosome obtained from Hela cells, observed under electron microscopy, scale bar = 1 μm (Hozier, Furcht and Wendelshafer-grabb, 1981).

The organisation of chromatin into higher-order structures and its condensation process represents one of the key challenges in structural biology. They supercoil to form a high-order structure known as the 30 nm chromatin fibre that folds into a compact mitotic (Figure 1.1) chromosome (Tremethick, 2007) (Maeshima *et al.*, 2014). The ratio of compaction for nucleosome is 1:6, 30 nm chromatin is 1:36 and for a mitotic chromosome is >1:10000 (Strachan and Read, 2004)**,** (Figure 1.2**).** The 30 nm structure has been reported as either Solenoid or Zigzag, (Maeshima *et al.*, 2014) based on their unique coiling patterns. However, there is some controversy surrounding this structure. Other factors such as monovalent and divalent cations play important roles in regulating the high-order structures of chromosomes. The concentration of monovalent Na^+/K^+ and divalent Ca^{2+}/Mg^{2+} increases from interphase to metaphase in the cell cycle (Maeshima and Eltsov, 2008).

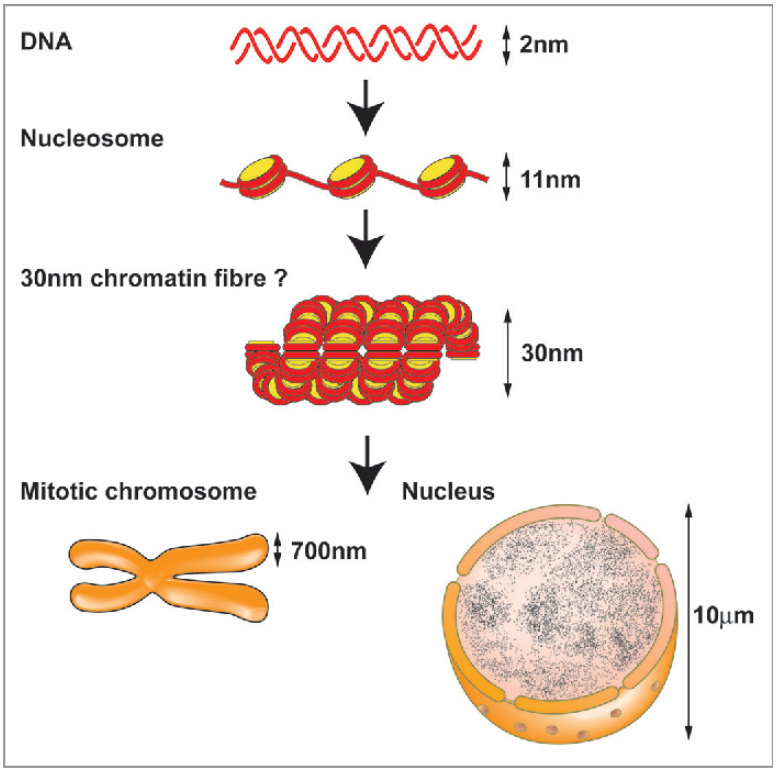

Figure 1.2: Packaging levels of human genome, starting from 2 nm double-helix DNA to 700 nm thick mitotic chromosome to fit into a 10 μm nucleus (Joti *et al.*, 2012).

1.3. Cell cycle

A typical eukaryotic cell division allows formation of two daughter cells from a parent cell. The cell cycle consist of two major phases; i) interphase that divides into G0- the resting phase, G1- the first gap phase to prepare the cells for DNA replication, S-phase- where DNA is duplicated, G2- regulation of proteins and other essential processes required for forthcoming M-phase (Figure 1.3), ii) the M-phase, further divides into mitosis and meiosis. The former, produces two identical diploid cells in somatic cells and the latter produces four unidentical haploid cells appears in gametes (Strachan and Read, 2004). Conventionally, the eukaryotic cell cycle lasts approximately 24 hours with G1 lasting around for 11 hrs, S-phase around 8 hrs, G2 around 4 hrs and M-phase for about an hour (Cooper, 2000). Nevertheless, this totally depended on the type of the cells.

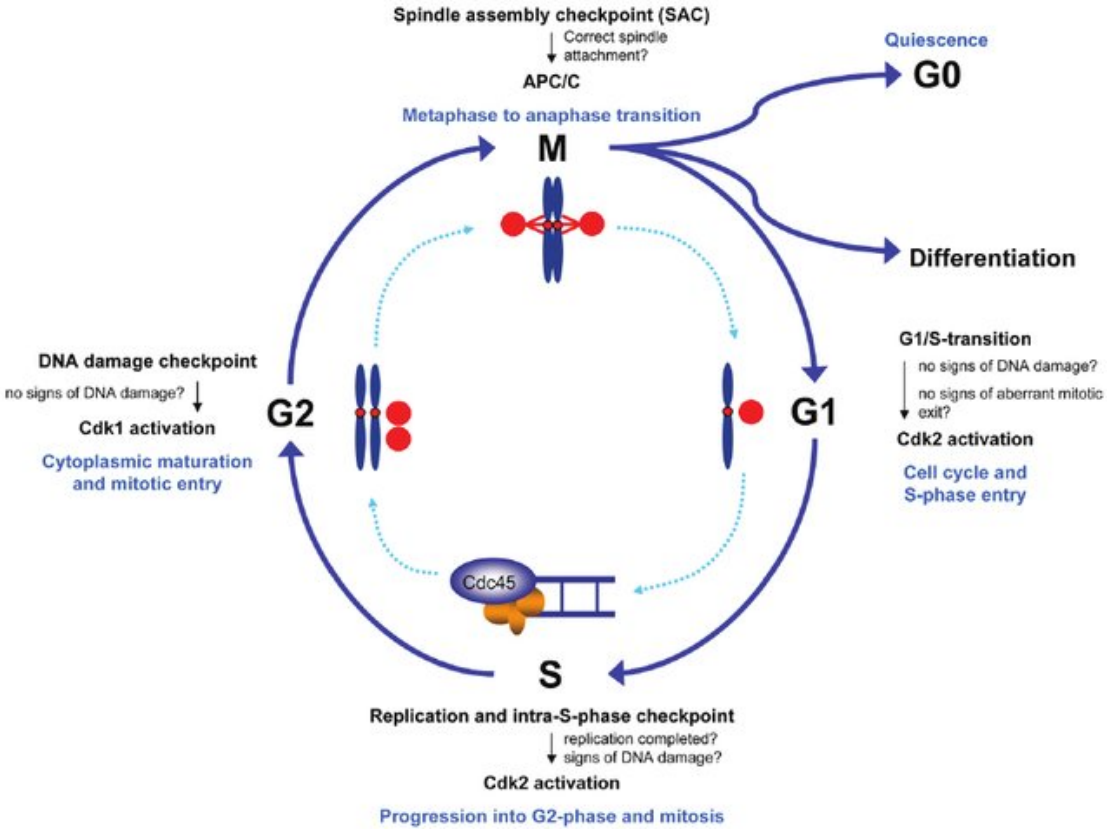

Figure 1.3: Mitotic cell cycle stages. Showing the three major checkpoints occurring in the mitotic cell cycle and shows the stages of cell cycle along with division of sister chromatids into a two identical daughter cells (Schnerch *et al.*, 2012).

Mitosis consists of four sub-phases; i) **prophase**- where the nucleolus disappears, and chromosome condenses followed by nuclear membrane breakdown ii) **metaphase-** the chromosomes align to the equator of cell and the chromosomes are at their most condensed state, iii) **anaphase**- the chromatids pull apart to opposite poles and iv) **telophase-** the nuclear membrane appears and the chromosome de-condenses and eventually the cell cleaves and divides into two daughter cells called **cytokinesis** (Morgan, 2007)**,** (Cooper, 2000)**.** In addition, there are three main checkpoints as shown in (Figure 1.3), i) G1/S point, to assure DNA replication and required growth factors ii) G2/M point, ensure DNA damage and spindle attachment and iii) M-phase checkpoint, insure spindle attachment and complete segregation of chromatids to the opposite poles (Morgan, 2007), (Schnerch *et al.*, 2012),

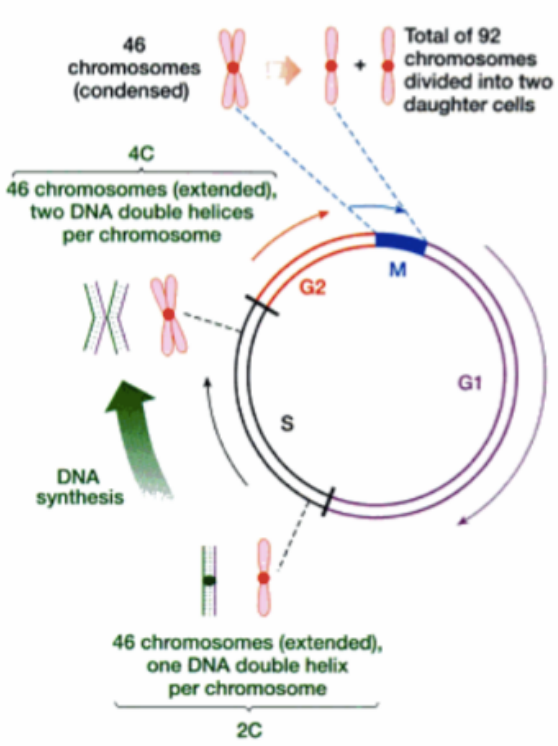

Figure 1.4: Chromosomal DNA content at a different stages of the cell cycle. At G0 and G1 stage the DNA content is 2C (The DNA content is double) and after synthesis of DNA at S-phase the DNA content increases to tetraploid (4C) before the anaphase (Strachan and Read, 2004).

Furthermore, the DNA content varies at different stages of the cell cycle; at the growth phase (G1), the DNA content is 2n, whereas, “n” is the amount of DNA. Moreover, when DNA replicates at S-phase the amount is doubled, which is 4n and it remains double until the metaphase and at following anaphase and telophase the sister chromatids separate to two daughter cells and with this the DNA content again reduces to 2n (Cooper, 2000) and finally goes to the rest phase until the following cell division. Consequently, a human nucleus will always consist of 46 chromatids but after replication at S-phase the DNA doubles to 92 chromatids prior to the separation (Figure 1.4).

1.4. Karyotyping

A karyotype is a way of classifying the full genetic complement, when chromosomes are arranged according to their size and shape (

Figure 1.6). This is the first stage of identifying any genetic aberrations such as structural and numerical aberrations in an organism (Grimwade *et al.*, 2010). Typically, chromosomes at the metaphase or prometaphase stage of the cell cycle are arrested and stained with an appropriate dye for karyotyping (Ried *et al.*, 1998) (Anderson, Stevens and Goodhead, 2002) (Yusuf *et al.*, 2011). Karyotyping has significant clinical applications and can be used for diagnosing genetic diseases (Cram *et al.*, 1988) (Grimwade *et al.*, 2010).

1.4.1. Classification of human chromosome according to centromeric positions

In 1960, Denver conference underpinned the 24-human chromosomes classification and divided them into a seven groups according to their lengths and sizes (Figure 1.5), (Gagula-Palalic and Can, 2013). Human chromosomes are classified on the bases of their centromeric positions and they are as follow: median, sub-median and acrocentric chromosomes (Figure 1.5) (Levan, Fredga and Sandberg, 1964). Henceforth, median-chromosomes have almost equal p and q-arm lengths, sub-median have short p-arm and long q-arm, and acrocentric-chromosomes almost have no p-arms, the centromere is located near at the end of the chromosomes. Nevertheless, Madian and Jayanthi (2014) had shown the fourth type, “very submetacentric” in chromosome 5 (Madian and Jayanthi, 2014).

a)

Chromosome Class	Denver Group
#1-#3	Group A
#4-#5	Group B
#6-#12,X	Group C
#13-#15	Group D
#16-#18	Group E
#19-#20	Group F
#21-#22,Y	Group G

b)

Denver report			
No.	r	d	Designation
1	1.1	0.5	median
2	1.6	2.3	"
3	1.2	0.9	"
4—5	2.7	4.6	submedian
X, 6—12	1.9	3.1	"
13—15	6.7	7.4	acrocentric
16	1.5	2.0	median
17—18	2.8	4.7	submedian
19—20	1.3	1.3	median
Y	(5.9)	7.1	acrocentric
21—22	3.4	5.1	"

Figure 1.5: Human chromosomes classification; a) chromosomes are divided into a seven groups according to Denver's group(Gagula-Palalic and Can, 2013), b) arranged on the ratio of length of short p-arm and the long q- arm of each individual chromosomes (Levan, Fredga and Sandberg, 1964).

A table of relative lengths of human chromosomes was revised by Patau in 1965 (Table 1.2), by measuring the long q-arm and short p-arm (Therman, 2012).

Chromosome		Average length (in % of autosomal genome) of:		Chromosome		Average length (in % of autosomal genome) of:	
Group	No.	Long arm	Short arm	Group	No.	Long arm	Short arm
	1	4.68	4.57		13	3.29	—
A	2	5.28	3.35	D	14	3.12	—
	3	3.80	3.32		15	2.89	—
	4	4.85	1.84		16	1.93	1.34
B	5	4.66	1.75	E	17	2.07	0.96
	6	3.87	2.36		18	2.04	0.76
	7	3.54	2.04	F	19	1.32	1.11
	8	3.45	1.63		20	1.30	1.05
C	9	3.23	1.72	G	21	1.26	—
	10	3.22	1.54		22	1.38	—
	11	2.90	1.88	Total autosomes		100.00	
	12	3.38	1.32				
					X	3.26	2.02
					Y	1.64	—

Table 1.2: Depicts the list of average lengths of p and q-arms of autosome +X+Y human chromosomes (Therman, 2012).

There are two types of constrictions, primary (centromere) and secondary. The primary constrictions are present in all the chromosomes whilst secondary constrictions are present only in a few chromosomes and more frequent found in chromosome 1 and 9 (Palmer and Funderburk, 1965). This secondary constriction is known as the Nucleolar Organisation Regions (NORs) since they contain genes to produce ribosomal DNA to form nucleolus at the end of mitosis stage of the cell cycle (Henderson, Warburton and Atwood, 1972). Moreover, the chromosomes from group D and G, listed as 13, 14, 15, 21 and 22 also possess NORs at the top of the p-arm (Henderson, Warburton and Atwood, 1972). The role of primary constriction is to secure the two sister chromatids and it's the bending site during separation at the anaphase although, secondary constriction is for chromosomal identification during anaphase (Bhatnagar and Bansal, 2009).

1.4.2. Identification of chromosomes with bandings

Several differential staining techniques are used to introduce visible "bands" in the structures. Caspersson et al in (1971) discovered the quinacrine (Q) fluorescence banding (observed patterns of dark and light bands) technique for identifying metaphase chromosome (Sumner, 1982). In addition, chromosome at metaphase can be identified by certain banding techniques such as Giemsa (G) and Reverse (R), are commonly in clinical practice for cytogenetic analysis (Shaw, 1973). The following banding techniques uses stains and fluorescence dye to create bands in the mitotic chromosomes which defines the heterochromatin (dark bands) and euchromatin (light bands) regions of the chromosomes (
Figure 1.6).

The G-banding highlights dark colour at the AT-rich regions (gene poor, heterochromatin) and the light colour at the GC-rich regions (gene rich, euchromatin) of a DNA (Hozier, Furcht and Wendelshafer-grabb, 1981). The euchromatin in less densely packed whereas the heterochromatin is more tightly packed. The former, localised at the centre and latter at the periphery of the nucleus (Cooper, 2000) (Cremer and Cremer, 2010). Moreover, the C-

banding only stains the constitutive heterochromatin present in the chromosome 1qh, 9qh 16qh and Yqh (Shaw, 1973).

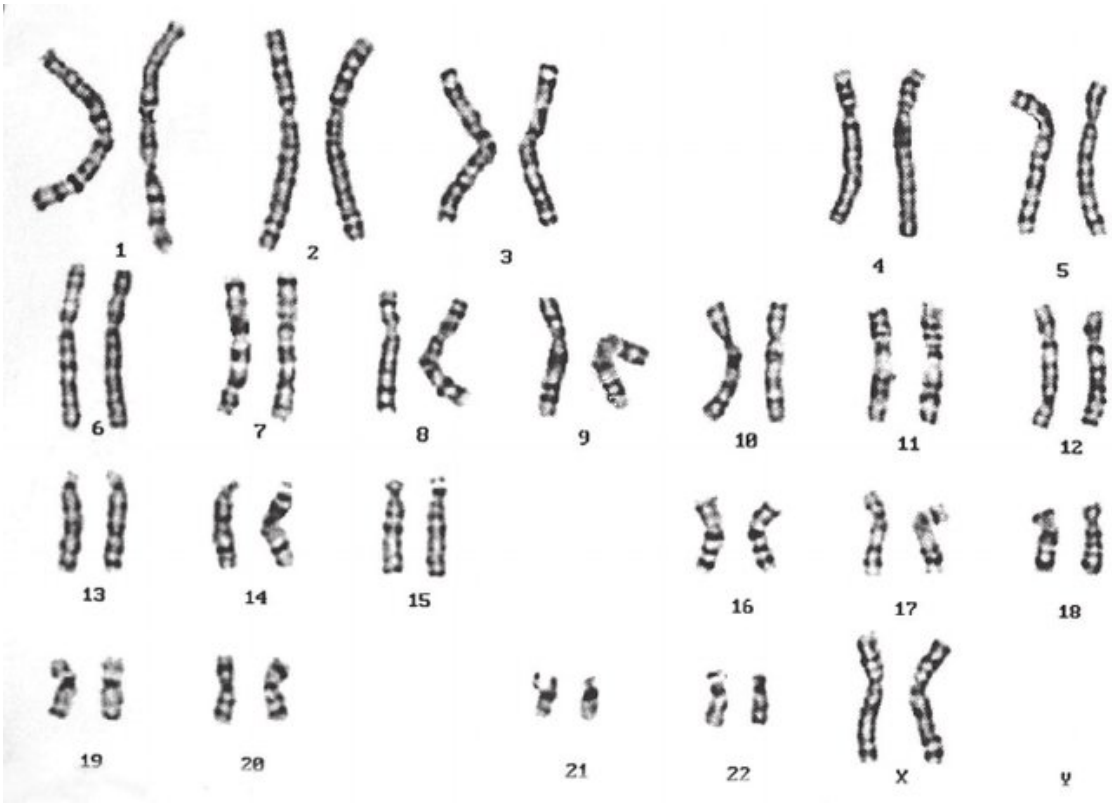

Figure 1.6: Karyogram showing 46 chromosomes from a normal human female cell representing G-bands (Huang *et al.*, 2010).

1.5. Chromosome staining

Generally native biological samples are difficult to image because of their weak scattering property. Therefore, to measure the sample, it is either dehydrated using ethanol/acetone/methanol (Barke *et al.*, 2015), chemically fixed using glutaraldehyde/osmium tetraoxide (Wako *et al.*, 2020) or cryopreserved (Yusuf *et al.*, 2017) (Dillard *et al.*, 2018). Staining methods are also applied to chromosomal identification during imaging such as platinum blue (Pt-blue) (Yusuf *et al.*, 2014) (Shemilt *et al.*, 2015) and uranyl acetate (UA) (Xu and Wu, 1983). The negative stain used in this thesis are uranyl acetate and platinum blue because they produce the highest electron density map and improves the contrast of the biological sample (Derksen and Meekes, 1984) (Ou *et al.*, 2017) (Shemilt *et al.*, 2015). The negative staining achieved when the ions of stains

are repelled by the ions of a specimen (Hayat and Miller, 1990). Uranyl acetate is present in the form of uranyl cation (UO_2^{2+}) when diluted in water and maintains the pH of 4.5 and when used as stain it repels the positively charged proteins (Hayat and Miller, 1990) and phosphate ions of nucleic acid and enhance the contrast (Derksen and Meekes, 1984).

Uranyl ions binds to proteins and DNA of mitotic chromosomes (Ou *et al.*, 2017) and induces conformational change in protein-protein or DNA-protein interactions (Lin, 2020). Platinum blue is an alternative to uranyl acetate because it is safer to handle, easily synthesizable and useful to enhance the contrast for electron density mapping (Inaga *et al.*, 2007). Staining is not sufficient for ultrathin sections and probably crystallizes on the sample (Inaga *et al.*, 2007) (Yusuf *et al.*, 2019). Platinum blue stains chromosome extremely well when mounted on the glass slides to collect back scattering signal from electron (Yusuf *et al.*, 2019).

1.5.1. DNA-DAPI banding of chromosomes

Chromosomes can be visualised using fluorescence microscopy after binding to 4',6-diamidino-2-phenylindole (DAPI) that is a popular nucleic acid stain, binding to AT-rich regions of DNA every 2-3 base pairs (Kapuscinski, 1995). It absorbs light at around 358 nm (peak absorption) wavelength and emits blue fluorescence at 461 nm wavelength (Karg and Golic, 2018). The quantum yield of DAPI is 0.92 when bound to DNA and 0.04 for unbound DAPI (Kapuscinski, 1995). When DAPI bounds to DNA, it greatly improves contrast of the image since the quantum yield is much smaller for unbound dye in solution (Estandarte *et al.*, 2016) (Barcellona and Gratton, 1990).

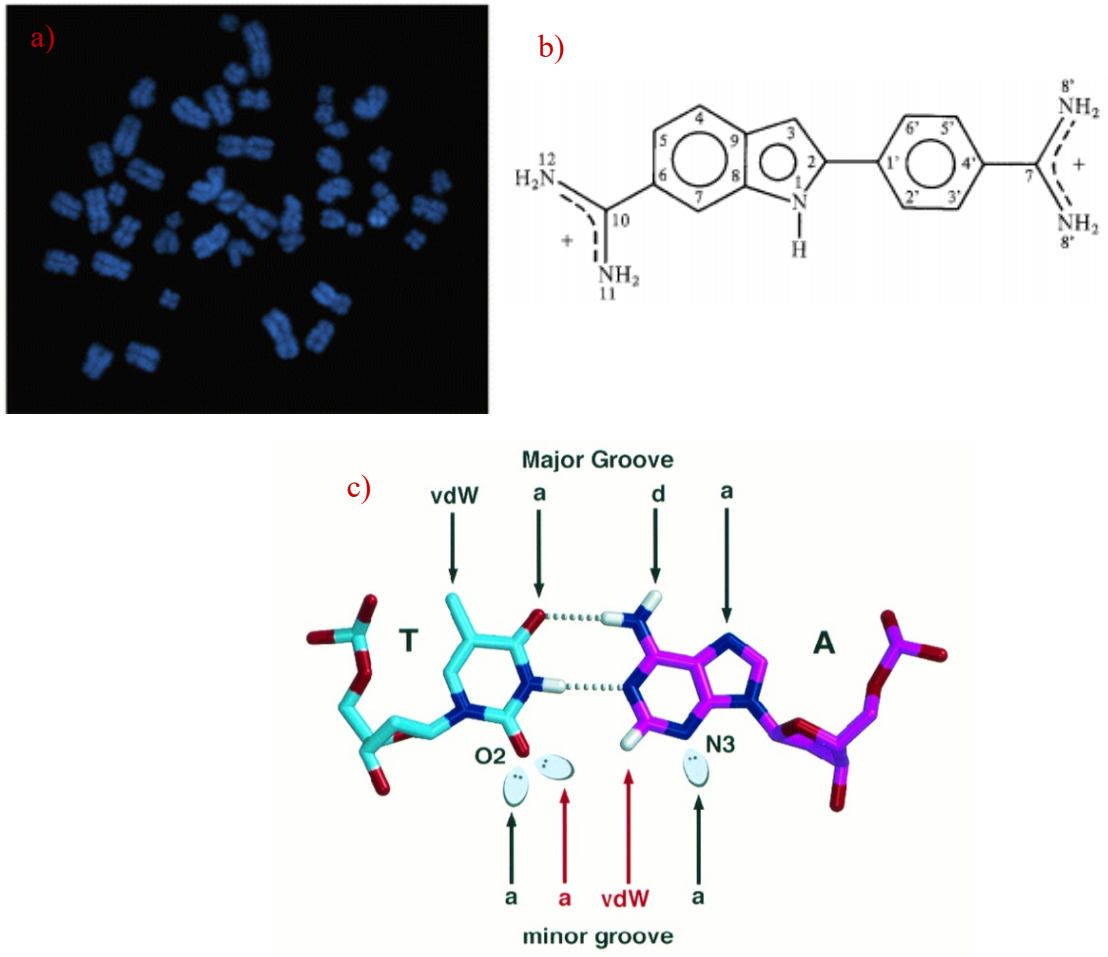

Figure 1.7: DNA-DAPI binding grove; a) DAPI stained chromosomes obtained from human induced pluripotent stem (hiPS) cells (Moralli *et al.*, 2011) , b) chemical structure of DAPI (Barcellona and Gratton, 1990) and c) shows the minor groove region where DAPI binds to a DNA (Kielkopf *et al.*, 1998).

FFigure 1.7 (b) shows the molecular structure of a DAPI with three hydrogen donor group, 2 amidino moieties at the end and one NH indole group carrying a positive charge that strongly interact with the three hydrogen-bond acceptor(a) regions of DNA (N3 of adenine and O2 of thymidine) in the minor grooves of the AT-rich regions. Hydrogen bonding and van der Waals forces as shown in FFigure 1.7 (c) which form the DNA-DAPI complex (Kielkopf *et al.*, 1998).

The fluorescence lifetime of a DNA-DAPI complex depends on various factors such as i) the specificity of a DAPI to bind to AT-rich regions of DNA at

minor grooves ii) DAPI is more prone to AT base pairs than GC because of presence of amino acid at the position 2 of an adenine iii) the complex has low anisotropy because of highly coiled structure of DNA. iv) The proton transfer process is inhibited when DAPI binds to AT clusters than GC clusters which increases its lifetime. These properties of DAPI makes it more specific to bind DNA and helps in structural determination of DNA and DNA- chromosomes. The excited state lifetime varies substantially on binding: the DNA-DAPI complex has 2.8 ns bound with AT and 0.2 ns for unbound DAPI in solution (Barcellona and Gratton, 1990). Therefore, DAPI is highly suitable for staining chromosomes (Estandarte *et al.*, 2016) (Moralli *et al.*, 2011) (Kapuscinski, 1995).

1.6. DNA content -based human karyotype

The two colours flow cytometry is a quantitative way of karyotyping, chromosomes when double stained with Hoechst 33258 and chromomycin A3 (Figure 1.8) with the sorting that occurs on the basis of amount of AT and GC content present in each individual chromosomes, respectively (Langlois *et al.*, 1982). The positive correlation between the base ratio and the brightness from fluorescence of Hoechst 33258 and chromomycin A3 generates a karyotype of human chromosomes, including the largest chromosome 1 to the smallest chromosome 21 (Langlois *et al.*, 1982). Although, the use of this method is uncertain because of presence of unequal proportion of base ratio in each individual chromosomes.

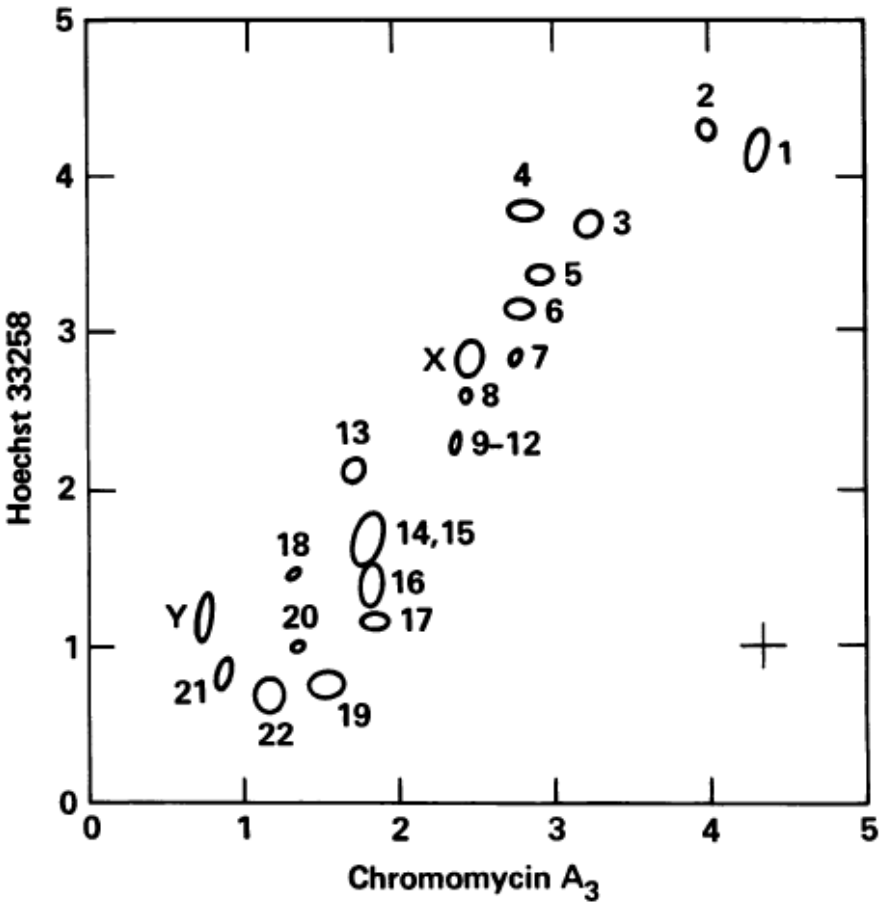

Figure 1.8: The bivariate flow cytometry shows the positive correlation between two dyes used for the karyotype. Ellipses indicates each chromosomes and the size of it corresponds to the variability of the base composition (Langlois *et al.*, 1982)

The classification of human metaphase chromosomes is based on the base pair composition and DNA content that is further classified into following manner; i) the variability of base ratio can be observed in a whole chromosome as well as within components of a chromosome (Korenberg and Engels, 1978) ii) the larger chromosomes are AT-rich than smaller ones that is examined by autoradiography, moreover, they are late replicating in the cell cycle, in addition, the extent of base ratio is higher in larger chromosomes relative to smaller ones determined by quinacrine-brightness (Korenberg and Engels, 1978), iii) A reasonable amount of variation in DNA content have been marked between the homologous chromosomes and between different donors measured by Cytophotometric Data Converter (CYDAC) (Mayall *et al.*, 1984).

The heteromorphic chromosomes 1, 9, 16 and Y showed a greater amount of variability in the DNA content due to presence of a constitutive heterochromatin followed by acrocentric chromosomes 13, 14, 15, 21 and 22 (Harris *et al.*, 1986). Among heteromorphic chromosomes , the Y chromosome showed greatest amount of variability followed by chromosomes 1, 16, 9 (Harris *et al.*, 1986) (Langlois *et al.*, 1982) (Mayall *et al.*, 1984). The sensitivity of flow cytometry has been unable to identify chromosomes 9-12 probably due to their same total DNA content (Langlois *et al.*, 1982).

1.7. Fluorescence lifetime Imaging Microscopy for assessment of molecular environment of chromosomes

Fluorescence lifetime imaging microscopy (FLIM) is a technique that can map the spatial nature of excited state lifetime and can act as a reporter to changes in the fluorophore's environment (Anthony, Guo and Berland, 2009). More recently, it is suggested that chromosome compaction at nanometre length scales has been suggested on the length of chromosomes imaged using FLIM after DAPI staining (Estandarte *et al.*, 2016) alone. This was performed on a classical spread of chromosomes whereby excited state lifetime measurements have been obtained on all 46 chromosomes. Crucial for analysing the FLIM data is the identification of each chromosome whereby M-FISH plays an important role (Estandarte *et al.*, 2016).

M-FISH is a fluorescence technique that uses computer-generated pseudo colours from a coding scheme, which analyses the fluorescence from various pairs of five paints (probes) and uses DAPI as a counterstain (Speicher, Ballard and Ward, 1996). M-FISH is an invaluable and powerful karyotyping tool that provides detailed analysis of structural rearrangements and maker chromosomes (Yusuf *et al.*, 2013). Its use has been expanded into validating and karyotyping complex clinical cases after G-banding (Jalal and Law, 1999) on the same sample. Furthermore, its use has been demonstrated in identifying and karyotyping chromosomes on the bases of phase contrast (Shemilt *et al.*, 2015) and fluorescence (Yusuf *et al.*, 2011) imaging methods.

1.7.1. Principle of FLIM

The fluorescence lifetime is an amount of time a fluorophore remains on average in its excited state before returning to the ground state by emitting a fluorescence photon or as a non-radiative decay. Fluorescence is a phenomenon that occurs when a photon excite the electrons of a molecule in the ground state, the electrons after absorbing the light emit photons and the electrons come back to ground state with loss of energy. It is summarised in the modified Jablonski diagram (Figure 1.9). The emission of a fluorescence photon from a fluorophore does not occur at a fixed time. Instead, a distribution of times is observed, which can be described by an exponential decay function (Lakowicza *et al.*, 1987).

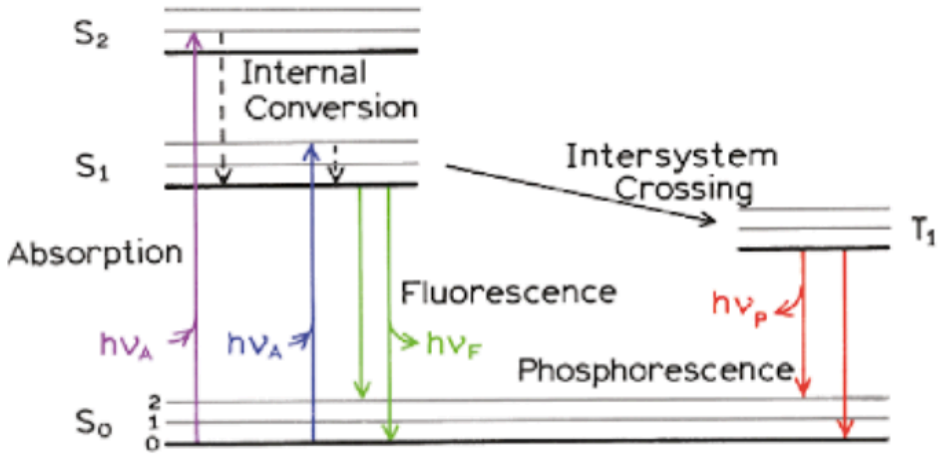

Figure 1.9: Jablonski diagram representing electronic energy levels (Lakowicz, 2006b).

The relaxation time correlates with the rate of internal molecular processes excited with incoming light. The absorbance typically lasts for approximately 10^{-15} seconds (s) while fluorescence lasts for 10^{-9} s (Lakowicz, 2006b), (Wang and Bai, 2006). The time during which the molecules stay in their excited state is called lifetime of fluorophore and it ranges from 10^{-8}-10^{-9} s (Lakowicz, 2006b). The fluorescence lifetime is defined by **Equation 1.1**:

$$\tau = \frac{1}{k_r + k_{nr}} \quad \textbf{(1.1)}$$

The fluorescence lifetime (τ) is inversely proportional to the sum of radiated rate constant (K_r) and non- radiated rate constant (K_{nr}) (Suhling *et al.*, 2015). The single exponential fluorescence decay is obtained from an **Equation 1.2:**

$$\mathbf{F(t)= f_0 e^{-t\backslash\tau}} \quad \textbf{(1.2)}$$

The lifetime value is generated from the fitted function model (equation 1.2), however, f_0 is the intensity at a time t = 0, t is the time after the absorption, and $\boldsymbol{\tau}$ is the fluorescence lifetime (Suhling *et al.*, 2015). However, instrument response function (IRF) should also be considered during fluorescence decay calculations. IRF is used to determine parameter that affect the measured lifetime from the instrumentation as a whole.

FLIM has the ability to distinguish two regions of an image with same brightness but different lifetime whereas an intensity image is unsuccessful in differentiating the same intensities (Lakowicz, 2006a). Hence, the FLIM image gives more information than the intensity image alone. In addition, FLIM is neither affected by photo-bleaching largely nor auto-fluorescence (which affect only the intensity) and has potential for single molecule monitoring (Becker, 2012). Photo-bleaching and the signal to noise ratio can be reduced unlike other fluorescence microscopy methods by adjusting the scan time of the samples and altering laser power according to the requirements to gain good resolution (Laptenok *et al.*, 2007). The main advantage of FLIM is that it is independent of the concentration of fluorophores. It calculates the lifetime from environmental change in the sample such as pH, viscosity, temperature, refractive index, ion concentrations and quantum efficiency of the probes (Suhling *et al.*, 2015). Lifetime obtained at the pixel-level are colour-coded to produce images. Thus,

the spatial information of molecules can be obtained by FLIM in a nanometre scale.

The FLIM data are acquired, when the samples are raster scanned in X and Y coordinates using high power Ti-sapphire laser pulses. In this work, the emitted photons are recorded by Time-Correlated Single Photon Counting (TCSPC) within each individual pixel with respect to time. Integrated photons analysed using computer software, to fit exponential decays at each pixel to get the lifetime of decayed fluorophores (Laptenok *et al.*, 2007) (see chapter 2, Materials and Methods).

1.7.2. Applications of FLIM

One of the important mechanisms underlying FLIM is the Forster Resonance Energy Transfer (FRET), which is also used to study protein-protein interactions and conformational changes in life science (Suhling *et al.*, 2015), estimates intermolecular distances on an angstrom scale. It is also employed to measure the compaction of chromatin from interphase to telophase of the cell division (Llères *et al.*, 2009). Interestingly, the combined FRET-FLIM utilized to understand the condensation and the de-condensation process of chromosomes, from prophase to prometaphase by regulating the amount of calcium (Ca^{+2}) divalent cations in the cells (Phengchat *et al.*, 2016). Recently, FLIM has been used to observe chromosomal structural changes such as compaction in DAPI-stained fixed methanol acetic acid metaphase human chromosomes (Estandarte *et al.*, 2016). According to Estandarte *et al* (2016), FLIM, with undamaged fixed human metaphase chromosomes, showed shorter lifetime in chromosome 1, 9, 15, 16 and Y at the heterochromatic regions in comparison to other chromosomes in the human genome (Estandarte *et al.*, 2016) as shown in Figure 1.10. The following chromosomes are commonly known as heteromorphic chromosomes. FLIM has been used to study the environmental condition of nuclei upon X-ray irradiation at 10 Gy at the dose rate of 1 Gy/s and global decompaction in the “living NIH/3T3 cells” observed which means the Hoechst 34580 lifetime increases after 10 Gy exposure from “1331 ± 39 ps to 1390 ± 46 ps” (Abdollahi, Taucher-Scholz and Jakob, 2018).

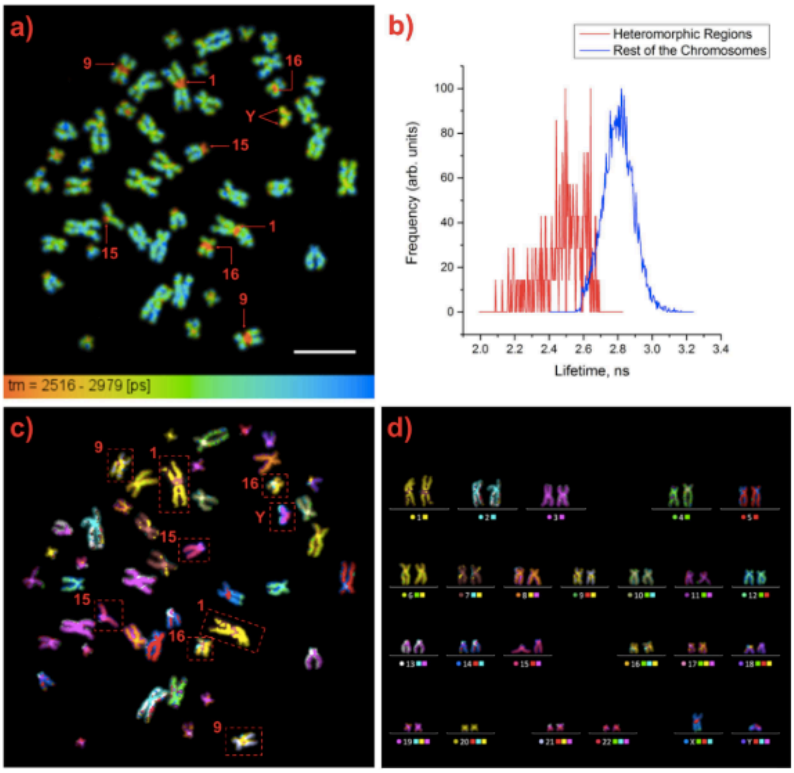

Figure 1.10: Identified heteromorphic human metaphase chromosomes from a spread; a) a human metaphase chromosome spread showing after FLIM. Red arrows show the heteromorphic chromosomes, scale bar = 10 µm b) normalised lifetime distribution of heteromorphic region and rest of the chromosomes and the former possess shorter DAPI lifetime relative to latter, c) M-FISH image of spread a) displaying 46 chromosomes that are all colour-coded in their respective pairs, d) the M-FISH karyotype of spread c) (Estandarte *et al.*, 2016).

FLIM also has been used to observe chromatin condensation in human endothelial cell nuclei at a different viscosity environment (Spagnol and Dahl, 2016). Though, a shorter lifetime was observed in a condensed chromosome than in de-condensed one (Spagnol and Dahl, 2016) (Estandarte *et al.*, 2016) (Phengchat *et al.*, 2016). Moreover, FLIM has the ability to distinguish the affected and the unaffected cells caused from the diseases in lifetime. For instance, chromosomes extracted from leukaemia affected cells showed shorter lifetime compared to the unaffected ones (Yahav *et al.*, 2016). Additionally, the DAPI lifetime of structural abnormalities such as translocation, formation of fragments and isochromosomes has been shown in this thesis (see chapter 3).

1.7.3. Constitutive heterochromatin

Heterochromatin was first coined by Emil Heitz in 1928 in an interphase cell (Allshire and Madhani, 2018) (Berger, 2019). The heterochromatin regions categorised into constitutive and facultative heterochromatin. The constitutive heterochromatin remains compact, gene-poor, enriched with repetitive and late replicating DNA sequences, in contrast, the facultative heterochromatins, shows temporal and spatial active and inactive behaviour of transcription (Woodcock and Ghosh, 2010). The compaction of the heterochromatin is a result of histone hypoacetylation and DNA methylation (Bannister *et al.*, 2001). The constitutive heterochromatin is the cause of trimethylation of lysine 9 of histone H3 (H3K9me3) (Nicetto and Zaret, 2019) (Bannister *et al.*, 2001) whereas, the facultative heterochromatin is designed as H3 lysine 27 trimethylation (H3K27me3) (Saksouk, Simboeck and Déjardin, 2015).

The block of constitutive heterochromatin regions are located at the pericentric region of chromosome 1, 9 and 16 (Tagarro, Fernández-Peralta and González-Aguilera, 1994), short p-arm of chromosome 15 (Friedrich *et al.*, 1996) (Chen *et al.*, 1981), and distal region of chromosomes Y (Estandarte *et al.*, 2016) (Bachtrog, 2014) (Choo, 1997) (Meyne *et al.*, 1984). The following chromosomes are defined as heteromorphic chromosomes, which was visualised by C-banding technique (Sahin *et al.*, 2008). The constitutive heterochromatin block is also present in the acrocentric chromosomes 13, 14, 15, 21 and 22. It has been reported in cytogenetics resource committee (of the College of American Pathologists and the American College of Medical Genetics) that chromosomes 1, 9, 16 and Y are considered as more heteromorphic chromosomes as compared to other chromosome in a genome (Brothman *et al.*, 2006). The heterochromatic chromosomes have also identified using electron microscopy (Sanchez, Martinez and Goyanes, 1991), molecular cytogenetics diagnostic kit (Speicher, Ballard and Ward, 1996) (Jalal and Law, 1999) and fluorescence microscopy (Estandarte *et al.*, 2016). In addition, it was observed that females contain higher heteromorphic variants, by 1.4 times than males (Kosyakova *et al.*, 2013).

Furthermore, both pairs of chromosome 9 are structurally highly polymorphic containing the largest autosomal block of heterochromatin making it heteromorphic in 6-8 % of the human genome 9 (Humphray *et al.*, 2004). Moreover, chromosome 9 contains some evolutionary conserved regions (ERCs) in their DNA sequence (Humphray *et al.*, 2004). Exceptionally, the pericentric inversion occur at the heterochromatin region, which makes chromosome 9 differ morphologically (Akbas *et al.*, 2010) (Humphray *et al.*, 2004) and its acceptable in "1-3 % of general population" (Akbas *et al.*, 2010).

Constitutive heterochromatin of each individual chromosomes are approximately of size "5 Mb to a few hundred bp" (Saksouk, Simboeck and Déjardin, 2015) and these regions consist of varied satellite DNA, which are defined as tandemly repeated sequences of DNA (Choo, 1997) . The satellites are alpha satellite DNA, DNA satellite I, II and III (Choo, 1997). Among them, Satellite II is poorly conserved than the satellite III (Tagarro, Fernández-Peralta and González-Aguilera, 1994). Centromere of all human chromosomes consist of AT-rich; 171 bp **α**-satellite repeats and its approximately "10 %" of the human genome plus the monomer of **α**-satellite repeats are "50- 60 % identical" (Sullivan, Chew and Sullivan, 2017). The **α**-satellites are conserved regions of repetitive DNA sequences from primates to human and they are considered to be more evolutionary divergence than any other sequence type (Jackson *et al.*, 1999). Whereas, satellite I is based on repetitive unit of 42 bp, AT-rich DNA sequences (Prosser *et al.*, 1986) (Tagarro, Fernández-Peralta and González-Aguilera, 1994).

Furthermore, satellite II and III considered to be heterogeneous in nature and are based on the 5 bp motif "GGAAT" (sense strand) and ATTCC (antisense strand) repeat DNA sequence (Figure 1.11) (Tagarro, Fernández-Peralta and González-Aguilera, 1994). Although, the functional role of satellite II and III is unclear. Subsequently, the chromosome 1 consist of satellite II (majority) and III (minor), chromosome 9, 15 and Y has satellite III, chromosome 16 has satellite II (Tagarro, Fernández-Peralta and González-Aguilera, 1994) (Figure 1.12). On other the hand, the telomere consist of repeat of

hexanucleotide (TTAGGG) DNA sequences (Humphray *et al.*, 2004) (Saksouk, Simboeck and Déjardin, 2015) (Nishibuchi and Déjardin, 2017).

Satellite 2 ATTCCATTCG(A/G)G(A/T)CCATTCGATGAT

Satellite 3 $(ATTCC)_n$ ATTCCA(T/C)TCGGGTTGATTCC $(ATTCC)_n$

Figure 1.11: The consensus DNA sequence of satellite 2 and 3 and the underline sequences are the designed oligoprobes of each satellites, respectively (Tagarro, Fernández-Peralta and González-Aguilera, 1994).

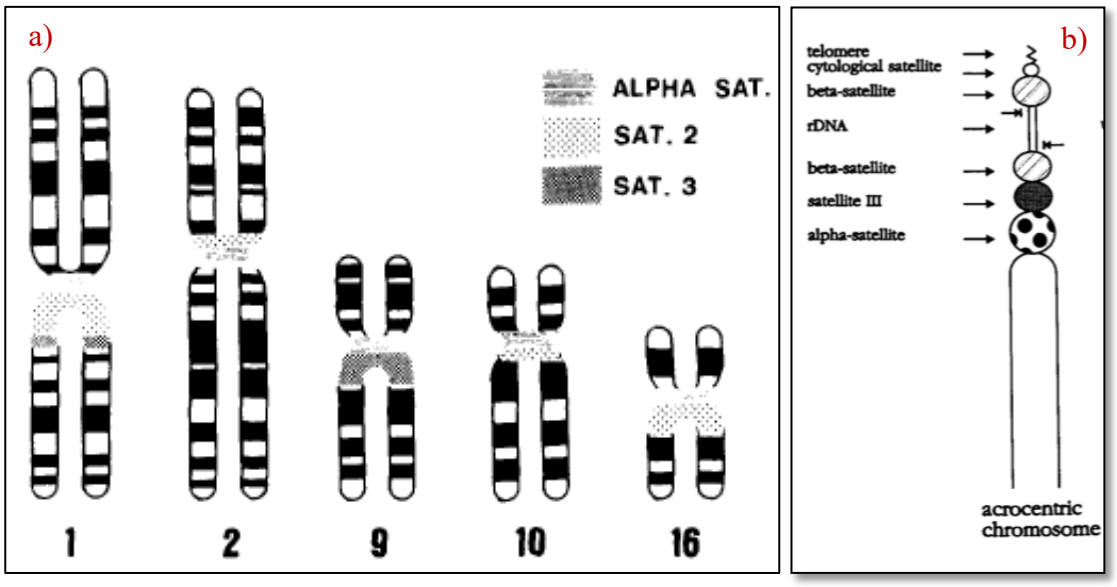

Figure 1.12: The proportional distribution of satellites at the pericentric centromere region of listed chromosomes; a) localisation of alpha satellite, satellite 2 and 3 (Tagarro, Fernández-Peralta and González-Aguilera, 1994), b) distribution of varied satellites, rDNA and telomere at the short p-arm of acrocentric chromosomes (Friedrich *et al.*, 1996).

Heterochromatin plays role in infertility (Madon, Athalye and Parikh, 2005) (Sahin *et al.*, 2008) (Bachtrog, 2014), "spindle attachment and chromosome movement, meiotic pairing and sister chromatid cohesion" (Madon, Athalye and Parikh, 2005). Constitutive heterochromatin are inheritable, and preserved (Allshire and Madhani, 2018), transcriptionally inactive (Bannister *et al.*, 2001) (Saksouk, Simboeck and Déjardin, 2015), genetically inert (Allshire and Madhani, 2018) (Choo, 1997). An instability in centromeric heterochromatin of chromosome 1, 9 and 16, is the ground source of a disease called

Immunodeficiency centromeric instability and facial dysmorphic syndrome (ICF) plus multiple branches originating from the centromeric heterochromatin of chromosome 1 and 16 (Maraschio *et al.*, 1988). Although, following variability was not observed in chromosome 15 and Y (Choo, 1997).

1.8. X-ray ptychography of chromosomes

The strength of penetration of X-ray microscopy aid the high-resolution imaging of biological sample with less technical issues (Larabell and Nugent, 2010). The detailed information can be obtained from atomic to molecular level without any sample processing such as fixing, staining or sectioning (Robinson *et al.*, 2016). X-ray microscopy is sensitive because a photon originated from X-ray source interacts with the inner shell of an atom of specimens and reveals atomic level of information depending on amount of energy absorption or an ability to extract electron from orbital of the matter (Howells *et al.*, 2006). The complex refractive index, $n = 1 - \delta + i\beta$, when X-ray interacts with the matter, the real component (δ) describes the phase change and the imaginary component (β) denotes the absorption of the beam (Hémonnot and Köster, 2017).

X-rays used for imaging biological samples can be divided into soft-X-ray and hard-X-ray depending upon their wavelength and photon energy. The wavelength range for soft-X-ray is 2 nm-5 nm and it operates in the 'water window' of spectral region between the carbon k-edge at 284 eV and the oxygen k-edge at 540 eV (Maser *et al.*, 2000). Soft x-rays are advantageous over other conventional methods because it protects from sample mass loss plus avoid morphological distortion of sample even at a radiation dose of 10^{10} Gray (1Gy=1J/Kg) and can also image frozen hydrated biological samples in parallel maintains structure close to its native state (Maser *et al.*, 2000). The technique used for investigating ultrastructure of cryopreserved female inactive X-chromosome by soft-X-ray tomography (SXT) in combination with cryogenic fluorescent microscopy (CFT) has been applied for the molecular localisation in a nucleus (Smith *et al.*, 2014). Moreover, a frozen hydrated yeast cell was

resolved at the resolution of ~ 25 nm using soft-X-ray diffraction imaging (Huang *et al.*, 2009).

Using hard-X-ray's, the spatial resolution of ~1 μm can be achieved because of its high penetrating capacity (Yamamoto and Shinohara, 2002) and the wavelength falls in angstrom therefore giving high resolution. This gives better images with contrast and does not require invasive staining. The third-generation synchrotron radiation source is used to generate photon energies between 5- 10 KeV and can image biological samples with a thickness of 100 nm (Guk *et al.*, 2008). Moreover, "lensless" hard-X-ray's gives improved three-dimensional images of biological samples through phase contrast, which provides an electron density map of matter (Nishino *et al.*, 2009), whereas soft-X-rays gives absorption information (Shapiro *et al.*, 2005). Soft-X-ray is limited to resolution but prevent radiation damage (Kirz, Jacobsen and Howell, 1995). Hard-X-ray is an efficient technique for thick samples, like chromosomes, because of its strength of penetrating power along with spatial resolution ability (Shemilt *et al.*, 2015).

Moreover, scanning X-ray fluorescence microscopy has been used to map the signal of iron (Fe), phosphorus (P) and sulphur (S) in human nuclei, whereas P and S presumed to be associated from DNA content in the nuclei (Robinson *et al.*, 2016). The first ever attempt to images micron-sized details of high order structure of chromosome using SCALA X-ray Free Electron Lasers (XFEL) facility in Japan using MAXIC chamber to avoid radiation damage to the biological sample (Robinson *et al.*, 2015), as a result, 400,000 diffraction patterns were collected.

1.8.1. Coherent X-ray diffraction imaging (CXDI)

Coherence is an interference of two waves and has been applied in a four different ways; i) plane wave CDI for fixed sample illumination, ii) ptychography CDI for non-periodic substances with a fixed illumination), iii) Bragg CDI for nanocrystal structures and iv) curved wave CDI for large field of view (Miao, Sandberg and Song, 2012) to investigate internal and external structure of the

samples and to understand the function of the molecules (Henry N Chapman *et al.*, 2006). CDI is a lensless method using computerised algorithms to reconstruct obtained diffraction patterns into a high-resolution and better phase contrast images (Robinson, 2015). In addition, Fresnel zone plate (FZP) is used to converge the planer incident beam onto the targeted positions (Schroer *et al.*, 2003). Basically, FZP are designed into concentric circles with different radial symmetry, which is divided into opaque and transparent rings, so that the beam can only pass through alternative transparent rings to obtain a constructive interference point (Batey *et al.*, 2019) (Rau *et al.*, 2016). The FZP is the best option for lensless imaging as it diffracts the upcoming monochromatic beam to converging point (Chapman and Nugent, 2010). Forward scattering CDI is a unique approach to image biological sample at a high resolution, here, far field, scattered diffracted patterns are collected once the incident beam hit the isolated sample to reconstruct into images (Chapman and Nugent, 2010).

An example of coherent X-ray imaging to study a human chromosome is the first attempt by Nishino et al, 2009, to image 3-D, ultra-structure of unstained human metaphase chromosome at photon energy of 8 KeV. The obtained diffraction patterns were processed using a hybrid input output (HIO) phase retrieval algorithms (Nishino *et al.*, 2009). Although, only axial structure was resolved (Figure 1.13) not the internal structure of the chromosome (Nishino *et al.*, 2009).

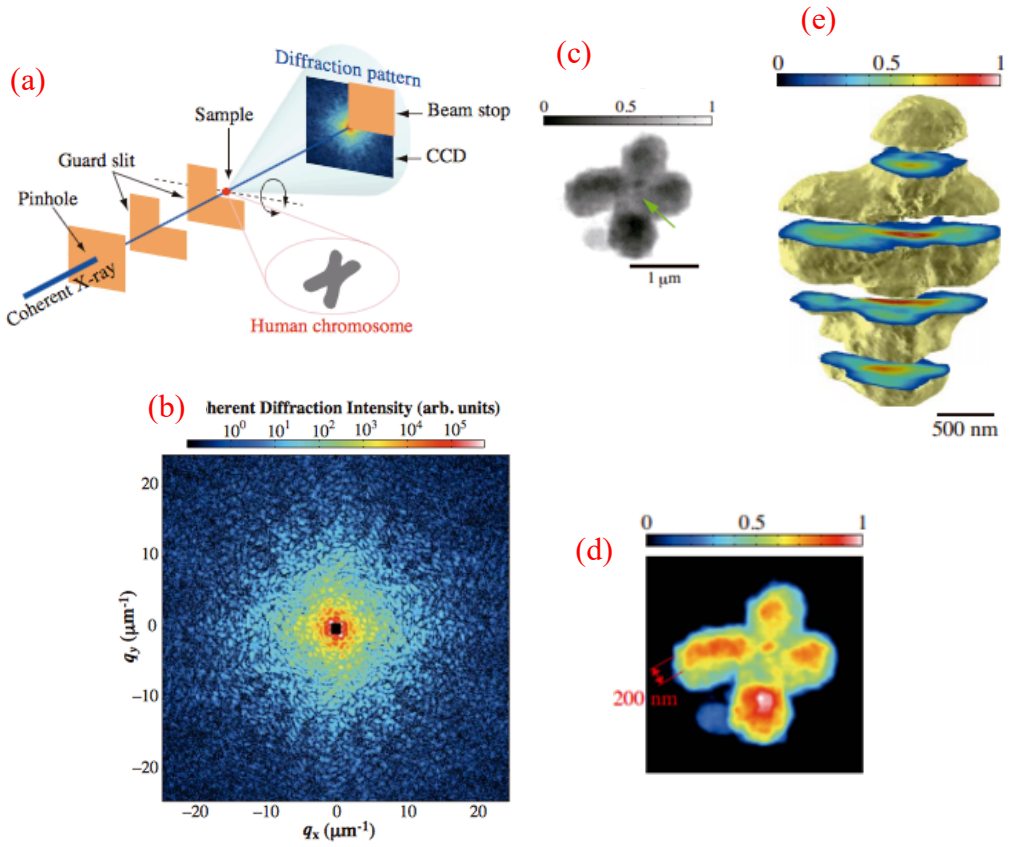

Figure 1.13: Hard-X-ray coherent diffraction imaging of an unstained human chromosome; a) schematic of the coherent X-ray setup, b) the obtained speckle pattern from the chromosome, c) gray scale image, green arrow indicate the centromere, d) indicate the axial structure at 200 nm resolution and e) cross-sectioned at a 409 nm intervals for 3D analysis (Nishino *et al.*, 2009).

Moreover, Yan et. al. (2016) developed a new technique of imaging by combining hard-X-ray with a nano-focusing optic which enabled to detect a platinum blue (Pt-blue) stained human chromosome even without sectioning. Therefore, the nanoscale information can be obtained from the absorption, phase contrast and fluorescence intensity, simultaneously (Yan *et al.*, 2016). Eventually, the ultra-structure of a thick chromosome was obtained.

1.8.2. Ptychography

In principle, ptychography CDI is a technique in which an object is illuminated and scanned in a step-wise fashion to produce an array of partially overlapped probe spots onto the object, furthermore, obtained diffraction patterns from each spots recorded and run through a complex inverse Fast Fourier Transform (FFT) algorithms (Figure 1.14) to reconstruct diffracted patterns into images

(Sidorenko and Cohen, 2016) (Rodenburg *et al.*, 2007). The output is a pair of images, one is amplitude- measures the extent of light absorbed by the sample and the other is phase- measures the phase delay introduced to the beam as it passed through the sample. Ptychography solves the phase problem by combining the diffraction patterns of overlapping images self consistently (Robinson, 2015) (Stachnik, 2012).

The combination of high penetration power of hard-X-rays and sensitivity of “lensless” CDI are benefits of ptychographic imaging (Dierolf *et al.*, 2010), which means it has potential for qualitative imaging with a nanometre of resolution, also minimises the loss of data from the sample. The method gives phase information (electron density maps) across the large field of view (Rodenburg *et al.*, 2007). Moreover, the ptychography corresponds to the “Nyquist-Shannon Theorem” of oversampling (Henry N. Chapman *et al.*, 2006) because it combines obtained overlapped images of an object into a fine image. Oversampling illumination spots make phasing easy by increasing the magnitude of Fourier transform by a factor of 2X (Miao, Sayre and Chapman, 1998).

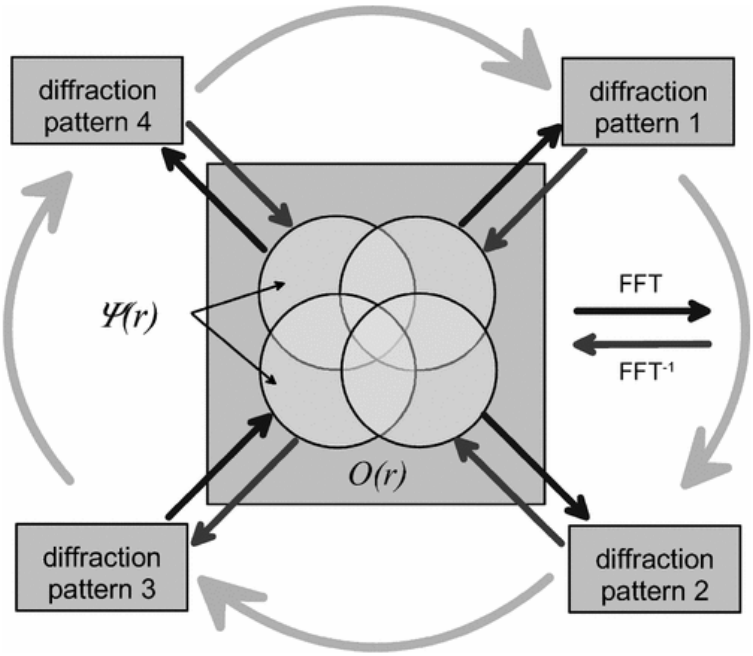

Figure 1.14: Ptychographic phase-retrieval algorithm used for reconstruction of diffraction patterns into relative images (Rodenburg *et al.*, 2007).

The reconstruction is an important step to retrieve frame-by-frame information of an object by using a basic ptychographic algorithm called Ptychographical Iterative Engine (PIE) to solve the phase problem, however, it has a drawback of constant illumination function of wave front (Rodenburg *et al.*, 2007). Although, the revised extended PIE (ePIE) algorithm considered both, object function and complex illumination (probes) function (Maiden, Johnson and Li, 2017) which constrain the image and give a better resolution. Furthermore, in ePIE, the simple Fourier transform wave front incident on the sample and obtained diffraction patterns processed with inverse FFT to reconstruct into a high-resolution image along with a decreased signal to noise ratio due to partial spatial coherence (Stachnik, 2012) (Robinson, 2015). The algorithms iterate between real and reciprocal space applying constrain in both spaces until a solution is reached. It is a powerful tool to study thick samples at a high spatial resolution.

In order to obtain a good reconstruction of an image from redundant scanning positions, certain parameters should be set priori, like illumination probe function and translation steps, the former should be smaller than the latter (Zhang *et al.*, 2013). Oversampling of the object is taken into account by measuring the distance between the detector and the sample, sample thickness, aperture size, pixel size and the wavelength of an incident beam to obtain diffraction patterns from the object (Miao, Sandberg and Song, 2012). Ptychography improves the spatial resolution and provides the phase information without a prior knowledge of the object (Howells *et al.*, 2009) (Rodenburg *et al.*, 2007).

Biological samples imaged using ptychography are freeze-dried diatoms at a resolution of 30 nm, bacteria at a 20 nm resolution, frozen-hydrated yeast at a 85 nm resolution and 3D nonporous glass at a resolution of 30 nm (Deng J. *et al.*, 2015). Corelative imaging of X-ray fluorescence microscopy (XRM) and X-ray ptychography used to image whole frozen-hydrated *C. reinhardtii* alga cells to mapping the elemental constituent in a 3-D fashion by including tomography to obtain 3-D view of the cells (Deng *et al.*, 2019). XRM used to get fluorescence signal from available element and ptychography for spatial

resolution and the acquired resolution is ~ 2 μm. Soft-X-rays ptychography has been applied to obtain chemical information from ~ 2 μm thick freeze-dried *Deinococcus radiodurans*, without slicing and staining at a photon energy of 512 eV in the water window (Beckers *et al.*, 2011). Moreover, ptychography CDI has been used to obtained quantitative information of human metaphase chromosome to build a karyotype on the basis of mass (Shemilt *et al.*, 2015), and an first attempt by Prof Robinson's group to image human nucleus under cryogenic condition (Yusuf *et al.*, 2017).

The other methods are resin embedding, the resin polymerizes at 60-70 °C and become a hard-plastic resin which further sliced into an ultrathin sections for imaging (Yusuf, *et al.*, 2014) (Chen *et al.*, 2017). In addition, the reliable and growing technique is plunge freezing for atomic to molecular level of investigation as it maintains the native state of the biological specimen also protect from radiation damage while imaging (Yusuf *et al.*, 2017). During plunge freezing the samples gets vitrified in liquid ethane and later stored in liquid nitrogen for future use.

1.8.3. Mass-based human karyotype

Karyotyping and identifying individual human chromosomes is an important cytogenetic analysis. The phase-contrast ptychography CDI scanning (Rodenburg *et al.*, 2007) used in current investigation to obtained nanoscale resolution across the extended field of view. In order to measure the quantitative mass of an isolated chromosomes obtained from reconstructed images of chromosome spread. It has been shown earlier that ptychography has sufficient resolution to karyotype chromosomes by their relative mass (Shemilt *et al.*, 2015).

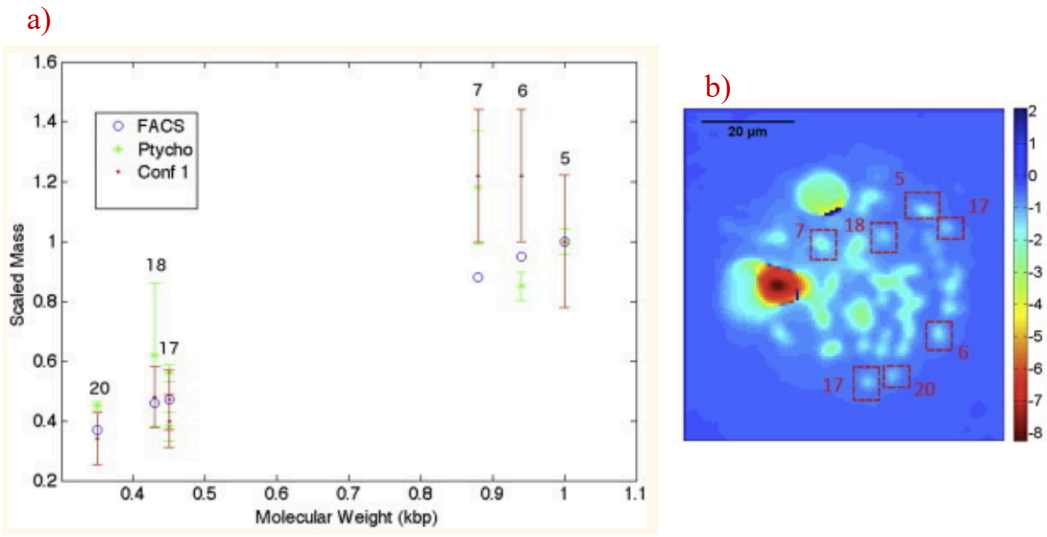

Figure 1.15: A first attempt to measure the mass of the human metaphase chromosomes using hard X-ray ptychography versus known molecular weight available from human genome sequence. a) Comparative partial karyotype using fluorescence-activated cell sorting (FACS), X-ray ptychography and confocal imaging b) phase image of human metaphase chromosomes spread obtained X-ray ptychography, scale bar= 20 µm (Shemilt *et al.*, 2015).

A partial karyotype was performed from the quantitative information obtained the measured mass of the chromosomes using phase-shift hard X-ray ptychography technique (Shemilt *et al.*, 2015). It was a first attempt to demonstrate that the phase-shift gives an accurate measure of the electron density map from X-ray ptychography method along with high spatial resolution of thick mitotic chromosomes (Shemilt *et al.*, 2015). The relative mass was calculated from the acquired largest chromosome 5, to build a partial karyotype (Figure 1.15), including chromosomes 5, 6, 7, 17, 18 and 20 versus known molecular weight from sequencing. Similarly, the mass of the human nuclei was obtained using quantitative phase-shift, hard X-ray ptychography and optimised ePIE algorithms which falls within range of hundreds of picograms (Schwenke *et al.*, no date), unpublished work). Both the X-ray ptychography experiment was performed at I-13-coherence branch, Diamond Light Source.

Moreover, quantitative 3-D structural information of 36 out of 46 chromosomes were obtained from a prophase nuclei using SBFSEM technique, from which the volume information was rendered to build a karyotype- between measured chromatid volume and

the known DNA sequences (Figure 1.16) and linear regression fit supports the relation (Chen *et al.*, 2017). The morphology and the localisation of chromosomes in the prophase nuclei were used to extract the volume of each individual chromosomes.

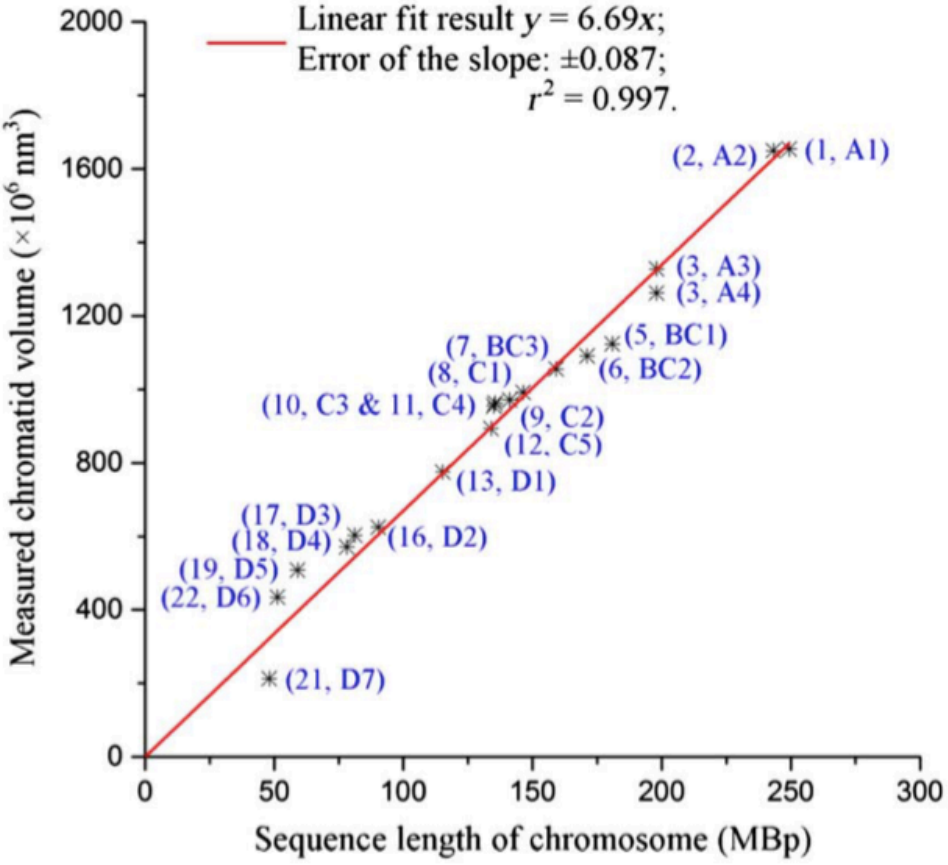

Figure 1.16: Volume karyotype of human chromosomes obtained from prophase nuclei against known DNA sequence length of chromosomes using using SBFSEM technique. Although only 36/46 chromosomes were recovered. The linear fit supports the relation between measured chromatid volume versus sequence length (Chen *et al.*, 2017).

1.8.3.1. Metaphase chromosomal proteins

The masses are the components of DNA and proteins, required for the packaging of each individual human metaphase chromosomes (Maeshima and Eltsov, 2008) (Maeshima *et al.*, 2014) (Gookin *et al.*, 2017). In this study, the accurate masses were measured using the X-ray phase sensitivity of ptychographic CDI technique, combined with reconstructing ptychographic

algorithms used in I-13-beamline, Diamond Light Source (DLS), Oxford, UK (Rau *et al.*, 2019). The known DNA sequences obtained from HGP and known histones (H3, H4, H2B and H2A) and non-histone proteins (example topoisomerase IIα and condensin) and many more from (Uchiyama *et al.*, 2005), used to estimate the mass of the chromosome to established linear regression relationship between measured and estimated masses of all 46 human metaphase chromosomes. However, the protein calculation has been shown in Table 4.2 And Table 4.3 (see chapter 4) of metaphase chromosome along with measured mass and expected masses of unstained irradiated chromosomes.

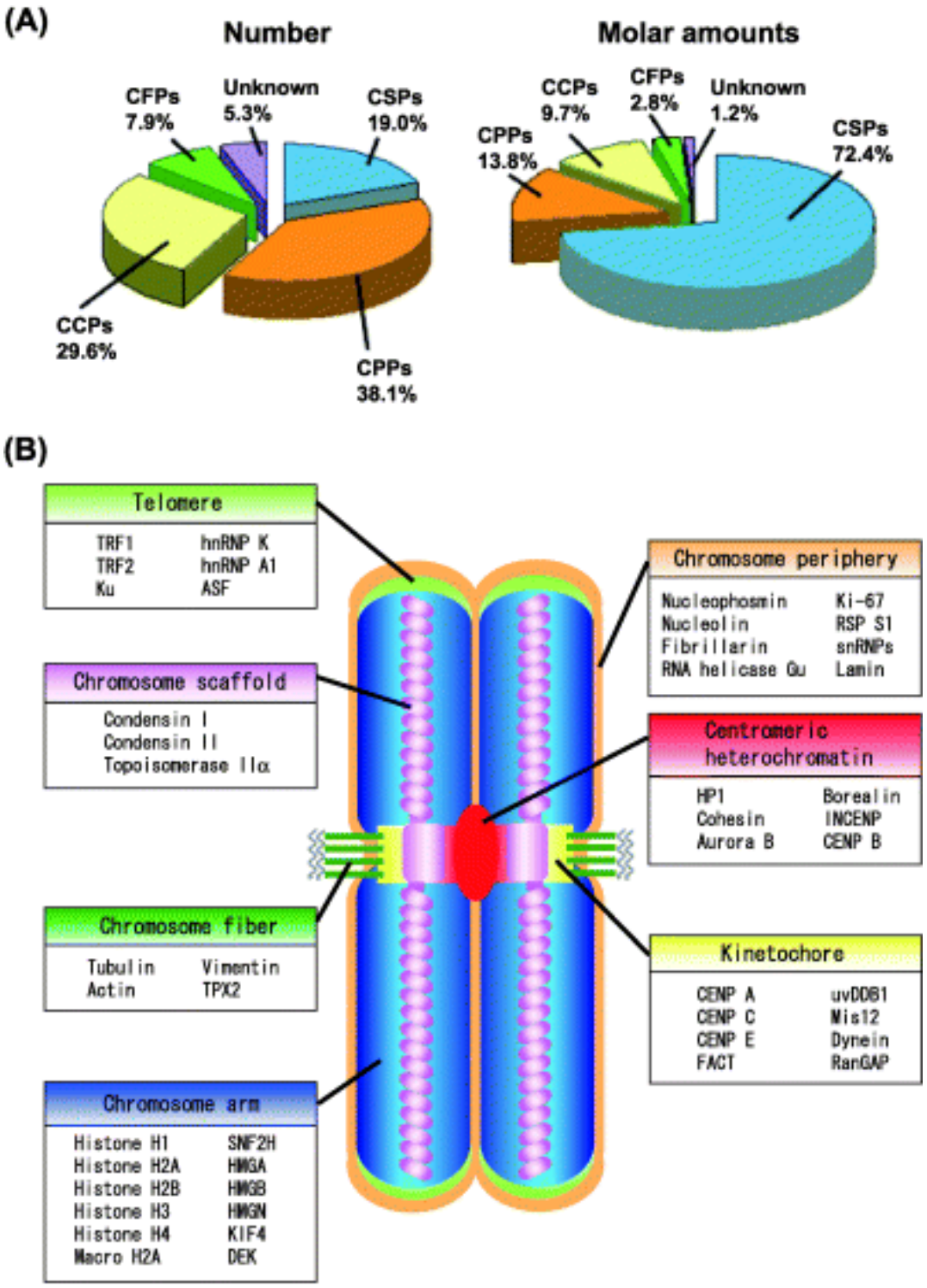

Figure 1.17: A list of isolated proteins obtained from polyamine treated metaphase chromosomes, classified into four groups: CSPs, CPPs, CCPs and CFPs, A) The pie charts shows the four groups of chromosomal proteins and their relative sub-proteins, represented in numbers and in molar amount and B) represents the different proteins classified into seven sub-regions of a metaphase chromosome (Takata *et al.*, 2007).

In 2007, Takata et al, identified more than 200 chromosomal proteins in an isolated HeLa cells using two proteomic analysis technique like one-dimensional-SDS-PAGE and radical-free and highly reducing two-dimensional electrophoresis (RFHR 2-DE) (Takata *et al.*, 2007). Moreover, they have classified chromosomal proteins into four groups: "i) chromosome coating proteins (CCPs), chromosome peripheral proteins (CPPs), chromosome structural proteins (CSPs) and chromosome fibrous proteins (CFPs)" from HeLa S3 cells (Takata *et al.*, 2007) as shown in Figure 1.17. Earlier, chromosome isolation and proteomic analysis technique were optimised to extract accurate amount of proteins present in a human metaphase chromosome (Uchiyama *et al.*, 2005). Consequently, chromosome isolated with percoll density gradient is 107 proteins, whereas, with polyamine buffer, 158 proteins were identified (Uchiyama *et al.*, 2005). Therefore, polyamine buffer is suitable for chromosome isolation without much of protein degradation and structural conformation distortion. Apparently, histone protein contributes 60 % to the chromosome structure (Uchiyama *et al.*, 2005). The amount of chromosomal proteins differs at a different stages of the cell cycle.

1.9. Ionisation radiation of chromosomes

Ionising radiation (IR) causes a wide spectrum of lesions including DNA single-strand breaks, double strand Breaks (DSBs), base damage and DNA–protein crosslinks. Among them, DSBs are considered to be lethal and possibly to cell killing. Most probably, the DSBs are non-repairable or mis-repaired which leads to chromosomal aberrations (CAs); (Balajee *et al.*, 2014). Aberrations can be caused by external factors like ultraviolet (UV), exposures to sunlight, ionising radiation (X-rays, gamma rays) and toxic chemicals and aberrations also rely on radiation quality, dose and dose rate. On other hand, internal factors like unequal cell divisions, replication errors and the enzymatic reactions can also cause aberrations (Jain *et al.*, 2017). Exposure to radiation can cause simple or clustered DNA damage. However, one or two aberrations per DNA helical turn leads to double DNA strand breaks (Lomax, Folkes and Neill, 2013).

The X-ray irradiation deposits some energy, characterised as low or high "Linear energy transfer" (LET) when passed through the biomolecules that results in chemical modifications in a DNA (Lomax, Folkes and Neill, 2013) (Desouky, Ding and Zhou, 2015). The energy absorbed by water content present in a biomolecule, causes water radiolysis, that breaks down water molecules into free radicals of H^+ and OH^- (Azzam, E. Jay-Gerin, J. Pain, 2012). Furthermore, the free radicals form reactive recombination such as toxic superoxide that leads to DNA damage (AbdulSalam, Thowfeik and Merino, 2017).

A recent finding confirms that apart from irradiated cells, the nearby, non-irradiated cells also become affected. This phenomenon is called the "Bystander effect" and it only occurs at low radiation dose (Desouky, Ding and Zhou, 2015). IR-induced DSBs can occur either in a random or non-random style (Balajee *et al.*, 2014), in either case inhibit the replication and the transcription process (Schwer *et al.*, 2016) in any upcoming cell divisions. All these CAs may cause major phenotypic problems; including cell death, mutations and genomic instabilities (Ojima *et al.*, 2015). The other factor is phosphorylation of histone variant H2AX into *γ*-H2AX that introduces DSB breaks (Dickey *et al.*, 2009) in chromosomes. In addition, *γ*-H2AX is an common aberration upon ionising radiation for the identification of DSB breaks by using *γ*-H2AX foci assay (Dickey *et al.*, 2009) (Nair *et al.*, 2019).

There are two major types of chromosomal aberrations such as numerical and structural aberrations. Numerical aberrations consists of aneuploidy (occurring due to improper distribution of chromosomes at the anaphase stage of the cell cycle for example trisomy and monosomy) and triploidy (missing of one homologous pair) (Tobias, 2011). These defects are known as non-dysjunction, and take place at mitosis and later at meiosis phase of the cell division (Tobias, 2011). The structural aberrations occur either due to breakage or irregular reunion, which is consequence of exposure to mutagens and/or ionising radiations.

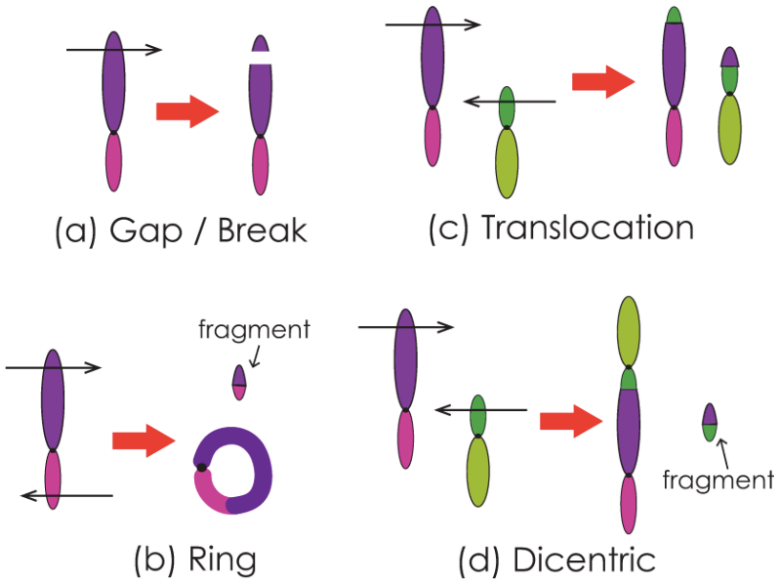

Figure 1.18: The four typical X-ray induced structural chromosomal aberrations (Ouchi, 2015).

The structural aberrations are classified as: I) duplication (gain of extra segment from another chromosomes), ii) deletion (loss of part of a chromosome), iii) translocation (transfer of DNA contents between homologues or non-homologous chromosome pairs), iv) inversion (rotation of gene sequence by 180 degrees), v) Isochromosomes (deletion of one arm with an addition of other), vi) dicentrics (presence of two centromeres in a chromosome) and vii) ring chromosomes (joining of two broken ends together) (Tobias, 2011) (Ouchi, 2015); (Figure 1.18). Though, chromosome aberrations induce "sticky" breakpoint ends which become joined by repair mechanism such as Non-Homologous End Joining (NHEJ) and Homologous Recombination (HR); (Blanpain *et al.*, 2011), with the help of specific enzymes (Figure 1.19). Subsequently, failure of the repair process can produce large-scale rearrangements and recombination of the human genome and eventually causes disease such as cancer (Aparicio, Baer and Gautier, 2015).

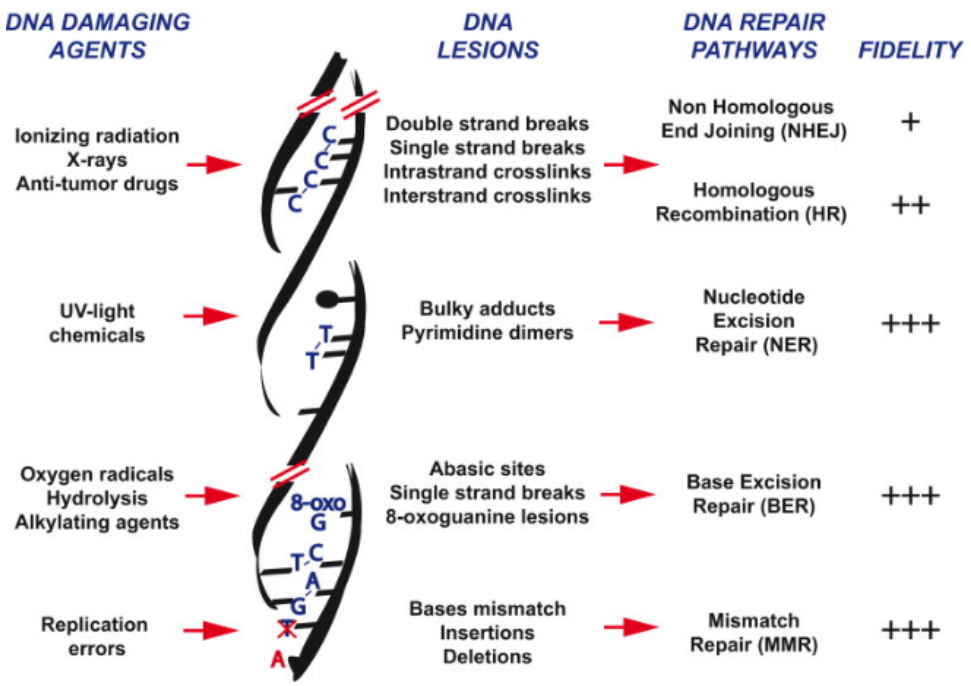

Figure 1.19: Potential regions prone to DNA damage and the response repair mechanism in mammalian cells (Blanpain *et al.*, 2011).

When chromosomes are radiated with X-ray ionising radiation, mutations and unusual genomic behaviours occur. Cells irradiated with 1 Gray (1 Gy = 1J/Kg absorbed dose) to 2 Gy can resist the radiation dose but slow down their cell division and DNA damage repair mechanisms. Subsequently, they have a decrease in cell viability and can have acute levels of DNA damage such as like exchanges and deletion of segments of chromosomes, though, this does not affect the transcription process (Borràs-fresneda *et al.*, 2016). Major aberrations usually occur with higher radiation doses starting from 1Gy to 5 Gy. This leads to a decrease of metaphase chromosome numbers and an increase in the frequencies of dicentric, acentric (with no centromere) and ring chromosomes (Ryu, Kim and Kim, 2016). Furthermore, the dicentric chromosome numbers decrease from first, second and to the third mitotic cell division. The number of acentric and the centric aberrations, which occurred due to deletion of telomeres, are found to increase from one mitotic cell division to another (Kaddour *et al.*, 2017).

However, acentric and the centric could be the reason for CAs transmission from subsequent mitotic cell cycles rather than dicentrics, and these leads to genomic instability.

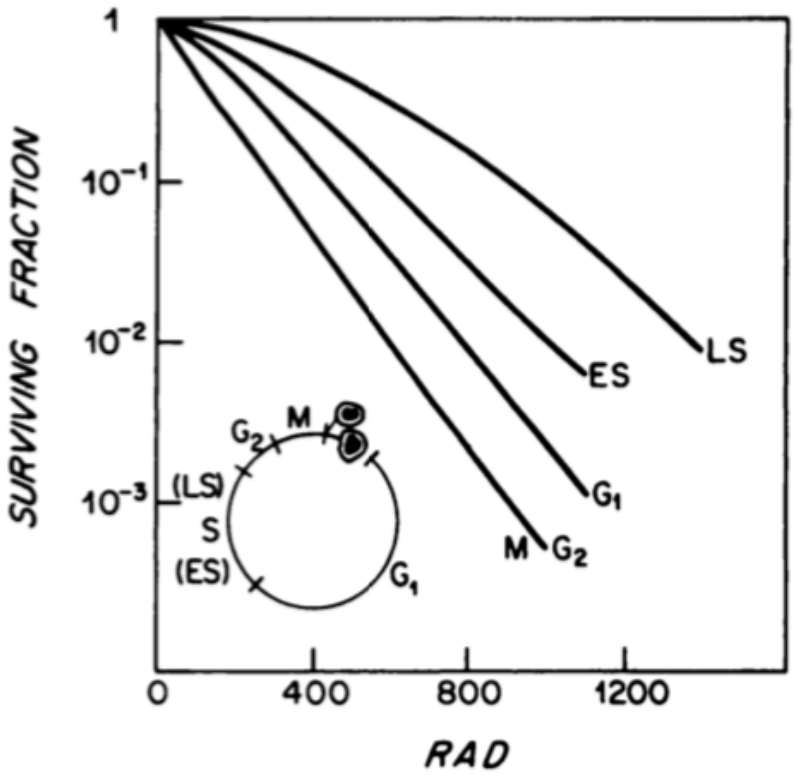

Figure 1.20: The surviving fraction of the mammalian cells at a different stage of the cell cycle upon low ionising radiation (x-axis). Interphase consist of G1, S and G2 phase, M=mitosis, LS= late synthesis and ES=early synthesis. The inset defines the duration of each stage of cycle and the two daughter cells separated during cytokinesis (Bloomer and Adelstein, 1982).

Figure 1.20 indicates that at low ionising radiation, the mammalian cells at S-phase are more resistant to irradiation especially at the late synthesis (LS) phase whereas G2 phase cells are more prone to radiation (Bloomer and Adelstein, 1982). Radiation leads to chemical modification in the genome which is main cause of cell death (Bloomer and Adelstein, 1982). There are considerable data showing a relationship between cell killing and the induction of chromosome aberrations. The frequency of inter-chromosomal aberrations calculated in chromosomes 1 , 2 and 4 at G0 phase of the cell cycle at X-ray dose of 0 Gy, 2 Gy and 4 Gy “(mean ± SE; 0.02 ± 0.02 for 0 Gy, 0.75 ± 0.21 for

2 Gy and 2.10 ± 0.48 for 4 Gy)" (Ryan *et al.*, 2019). Moreover, it was also analysed that q-arm is 10x times more prone to breaks than p-arm (Ryan *et al.*, 2019). Henceforth, the frequency of chromosome aberrations is a linear function of radiation dose. With long-term exposure of low-level of ionising radiation raises the risk of chromosomal aberration comparative to haematological alterations (Rozgaj *et al.*, 1999).

Techniques used for CAs analyses are Giemsa staining (Sumner, 1982), Fluorescence *In Situ* Hybridisation (FISH) (Bishop, 2010), flow cytometry and 24-colour multiplex Fluorescence *In Situ* Hybridisation (M-FISH) (Anderson, 2010). These techniques have their limitations such as Giemsa metaphases can mislead the results if the procedure of Giemsa staining alters in the terms of the duration of staining, pH variation or trypsin treatment (prior to staining) is imbalanced (Duijn, Prooijen-Knegt and Ploeg, 1985) whereas FISH and M-FISH are insufficient to identify minor changes within chromosomes (Bishop, 2010) (Anderson, 2010) such as intrachromosomal arrangements. Flow cytometry is only significant for detecting numerical aberrations (Muehlbauer and Schuler, 2005).

However, in this study, FLIM and X-ray ptychography has been used to investigate the CAs occurred upon X-ray radiation at low-level doses of X-ray, in chromosomes obtained from B and T-lymphocytes. The study has been done on different generation starting from G0 (straight after X-ray exposure) to G2 (48 hrs after exposure) (see chapter 2, Materials and Methods).

1.10. Aims and objectives of this thesis

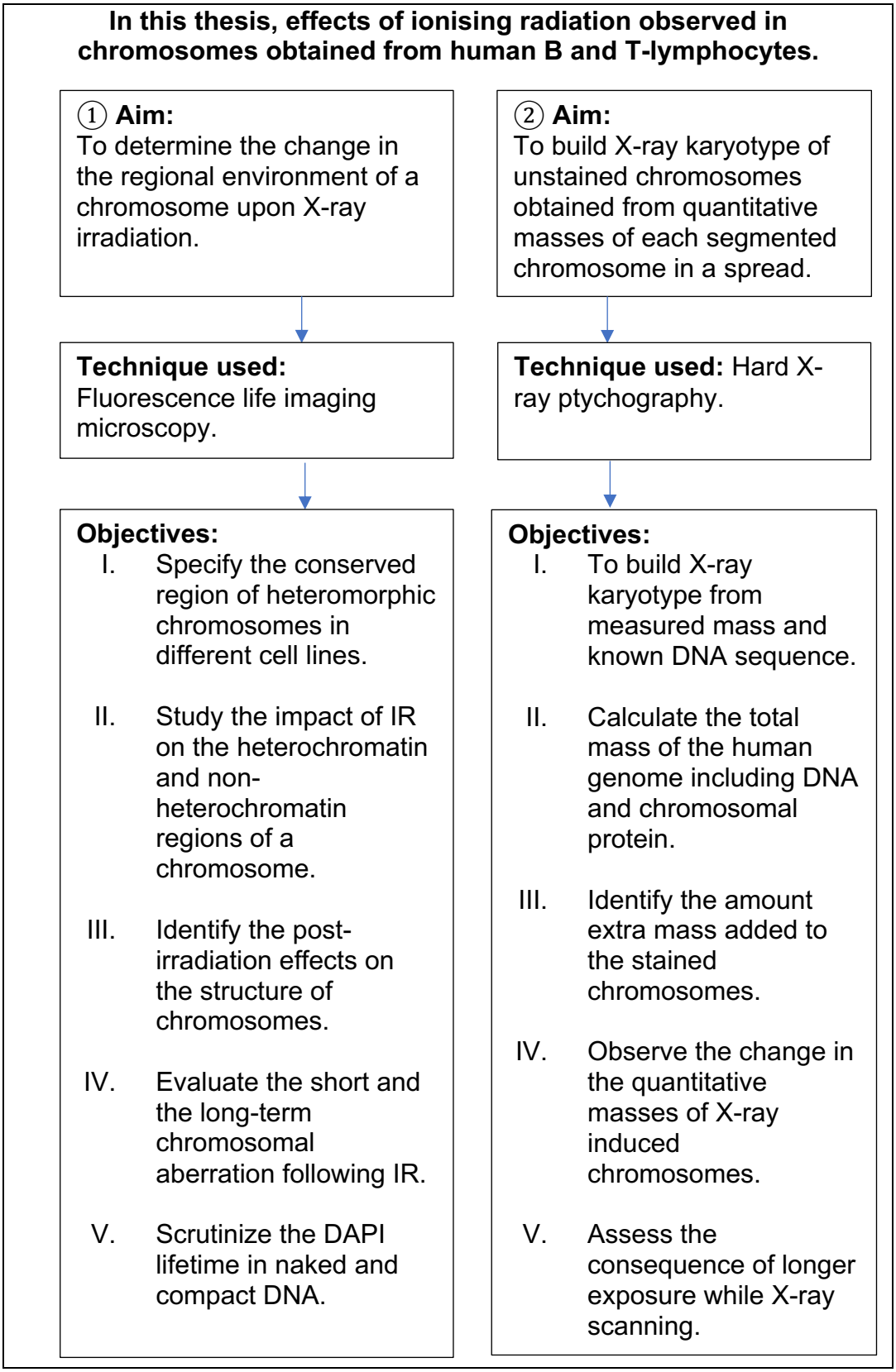

Figure 1.21: The outline of this thesis.

Chapter 2

2. Materials and Methods

All solutions were prepared using milliQ Millipore water (prepared by purifying deionized water, to attain a sensitivity of 18 MΩ -cm at 25 °C). Though chemical compounds described were purchased from Sigma Aldrich, UK, unless otherwise stated. All cell culture processes were performed inside a Laminar Air Flow (LAF) under a sterile condition.

Primary T- lymphocytes cells were donated by a 22 years old female. T-lymphocytes was a gift from Dr Ken Raj's group, Public Health England (PHE), Oxford, UK. Additionally, lethally irradiated lymphoblastoid cells (GM1899A, provided from PHE) were used as feeder cells. The primary T-cells were cultured in the laboratory of PHE and maintained by Dr Ken Raj's group (Dr Sylwia Kabacik, PHE). The T-cells are suspension cells and were used at passage 3, 4 and 5 in a current investigation.

2.1. Primary T-lymphocytes cell culture

2.1.1. Lymphoblastoid cell line culture

3 x 10^6 cells were thawed at 37 °C in a water bath for two minutes and then transferred in a 15 ml conical bottom tube containing 10 ml of lymphoblastoid cell growth medium (LCGM), consisting of Roswell Park Memorial Institute (RPMI-1640 (1X)) medium supplemented with 20% heat inactivated foetal bovine serum (FBS), 1 mM sodium pyruvate, 2 mM L-glutamine, 100 U/ml penicillin, 100 µg/ml streptomycin (all from Invitrogen/Life Technologies). Cells were mixed by inverting the tube (until the solution homogeneous) and centrifuged for 5 mins at 1200 revolution per minute (rpm). The supernatant was aspirated followed by the cell pellet resuspended in 10 ml of LCGM and

transferred in a vented 25 cm^2 culturing flask. Flasks of cells were incubated at 37 °C with 5 % CO_2 in the upright position for 3 days. At this stage, cells were disaggregated by trypsinizing and counted at daily intervals using an ADAM cell counter (see section 2.1.5.). When cell numbers reached to 0.8 x 10^6, 10 ml of fresh LCGM was added and the cells were transferred to a 75 cm^2 flask. The cell number was maintained between 0.6 to 0.8 x 10^6 per ml by adding fresh LCGM medium.

2.1.2. Feeder cell preparation

Lethally irradiated lymphoblastoid GM1899A cells were used as feeder cells for human T-lymphocytes. The culturing conditions for this lymphoblastoid cell line are described in the section 2.1.1. The feeder cells were prepared as follows: when the culture reached to 5 x 10^7 cells, the cells were transferred in one or two 50 ml conical bottom tubes (depending on the volume) and centrifuged at room temperature for 5 mins at 1200 rpm. The supernatant was aspirated and cell pellets were resuspended in 5 ml of LCGM. The cells were lethally irradiated with x-rays at room temperature with a dose of 40 Gray (Gy), at dose rate of 1.7 Gy/min. The lethally irradiated cells were mixed with freeze mix consisting of 10 % dimethyl sulfoxide (DMSO, Sigma-Aldrich Company Ltd., Gillingham, UK) and 90 % of FBS (Life Technologies) to 3 x 10^6 cells per ml. One millilitre aliquots of the mixture were transferred to cryovials and frozen at -80 °C in Mr. Frosty™ (Thermo Scientific) containers which allow cooling at rate of 1 °C per minute. The next day, the vials were transferred to the liquid nitrogen container for long-term storage.

2.1.3. Preparation of human stimulated T-lymphocytes

The stimulated human T-lymphocytes were prepared as follows: 10 ml of blood from a 22-year-old female donor was collected into BD Vacutainer® lithium heparin tubes (Becton Dickinson). 5 ml of Histopaque-1077 (Sigma-Aldrich) pre-warmed to room temperature was aliquoted into four 15 ml conical bottom centrifuge tubes. 10 ml of blood was mixed with 10 ml of Hank's Balanced Salt Solution (HBSS, Life Technologies) pre-warmed to room temperature in a 50

ml conical bottom tube (Figure 2.1). 5 ml of diluted blood was layered slowly onto each of the four tubes containing Histopaque-1077 using a sterile pastette (Alpha Laboratories, Eastleigh, UK). Tubes were centrifuged at room temperature at 1600 rpm for 20 min. Following phase separation, the top serum layer was aspirated from each tube leaving around 0.5 cm of liquid above the buffy coat cell layer. The buffy coats from sample tubes were collected and transferred into fresh 15 ml tube containing 10 ml of HBSS and mixed by inverting 5 - 6 times. The tubes were centrifuged at room temperature at 1200 rpm for 5 mins. The supernatant was aspirated followed by re-suspending cell pellet in 5 ml of HBSS. Suspended cells were combined into one tube and centrifuged again at room temperature at 1200 rpm for 5 mins. After the supernatant was aspirated, the cells were washed twice with 10 ml of HBSS and a 20 µl aliquot of cell suspension was taken for cell counting. The tube was centrifuged at room temperature at 1200 rpm for 5 mins and the supernatant was aspirated. Next the cells were re-suspended at a concentration of 3 x 10^6 cells per ml in freeze mix, then transferred to cryogenic vials in Mr. Frosty™ container and frozen at -80 °C. The next day vials were transferred to liquid nitrogen container for long-term storage.

2.1.4. Culturing conditions of T-lymphocytes

A cryovial containing 3 x 10^6 cells, passage-5, was thawed at 37 °C in a water bath for two minutes. The cells were transferred to a 15 ml conical bottom tube containing 10 ml of stimulating growth medium (SR10) containing of RPMI 1640 (Dutch modification) supplemented with 10 % heat inactivated FBS, 1 mM sodium pyruvate, 2 mM L-glutamine, 100 U/ml penicillin, 100 µg/ml streptomycin, 50 µM 2-mercaptoethanol (GIBCO/Life Technologies), 20 U/ml recombinant interleukin-2 (IL2; Sigma-Aldrich) and 0.4 µg/ml phytohaemagglutinin (PHA; Sigma-Aldrich). Cells were mixed by inverting the tube and centrifuged at room temperature for 5 mins at 1200 rpm. The supernatant was aspirated, cell pellet was re-suspended in 10 ml of SR10 and centrifuged at room temperature for 5 mins at 1200 rpm.

Prior to mixing feeder cells into T-lymphocytes, a cryovial of feeder cells was thawed in the water bath at 37 °C for two minutes. The supernatant from T-lymphocytes was aspirated and the cells were re-suspended in 10 ml of SR10 (Figure 2.1). The feeder cells were transferred into a 15 ml conical bottom tube containing T-lymphocytes, mixed by inverting the tube several times and centrifuged at room temperature for 5 mins at 1200 rpm. The supernatant was aspirated and the cell pellet was re-suspended in 10 ml of SR10. The cell suspension was transferred to a vented 25 cm^2 flask and incubated at 37 °C with 5 % CO_2 at an angle of about 10° from the horizontal. Cells were left undisturbed for 4 days and thereafter they were disaggregated and counted daily using an ADAM cell counter (see section 2.1.5.). When the cells reached a density of 0.8 x 10^5 cells per ml they were diluted 1:2 with growth medium (GR10) that contained SR10 without PHA.

2.1.5. Cell viability assay

For cell counting and viability, the ADAM cell counter (Labtech International Ltd., Uckfield, UK) was used. Briefly, for every cell count, two 0.5 ml Eppendorfs were prepared. 20 µl of “T” solution (accuStain T for total cell count with a propidium iodide dye) was aliquoted into one and 20 µl of “N” solution (for counting non-viable cells with fluorescent dye) into a second Eppendorf. Cells for counting were disaggregated by vigorous shaking, then two 20 µl aliquots were taken and mixed in tubes containing N and T solutions respectively and samples were incubated for 2 min at room temperature. After incubation, the samples were loaded into appropriate T and N positions in the cartridge and loaded into counter. The cell counter provides a value for total cell number (T), viable cell number (N) and percentage of viable cells.

2.1.6. Exposure to ionizing radiation

Confluent T-lymphocytes cells, 5 x 10^6 cells per ml in a T75 vented cell culture flask were transported to PHE for x-ray irradiation. Briefly, the PHE’s AGO X-ray setup, model CP160/1 (AGO X-RAY Ltd, Martock, UK) was used with x-rays energy kept set at 250 KVp (maximum voltage applied across an x-ray

tube during the creation of x-rays within the X-ray system) with a half value layer of 2 mm of copper and aluminium compound filters and 13 mA current, giving a dose rate of 0.5 Gy/min. Three out of four flasks with 11 ml cell media, keeping one flask as a control, were irradiated with a different radiation doses such as 0.1 Gy, 0.5 Gy and 1 Gy with a duration of 12 seconds (secs), one min, two mins respectively. After irradiation 9 ml of fresh SR10 media was added in each flask and mixed well by shaking manually. Thereafter, to arrest chromosomes at their mitotic (most condensed) stage, colcemid (Karyomax, Gibco by Life technologies (10 µg/ml)) was added at the final concentration of 0.2 µg/ml into each flask. The flask was kept for 16 hours in the incubator at 37 °C with 5% of CO_2 before harvesting.

To attain metaphase chromosomes at their first (24 hrs), second (48 hrs) and the third (72 hrs) generation of the cell cycle, the T-lymphocytes cells were irradiated with a radiation dose of 0.5 Gy at dose rate of 0.5 Gy/min. After irradiation, the cells were kept for 24 hrs, 48 hrs and 72 hrs in the incubator at 37 °C with 5% of CO_2 before adding colcemid (0.2 µg/ml). The cells were incubated with colcemid at 37 °C with 5% of CO_2 for 16 hrs before harvesting. The cell media was replaced with fresh media for flasks left for 48 hrs and 72 hrs.

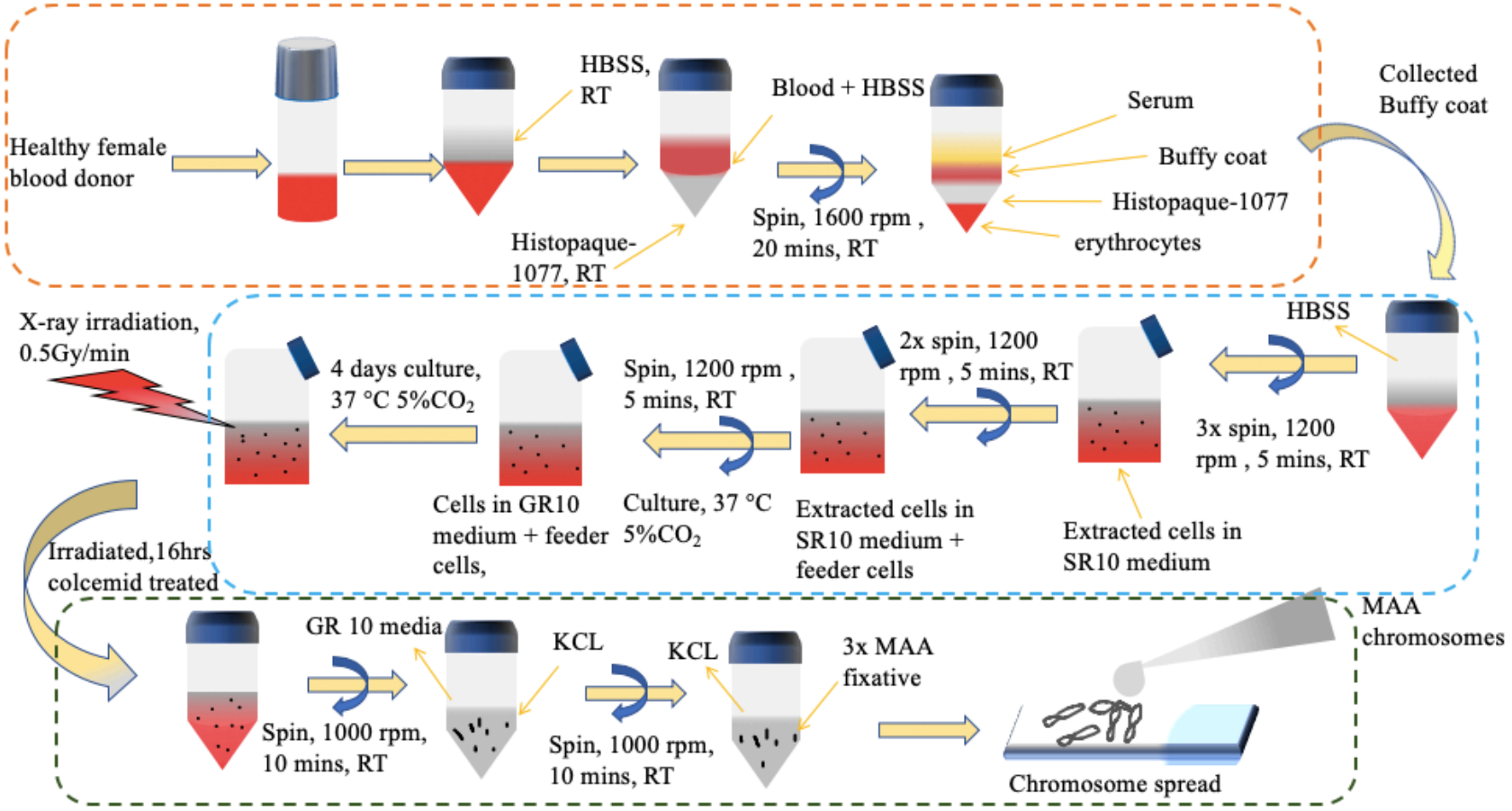

Figure 2.1: Preparation of X-ray irradiated chromosomes from donor's blood. The top panel (orange dotted rectangle) shows the process of extracting T-lymphocytes from the donor's blood. The middle panel (blue dotted rectangle) represents the process of purifying T-lymphocytes, culturing cells and then irradiating with x-ray doses at the rate of 0.5 Gy/min. The bottom panel (green dotted rectangle) represents the process of chromosomes extraction from the obtained cells, fixation with methanol acetic acid (MAA) followed by preparing chromosome spreads for FLIM imaging.

2.2. Yoruba cell line (B-lymphocytes)

2.2.1. Cell culture condition for Yoruba cell line

The B-lymphocytes cells from the Yoruba male cell line (GM18507, International HapMap Project) for the chromosome studies (Shemilt *et al.*, 2014) (Estandarte *et al.*, 2016). The B-cells are suspension cells and were used at passage 15 in this study.

The reagents, 100 ml of thawed FBS (product code- 12103C), 5 ml of penicillin (100 U/ml) streptomycin (100 µg/ml) (product code- P0781), 5ml of L-glutamine (2mM) (product code- 56-85-9) and a 500 ml bottle of RPMI-1640 (1X, product code- R6504) in 37 °C water bath, were mixed well with RPMI-1640 medium. The media was prepared and stored in a 4°C fridge for further use. All regents are from Sigma-Aldrich, UK.

A cryovial containing 2.6 x 10^6 cells /ml, passage-15, was thawed for one minute at 37 °C in a water bath. The cells were transferred to a 15 ml tube containing 5 ml of pre-warmed fresh media. The tube was centrifuged at 1000 rpm for 3 mins and the supernatant aspirated followed by re-suspension of the pellet in 5 ml of fresh media. The cell media was transferred to a vented T25 cell culture flask and left in the incubator at 37 °C for 2-3 days. After 3 days, the cells were transferred into a 15 ml tube and centrifuged at 1200 rpm for 10 mins, then aspirated supernatant and the pellet was re-suspended with 5 ml of fresh media and transferred to a vented T75 cell culture flask. An extra 15 ml of fresh media were added and allowed to grow with sub-culturing every 2 days.

The density of the cells was determined by performing a cell count. 10 µl of media containing cells and 10 µl of Trypan blue dye (0.4%, Life Technology) were mixed in an Eppendorf tube and 10 µl of mixture loaded into the cell

counting cartridge of the cell counter (BIO-RAD) and a measurement was taken.

2.2.2. X-ray exposure for Yoruba cell line

Confluent B-lymphocytes cells, 7.55 x 10^5 cells per ml in a T25 vented cell culture flask were transported to PHE for x-ray irradiation using the AGO X-ray setup (described in section 2.1.6.). Four of five flasks with 5 ml cell media, keeping one flask as a control, were irradiated with a different radiation doses such as 0.1 Gy, 0.2 Gy, 0.5 Gy and 1 Gy with a duration of 12 secs, 24 secs, 1 min, 2 mins respectively. After irradiation, cells were allowed to stand in the incubator at 37 °C with 5% of CO_2 until first (24 hrs), second (48 hrs) and the third (72 hrs) generation of the cell cycle. Afterwards, to arrest chromosomes at their mitotic stage at a different cell cycle, colcemid (10 µg/ml) was added for 16 hrs at the final concentration of 0.2 µg/ml in each flask before harvesting. The cell media was replaced with fresh media for 48 hrs and 72 hrs generation.

2.3. Chromosome preparation from irradiated T and B lymphocytes

Following the process of irradiation and arresting chromosomes at the mitotic stage for both T and B lymphocytes, the cell media from the vented culture flasks were transferred to 50 ml falcon tubes and centrifuged at 1000 rpm for 10 mins. Prior to this, 20 µl of cell media from each flask was used to count the cells using an ADAM cell counter. The cell count ranged from 0.32 - 0.35 x 10^6 cells per ml in each flask for T lymphocytes.

The supernatant from each centrifuged tubes was aspirated followed by addition of 6 ml pre-warmed (37 °C), hypotonic solution (KCl ,75 mM) was slowly added in the falcon tubes (Figure 2.1). The tubes were immediately transferred to the pre-warmed water bath at 37 °C for 8-10 mins and then spun at 1000 rpm for 10 mins. Meanwhile, a prepared fresh methanol : acetic acid solution (MAA) was prepared in the ratio of 3:1 to fix the extracted

chromosomes. After the supernatant was aspirated, 6 ml of MAA were quickly added dropwise and shake immediately to dislodge the pellet in each tube. The tubes were spun at 1000 rpm for 10 mins and then the supernatant was aspirated. The washing procedure with MAA was repeated three times to get clear solutions of chromosomes from both T and B lymphocytes. The prepared chromosome solutions were stored at -20 °C for future use.

2.4. Chromosome mounting

Glass slides (SuperFrost, VWR^{TM}) were first cleaned by soaking overnight in a 70% ethanol solution that effectively removes grease. The slides were wiped with soft tissues and placed in the freezer for 30 mins, for later use for mounting chromosomes on them. Chromosome spreads were prepared on cleaned slides initially stored in a freezer at -20 °C, blown on to create local humidity. 20 µl to 30 µl (depending upon the concentration of chromosomes in the solution) of methanol : acetic acid fixed chromosomes were then dropped from a height of around 40 cm (Figure 2.1). This is the established procedure known to obtain a sufficient number of well-dispersed chromosome spreads on the slides.

The prepared slides were immediately transferred onto the hot plate (45 °C) to dry for 5 mins to 10 mins. Once the slides were dried they were stained with 4', 6-Diamidine-2'-phenylindole dihydrochloride (DAPI, Sigma, H-1200, 5 µg/ml) then covered with a 22 x 50 sized cover slip. The slides were incubated for 10 mins and observed under the fluorescence microscope (Zeiss Z2Axioimager with Isis software). A 10x objective was used to locate the chromosomes and observe the quality (maximum number of chromosome spreads on the glass slides) of the prepared chromosome spreads and a 63x objective (with immersion oil) was used to observe the magnified views of DAPI stained chromosomes. Some chromosome spread slides were left unstained for FLIM imaging.

2.5. Fluorescence lifetime imaging microscopy

This is an imaging technique that records the decay lifetime of a fluorophore from its excited state (Suhling *et al.*, 2012) (see chapter 1, Introduction). It has been applied here to understand the sub-structures of human chromosomes at the submicron level following staining with DNA-binding dye called DAPI (Estandarte *et al.*, 2016).

2.5.1. Preparation of DAPI

4', 6-Diamidine-2'-phenylindole dihydrochloride (DAPI, product code-D1306, ThermoFisher Scientific) is a DNA-specific dye and used as a chromosome counterstain. It excites at a wavelength of around 358 nm and emits blue fluorescence at the wavelength with maximum around 461 nm. DAPI was prepared from powder as follows: a stock solution was prepared by dissolving 5 mg of DAPI in 1 ml of milliQ millipore water to achieve a final concentration of 14.3 mM as a stock solution. For thorough mixing the solution was sonicated for 10 mins then wrapped in aluminium foil and stored in a -20 °C freezer for up to a year. The required 4 µM DAPI for chromosome staining was prepared from the stock solution, also wrapped in aluminium foil and stored at -20 °C for up to a year.

2.5.2. Staining chromosomes with DAPI

The chromosomes spreads were prepared according to sections 2.3. and 2.4 prior to lifetime measurement. Spreads on the slides were stained with a freshly prepared 4 µM DAPI (see section 2.5.1.) and incubated at room temperature for 20 mins in the dark. Following the incubation, the stained slides were soaked in 1x phosphate buffered saline (PBS, pH-7.4, Sigma-aldrich) for 4 mins. Afterwards, the slides were rinsed with milliQ Millipore water, mounted with 3 µl of PBS and covered with a coverslip (22 x 50 mm^2, No.1 or 1.5 depending on the cover glass thickness specifications of the imaging objective).

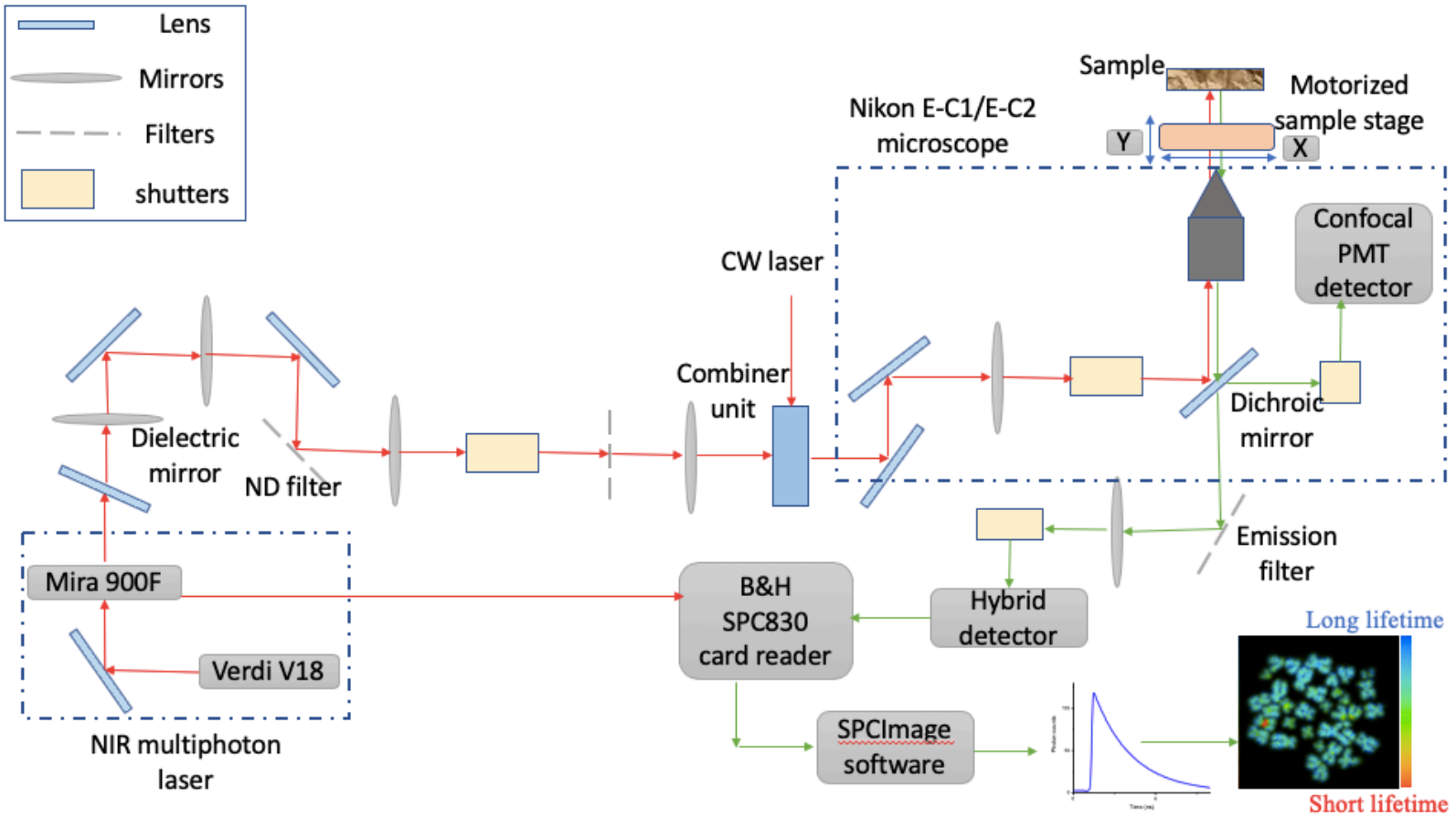

Figure 2.2: Schematic of multiphoton excitation FLIM with a confocal laser scanning microscopy setup. Excitation sources for the multiphoton FLIM were from a Mira 900F (Ti-sapphire laser (Coherent Ltd., UK, Tunable 700-980 nm, pulse length 180-200 fs) pumped by a Verdi V18, operating at 532 nm with a CW outputs. In this study, the laser was tuned to 760 nm. Photons were detected by a hybrid detector HPM 100-40, connected to a time correlated single photon counting PC module, SPC830 (Becker and Hickl). The data were then analysed using SPCImage that calculates the decay curve of the fluorophores and generates a lifetime value at each pixel of the image.

2.5.3. Calibration of the sample stage to correlate the FLIM and the epi-fluorescence microscope

Since the steady state epifluorescence and FLIM microscopes are separate instruments, there is a need to correlate the Field of View (FOV) and region of interest. Here we describe a step by step procedure combining FLIM for investigating chromosome substructure and M-FISH for chromosome identification and karyotyping. Following are the steps for correlative imaging:

1) A reference glass slide “The England Finder” also known as a graticule (Pyser-SGI Ltd.) was used to correlate chromosome images between the two microscopes. The graticule is 3” x 1” in size is the same as a standard glass slide. This has marked square grids at 1 mm intervals. Approximately 20 x, y coordinates on the graticules using both microscopes were recorded. We then calculated a linear equation for both X and Y directions from the obtained coordinates and then applied the same linear equation to transfer the locations of the chromosome spreads from the FLIM to the Zeiss epifluorescence microscope. This allowed identification of the same chromosome spreads imaged from the inverted-configuration multiphoton confocal to the upright- configuration epifluorescence microscope.

2) The first step to FLIM data acquisition is to measure the instrument response function (IRF) of the FLIM setup prior to any data acquisition to check the excitation pulse profile of the instrument. The IRF peak should be at least up to 100 photon counts to check the IRF response and, depending on the laser pulse width, this should not be larger than the detector response so long as the laser width is narrower. We used potassium dihydrogen phosphate (KDP) crystals to determine the IRF. The NIR laser is tuned to 740 -760 nm to excite the crystal and the second harmonic signal is detected. With our instrument, it appears the IRF is mostly defined by the detector response. So that we obtained 20

ps for a detector with a 25 ps response and 110 ps for a detector with 110 ps response. A BG39 band filter is then used to remove the NIR laser light and transmit the DAPI fluorescence signal

3) We calibrated the setup with standard fluorophores such as 100 μM rhodamine B, 100 μM erythrosin B and fluorescein, all prepared in water. 50 μl aliquots of the required fluorophore solution were places on round glass coverslips with thickness number -1 or 1.5 (VWR international). The fluorophore standards were placed on the multiphoton confocal microscope stage and raster scanned using NIR light, in the dark to avoid damage to the detector. The excited fluorescence signals were detected by a hybrid detector HPM 100-40. The lifetime value of the fluorophores, 1.65 ns, 0.12 ns and 3.7 ns were obtained respectively. This is within 5% of the standard literature values and in line with our daily calibration operation values. Once an instrument test and calibration was completed, we recorded the coordinates of the chromosome spreads on which FLIM measurements were taken and then located the same coordinates on the Zeiss epi-fluorescence microscope.

2.5.4. Collection of FLIM data

Chromosomes on prepared slides, stained with 4 μM DAPI (see section 2.5.2.), were located by their x, y coordinates using the epifluorescence microscope initially, followed by the multiphoton FLIM microscope imaging. This was at time done in reverse. In the multiphoton microscope, it was found to be easier to use a 405 nm excitation wavelength initially before using the multiphoton mode to identify the region of interest. Prior to multiphoton imaging mode, it was necessary to make sure the 405 nm laser was switched off. Due to chromatic aberration in our microscopes there is a need to adjust the focus for the 760 nm multiphoton excitation wavelength compared to that at 405 nm. We chose optimal excitation average power to avoid photobleaching of the DAPI during scanning. Using the software SPCM (version 9.80, 64 bit), we set out parameters such as number of cycles and the resolution of the image, 512 x 512, to acquire a clear set of FLIM data with each chromatid visible.

2.5.5. Processing steps for the FLIM data

1) Import of raw FLIM data file from the TCSPC into the SPCImage software for further processing.
2) In the SPCImage software, discard pixels with poor photon signal to noise ratio and adjust the threshold range between 25–35. Ideally pixel binning should be kept to a minimum between 1- 3, depending on intensity of the image.
3) Choose “Incomplete Multiexponential” decay model as a fitting model to calculate accurate fluorescence lifetime of a fluorophore (under “Option - Model-Incomplete Multiexponential”) due to our laser operating at 80 MHz and the lifetime of DAPI does not decay to the baseline before the next pulse.
4) Chi-square (χ^2) is the best option to check the fitting model of the decay curve. A chi-square value of unity indicates a good decay curve fitting that is desirable. Chi-square (>1.4) denotes presence of multiple fluorophore components and (<0.8) represents poor fit of the data points.
5) Set appropriate “scatter” and “shift” values then run decay matrix (under “calculate – Decay Matrix”), for whole image to get lifetime distribution of whole image. BH software converts intensity image to false – coloured image to generate lifetime values of each pixel (Becker, 2012).
6) Set the false-colour range from “Minimum” and “Maximum” (continuous colour mode), (under “Option – Colour”) according to our expectation of the lifetime map of chromosome.
7) Pseudo coloured histogram denotes the range of short and long lifetime of the fluorophore- stained chromosomes. Here, we consider red represent shorter lifetime and blue to represent longer lifetime.
8) Locked the fitting process and set it to “global fitting mode” in order to speed up the lifetime measurements.

2.6. Multi-colour chromosomes detection after In Situ hybridisation

To identify the chromosomes from the FLIM measurement, we used the standard 24XCyte Multiplex – Fluorescence *In Situ* Hybridisation (M-FISH, MetaSystems, Germany) probe kit and software on the Zeiss microscope (Yusuf *et al.*, 2011). The kit identifies 24 colour combinations specific for the 24 human chromosomes. Each probe was labelled with up to 5 different fluorophores in a combination manner. The five fluorophores are FITC, Orange, TexasRed®, Aqua and Cy^{TM}5 and used DAPI as a counterstain. The probe kit is sensitive to light and should be stored in the dark at -20 °C. The M-FISH labelled chromosomes were visualized using a fluorescence microscope (Zeiss Z2Axioimager) in combination with ISIS software for capturing and analysis.

2.6.1. Buffers prepared for M-FISH hybridisation

Several buffers were prepared prior to the start of the experiment. Some are pre-hybridisation and some are post-hybridisation buffers, for example; 0.1 x and 2 x Saline-sodium citrate buffer (SSC), series of ethanol (100%, 95% and 70%), 0.07 mol/L as DNA denaturing buffer on the day, prior to the start of the experiment. 0.4 x SSC and SSCT (SSC with 20 % Tween) are washing buffers after hybridisation. Listed buffers are given below:-

1) 0.1 x SSC stock: Added 1 ml of 20 x SSC (Sigma-Aldrich) in a 200 ml milliQ water, pH 7.25. Transferred 50 ml of solution in two coplin jars, keeping one jar at room temperature and the other in a fridge at 4 °C.
2) Repeated the above procedure to prepare 2 x SSC stock, adding 20 ml of 20 x SSC in a 200 ml milliQ water, pH 7.45. Poured 50 ml of solution into two coplin jars, keeping one jar at 70 °C (+/- 1°C) in a hot water bath and another in a fridge at 4 °C.
3) Prepared 0.07 mol/L by adding 1 ml of 7 M stock solution in a 100 ml of milliQ water and transferred 50 ml of solution in a coplin jar and stored at room temperature.

4) 100 %, 95% and 70% of ethanol series were prepared in a milliQ water and kept at room temperature.
5) Prepared 0.4 x SSC by mixing 1 ml of 20 x SSC in a 50 ml of milliQ water, pH 7.2. Kept at 72 °C (+/- 1°C).
6) Prepared 2 x SSCT by dissolving 0.05 % Tween-20 (Polyoxyethylenesorbitan-monolaurate syrup, sigma P-1379) in a 50 ml of a 2 x SSC, pH 7.45 and kept at room temperature.

2.6.2. Protocol for multi-colour FISH

1) Prepared 0.1 x SSC and 0.2 x SSC, poured into coplin jars and placed into the refrigerator at 4 °C.
2) Prepared 2 x SSC, poured into a coplin jar and placed into a water bath at 70 °C (+/- 1°C).
3) Carefully removed coverslip from the glass slide used for the FLIM data acquisition.
4) Placed the required slides in a series of ethanol washes: 70%, 95%, 100% for 30 secs in each solution and left to dry in air.
5) Incubated the slides for 30 mins in the prewarmed 2 x SSC at 70 °C (+/- 1°C) coplin jar.
6) Removed the coplin jar from the water bath and let it cool for 20 mins at room temperature.
7) Meanwhile prepared the M-FISH probe cocktail according to the intended area for hybridisation e.g. 9 µl for a 18 x 18 mm^2 cover slip, 12 µl for a 22 x 22 mm^2 cover slip.
8) Denatured the probe by incubating at 75 °C (+/- 1°C) for 5 mins on the prewarmed hot plate.
9) Placed the probe on ice for 15 sec.
10) Incubated the probe at 37 °C (+/- 1°C) for 30 mins on the prewarmed hot plate.
11) Once the slides are cooled to room temperature, placed the slides in the coplin jar containing 0.1 x SSC at room temperature for 1 min.
12) Denatured slides in 0.07 N NaoH at room temperature for 1 min.
13) Placed the slides into 0.1 x SSC 4 °C for 1 min.

14) Placed the slides into 2 x SSC 4 °C for 1 min.
15) Transferred to a coplin jar with 70 % ethanol for 1 min.
16) Transferred to a coplin jar with 95 % and 100 % ethanol and incubate for 1 min, then allowed the slides to air dry
17) Pipette the denatured probe cocktail onto the denatured chromosome preparation and covered it with the required sized coverslip prior to fluorescence imaging.
18) Sealed the coverslip to the slide using rubber cement.
19) Incubated the slides for 1-2 days in a humidified chamber at 37 °C (+/- 1°C).
20) Following incubation, carefully removed the rubber cement and the cover slips.
21) Placed the slides into the coplin jar containing prewarmed (72 °C (+/- 1°C) 0.4 x SSC for 2 mins.
22) Incubated the slides in the coplin jar containing 2 x SSCT for 30 secs.
23) Washed the slides briefly with milliQ water to avoid crystal formation and left them to dry in air at room temperature.
24) Applied 20 µl of the DAPI/ antifade compound and overlaid the sample with a 24 x 60 mm^2 cover slip and incubated for 10 mins.
25) Proceed with imaging and analysis. The samples can be stored at -20 °C for up to 2 weeks.

2.7. Coherence X-ray imaging

2.7.1. Sample preparation on silicon nitride windows

Two different sized silicon nitride membrane X-ray windows (Silson Ltd.) also called transmission electron microscopy (TEM) grids, were used. These were categorized as; 0.25 mm x 0.25 mm window opening, membrane thickness 30 nm and 100 nm or 0.50 mm x 0.50 mm window opening, membrane thickness 30 nm and 100 nm. In each case, the silicon nitride membrane was located at the center of a 3 mm octagonal silicon frame of thickness 200 µm (Figure 2.3).

With the flat side of the membrane facing upward, the membrane windows were mounted on a parafilm-wrapped glass slide and placed inside the air-chamber of an automated GloQube glow discharge system (Quorum Technologies Ltd., Sussex, England) designed for negative hydrophilization of TEM grids. The treatment was carried out for 30 secs at 30 mA current. This treatment causes chromosomes in suspension to adhere evenly on the surface of the silicon nitride windows.

Once the grids were made hydrophilic, 5 µl of MAA fixed chromosomes were dropped immediately from a height of 10 cm (to get well scattered metaphase chromosome spreads) and left to air dry to produce chromosome spreads. Grids were validated using an Olympus LEXT laser scanning confocal microscope in combination with custom analysis software, LEXT. A 10x objective was used for localisation of spreads and 20x or 50x were used for conformation of the presence of chromosomes, to be used for alignment and localisation of spreads during the X-ray imaging.

150 nm gold nanoparticles (Sigma-Aldrich) were used as a test pattern (fiducial markers) for X-ray imaging. 2 µl of gold nanoparticles were dissolved in 8 µl of milliQ water and then dropped (3 µl) on the silicon window (0.50 mm x 0.50 mm, membrane thickness 30 nm) and left to dry before imaging at room temperature.

2.7.2. Heavy metal stains

Two types of heavy metal stains were used for staining the chromosomes, once placed on the silicon nitride windows:

a) platinum blue, synthesised in our laboratory (Yusuf *et al.*, 2014) at Research Complex at Harwell (RCaH), Oxford, UK, at 5 mM concentration: 0.015 g of platinum blue powder dissolved in 5 ml of milliQ water and stored in a fridge at 4 ℃.

b) uranyl acetate (UA) which is a negative stain, was prepared at 1% from a stock solution of 2% UA (Taab Laboratories Equipment Ltd.), in equal proportion of milliQ water and stored in fridge at 4 ℃.

2.7.2.1. Procedure for staining

Chromosomes samples were mounted on the silicon nitride windows (see section 2.7.1.) and, once dry, they were stained either with 5 mM platinum blue or 1% uranyl acetate. To stain with platinum blue, 2 µl to 3 µl of 5 mM platinum blue solution was dropped on the silicon windows containing chromosome spreads at room temperature. Excess dye was blotted off using Whatman filter paper and left to air dry. The dried grids were stored in a grid box and used during X-ray imaging.

To stain with 1% UA solution, the grids containing chromosome spreads were first washed twice, for 30 secs each wash, in milliQ water and then stained twice, for 30 sec, each stain, with 1% UA solution. After every wash and staining, the grids were blotted using Whatman filter paper. After the last stain cycle, the sample was blotted for longer time, 1 min, to get rid of excess UA. This staining was performed in a radioactive laboratory with a full safety and training. The stained chromosome samples were stored in the radioactive laboratory for 24 hrs to 48 hrs before taking them for X-ray imaging.

2.7.3. Sample loading in the holders

The chromosomes mounted on silicon nitride windows were loaded into the sample holders, either in a single grid holder (prepared on SEM stubs in our

laboratory) or on a 4 x 4 array 3D printed holder from I-13 beamline, DLS) (Figure 2.3) depending on the number of samples to be imaged at a time. In the 4 x 4 array holder, the recessed holes fit the 3 mm grids, which are captured by the protruding ring on the mating part (Figure 2.3). The lid of the holder screwed carefully to avoid cracking the grids.

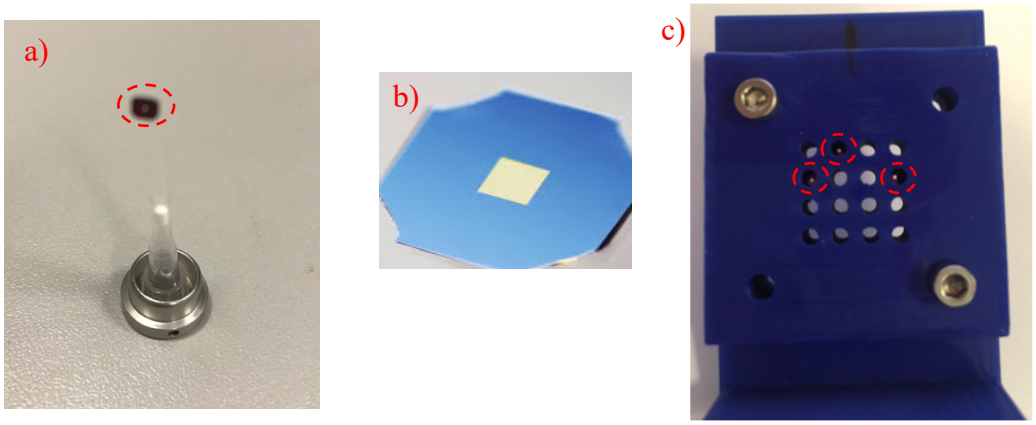

Figure 2.3: Silicon nitride window holders for X-ray imaging. a) A single grid holder, prepared on a SEM stub, b) Square shaped silicon nitride membrane at the centre of a 3 mm octagonal silicon frame and c) 3D printed 4 x 4 array of grid holder which contains 3 silicon nitride windows (red dashed circle).

2.7.4. Experimental set-up for ptychography

The collimated X-ray beam from DLS, entered the experimental hutch (I-13-1) through entrance slits, 2 x 3 mm, of the double-crystal monochromator. The beam was focused using a Fresnel zone plate (FZP) of diameter 400 µm and outer zone-width of 150 nm. A 50 µm order sorting aperture (OSA) further downstream was centred to allow only the first order diffraction from the FZP to pass through. A central stop (CS), made of 60 µm diameter of gold to occlude the OSA, was used to eliminate the un-diffracted zero order beam. The beam was slightly defocused to ~10 µm at the sample plane which lies slightly beyond the focal plane of FZP, as shown in

Figure 2.4. The measured beam size on the sample was later found to be ~7 µm as planned. The sample was mounted on a high-precision piezo stage and

scanned in a raster fashion. A helium gas pipe was placed between the sample and detector to minimize the air scattering so that sample scattering signal can be maximized. The X-ray photon-counting Excalibur detector (Marchal *et al.*, 2013)x (Medipix3 chip, 1806 x 1548 pixels and Pixel size: 55 μm x 55 μm), used for recording the X-ray diffraction pattern, was placed 8 m beyond the sample.

The scanning parameters for 2D integral scanning. First is to select the region of interest, in our case the most common values were, 64 μm x 64 μm/ 32 μm x 32 μm, depending upon the size of the spread. Second, to choose the position (1μm X 1μm) of the scan and lastly to select the exposure time of the scan. The following variable were set to be the best scan parameters to obtain a 2D integral phase contrast image of the chromosome spread.

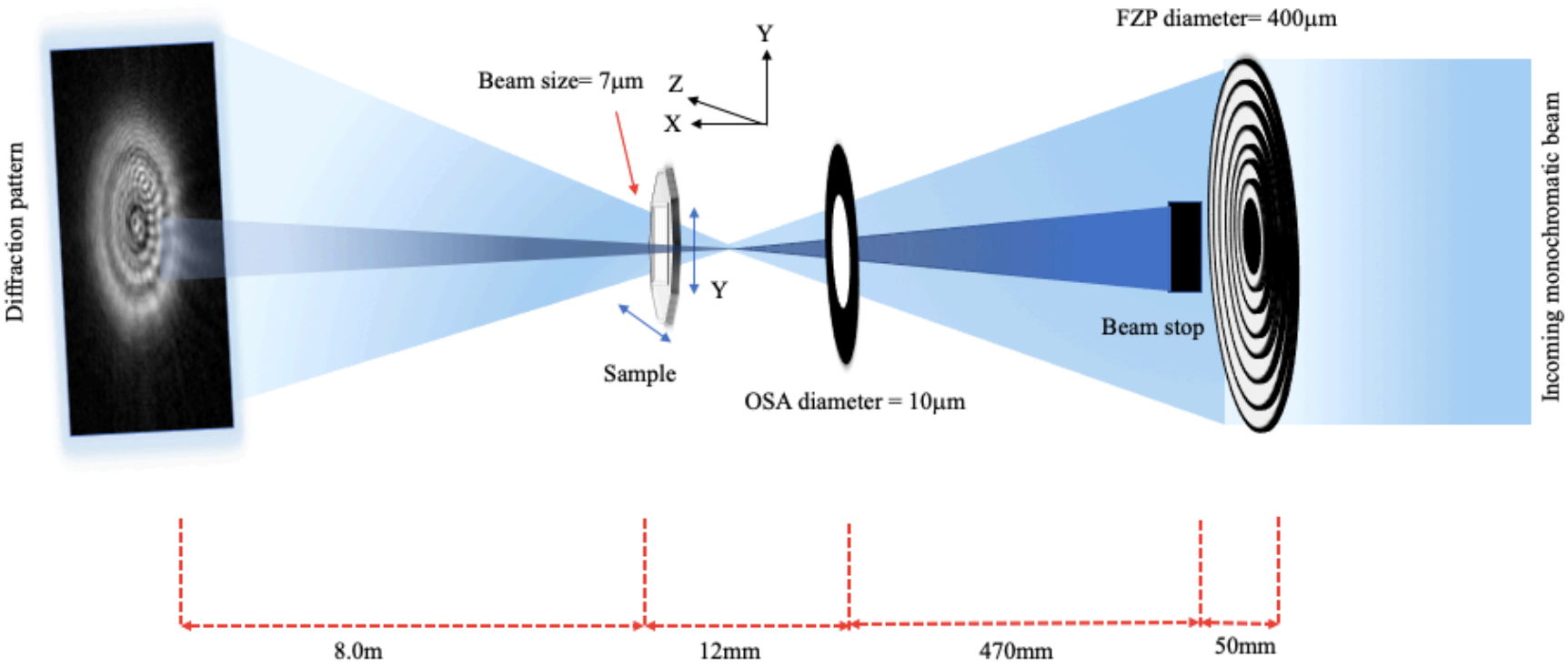

Figure 2.4: Schematic diagram of the beamline setup at I-13-1 Diamond light source for X-ray ptychography imaging.

Chapter 3

3. X-ray induced chromosomal changes analysis using FLIM

Presence of human chromosome aberrations can be determined by examining the structure of the chromosome (Tubbs and Nussenzweig, 2017). Ionising radiation, including X-rays and gamma rays leads to DNA DSBs, a highly deleterious event, that inhibits replication and transcription processes (Schwer *et al.*, 2016). If the DSBs are not repaired faithfully by the mechanism of homologous recombination or nonhomologous end-joining (Ojima *et al.*, 2015), the damage may lead to numerous chromosomal aberrations (CAs). All these defects can produce large-scale rearrangements of the human genome and may cause major phenotypic and biological alterations, including cell death and mutations (Ojima *et al.*, 2015).

Current established techniques to study chromosome aberrations are M-FISH and flow cytometry. However, these techniques can only detect major aberrations such as translocations and numerical changes, respectively (Sotnik *et al.*, 2014), and they have not been shown to detect early events such as bases response (including modifications), chromosomal compaction and intra-chromosomal aberrations, which in turn leads to major structural changes. There is now some evidence that cell irradiation leads to loss of histones as well as nuclear morphological changes (Hauer *et al.*, 2017) (Lowe *et al.*, 2020). We have recently shown that upon staining chromosomes with DAPI stain, FLIM can be used to assess chromosomal changes, possibly compaction (Estandarte *et al.*, 2016). FLIM performed on undamaged fixed human metaphase chromosomes showed shorter lifetimes in the tightly packed heterochromatin regions of chromosomes 1, 9, 15, 16 and Y, among 23 pairs of chromosomes, as shown in a spread (Figure 1.10) (Estandarte *et al.*, 2016). FLIM has also been used to observe chromatin condensation in human endothelial cell nuclei in different viscosity environments (Spagnol and Dahl, 2016). These encouraging results indicate that FLIM could be applied to

investigate DNA base pair sequence dependence as well as the early changes (compaction/intra-chromosomal aberrations) and long-term changes (onset of CAs) following irradiated cells and their subsequent aberrations. Studying chromosomal aberrations is a crucial step in diagnostics, prognostics, and developing targeted therapeutics for diseases such as cancer (Beroukhim *et al.*, 2007).

In this chapter, the effect of X-ray radiation on the DNA base pair sequences and sub-structures of chromosomes has been studied using FLIM. The effect of a low X-ray irradiation dose on heterochromatin regions of heteromorphic chromosomes is examined to determine if they maintain their compaction. In addition, the effect of irradiation was also examined in euchromatin regions (referred as “non-heterochromatin regions”) in all 46 human chromosomes. Moreover, the effect of X-ray radiation was investigated on first, second and third generations of human cells with a focus on heterochromatin (condensed) and non-heterochromatin (decondensed) regions in all 46 chromosomes.

The investigation was carried on the B and T-lymphocytes. The cells were X-ray irradiated at low-level doses such as 0.1 Gy, 0.5 Gy and 1 Gy at room temperature and physiological conditions, followed by chromosome preparation and mounting, as described previously in (see chapter 2, Materials and Methods). The prepared glass slides, mounted with chromosomes were stained with freshly prepared 4 µM DAPI and observed under an epifluorescence microscope (Figure 3.1).

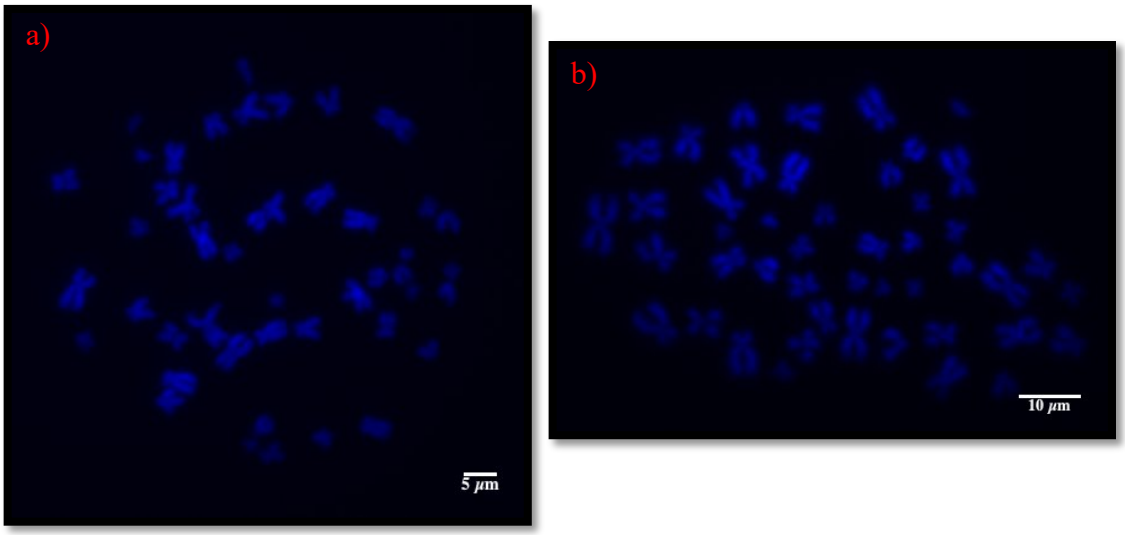

Figure 3.1: DAPI stained non-irradiated chromosomes. These preparations were obtained from a) B-lymphocytes cells, scale bar = 5 µm and b) T-lymphocytes cells, scale bar = 10 µm. Objective used was 63x with immersion oil.

(X, Y) chromosomes and T- lymphocytes contains 46 (X, X) chromosomes. Chromosomes obtained from a single cell is called “spread”. The focused was to acquire 20-30 spreads per slide of size, 3 mm x 2 mm, in order to identify isolated chromosome spreads for further FLIM and M-FISH imaging. The chromosome sample prepared from non-irradiated B- lymphocytes, passage 15 and T- lymphocytes cells, passage 3, were free from any structural aberrations, moreover, 25 spreads were scored from the each cell line for validation. Afterwards, well-scattered chromosome spreads were marked onto the glass slides and were taken for FLIM measurements as previously described in chapter 2, Materials and Methods.

3.1. Identification of lifetime components in a FLIM image

A colour-coded map produced by FLIM imaging helps to identify the sub-structures of biological specimens from the change in their lifetime components, in this case the chromosomes extracted from a human T-lymphocytes. Using the lifetime measurement it was observed that DAPI stained chromosome 1 and 9 in a spread showed shorter lifetime (red 2.76 ± 0.07 ns) at the proximity of centromere called pericentric heterochromatin and other chromosomes showed longer lifetime (blue 2.95 ± 0.04 ns) at the heterochromatin region (Figure 3.2). For example, the region with pseudo red colour in a FLIM image have shorter lifetime and with pseudo blue colour regions possess longer lifetime as shown in Figure 3.2.

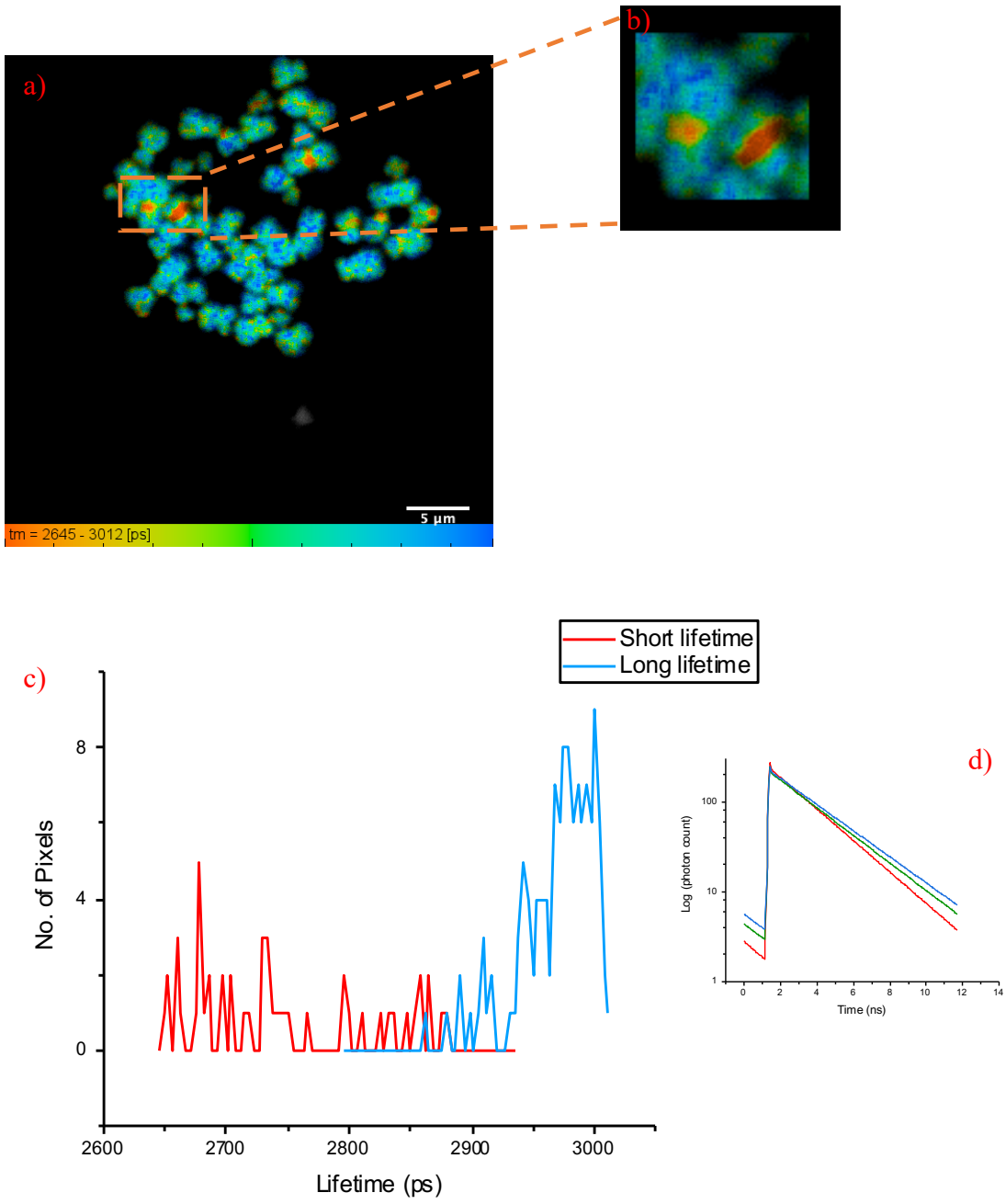

Figure 3.2: FLIM measurements of 4 µM DAPI stained, fixed metaphase chromosomes: a) shows lifetime change along the length of an individual chromosome, obtained from human T-lymphocytes. The lifetime values range from 2.76 ± 0.07 ns to 2.95 ± 0.04 ns within a field of view of 35 µm and scale bar of 5 µm. b) Zoomed image of chromosome 1 and 9 from figure a. c) Lifetime distribution of chromosomes measured from figure b, showed shorter lifetime (red 2.76 ± 0.07 ns) and longer lifetime (blue 2.95 ± 0.04 ns) values of DAPI stained chromosomes. d) fluorescence decay curve obtained from selected pixel of red, green and blue region of chromosome 9 from figure b.

3.2. DAPI lifetime of chromosome obtained from T-lymphocytes

DAPI lifetime of chromosomes obtained from T-lymphocytes were studied. The chromosomes were prepared and mounted as described in (see Chapter 2, Materials and Methods). A single spread of non-irradiated metaphase chromosomes imaged using FLIM to identify the heteromorphic chromosome with short lifetime in T-lymphocytes of human cells (Figure 3.3). Furthermore, karyotyped the same spread using M-FISH probe to locate each individual chromosomes in a spread. The same procedure applied further in this work to determine the lifetime components in X-ray irradiated chromosomes obtained from T-lymphocytes.

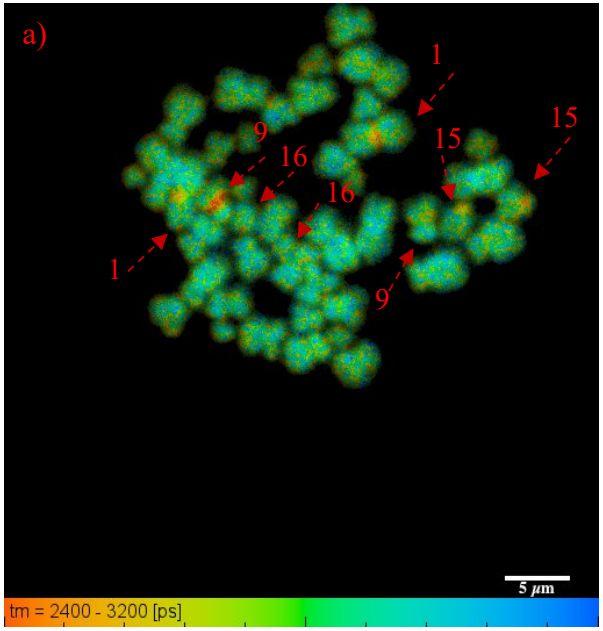

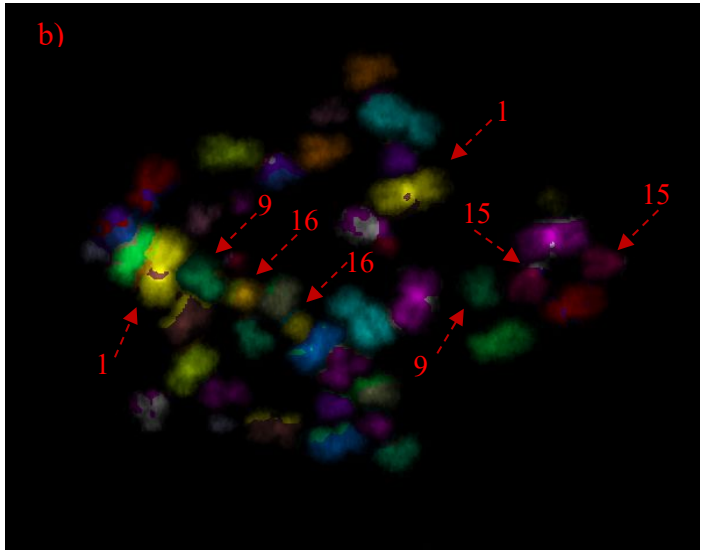

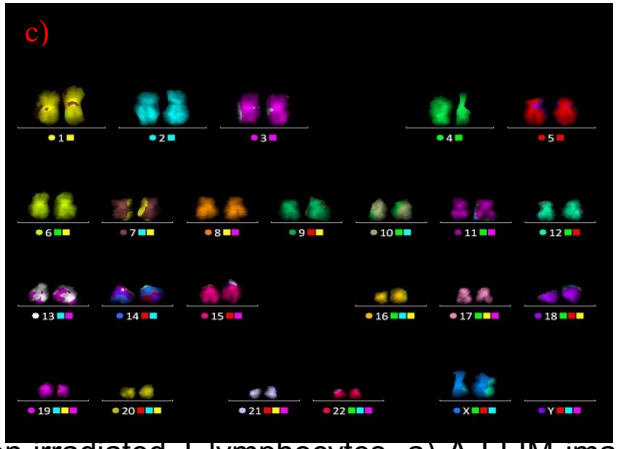

Chromosomes d)	Mean lifetime (τ_m)
Chr 1	2.71
Chr 9	2.69
Chr 15	2.70
Chr 16	2.83

Figure 3.3: A single metaphase chromosome spread obtained from non-irradiated T-lymphocytes. a) A FLIM image shows DAPI lifetime of all 46 (X,X) chromosomes in a spread, scale bar = 5 μm. 60x water objective was used with an image size of 512 x 512 b) M-FISH image of the same spread as a, c) karyotype of image b, 63x oil objective used and d) representation of mean lifetime of two homologous chromosome (shown with red dashed arrows in a spread, figure 3.3a and 3.3b) in a spread with shorter lifetime at their heterochromatin region.

Figure 3.3 shows the DAPI lifetime of methanol: acetic acid (3:1) fixed human metaphase chromosomes obtained from T-lymphocytes. The chromosomes 1, 9, 15 and 16 shows variation in lifetime along the length of chromosome. Each of these individual chromosomes showed a short DAPI lifetime at the proximity of the centromere, heterochromatin regions, and a longer lifetime at the distal (away from the centromere) regions of the chromosomes. The following chromosomes are known as heteromorphic chromosomes because of presence of many variants of DNA sequence repeats from one species to another species (Tagarro, Fernández-Peralta and González-Aguilera, 1994).

Figure 3.3 (figure d) shows a table of heteromorphic chromosomes and their mean DAPI lifetime, obtained by averaging the mean lifetime of a two homologous chromosomes present in a single cell of human, that have similar DAPI lifetime at the heterochromatin regions.

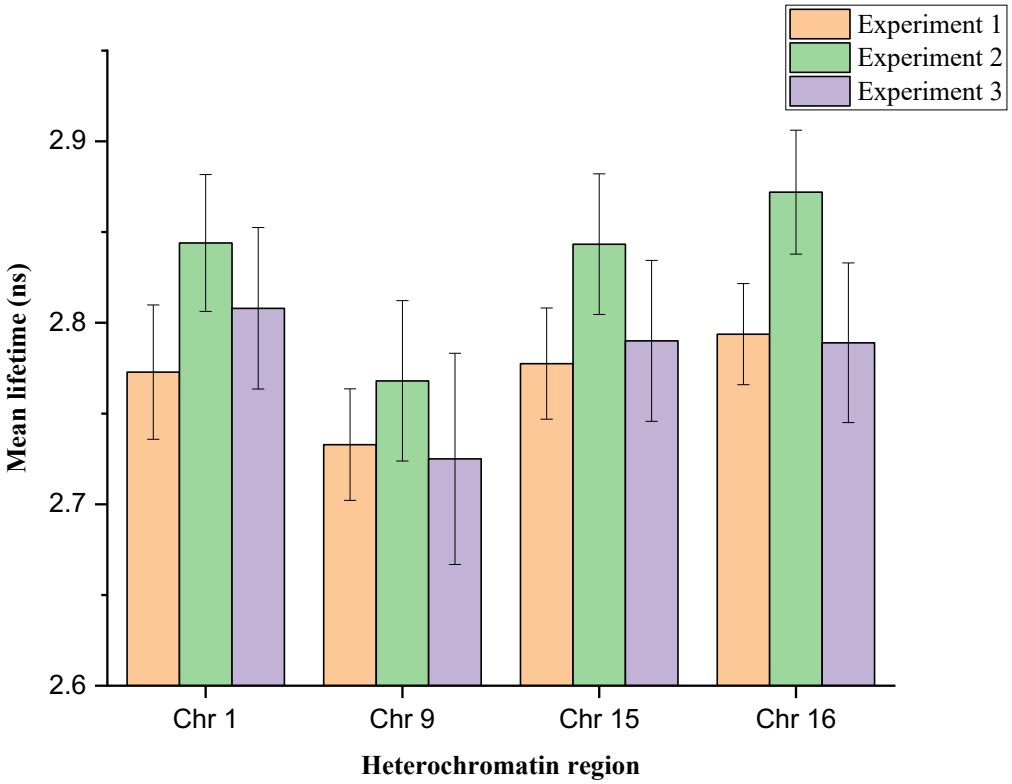

Figure 3.4: Representation of DAPI lifetime of heterochromatin regions of chromosomes 1, 9, 15 and 16, obtained from three independent repeated experiments performed on non-irradiated T-lymphocytes, number of spreads (n = 5). The error bar represents the SEM (standard error of the mean) values, *p-value*< *0.05*. Each colour of the bar represents the repeated independent experiment (n=3).

Figure 3.4, shows the mean lifetime of DAPI- bound chromosomes obtained from non-irradiated T-lymphocytes. The three independent repeated experiments are from following different passage numbers, 3, 4 and 5, respectively. The repeats performed to ensure that the average result is more accurate than a single repeat. Lifetime of DAPI-bound heteromorphic chromosomes of each experiment features an averaged lifetime from five individual chromosome spreads. The lifetimes values are displayed in this manner (X- represent the averaged lifetime ± SEM), for each heteromorphic chromosome. Thus, the averaged lifetime from three independent experiments are 2.81 ± 0.04 ns for chromosome 1, 2.74 ± 0.04 ns for chromosome 9, 2.80 ± 0.04 ns for chromosome 15, and 2.82 ± 0.04 ns for chromosome 16 (Figure 3.4).

3.2.1. DAPI lifetime of irradiated chromosomes obtained from T-lymphocytes

The lifetime measurement of DAPI-bound chromosomes was studied, by observing changes along the length of non-irradiated heteromorphic chromosomes. The FLIM technique was also applied to study the X-ray induced chromosomes to investigate the early onset and the long-term aberrations in chromosomes occurring due to X-ray exposure to the T-cells. With the view to identify intra-chromosomal (translocation of DNA segment between two homologous pair) and inter-chromosomal (translocation of DNA segment between two non- homologous pair) aberrations.

The T-cells were cultured from, passage 3 and 4, followed by irradiation with X-rays at different doses (i:e. 0.1 Gy, 0.5 Gy and 1 Gy) at a rate of 0.5 Gy/min. After irradiation, the X-ray induced chromosomes were prepared (see Chapter 2, Materials and Methods) for FLIM imaging.

	FLIM	M-FISH	Karyotype
0.1 Gy	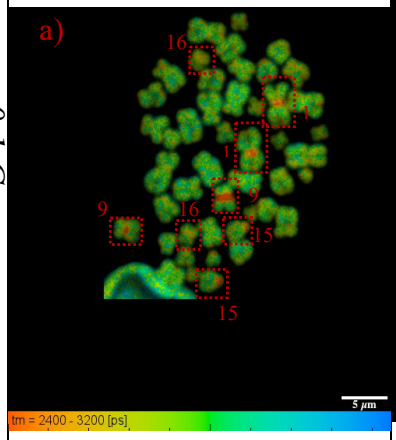	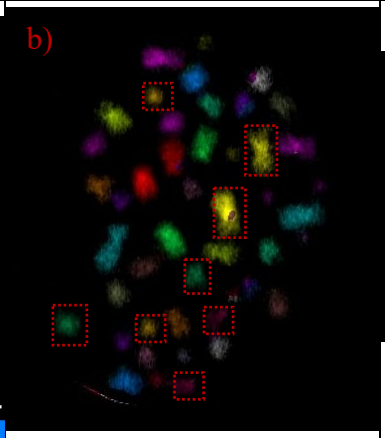	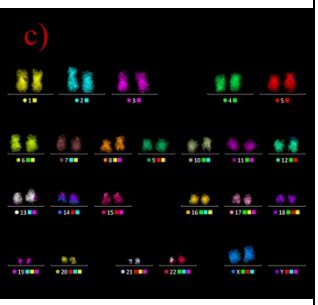
0.5 Gy	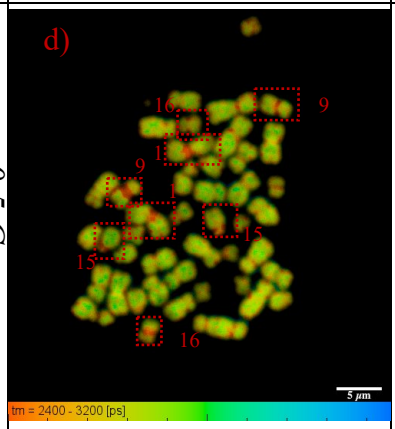	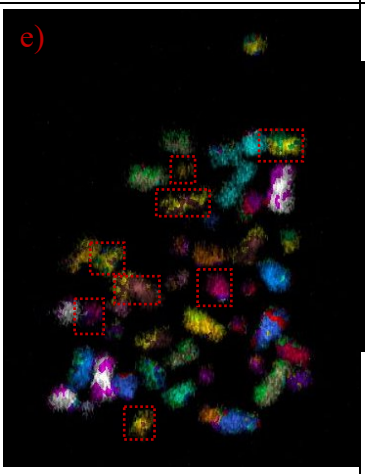	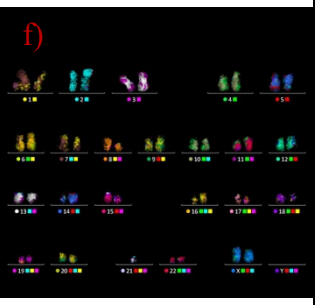
1 Gy	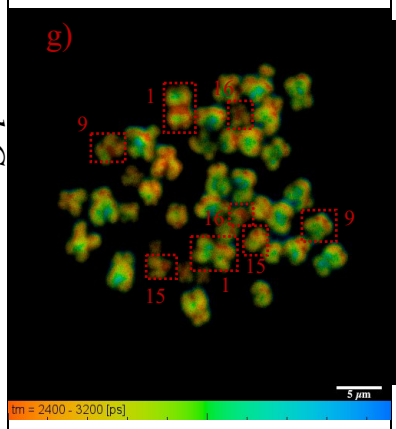	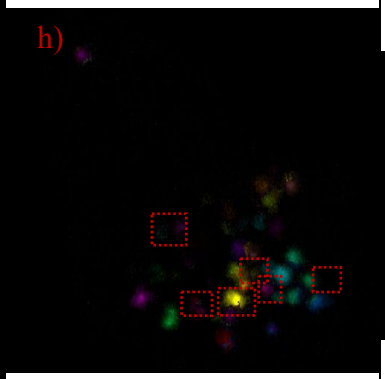	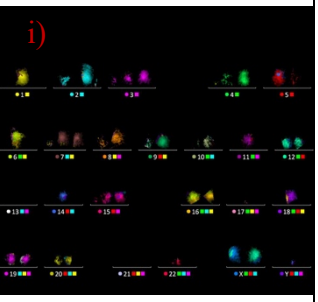

Figure 3.5: X-ray irradiated chromosomes spreads from a three different radiation doses and the spreads shown are imaged using FLIM and M-FISH, followed by karyotypes. The rows defines the three X-ray radiation doses and column defines the imaging techniques and the karyotype. Figure a), d) and g) are the FLIM images, b), e) and h) are the M-FISH images of the same spread, respectively, and c), f) and i) are the karyotype of the same spread obtained from the respective M-FISH spread. Red boxes denotes homologous heteromorphic chromosomes with a short lifetime at their heterochromatin region in all three independent spreads. A map of DAPI lifetime ranged between 2.4 ns to 3.2 ns, and scale bar= 5 µm. Objectives used for FLIM imaging is 60x water and for M-FISH is 63x immersion oil.

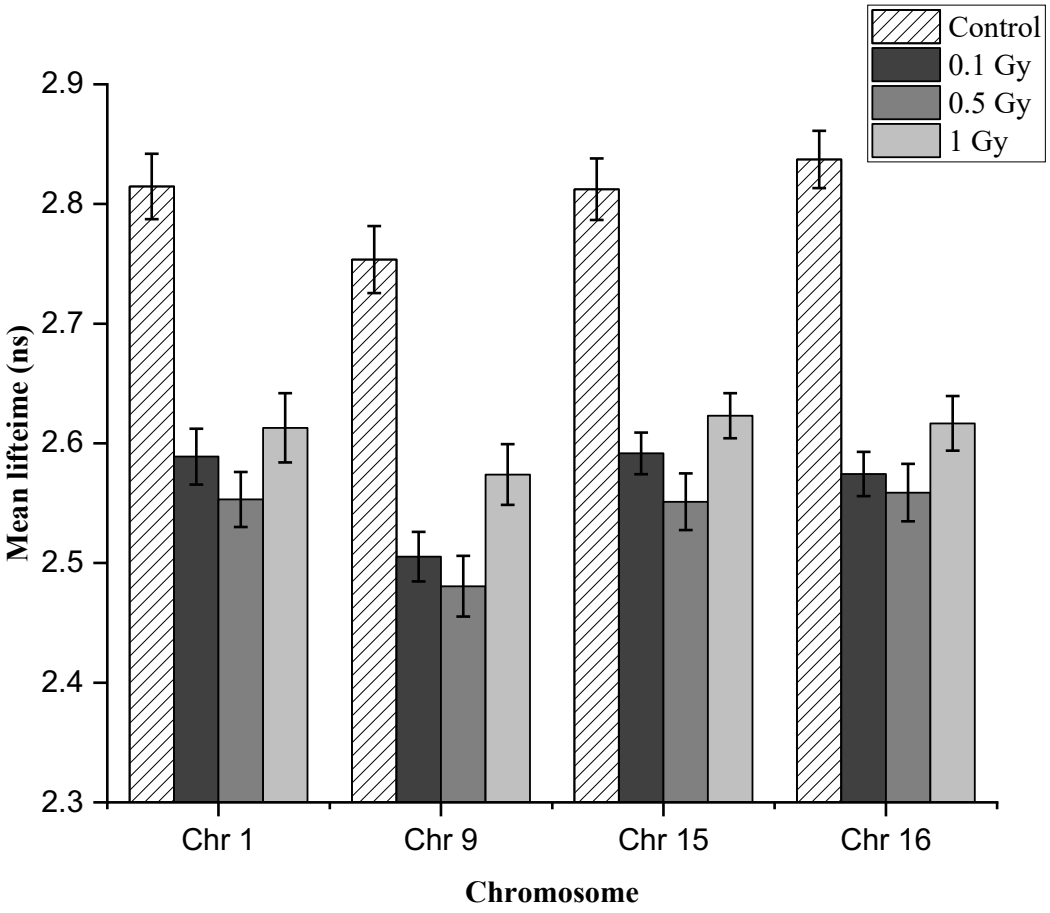

Figure 3.6: Representation of a different homologous pair of heteromorphic chromosomes with a short lifetime at their heterochromatin region at different radiation doses, number of spreads (n = 9). Error bar represents SEM , *p-value < 0.05*

Figure 3.5 shows the FLIM and the respective M-FISH images of chromosome spreads obtained from X-ray induced T-cells at radiation doses of 0.1 Gy, 0.5 Gy and 1 Gy. The FLIM measurement of all 46, fixed human metaphase chromosomes was obtained. Although, in Figure 3.5, the M-FISH images does not show all 46 chromosomes with 0.5 Gy and 1 Gy irradiation because we did not manage to rescue all 46 chromosomes while performing M-FISH hybridisation on the same spread on which FLIM was already done.

The lifetime of DAPI decreases in X-ray induced chromosomes in comparison to the control sample (non-irradiated chromosomes) as shown in Figure 3.6. Data in Figure 3.6 represents the averaged mean lifetime from nine independent chromosome spreads for each heteromorphic chromosome. The nine independent chromosome spreads were pooled from two independent experiments performed separately. Additionally, Figure 3.6 represents the mean lifetime of both non-irradiated control and irradiated chromosomes obtained from T-lymphocytes.

A pattern can be seen in Figure 3.6, which represents the heterochromatin regions of heteromorphic chromosomes, after averaging the nine independent chromosome spreads pooled from two independent experiments. Further, the obtained lifetimes values are displayed as X- represent the averaged lifetime ± SEM, for each heteromorphic chromosome. The average DAPI lifetime for non-irradiated chromosomes is 2.8 ± 0.03 ns and decreases to 2.57 ± 0.02 ns for 0.1 Gy irradiation and 2.54 ± 0.02 ns for 0.5 Gy irradiation. Interestingly, the average lifetime of 1 Gy appear to rise to 2.61 ± 0.02 ns in comparison to other radiation doses in Figure 3.6. The averaged mean lifetime follows a sequence of, control>1 Gy>0.1 Gy>0.5 Gy.

Surprisingly, the average DAPI lifetime in Figure 3.6 indicates that on average there is a difference of ~0.23 ns between non-irradiated and irradiated chromosomes. Beside this, chromosome 9 has the shortest DAPI lifetime relative to other heteromorphic chromosomes in both the cases of irradiated and non-irradiated chromosomes (Figure 3.6).

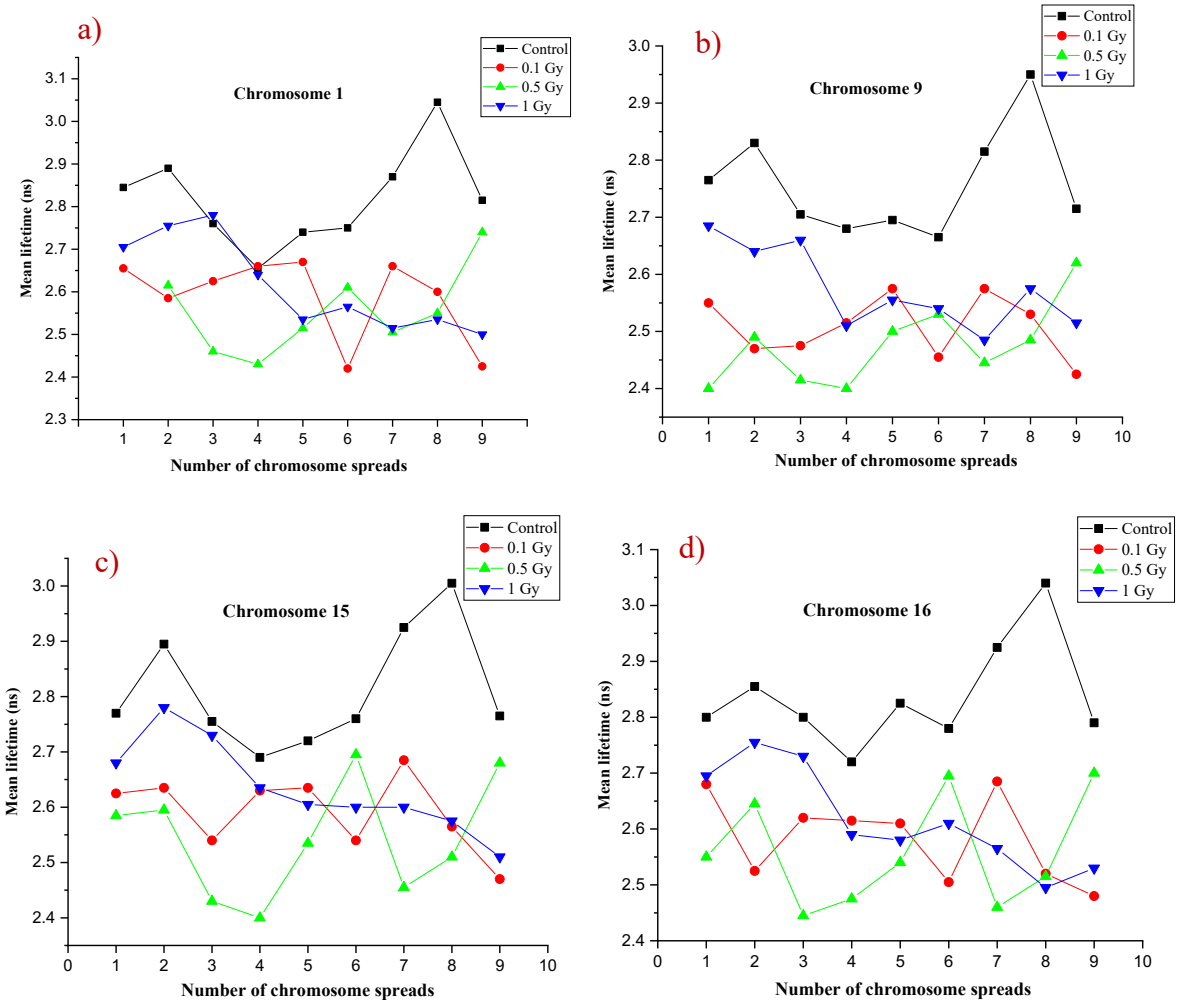

Figure 3.7: Representation of short DAPI lifetime at the heterochromatin regions of each heteromorphic chromosomes 1 (a), 9 (b), 15 (c) and 16 (d), obtained from both non-irradiated and irradiated chromosomes. Data points are the averaged lifetime of two homologous pair of chromosomes present in a single chromosome spread. This is combined data from a nine independent chromosome spreads (n = 9).

In Figure 3.7, each data point represents the averaged lifetime of two pair of homologous chromosomes obtained from T-lymphocytes. For each heteromorphic chromosome (1, 9, 15 and 16) it is clearly observed in Figure 3.7 that the lifetime values are longer for non-irradiated control chromosomes relative to irradiated ones. Furthermore, it also indicates that X-ray induced chromosomes do have an effect on the lifetime of DAPI-bound chromosomes and the differences in DAPI lifetime can be observe within chosen low X-ray doses and each doses has distinct mean lifetime values for heteromorphic human metaphase chromosomes (Figure 3.6 and Figure 3.7).

3.2.2. DAPI lifetime of non-heterochromatin regions of chromosomes

DAPI lifetime variation depends on the molecular environment of the chromosomes. Here, DAPI lifetime variation is being investigated for varied base pair sequence and also for the most condensed (heterochromatin) and least condensed (non-heterochromatin) sub-structures of the chromosomes in non-irradiated and irradiated chromosomes. The heterochromatins are denoted as the regions with a short lifetime at the proximity of centromere of each heteromorphic chromosome (1, 9, 15 and 16) and the chromosomes apart from the heteromorphic chromosomes have longer DAPI lifetime at the heterochromatin regions (Figure 3.3 and Figure 3.5) in different chromosome spreads, that can be visualise with the change in the DAPI lifetime components. The red regions are donated short lifetime component and the blue/green regions represents long lifetime components.

T-lymphocytes were irradiated with low energy doses of X-ray (i.e. 0.1 Gy, 0.5 Gy and 1 Gy) at a rate of 0.5 Gy/min to investigate the decay of DAPI-bound chromosomes. The DAPI lifetime of non- heterochromatin regions were also measured along with heterochromatin regions. The FLIM measurements for non-heterochromatin regions were pooled from the same nine independent chromosome spreads (pooled from a two independent experiments), from which the lifetime of heterochromatin regions of DAPI -bound chromosomes were measured.

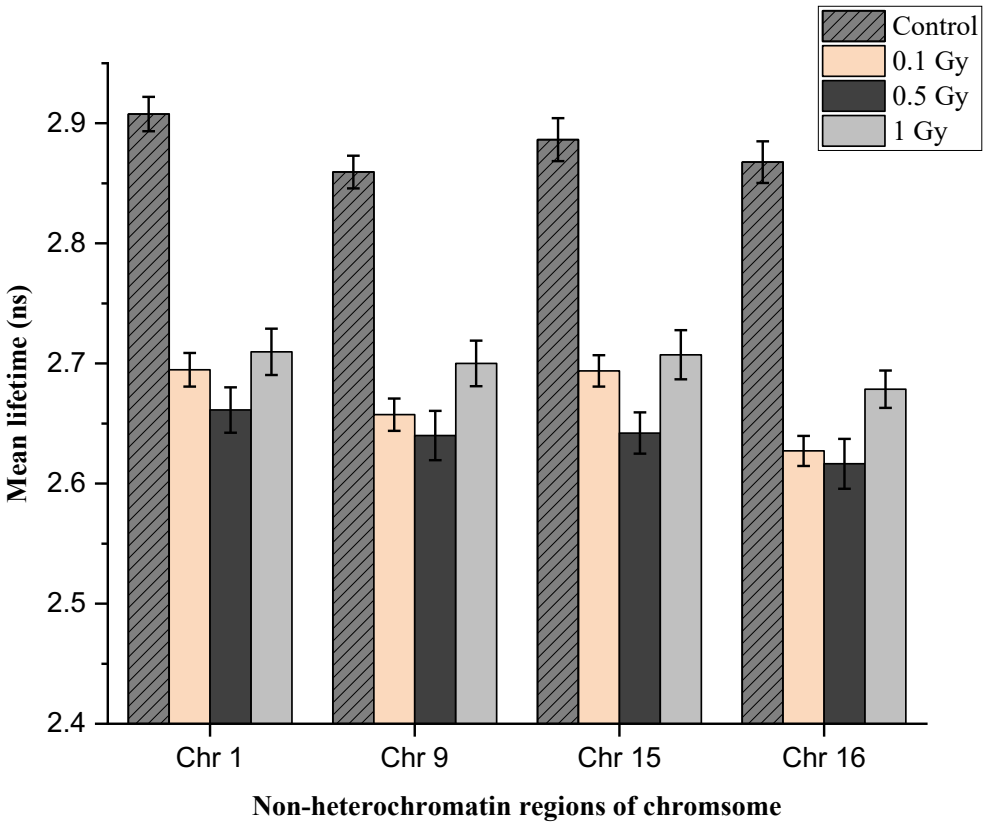

Figure 3.8: Represents mean lifetime of non-heterochromatin regions of DAPI-bound chromosomes obtained from T-lymphocytes. The chromosomes are from both non-irradiated and irradiated T-cells, number of chromosome spreads (n = 9). Error bar represents SEM, *p-value* < *0.02*.

The lifetime of non-heterochromatin regions of heteromorphic chromosomes 1, 9, 15 and 16 are represented as averaged lifetime obtained from nine independent chromosome spreads. It followed similar pattern to the lifetime measurement of heterochromatin regions of heteromorphic chromosomes (Figure 3.6). The averaged lifetime of non-irradiated chromosomes calculated is, 2.88 ± 0.02 ns, which is higher than the irradiated chromosomes (Figure 3.8). Furthermore, the average lifetime for 0.1 Gy irradiated sample is, 2.67 ± 0.01 ns, followed by 2.64 ± 0.02 ns for the 0.5 Gy sample. Interestingly, there is significant increase in the averaged lifetime of 1 Gy at 2.70 ± 0.02 ns.

Among all the X-ray induced chromosomes, the 0.5 Gy sample has the shortest averaged mean lifetime and the 1 Gy sample has the longest lifetime. Although the averaged mean lifetime of non-heterochromatin regions of all

heteromorphic chromosomes displayed (Figure 3.8) have significantly higher mean lifetime in comparison to heterochromatin regions, the averaged mean lifetime follows a sequence of, control>1 Gy>0.1 Gy>0.5 Gy.

3.2.3. FLIM measurement of heterochromatin and non-heterochromatin regions of all 46 chromosomes

FLIM imaging facilitated the identification of X-ray induced chromosomes by showing shorter lifetimes in both the heterochromatin and non-heterochromatin regions of chromosomes upon irradiation relative to non-irradiated chromosomes. This is demonstrated in heteromorphic chromosome 1, 9, 15 and 16 (Figure 3.6, Figure 3.7 and Figure 3.8) obtained from T- lymphocytes. It was decided that FLIM imaging should also be done on all 46 chromosomes combined with M-FISH hybridisation. The lifetime of all 46 DAPI-bound chromosomes was measured (Figure 3.9). The purpose of the correlative imaging was to detect any intra or inter-chromosomal aberrations occurred upon irradiation as well as to observe fluorescence decay maps of all 46 chromosomes to investigate the onset of ultrastructural aberrations at nanosecond (ns) time scale upon irradiation.

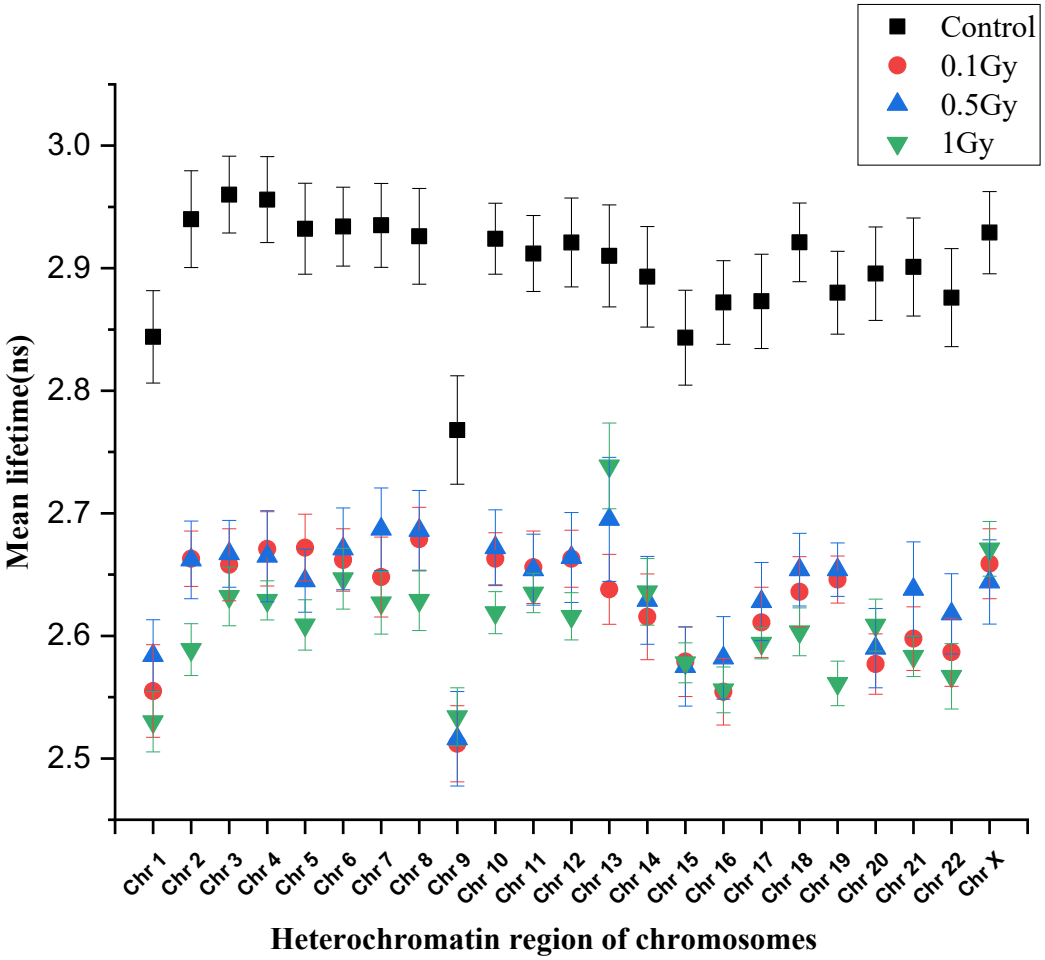

Figure 3.9: Measured mean lifetime of heterochromatin region of all 46 chromosomes obtained from T-lymphocytes, number of chromosome spreads (n = 5). Error bar represents SEM, *p-value* < 0.05.

Data represented in the Figure 3.9 is the averaged mean lifetime of five individual chromosome spreads obtained from T-lymphocytes, passage 4. It shows the averaged mean lifetime of heterochromatin regions of all 46 DAPI-bound chromosomes. Figure 3.9 shows that the averaged mean lifetime of non-irradiated chromosomes (~ 3.0 ns), is longer than that of the X-ray induced chromosomes (~ 2.65 ns). The averaged mean lifetime of heteromorphic chromosomes 1, 9, 15 and 16 are exceptionally short in both non-irradiated and irradiated chromosomes, determined in Figure 3.9.

On average the mean lifetime of all 46 DAPI-bound chromosomes in case of heterochromatin regions (Figure 3.9), the control (non-irradiated) sample is

determined to be 2.90 ± 0.04 ns, then it falls to 2.64 ± 0.03 ns for 0.5 Gy sample, following 0.1 Gy irradiation, 2.63 ± 0.03 ns and then 1 Gy irradiation has the lowest mean lifetime, 2.61 ± 0.02 ns. The averaged mean lifetime follows a sequence of, control>0.5 Gy>0.1 Gy>1 Gy (Figure 3.9). From the obtained mean lifetime of DAPI-bound chromosomes, induced with ionising radiation shows the decrease in the lifetime values. Thus, it can be assumed that the low-level X-ray irradiation doses causes chemical perturbs on the structure of human chromosomes.

The fluorescence decay of all 46 DAPI-bound chromosomes were used to extract the mean lifetime of non-heterochromatin regions of chromosomes (Figure 3.10), using the same five individual chromosome spreads from which the DAPI lifetime of heterochromatin regions were elucidated (Figure 3.9).

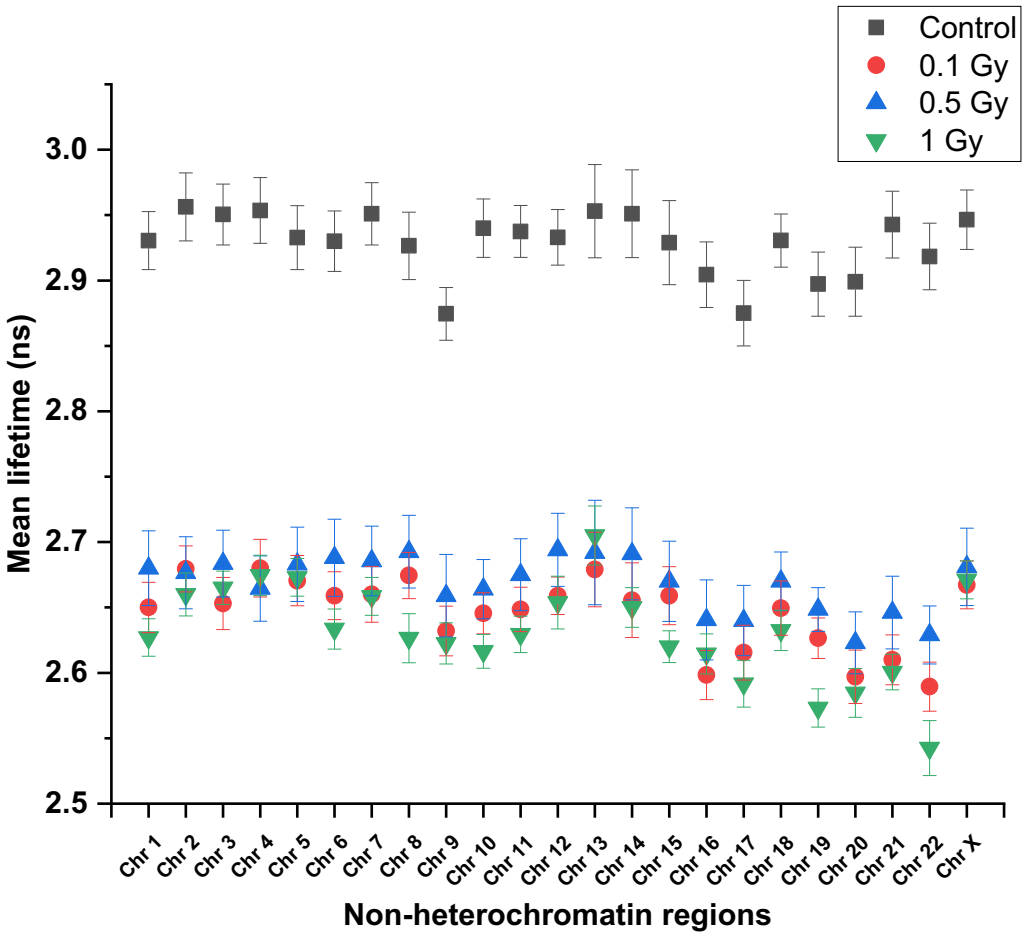

Figure 3.10: Measured mean lifetime of DAPI-bound, non-heterochromatin regions of all 46 chromosomes obtained from T-lymphocytes, number of chromosome spreads (n = 5). Error bar represents SEM, *p-value* < 0.04.

Figure 3.10 shows the averaged mean lifetime of non-heterochromatin regions of all 46 chromosomes. A major lifetime variation was not observed between heterochromatin (Figure 3.9) and non-heterochromatin (Figure 3.10) regions of all 46 chromosomes. Although, in Figure 3.10, a difference in averaged mean lifetime can be observed between non-irradiated and irradiated chromosomes similar to heterochromatin regions (Figure 3.9). Moreover, the averaged mean lifetime of non-heterochromatin regions of heteromorphic chromosomes 1, 9, 15 and 16 significantly varied in comparison to the lifetime values of rest of the chromosomes present in chromosome spreads (number of chromosome spreads, n=5), in non-irradiated (control) chromosomes. However, the averaged mean lifetime of heteromorphic chromosomes in case of X-ray induced chromosomes is not significantly separable from rest of the chromosomes present in the spreads (Figure 3.10).

The averaged mean lifetime values for non-irradiated (control) sample is 2.93 ± 0.02 ns, that reduces to 2.67 ± 0.03 ns for 0.5 Gy irradiation, following 0.1 Gy irradiation with 2.65 ± 0.02 ns and the 1 Gy irradiation has the lowest lifetime values 2.63 ± 0.02 ns. Hence, the averaged mean lifetime follows a sequence of, control>0.5 Gy>0.1 Gy>1 Gy (Figure 3.10).

3.3. FLIM performed on a different generations of T-lymphocytes

Variation in lifetime components was observed in control (non-irradiated) sample and in the X-ray induced chromosomes at low-level of X-ray doses, in all 46 fixed human metaphase chromosomes stained with 4 μM DAPI (Figure 3.9 and Figure 3.10). The lifetime components in metaphase chromosomes was observed at 0 hr generation (straight after irradiation doses) of the cell cycle.

As a result, for further investigation, it was decided to investigate the onset of chromosomal aberrations in four different generations of the cell cycle obtained from X-ray induced T-lymphocytes using FLIM imaging technique. The different chosen generations in this work included the following: 0 hr (0-

generation, passage 4), 24 hrs (first-generation, passage 5), 48 hrs (second-generation, passage 6) and 72 hrs (third-generation, passage 6) along with a control (non-irradiated chromosomes, passage 5) sample. The T-lymphocytes cells were X-ray irradiated at a rate of a 0.5 Gy/min and left to grow until different generations. At each generation the cells were arrested at metaphase stage of the cell cycle and once the metaphase chromosomes obtained (see Chapter 2, Materials and Methods), they further stained with 4 μM DAPI prior to FLIM imaging.

Unfortunately, the chromosomes extracted after 72 hrs did not show enough metaphase spreads on the glass slides to perform FLIM and M-FISH. Therefore, the chromosomes obtained after 72 hrs of generation were not available for further analysis. In the following generation, it is possible that the cells died due to prolonged culture after exposure to ionising radiation and did not reach to the metaphase stage of the cell cycle.

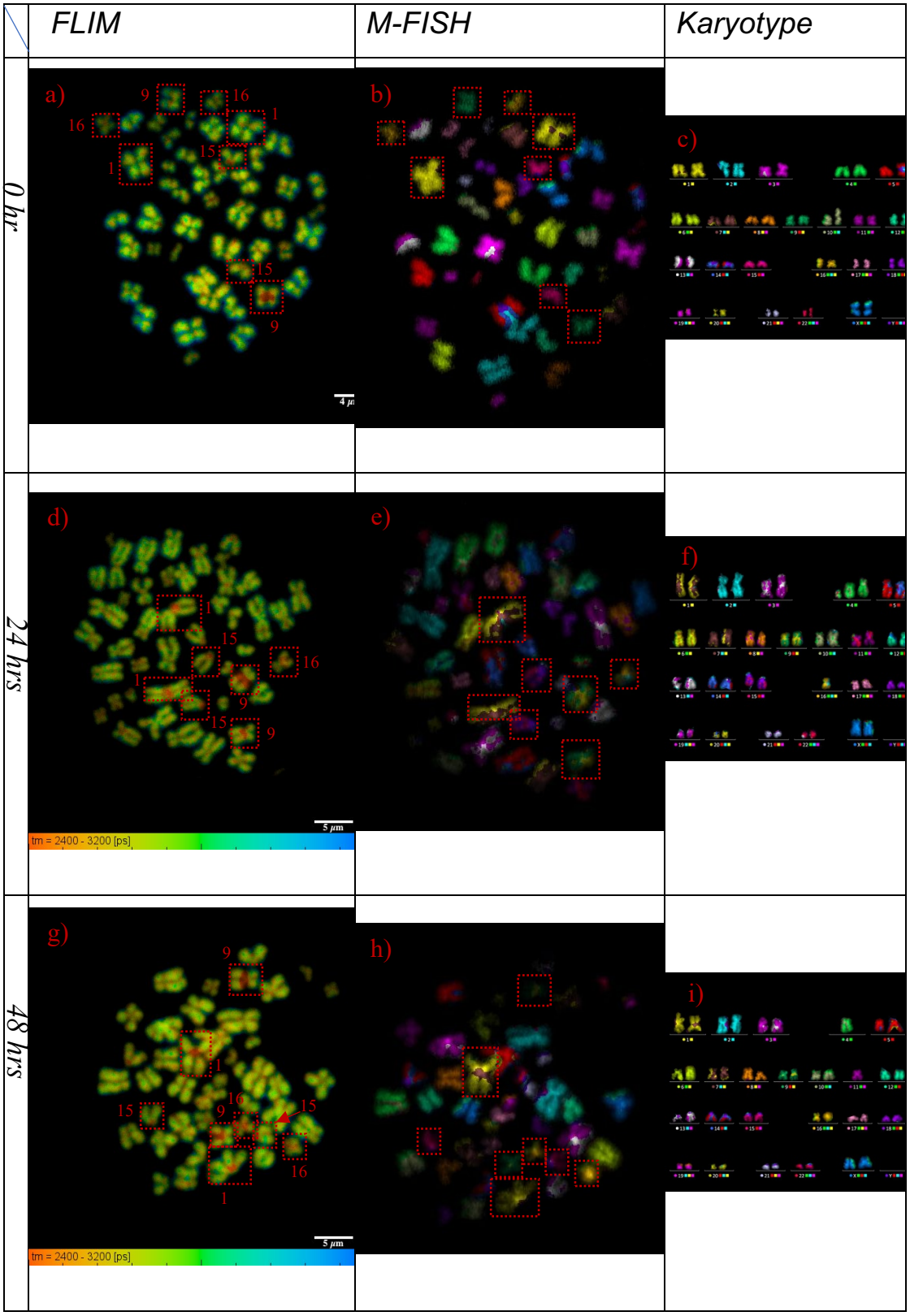

Figure 3.11: X-ray irradiated chromosome spreads from three different generations, irradiated at the rate of a 0.5 Gy/min. It represents the DAPI lifetime maps of each spread imaged using FLIM and with their corresponding M-FISH images and karyotypes. The row defines the three generations and column defines the imaging techniques and the karyotype. Figure a), d) and g) are the FLIM images; b), e) and h)

are the M-FISH image of the same spread, respectively, and c), f) and i) are the karyotypes of the same spread obtained from M-FISH spreads. Red boxes denotes homologous pair of chromosomes with a short lifetime at their heterochromatin regions in all three spreads. Maps of DAPI lifetime ranged between 2.4 ns to 3.2 ns. Scale bar for FLIM images are as follow: 4 µm (figure a) and 5 µm (figure d and g), and the image are of size 512 x 512 pixels. Objectives used for FLIM imaging is 60x water and for M-FISH is 63x immersion oil. Though, the chromosome 16, one out of two, is wrongly placed on position 4 in the M-FISH karyotype in 24 hrs-generation row.

FLIM imaging was accomplished on the following generations (i.e. 0 hr, 24 hrs and 48 hrs) and later on M-FISH was carried out and karyotyped to identify each individual chromosome. The change in the lifetime components was observed in DAPI-bound chromosomes upon X-ray irradiation at different generations (Figure 3.11). The short lifetime component at the heterochromatin regions and long lifetime component at the non-heterochromatin of heteromorphic chromosomes were observed (Figure 3.11). Moreover, the varied lifetime components can also be seen in chromosomes apart from the heteromorphic chromosomes (Figure 3.11).

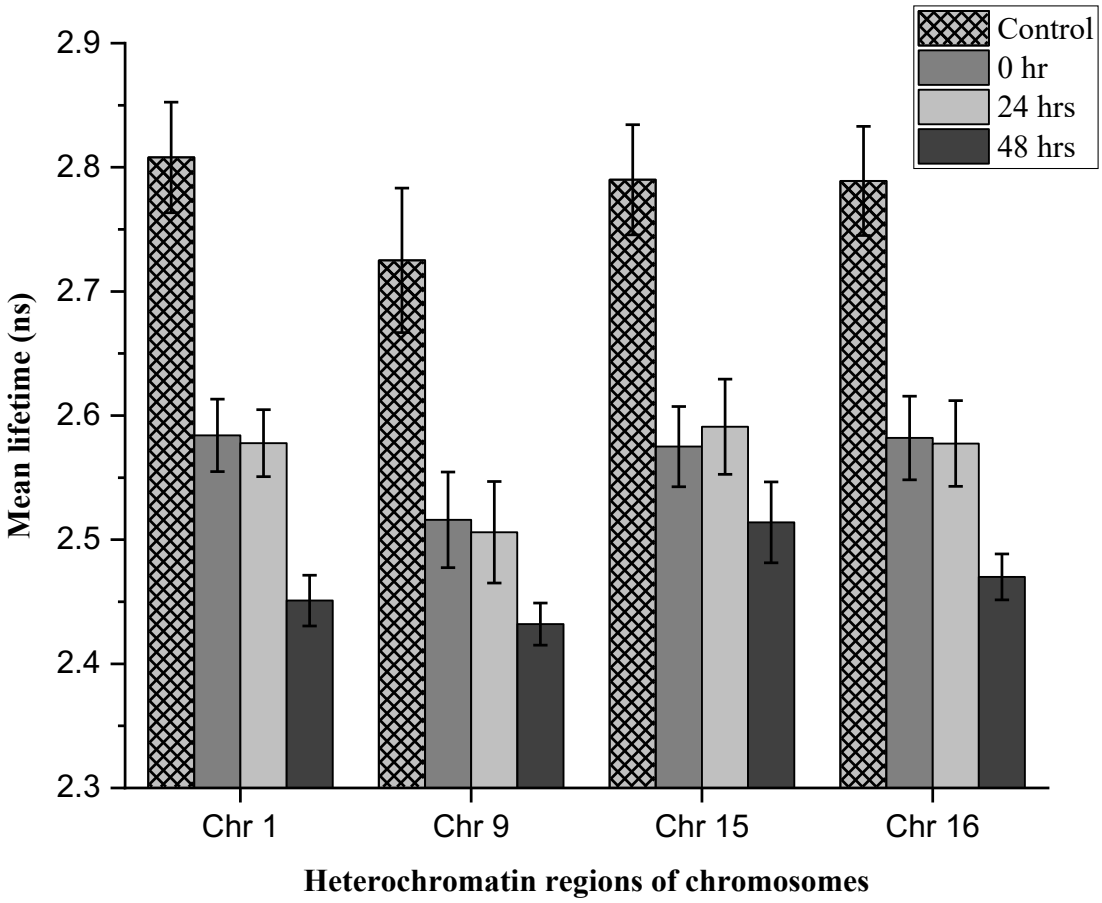

Figure 3.12: Measured mean lifetime of DAPI stained chromosome (1, 9, 15 and 16). The mean lifetime of the heterochromatin regions were obtained from T-lymphocytes. The cells were X-ray irradiated at a rate of 0.5 Gy/min. The different generations are as follow: 0 hr, 24 hrs and 48 hrs along with a control sample, number of chromosome spreads (n = 5). Error bar represents the SEM, *p-value* < *0.05*.

In Figure 3.12, the DAPI lifetime decreases in the X-ray induced chromosomes relative to non-irradiated chromosomes. In addition, the DAPI lifetime of heteromorphic chromosomes decreases with increasing generations (Figure 3.12). However, with chromosome 15, there is a slight increase in the lifetime value with 24 hrs of generation compared to 0 hr of generation. The Figure 3.12 represent the integrated data from a five independent chromosome spreads (pooled from a two independent experiments).

All the lifetimes values are expressed in this manner: X- is an averaged lifetime values ± SEM. The averaged mean lifetime for the control sample is determined to be 2.78 ± 0.05 ns and then it drops to 2.56 ± 0.03 ns, 2.56 ± 0.04 ns and 2.47 ± 0.02 ns for 0 hr, 24 hrs and 48 hrs respectively (Figure 3.12). The DAPI lifetime for 0 hr and 24 hrs came out to be similar but with different SEM value. However, a steep decrease in the DAPI-lifetime of chromosomes observed in 48 hrs of generation but with chromosome 15, there is slight increase in the lifetime at 48 hrs of generation relative to heteromorphic chromosome 1, 9, and 16 (Figure 3.12).

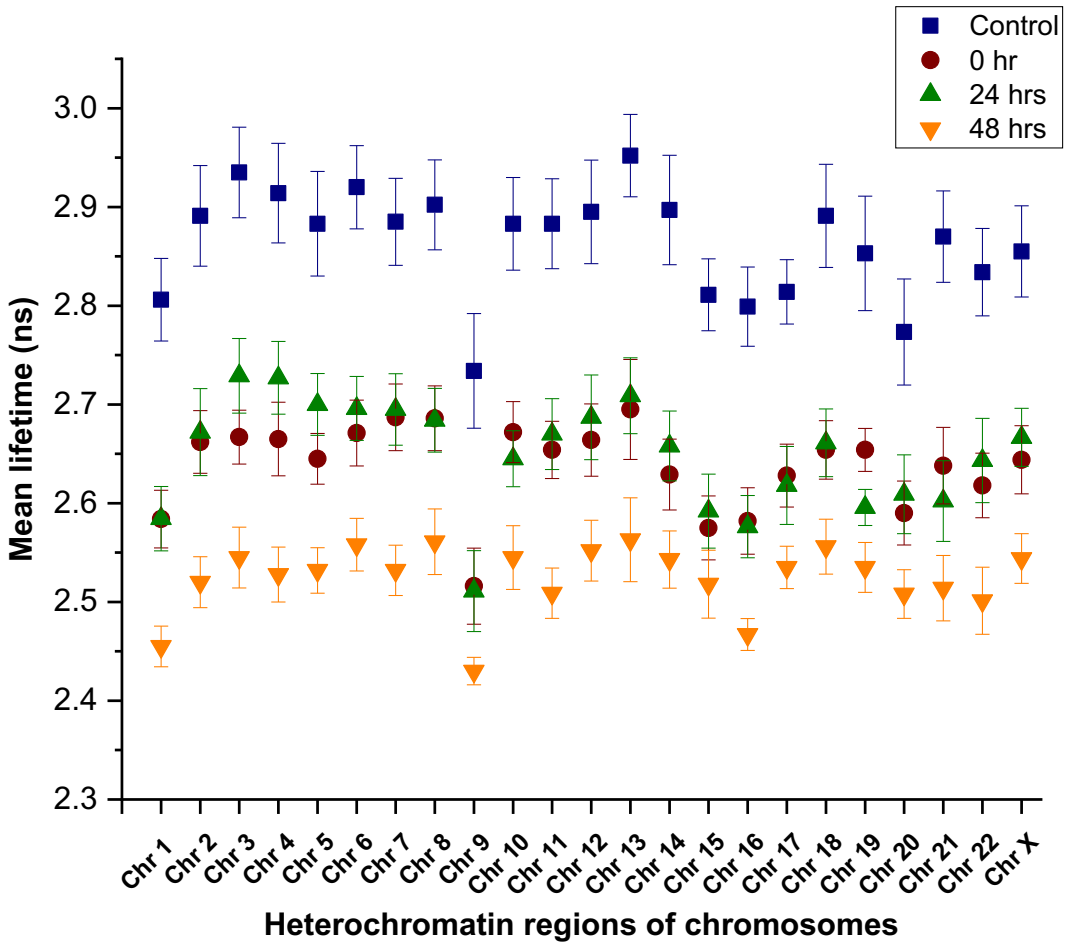

Figure 3.13: Measured mean lifetime of DAPI-bound, heterochromatin regions of all 46 chromosomes obtained from T-lymphocytes at different generation of the cell cycle, number of chromosome spreads (n = 5). Error bar represents SEM, *p-value* < *0.05*.

Moreover, the DAPI-lifetime of all 46 chromosomes was also measured with focus on heterochromatin regions from X-ray induced chromosomes (

Figure 3.13), for each generation (i.e. 0 hr, 24 hrs and 48 hrs) along with the control sample. The data is the averaged of five different chromosome spreads, pooled from a two independent experiments. The DAPI-lifetime of heteromorphic chromosomes diverge a lot and show reduced lifetime compared to other chromosomes present in the spreads as shown in Figure 3.13.

Similarly, the DAPI lifetime of non-heterochromatin regions of heteromorphic chromosome was also measured (Figure 3.14). The data is the averaged of the same five independent chromosome spreads (pooled from a two independent experiments) from which the heterochromatin regions was measured for heteromorphic chromosomes (Figure 3.12) and also for the DAPI lifetime of all 46 chromosomes (Figure 3.13).

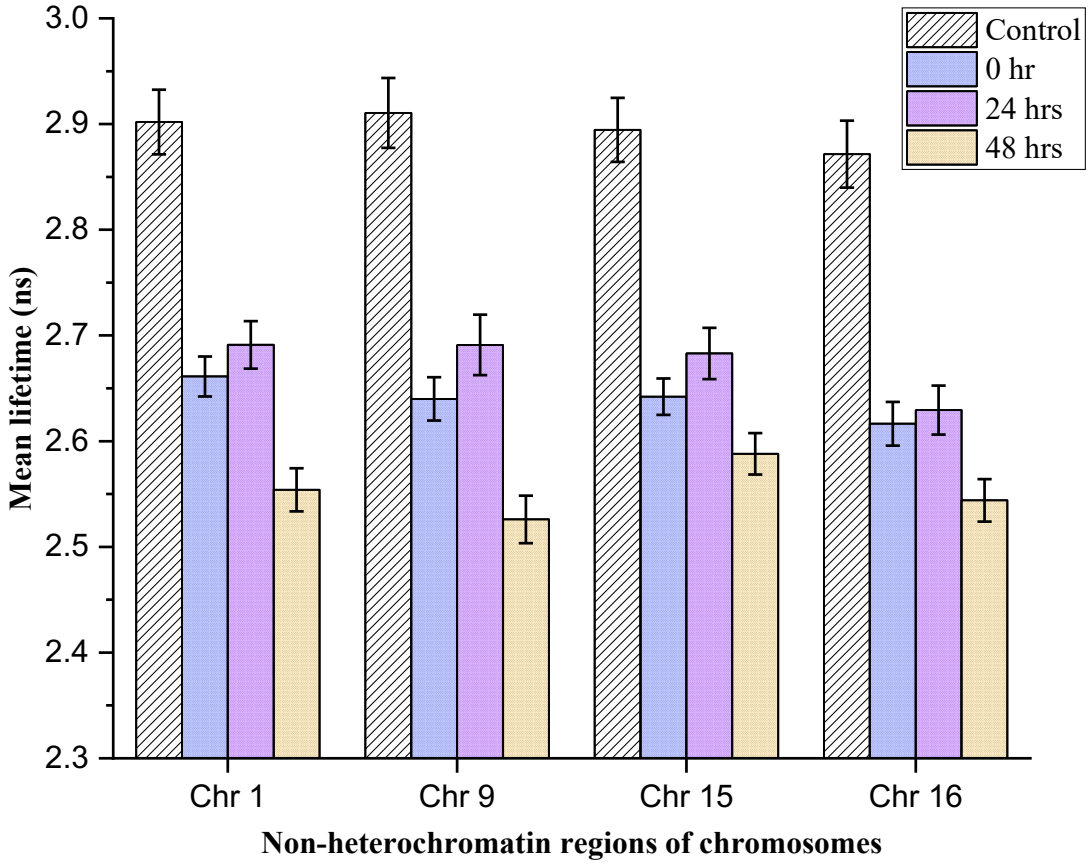

Figure 3.14: Measured mean lifetime of DAPI-bound heteromorphic chromosomes. The mean lifetime measurements are from non-heterochromatin regions of chromosomes (obtained from T-lymphocytes). The cells irradiated at a rate of 0.5 Gy/min of X-ray. The different generations are 0 hr, 24 hrs and 48 hrs along with a control sample, number of chromosome spreads (n = 5). Error bar represents the SEM, *p-value* < 0.04.

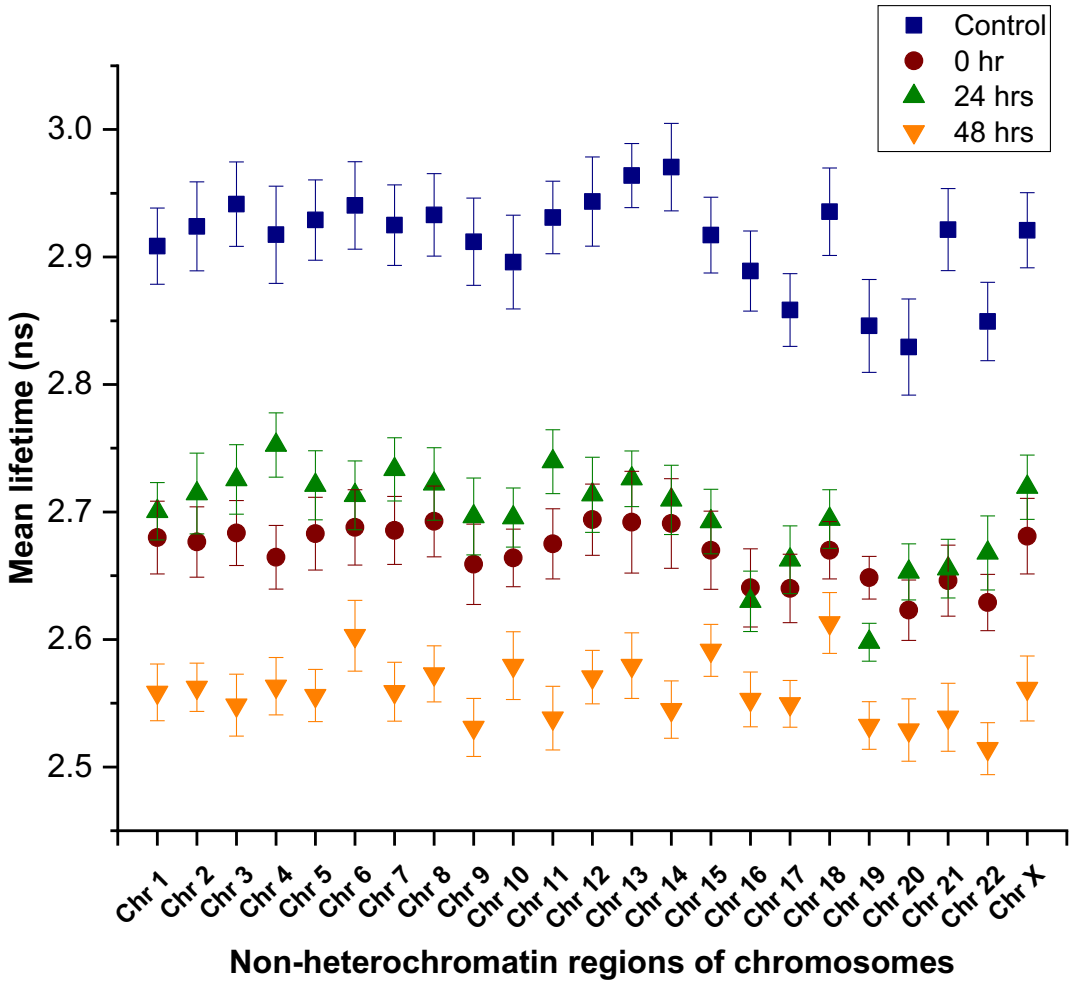

Figure 3.15: Measured mean lifetime of DAPI-bound, non-heterochromatin regions of all 46 chromosomes obtained from T-lymphocytes at different generation of the cell cycle, number of chromosome spreads (n = 5). Error bar represents SEM, *p-value* < 0.03.

As shown in Figure 3.12 the DAPI lifetime of heterochromatin region of chromosomes 1, 9, 15 and 16, decreases with increasing generations of the cell cycle. Nevertheless, the averaged mean lifetime of non- heterochromatin regions contradict the following pattern (Figure 3.14) as shown by heterochromatin regions (Figure 3.12). Though, the reduced DAPI lifetime can be seen in X-ray induced chromosomes (Figure 3.12 and Figure 3.14). The average mean lifetime of heteromorphic chromosomes for the control sample is determined to be 2.89 ± 0.03 ns, followed by the 24 hrs generation (2.67 ± 0.02 ns), 0 hr generation (2.64 ± 0.02 ns) and 48 hrs generation (2.55 ± 0.02 ns) (Figure 3.14).

Though the mean lifetime for non-heterochromatin regions are slightly higher than the heterochromatin regions of heteromorphic chromosomes. The same five independent chromosome spreads have been employed to determine the mean DAPI lifetime of non-heterochromatin regions of all 46 fixed human metaphase chromosome (Figure 3.15) from which the DAPI lifetime of heterochromatin (Figure 3.12) and non- heterochromatin (Figure 3.14) regions of heteromorphic chromosomes obtained, also the heterochromatin regions of all 46 fixed human metaphase chromosomes were measured (Figure 3.13). Thus, the difference in DAPI lifetime between two sub-regions can be observed in all 46 metaphase chromosomes. In Figure 3.15 reduced DAPI lifetime can be observed with increasing generations. The chromosomes following 48 hrs of generation has the lowest lifetime values and the chromosomes with 0 hr and 24 hrs have a similar lifetime for all 46 chromosomes.

3.4. Determination of chromosomal structural abnormalities using FLIM

The chromosomes irradiated with a less than 2 Gy doses of X-ray irradiation are liable to suffer from random molecular and structural aberrations such as DSBs, SSBs, base lesions, deletions, translocations and many more (Shimura and Kojima, 2018). The aberrations that follows, leads to diseases and cell deaths (Lomax, Folkes and Neill, 2013).

Furthermore, the FLIM measurements were also extracted from the chromosomes containing structural aberrations. The chromosomes with aberration were isolated from the same five independent chromosome spreads (pooled from a two independent experiments). Moreover, the structural chromosomal aberrations were observed in the human metaphase chromosomes (fixed with methanol: acetic acid, 3:1) obtained from X-ray induced chromosomes at low radiation doses (i.e. 0.1 Gy, 0.5 Gy and 1 Gy) as shown in Figure 3.16.

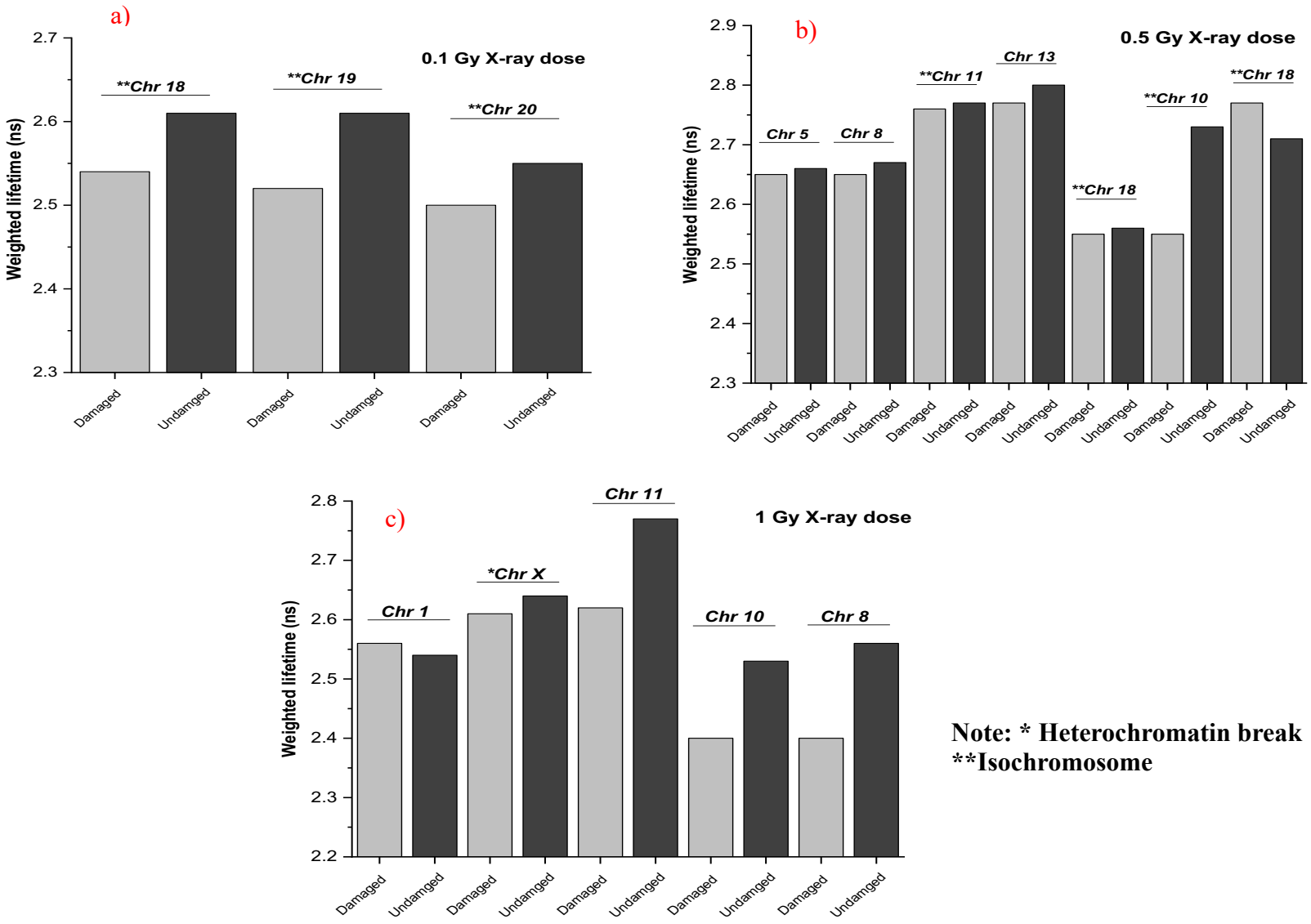

Note: * Heterochromatin break
****Isochromosome**

Figure 3.16: Representation of DAPI-lifetime of irradiated fixed human metaphase chromosomes containing structural aberrations upon X-ray irradiation. The histograms represents the damaged and undamaged chromosomes from the same spread. Following aberrations are 0.1 Gy (a), 0.5 Gy (b) and 1 Gy (c).

Individual chromosomes were analysed from different chromosome spreads induced with different radiation doses (i.e. 0.1 Gy, 0.5 Gy and 1 Gy). The lifetime values states that the damaged chromosomes has lower lifetime in comparison to undamaged chromosomes, present in the same spread (Figure 3.16). A fewer number of aberrations observed in 0.1 Gy irradiation and later increased with a higher doses. Nevertheless, in this work, 0.5 Gy irradiation showed more structural aberrations than with 1 Gy irradiation (Figure 3.16).

In

Figure 3.17 chromosome 18, 19 and 20 from the single chromosome spread experiences “centromeric breaks” which has been labelled as “isochromosomes” (Figure 3.16, 0.1 Gy X-ray dose) because the following individual chromosomes appeared as structurally detached, separating p-arm and q-arm when examined using FLIM and M-FISH techniques (

Figure 3.17). The lifetime values represents the averaged mean lifetime of both heterochromatin and non-heterochromatin regions of damaged an undamaged part of a chromosome (Figure 3.16, 0.1 Gy X-ray dose). For example, DAPI lifetime of undamaged chromosome 18 and 19 determined to be ~2.6 ns and damaged chromosome is ~2.52 ns. Moreover, the DAPI-lifetime for damaged and undamaged chromosome 20 are ~2.5 ns and ~2.54 ns (Figure 3.16, 0.1 Gy X-ray dose), respectively.

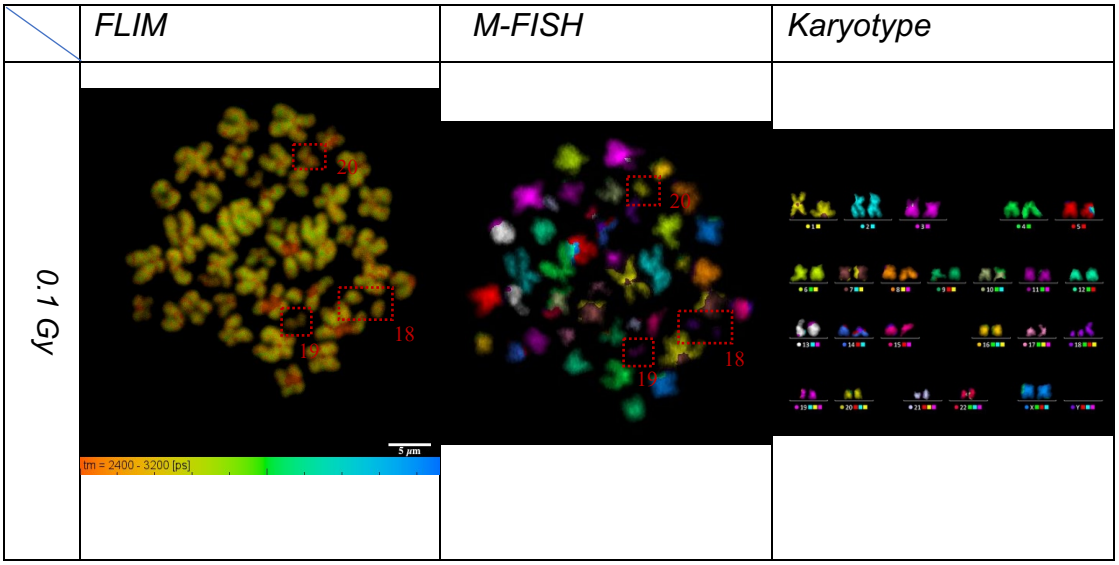

Figure 3.17: Representation of isochromosome aberrations originated from T-cells exposed to 0.1 Gy X-ray exposure. Red dotted squares shows chromosome underwent isochromosome aberrations. Scale bar= 5 µm.

In

Figure 3.18, DAPI lifetime of structurally damaged chromosomes has been shown. The translocation aberration has been observed between chromosome 8 and 5 using FLIM and M-FISH, the q-arm of the chromosome 8 translocated onto the q-arm of the chromosome 5 (

Figure 3.18). The lifetime of translocated q-arm of chromosome 8 and truncated q-arm of chromosome 5 is 2.65 ns. Similarly, the chromosome 13 undergone non-heterochromatin break (Figure 3.16, 0.5 Gy X-ray dose) and the lifetime acquired is 2.78 ns and for undamaged chromosome is 2.8 ns.

Chromosomes 18, 10 and 18 have undergone isochromosome/centromeric breaks, (all three chromosomes are from three different spreads) (Figure 3.16, 0.5 Gy X-ray dose), the DAPI lifetime of both damaged and undamaged chromosomes are shown in Figure 3.16 (0.5 Gy X-ray dose). Unfortunately, a few chromosomes are missing in the M-FISH and in the karyotype (Figure 3.18) due to difficulties to rescue them during the M-FISH hybridisation although FLIM measurement for all 46 chromosomes were obtained prior to the M-FISH hybridisation.

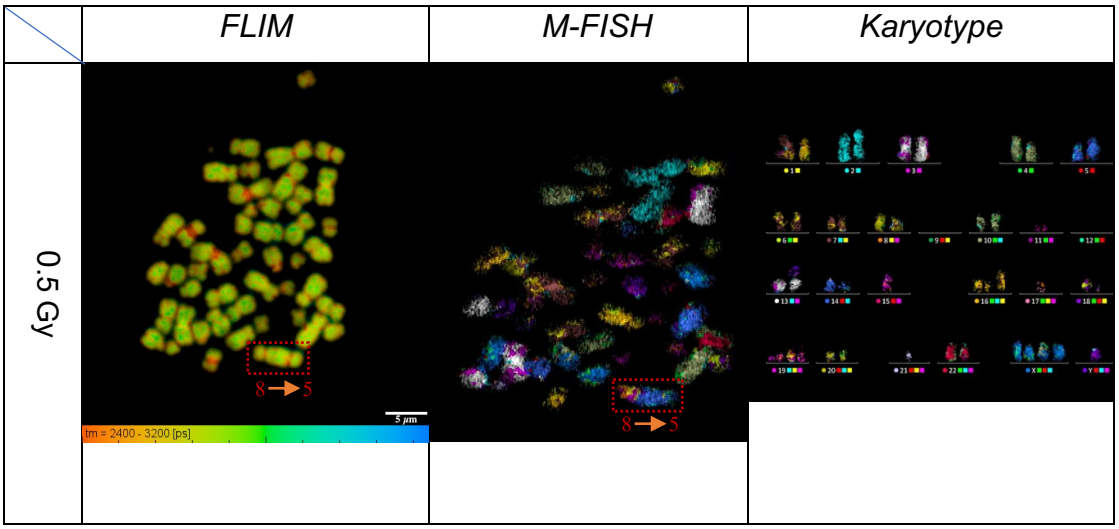

Figure 3.18: A spread irradiated at a 0.5 Gy X-ray exposure. The red dotted box represents translocation of q-arm of chromosome 8 into the q-arm of chromosome 5, shown in both FLIM and M-FISH image. Scale bar= 5 µm.

Similarly, with exposure to 1 Gy irradiation we have observed some heterochromatin (chromosome X) and non-heterochromatin breaks such as chromosome 1 (Figure 3.19) and chromosome 11 (Figure 3.16). These three aberrations were found in three different spreads. Also, chromosomes 10 and 8 have found truncated and with lost arms obtained from a single spread. Henceforth, the difference in DAPI lifetime can be observed between damaged and undamaged chromosomes in Figure 3.16 (1 Gy X-ray dose).

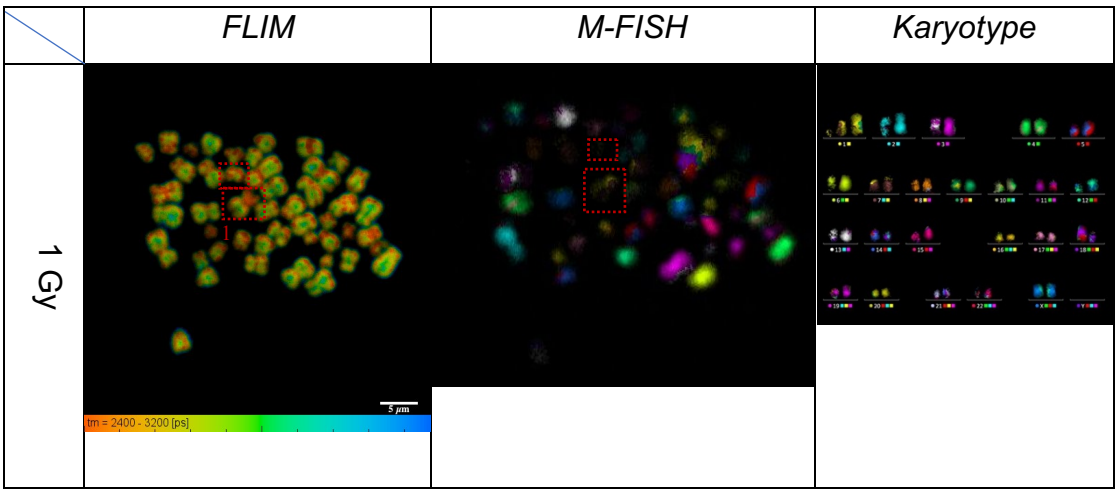

Figure 3.19: A spread irradiated at 1 Gy X-ray exposure. The red dotted box represents non-heterochromatin break of chromosome 1 and its fragmented pieces, shown in both FLIM and M-FISH image. Scale bar= 5 μm.

Chromosome 18 following 0.5 Gy and chromosome 1 following 1 Gy have showed unusual behaviours. For example, the DAPI lifetime of damaged chromosomes 18 and 1 have significantly higher than undamaged ones regardless of sub-regions of chromosomes (Figure 3.16). All the DAPI lifetime measurements were done in methanol: acetic acid (3:1) fixed metaphase chromosome. In addition, the lifetime values are independent of morphology and the category of aberrations occurred in the chromosomes.

3.5. FLIM on DAPI-bound chromosomes from B-lymphocytes

FLIM imaging was also performed on the B-lymphocytes cells provided by Prof Ian Robinson's group but with the higher passage number, 15. The lifetime measurement was performed to observe the change in lifetime components in the heteromorphic chromosomes obtained from B-lymphocytes even at the higher passage number and to correlate with the finding that the heterochromatin region of heteromorphic chromosome have shorter lifetime such as for chromosome 1 is 2.58 ± 0.06, for chromosome 9 is 2.3 ± 0.06, for chromosome 15 is 2.43 ± 0.05, for chromosome 16 is 2.55 ± 0.06 and for chromosome Y is 2.58 ± 0.03 (Figure 3.20), in comparison to other chromosomes in a spread (Estandarte *et al.*, 2016). Nevertheless, the imaging was performed only on the non-irradiated chromosomes stained with 4 μM freshly prepared DAPI. According to Estandarte *et al*., (2016) the short lifetime component was observed in heteromorphic chromosomes are due to highly dense packing of heterochromatin regions.

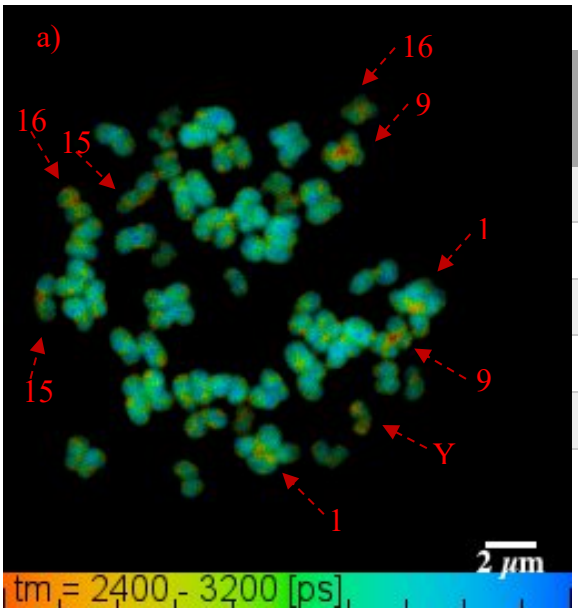

Chromosomes b)	Mean lifetime (τ_m)
Chr 1	2.81
Chr 9	2.65
Chr 15	2.66
Chr 16	2.73
Chr Y	2.76

Chromosome #	c) Mean Lifetime ± SD, ns
1	2.58 ± 0.06
9a	2.38 ± 0.06
9b	2.21 ± 0.05
15	2.43 ± 0.05
16	2.55 ± 0.06
Y	2.58 ± 0.03

Figure 3.20: FLIM imaging performed on a spread obtained from non-irradiated B-lymphocytes, a) shows the lifetime components of heteromorphic chromosomes, indicated with red arrows. The lifetime distribution ranged between 2.4 ns to 3.2 ns (mentioned below the FLIM image), scale bar = 2 µm, image size is 256 x 256 pixel and the objective used is 60x water. b) the table shows chromosomes with a short lifetime at the heterochromatin regions of chromosomes along with their SEM values. Table c) represents the mean lifetime of heteromorphic chromosomes, from a five-individual spreads, along with standard deviation of each, taken from (Estandarte *et al.*, 2016).

In Figure 3.20, the colour-coded map of FLIM image shows that each heteromorphic chromosomes has a short lifetime at the heterochromatin regions of chromosomes. Moreover, the mean lifetime values displayed in table (Figure 3.20, table b) are the averaged mean lifetime of a homologous pair of chromosomes present in an individual spread.

The lifetime of non-heterochromatin regions was also measured of heteromorphic chromosomes to observe the variation in the lifetime of two

major sub-structures along the length of a methanol: acetic (3:1) fixed human metaphase chromosome (

Figure 3.21). The purpose was to understand the change in lifetimes at the pixel-level from a colour-coded map obtained through FLIM imaging in B-lymphocytes.

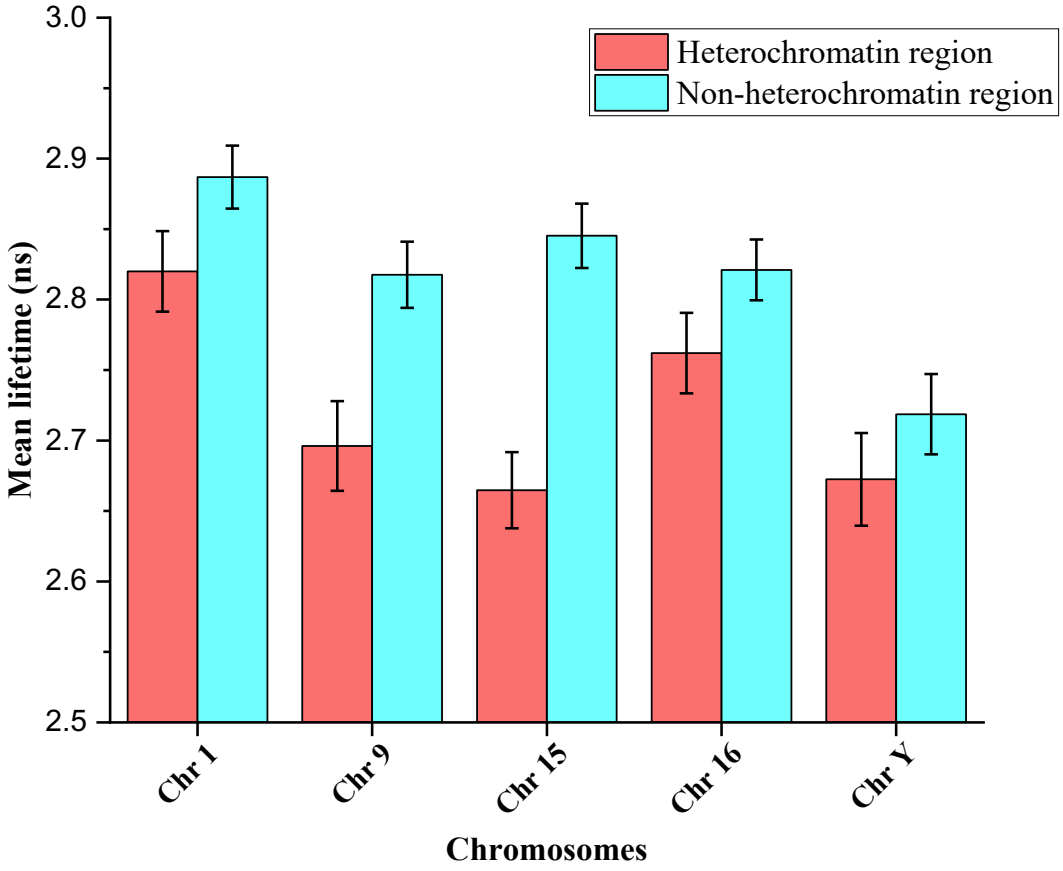

Figure 3.21: Represents the mean lifetime of both heterochromatin and non-heterochromatin regions of chromosome 1, 9, 15, 16 and Y obtained from non-irradiated B-lymphocytes cells, number of spreads (n) = 13. The bars represents the SEM and $p < 0.05$.

Figure 3.21 shows the mean lifetime of heterochromatin and non-heterochromatin regions of chromosomes obtained from B-lymphocytes and the lifetime values are pooled from a 13 independent chromosome spreads. It can be observed from the

Figure 3.21, that the heterochromatin regions of heteromorphic chromosomes have a shorter lifetime relative to non-heterochromatin regions

of chromosomes. The averaged lifetime of heterochromatin region is determined to be 2.72 ± 0.03 ns and the non-heterochromatin region is 2.82 ± 0.02 ns. Furthermore, it can be concluded that the averaged lifetime of both the components of B-lymphocytes have shorter lifetimes compared to the T-lymphocytes.

On the other hand, the averaged (lifetime values pooled from 5 independent chromosome spreads) mean lifetime of the heterochromatin regions of heteromorphic chromosomes obtained from T-lymphocytes is determined to be 2.8 ± 0.03 ns (Figure 3.6) and for the non-heterochromatin region is 2.88 ± 0.02 ns (Figure 3.8).

3.6. DAPI lifetime of DNA oligomers

After investigating high order structure of mitotic chromosomes obtained from T-lymphocytes in X-ray induced chromosomes, using FLIM technique. FLIM measurement from non-irradiated B and T-lymphocytes using FLIM was also carried out. We carried investigation of DAPI lifetime of naked DNA to observe variation of DAPI lifetime due to alteration of DNA base sequences. 7 oligomers of 20 mM concentration (each containing 10 bases of DNA) were prepared with 4 μM freshly prepared DAPI.

The following mean lifetimes were obtained for each oligomers (Figure 3.22) is an average of six data taken on the same glass slide but with different laser power. The lifetime value for 100 % AT-rich oligomers has a longer single lifetime component such as for TTA-AAT-TTT-T is 3.99 ns and for AAA-TAT-ATA-A is 3.74 ns, compared to 100% GC-rich oligomers. The oligomer CGG-CGG-CGG-C and GCC-GCC-GCC-G has a decreased mean lifetime value and contains two lifetime components for example t1 = 0.89 ns, t2 = 5.37 ns and t1 = 0.96 ns, t2 = 3.68 ns respectively (Figure 3.22). 40% GC content produced a single lifetime component (t1 = 3.49 ns) whilst 60% GC (AAC-CCG-GGT-A) content gave two lifetime components (t1 = 0.41 ns, t2 = 3.89) (Figure 3.22).

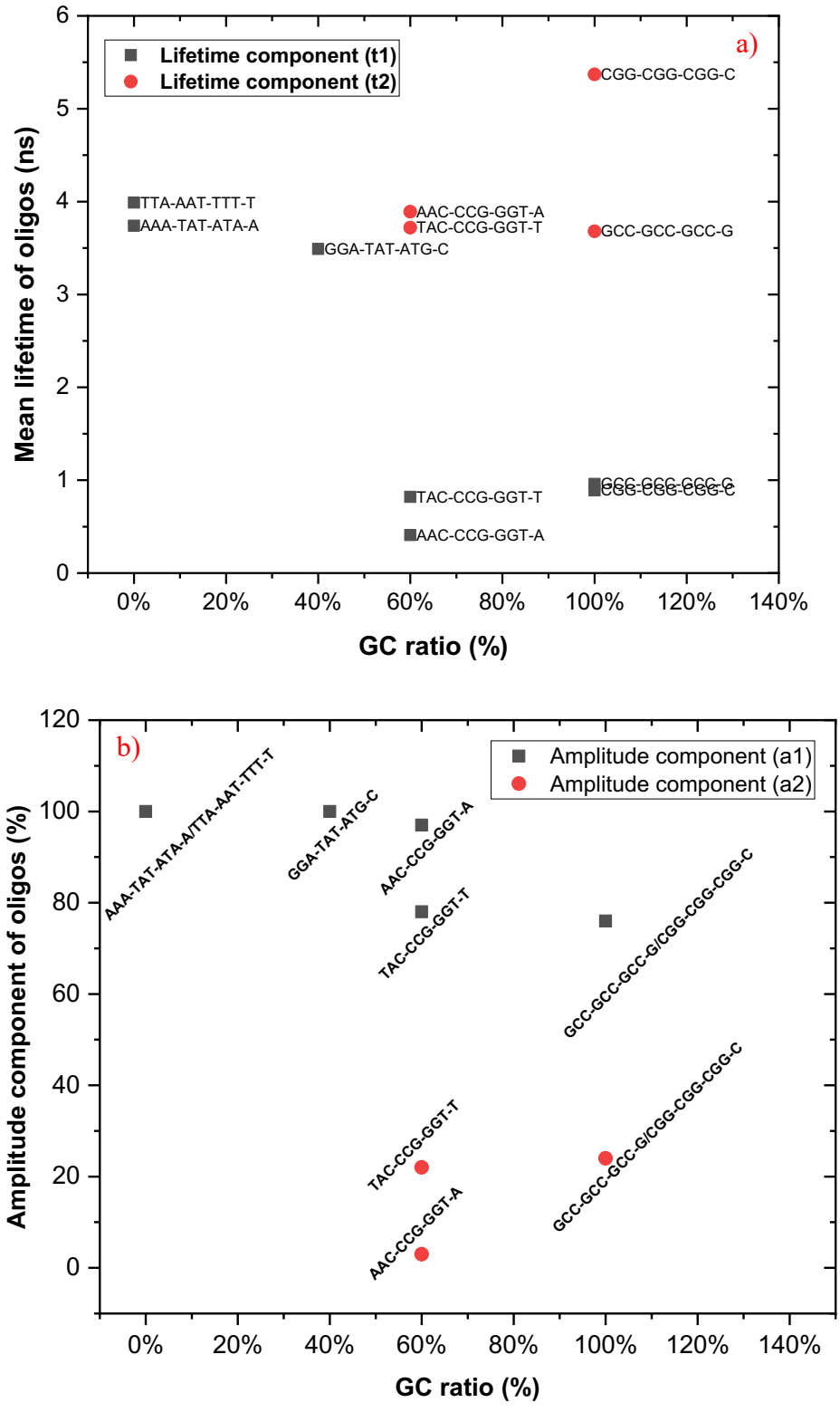

Figure 3.22: FLIM measurement of 4 µM DAPI labelled DNA oligomers, a) representing the mean lifetime *versus* % of GC ratio present in the oligomers. With 0% to 40% content of GC, the oligomers shows single lifetime component(black square) and above 60% of GC shows two lifetime components (1st-black box and 2nd-red circle). b) following this, the amplitude component was also measured of the same oligomers.

3.7. Discussion

The objective of this chapter is to understand the short and the long-term effects of ionising radiation in the X-ray induced chromosomes using nanosecond excited state lifetime imaging along the length of the chromosome obtained from T-lymphocytes. The effect of ionising radiation was studied on both the heterochromatin and non-heterochromatin regions of a chromosome as described previously in the chapter 3. Furthermore, chromosomal aberrations occurring at different generations of the cell cycle was also investigated. These investigations were carried out using the FLIM technique followed by M-FISH for the identification of each individual chromosomes in a spread.

The combined techniques of laser scanning confocal microscopy and multiphoton microscopy have been used to study the suggested compaction and the condensation state of chromatin during mitotic cell division (Estandarte *et al.*, 2016) (Phengchat *et al.*, 2016). According to Estandarte et al, (2016), the lifetime changes in DAPI stained metaphase chromosomes show the presence of condensed (heterochromatin) and de-condensed (non-heterochromatin) regions along the length of the chromosomes, measured by FLIM. Following this study, the combined FLIM and M-FISH techniques used to study the effects of ionising radiation on the substructures of chromosomes obtained from B and T-lymphocytes, and in addition, studies on the effect of X-rays on different generations of the cell cycle have been performed.

The centromere size of heteromorphic chromosome 1, 9, 15 and 16 are considerably extended relative to other chromosomes present in the human genome and the extended regions are located at the pericentric heterochromatin region and the following regions possess unusual de-condensation process when treated with 5-azacytidine (Sanchez, Martinez and Goyanes, 1991). Moreover, the same pattern was also noticed at the distal

region of chromosome Y (Sanchez, Martinez and Goyanes, 1991). Moreover, the de-condensation process was observed by electron microscopy (Sanchez, Martinez and Goyanes, 1991). Similarly, the anomalous behaviour has been observed using G and C- banding (Sahin *et al.*, 2008). In our result each heteromorphic chromosome showed shorter DAPI lifetime component at the heterochromatin regions in both the selected cell types (B and T-lymphocytes) relative to rest of the chromosomes in a spread. The initial data from the studies reported here correlate with the findings of (Estandarte *et al.*, 2016). After decades of studies it is well known that these individual chromosomes have highly heteromorphic variants (Sanchez, Martinez and Goyanes, 1991) (Tagarro, Fernández-Peralta and González-Aguilera, 1994) (Chen *et al.*, 1981).

Each individual chromosomes composed of a specific pentanucleotides of DNA sequences as listed, chromosome 1 consist of satellite II and III, chromosome 9, 15 and Y has satellite III, chromosome 16 has satellite II (Chen *et al.*, 1981) (Tagarro, Fernández-Peralta and González-Aguilera, 1994) (Choo, 1997). The following satellites consist of tandem repeats of 5 bp nucleotides of GGAAT- sense strand and ATTCC- antisense strand. The oxidation potential of guanosine (G) is high compared to the other DNA bases. Furthermore the pyrimidine bases have lower oxidation potential than the purine bases, following an order of: G>A>C>T in terms of oxidation potential efficiency (Seidel, Schulz and Sauer, 1996). The constitutive heterochromatin of heteromorphic chromosomes (1, 9, 15 and 16) consists of tandem repeats of GGAAT DNA bases. Henceforth, it is possible that guanosine bases present in the heteromorphic chromosomes oxidises faster upon laser excitation and gives shorter lifetime compared to the rest of the chromosomes.

The functional role of pericentromeric heterochromatin and polymorphic tandem repeats and condensed nature are largely unknown (Nishibuchi and Déjardin, 2017). Relative DNA content has been calculated from 16 healthy individual donors of all 46 chromosomes using flow cytometry (Mayall *et al.*, 1984). The heteromorphic chromosomes 1, 9, 16 and Y showed a greater amount of variability in the DNA content due to presence of a constitutive heterochromatin followed by acrocentric chromosomes 13, 14, 15, 21 and 22

(Harris *et al.*, 1986). Heteromorphic variants of chromosomes have an undefined phenotypic role (Madon, Athalye and Parikh, 2005). An instability in centromeric heterochromatin of chromosome 1, 9 and 16, is the ground source of a disease called Immunodeficiency centromeric instability and facial dysmorphic syndrome (ICF) (Maraschio *et al.*, 1988).

In our data, the distribution of DAPI lifetime was measured at the heterochromatin and non-heterochromatin regions of each individual chromosomes as described previously in the chapter. In this work, the averaged DAPI lifetime of heterochromatin regions possess shorter DAPI lifetime and non-heterochromatin regions possess longer DAPI lifetime as shown in the results sections above. The shorter lifetime is due to the compact architecture of heterochromatin regions and longer lifetime is due to least compact architecture of non-heterochromatin regions of heteromorphic and the rest of the chromosomes in a spread (Estandarte *et al.*, 2016).

A global compaction and decompaction in Hoechst 34580 stained chromatin observed due to hyperosmolarity and histone deacetylase respectively (Abdollahi, Taucher-Scholz and Jakob, 2018). Also, reduced lifetime observed in differentiating cells due to compaction though some decompaction regions also observed which probably represents transcription repositories in a fixed cell, on the other hand increased lifetime observed in stem cells due to decompaction and the cells were stained with SiR-DNA stain (Hockings *et al.*, 2020). It can be determined that the DNA stains shows variation in lifetimes due to labelled chromosomes conformation.

It is observed from the results that the measured lifetime of DAPI-bound chromosomes has slightly shorter lifetime at the heterochromatin regions relative to non-heterochromatin regions of the chromosomes, irrespective of the cell type. We can hypothesize that the heteromorphic chromosomes have conserved heterochromatin regions in different cell types but may differ in heteromorphic variants present in each individual chromosomes (Tagarro, Fernández-Peralta and González-Aguilera, 1994) (Estandarte *et al.*, 2016). Moreover, each individual heteromorphic chromosomes has conserved

heterochromatin regions, even in the cancerous cells such as HeLa cells (Estandarte *et al.*, 2016).

According to Pita *et al*. the pericentromeric region of human chromosome 9 incorporate repeated sequence of satellite III DNA, that are considered to be an evolutionary fragments derived from gorilla genome whose functional role is still remains unclear (Pita *et al.*, 2010). In our finding it is observed that the chromosome 9 has the lowest DAPI lifetime compared to other heteromorphic chromosomes along the length of the chromosomes (Figure 3.6) and it could be because of its highly polymorphic variants at the heterochromatin regions (Humphray *et al.*, 2004) (Madon, Athalye and Parikh, 2005). Various speculative studies reported data on damaged heteromorphic chromosome 9 that it can leads to infertility and miscarriages (Madon, Athalye and Parikh, 2005) (Sahin *et al.*, 2008). The human sex chromosome Y is thought to have evolved from the primates like, chimpanzees (Charlesworth, 2003). It is hypothesis that the existence of Y chromosome is disappearing due to decay of the euchromatin genes into heterochromatin genes with passing years (Charlesworth and Charlesworth, 2000). The heterochromatin block of Y chromosome is almost 40 Mb long (Bachtrog, 2014). In addition, a report suggests that the variants of chromosome 16 leads to body dysmorphic features observed in a four-year-old child (Tadao ARINAM, 1988).

The heterochromatin region of each individual heteromorphic chromosomes are conserved at low-level of ionising radiation doses that has been shown using FLIM in this chapter. Heteromorphic chromosomes 9, 15 and a portion of chromosome 1 consist of DNA satellite III that's shows reduced DAPI lifetime compared to chromosome 16 which consist of DNA satellite II (Figure 3.4) (Tagarro, Fernández-Peralta and González-Aguilera, 1994). It is assumed that reduced lifetime of DNA satellite III may be because of arrangement of base pair sequences and the chemistry of satellite III. Constitutive heterochromatin of heteromorphic chromosomes are inheritable, and preserved (Allshire and Madhani, 2018). Although the molecular mechanism behind the lifetime variation at the pericentric region of heteromorphic chromosomes is certainly unclear.

3.7.1. Post-irradiation effects on the sub-structures of the chromosomes.

The difference in DAPI lifetime of heterochromatin and non-heterochromatin regions along the length of the chromosomes has been observed in non-irradiated samples as described previously in this chapter. The heterochromatin regions which is responsible for the stability of genome, were explored after exposure to ionising radiation.

According to the literature, DNA is damaged even at low radiation doses, ranges from 1 mGy to 0.5 Gy (Shimura and Kojima, 2018). Chromosomal aberration at 0.5 Gy irradiation can cause 8.02 ± 5.38 DSB and with 1 Gy irradiation causes, 37.96 ± 2.23 DSB (Schröder *et al.*, 2019). With continuous exposure of γ-irradiation at the rate of 6-20 mGy/h for 7 days, instigate DNA damage and loss of histone proteins up to 40 % noticed (Lowe *et al.*, 2020). Core histone protein such as H2A, H2A.Z, H2B, H3, H4 and linker histone H1 were reduced on chronic irradiation at 20 mGy/h also reduction in H2AX histone was also observed in (Lowe *et al.*, 2020). We have investigated DAPI-lifetimes changes occurring immediately after exposure to X-ray irradiation in chromosomes obtained from T-lymphocytes (Figure 3.6, Figure 3.8, Figure 3.9, and Figure 3.10). The data was pooled from five independent chromosome spreads of the same preparation. The differences in DAPI lifetime calculated between non-irradiated and irradiated chromosomes are as follows: ~270 picosecond (ps) for 0.1 Gy dose, ~260 ps for 0.5 Gy dose and ~290 ps for 1 Gy irradiation. Therefore, the reduced lifetime observed even with low-level doses below 2 Gy that means the base sequences or the chromatin fibres must have undergone conformational changes or it might have affected the chromosomal proteins.

The chromosomes 1q, 9q, 15q and 17q irradiated using ^{60}Co radiation showed more number of translocation at 0.5 Gy than at 1 Gy (Lin, Wu and Lee, 2019). Considering this, the molecular environment change occurring in X-ray induced chromosomes was investigated using FLIM, because the information of the environmental change of DAPI fluorescence on a nanosecond time scale can be acquired by the fluorescence lifetime decay map (Suhling *et al.*, 2015). In this work averaged DAPI lifetimes for non-heterochromatin regions of all 46 X-ray induced chromosomes measured (pooled from five independent chromosome spreads). We have observed reduced lifetime at the non-heterochromatin of chromosome 17 along with chromosomes 1, 9, 15 and 16 (Figure 3.10) but did not observe lifetime change at the heterochromatin regions of chromosomes maybe because chromosome 17 does not have tandem repeats of GGAAT like heteromorphic chromosomes. The mean lifetime differences between non-irradiated and irradiated chromosomes are as follow ~280 ps for 0.1 Gy, ~260 ps for 0.5 Gy and ~300 ps for 1Gy for non-heterochromatin regions. The following results suggest that the chromosomes induced with 1 Gy dose has the shortest DAPI-lifetime along the length of the chromosome. Conclusively, the ionising radiation has almost similar effect all over the length of chromosomes irrespective to different regions of chromosomes.

The DAPI lifetime reduces in the X-ray induced chromosomes almost by 26% to 30%. This means that the sub-structure regions are conserved at a selected low-level ionising radiation doses but probably underwent to chemical modification which is detected by the FLIM technique. Therefore, irradiated chromosomes showed reduced DAPI lifetime compared to non-irradiated chromosomes. It was also observed that the effect of ionising radiation is independent of radiation doses. The results of DAPI-lifetime observed at different doses in this chapter indicates the same.

Irradiation is known to cause several significant structural (Anderson *et al.*, 2006) and numerical (Cho *et al.*, 2015) chromosomal aberrations depending on the dose (Lin, Wu and Lee, 2019) and the dose rate (Nair *et al.*, 2019) in the live cells. DNA double strand breakage, gene sequence rearrangements and

recombination are the major aberrations at the initial stage (Pfeiffer, Goedecke and Obe, 2000), which continues to chromosomal aberrations in future cell generations (Aparicio, Baer and Gautier, 2015). The aberrations range from point mutations to a missing set of homologous chromosomes, which further leads to lethal and non-lethal diseases including cancer (Gospodinov and Herceg, 2013) (Durante and Formenti, 2018).

Our results show that the low-level ionising radiation below 2 Gy perturbs the chemical aberration in chromosomes rather than the structurally. Exposure between 0.1 Gy to 1 Gy, following aberrations has been scored such as formation of micronuclei, nucleoplasmic bridges (NPBs), protein cross links, damages protein-protein interactions and affects the protein expressions (Schröder *et al.*, 2019) (Shimura and Kojima, 2018). According to (Schröder *et al.*, 2019), neither cytotoxic nor genotoxic effects were observed after 0.1 Gy radiation doses. Rather, it enhances the proliferation rate of the “Adipose-Derived Stem Cells” (ADSCs) (Schröder *et al.*, 2019).

3.7.2. Cell growth enhances the effect of X-ray radiation

Exposure to X-rays affects the DNA and the chromosomes and causes aberrations: from point mutation to loss of the chromosomes and influences the karyotypic instability (Shimura and Kojima, 2018). The effect of ionising radiation at G0 generation has been shown (Figure 3.6, Figure 3.8, Figure 3.9 and Figure 3.10). Following this, we elucidated the effect of radiation in the G1 (24 hrs), G2 (48 hrs) and G3 (72 hrs) generation of the cell growth (Figure 3.12,

Figure 3.13, Figure 3.14 and Figure 3.15). Fluorescence lifetime distribution of DAPI-bound chromosome were measured for G1 and G2 phase but chromosomes obtained from G3 were not analysed further because of insufficient of chromosomes number in chromosome spreads and maximum number of dead cells were seen in the preparation . It was noticed that the DAPI

lifetime for G2 generation is significantly decreased, indicating that the irradiation effects also occurred at the second generation of the cell growth. Therefore, our results indicates that it is possible that the low ionising radiation perturbs DNA, possibly through free reactive radicals (Park *et al.*, 2013) .

Moreover, according to Schröder *et al.*, the ADSCs cells proliferate after 24 and 48 hrs of irradiation at low ionising radiation (Schröder *et al.*, 2019). In experiments done here, no structural aberrations has been observed at G1 and G2 stage in the cell cycle but major DAPI lifetime change along the length of the chromosomes in the G2 generation of the cell cycle (Figure 3.12 and Figure 3.14) has been noticed. Therefore, it can be assumed that chromosomal aberrations are more severe in the case of immediate extraction of chromosome after exposure in comparative to different generation of the cell cycle in terms of structural aberration (Figure 3.16, 0.5 Gy X-ray dose). Nevertheless, chemical modification of DNA can be predicted from the obtained DAPI lifetime at the second generation of the cycle upon exposure to low ionising doses as fluorescence decay gives information about the molecular environment of the sample (Suhling *et al.*, 2015) (Estandarte *et al.*, 2016). The direct effect of ionising radiation on chromosomes can be deleterious (Reisz *et al.*, 2014).

Enough covalent bonds may be disrupted when chromosomes struck by a high energy wave or particle (Cannan and Pederson, 2016); it may break into DNA fragments (Newman *et al.*, 1997). Even if the chromosome manages to remain intact, an individual gene along its length maybe badly damaged and a mutation may be produced in the local chromatin (Reisz *et al.*, 2014) (Sanders *et al.*, 2019). In this work we have seen a very small amount of chromosomal breaks at selected low radiation doses but more number of intact chromosomes with a reduced lifetime after exposure to X-ray irradiation. This means that chromosomes expose to low radiation undergone mutation in the local regions of chromatin.

Chromosomal aberrations like dicentric, acrocentric and telomeric deletions occurred with exposure to γ-rays at a radiation doses of 4 Gy . These dicentrics decreases with every successive cell division, on the other hand,

telomeric deletions increases with progressive cell division (Kaddour *et al.*, 2017). According to Truong *et al.*, in fibroblast cells, at low X-ray radiation (0.5 mGy) doses, the damage DNA goes to halt state immediately after exposure to radiation possibly to repair the damaged DNA and reduces the prolonged effects of radiation in further cell growth (Truong *et al.*, 2018).

In this chapter, we have described how both the sub-structures (heterochromatin and non-heterochromatin regions) of chromosome after 48 hrs of post-irradiation leads to reduction in the fluorescence decay of DAPI-bound chromosomes relative to the non-irradiated chromosome (Figure 3.12, Figure 3.13, Figure 3.14 and Figure 3.15). The difference in DAPI lifetime is determined to be ~310 ps and ~340 ps for heterochromatin and non-heterochromatin respectively. Though, the structural aberration was not observed in the different generation of the cell cycle but possibly some chemical changes might persist in the X-ray induced chromosome structure which gives reduced DAPI lifetime. Moreover, it has been observed in the human lymphocytes that either with high-dose rate (HDR) or low- dose rate (LDR) the repair mechanism starts within 30 mins of post-irradiation to repair the damaged DNA (Nair *et al.*, 2019). The repair mechanism repairs the DSBs up to 40 % within 24 hrs of post-irradiation, that is observed with reduced *γ*-H2AX foci (Nair *et al.*, 2019).

3.7.3. FLIM measurement of chromosomal structural abnormalities of T-lymphocytes

FLIM has been used to measure lifetimes of DAPI-bound chromosomes containing structural abnormalities such as translocation, isochromosomes, and heterochromatin and non-heterochromatin breaks (Figure 3.16). The chromosomes irradiation with a low doses of X-ray (0.5 Gy) are liable to suffer

from random molecular and structural aberrations such as DSBs, SSBs, base lesions, deletions, translocations and many more (Shimura and Kojima, 2018). The following aberrations leads to diseases and cell deaths (Lomax, Folkes and Neill, 2013). Number of DSBs increases in DNA with the increasing doses in both the case of HDR and LDR (Nair *et al.*, 2019). The number of DSBs for 1 Gy is ~40 DSBs and for 0.5 Gy is approximately half of it.

Inter and intra-chromosomal aberrations observed in X-ray induced chromosomes at low radiation doses (i.e. 0.1 Gy, 0.5 Gy and 1 Gy) using FLIM technique. The aberrations were observed in all 46 fixed human metaphase chromosomes obtained from a single chromosome spread, including heteromorphic chromosomes. The purpose is to address random structural chromosomal aberrations occurring randomly upon excitation with low ionising radiation. In this work, upon low irradiation, large amount of structural chromosomal aberration can be observed in metaphase chromosomes extracted immediately after X-ray exposure (Figure 3.16) than in chromosomes extracted at different generation of the cell cycle. This could be because the stress-response mechanism is activated (El-Saghire *et al.*, 2013) and repairs the damaged cells within 24 to 48 hrs of post-irradiation (Schröder *et al.*, 2019).

The lifetime values shows that the damaged chromosomes has lower lifetime in comparison to undamaged chromosomes, present in the same spread (Figure 3.16). Less number of structural chromosomal aberration observed with 0.1 Gy which increases for the 0.5 Gy irradiation and again the number reduces at 1 Gy irradiation. The Figure 3.16 shows the combined chromosomal structural aberrations from a five independent chromosome spreads, obtained from a two independent experiments. Chromosomal aberrations occur straight after 0.1 Gy X-ray exposure induces almost 7.76 ± 2.53 DSBs (Schröder *et al.*, 2019). Typically, chromosomal aberrations are random upon exposure to ionising radiation (Reisz *et al.*, 2014) (Shimura and Kojima, 2018). For example, in this work, structural aberration observed were “centromeric breaks” in chromosome 18, 19 and 20 from the single chromosome spread (Figure 3.16, 0.1 Gy X-ray dose), translocation observed between chromosome 8 and 5 at 0.5 Gy (Figure 3.18). Similarly, with exposure

to 1 Gy irradiation we have observed some heterochromatin (chromosome X) and non-heterochromatin breaks such as chromosome 1 (Figure 3.19) and chromosome 11 (Figure 3.16).

It was noticed that FLIM measurements are independent of structural chromosomal aberrations at different doses but dependent on the region of a chromosome damaged as described in the chapter (Figure 3.16, section 3.4.). It can be presumed that the condensed and de-condensed nature of a chromosome and the chemical modification in the DNA upon exposure of low-level X-ray doses were identified using FLIM. Therefore, at 1 Gy, chromosome 11 has non-heterochromatin breaks and has longer lifetime compared to the chromosome X, which has reduced lifetime because of heterochromatin break (Figure 3.16). Though, it can be also assumed that the chemical alterations are not uniform, thus, we see random structural chromosomal aberrations throughout the length of the chromosomes which is also identified by the FLIM (Figure 3.16).

Interestingly, the lifetime of naked DNA labelled with DAPI is longer, at >3.5 ns (Figure 3.22) and when polynucleotide wrapped around histone proteins this leads to a more compact structure with a lifetime of < 2.88 ns. DAPI binding to AT-rich regions does not have free electrons therefore, it gives longer DAPI lifetime (FFigure 1.7) and DAPI intercalating to GC-rich has free electrons thus, it gives short DAPI lifetime (Figure 3.22). It is observed that DAPI binds to AT-rich regions of DNA to give a single exponential lifetime component.

The large constitutive heterochromatin blocks of heteromorphic chromosomes are made up with classical satellite II and III and the following satellites consist of tandem repeats of 5 bp nucleotides of GGAAT- sense strand and ATTCC- antisense strands of DNA. Consequently, the mean excited sate lifetime of oligomer GGA-TAT-ATG-C is one of the closely oligomer which relates with the classical pentanucleotide, GGAAT, a DNA sequence present at the heterochromatin regions of the heteromorphic chromosomes 1, 9, 15, 16 and Y. The following purine-rich pentanucleotide DNA sequence possess unusual hydrogen bonding and thermal stability, moreover, it is also considered

as highly conserved regions at the proximal of the human centromere (Grady *et al.*, 1992). The same sequence has been found in the central region of the yeast (Grady *et al.*, 1992). The guanosine has a high rate of damage upon excitation, even with low-level of ionising radiation, because its oxidising characteristic and high ionising potential (Melvin *et al.*, 1998).

3.8. Summary

FLIM imaging has been used to investigate the sub-structures of a fixed (using fixative methanol: acetic acid at a ratio of 3:1) human metaphase chromosome using DNA specific-DAPI dye and upon exposure to ionising radiation. The three main investigations were: 1) identification of the effects of X-ray radiation at a low doses (i.e. 0.1 Gy, 0.5 Gy and 1 Gy) immediately after the exposure of ionising radiation, 2) studies of the change in the DAPI lifetime values in the two main sub-structures in X-ray induced chromosomes, and the substructure regions: heterochromatin (condensed region) and non-heterochromatin (decondensed region) and 3) from the effects of ionising radiation at the different generation (i.e. 0 hr, 24 hrs and 48 hrs) of the cell cycle.

The change in the DAPI excited state lifetime has been observed in all 46 chromosomes and heteromorphic chromosomes (chromosomes 1, 9, 15 and 16) obtained from T-lymphocytes and in Y-chromosome, obtained from B-lymphocytes. A short lifetime value can be observed at the heterochromatin regions of the chromosome and a long lifetime component at the non-heterochromatin regions of the chromosomes. The change in DAPI lifetime was observed in the sub-structures of X-ray induced chromosomes. The short lifetime value was observed at the heterochromatin region because possibly a compact nature of heterochromatin/centromere and the long lifetime component was observed at the non-heterochromatin region, because of least compact nature of the sub-structure of a chromosome. However, a DNA base sequence specific is also likely a contributor to the reduced lifetime observed. Moreover, the heteromorphic chromosome shows much more reduced DAPI lifetime in comparison to the rest of the chromosomes present in a spread.

In addition, the heteromorphic chromosomes contains tandem repeats of DNA pentanucleotide (GGAAT) sequences, which is a type of a DNA satellites present at the pericentric region of the chromosome and the distal region of Y-chromosome. Although, the presence of guanosine nucleotide in the repeat of DNA pentanucleotide sequence leads to short lifetime component possibly due to low ionisation potential of guanosine compared to the rest of the DNA bases. The short lifetime component was observed in both non-irradiated control sample and X-ray irradiated heteromorphic chromosomes. Furthermore, the naked DNA has longer lifetime component than the compact mitotic chromosomes.

Chapter 4

4. Mass measurement of chromosomes from the phase-contrast imaging

There have been many studies on the structural and functional role of chromosomes in cytogenetics spanning more than 10 decades. In this chapter, we aim to extract the individual masses of all 46 chromosomes of both stained and unstained spreads obtained from B and T-cells, using hard X-ray ptychography, to produce “X-ray karyotypes”. The obtained quantitative information will help to determine the gain or loss of genetic material upon low-level X-ray irradiation doses also to determine mass loss due to radiation damage.

All the experiments performed at the I-13 beamline, Diamond Light Source, Oxford, UK, using the ptychography reconstruction algorithms (Batey, 2014) of Dr Darren Batey.

The ptychography set-up was configured according to the

Figure 2.4. A 9.7 kiloelectron volt (keV) energy was used on a “Siemens star” test sample with 500 nm, 200 nm and 100 nm radially separated spokes (Batey *et al.*, 2019), This was done to check the accuracy of the set-up to obtain an accurate image of the complex probe on the sample. The sharp contrast of the spokes in the Siemens star help for the characterisation of coherent beam and allow measurement of the spatial resolution of the imaging system.

The probe was reconstructed from the Siemens star using a PtyREX ptychographic reconstruction package (Batey, 2014) using e-PIE reconstruction algorithms (Maiden and Rodenburg, 2009) (Rodenburg *et al.*, 2007). The reconstructed probe (Figure 4.1) was optimised and later used to assist the reconstructions of chromosomes samples as an initial starting probe. As a further calibration, 150 nm gold nanoparticles were first scanned and then reconstructed for the optimization of the phase contrast. All the obtained diffraction patterns obtained from the weak scattering chromosome samples were reconstructed by using the ptychography algorithms (Batey, 2014).

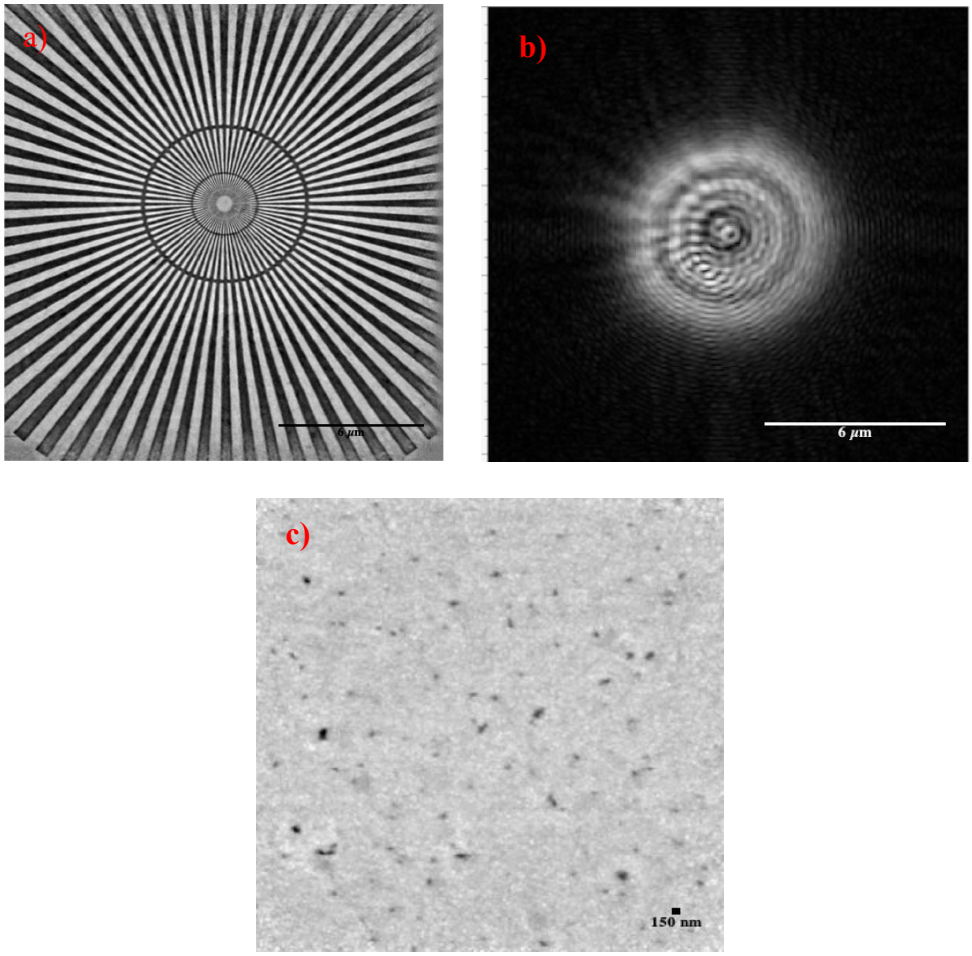

Figure 4.1: Measured test samples a) reconstruction of a Siemens star for measurement of spatial resolution. Field of view (FoV): 64 μm x 64 μm, X-ray exposure time: 0.01 sec, scale bar = 6 μm and b) probe modulus, scale bar = 6 μm. c) 150 nm gold nanoparticles reconstruction for characterisation of phase contrast. FoV is 32 μm x 32 μm and exposure time is 0.1 sec.

Due to the very low absorption coefficient of chromosomes at 9.7 keV energy, only the phase component of the reconstruction was extracted and analysed further. Ptychographic reconstruction images are quantitative therefore the phase values extracted from the images can be converted into the absolute number of the electrons in the sample, giving an absolute measure of its mass. The phase component of the reconstruction was analysed using ImageJ software where the mass of the chromosomes was determined.

4.1. Analysis of the phase value obtained from the chromosome reconstructions

From the ptychography experimental results, the mass of the individual chromosomes was calculated from the phase value of the reconstructed chromosomes scanned at 9.7 keV. The reconstructed phase image of the chromosome spread was processed in an ImageJ software then a Gaussian filter and an optimum threshold were applied for further calculations. Several other parameters were needed for the calculations of the electron count of the objects. The summation of the phase shift pixel values ($\sum_j \emptyset_j$) across the chromosome area (Shemilt *et al.*, 2015) was calculated using the free hand tool in ImageJ software; the wavelength of X-ray beam, λ = 0.13 nm; the real space pixel size of 2 dimensional (2D) chromosome images, $P_x P_y$ = 32 nm x 32 nm or 35 nm x 35 nm (depending upon the experiment) and the constant classical radius of the electron, $r_0 = 2.82 \times 10^{-6}$ nm.

The number of electrons, M, within an individual chromosome is obtained by summing up the phase shift values inside each image pixel, counted by j, so can be calculated by using **Equation** M = $j \emptyset_j \lambda r_0 P_x P_y$ (4.1) (Als-Nielsen and McMorrow, 2011):

$$M = \sum_j \frac{\emptyset_j}{\lambda r_0} P_x P_y \qquad (4.1)$$

The diploid (2-copy) human genome consists of slightly more than 6.4 billion base pairs (bp) (Goldfeder *et al.*, 2017) located within 22 pairs of autosome chromosomes and one pair of sex chromosomes (Brown., 2002). The chromosomes are numbered according to their size determined by flow cytometry (Harris *et al.*, 1986). Chromosome 1 is the largest and has a 248,956,422 base pairs (per copy) and the smallest chromosome is made up of 46,709,983 base pairs. In the whole genome of human only 30,000-40,000 genes (information carrying fragments of DNA) are protein-coding genes (Lander *et al.,* 2001).

The average molecular weight of a DNA base pair is 660 g/mol (Dalton) (Bench *et al.*, 1996) and so a single base is 330 g/mol. The DNA base pairs are measured in picograms (pg), mega base pairs (Mbp) or in Dalton (Da) (Doležel *et al.*, 2003).

Where in (Doležel *et al.*, 2003):

1 Da = 1.67 x 10^{-12} pg and 1 Mbp = 10^6 base pairs

DNA content (pg) = genome size (Mbp) x 660 Da

With this understanding (average MW of base pair is 660 Da), we calculated the masses of known base pairs of each human chromosome. Since only light atoms are involved in DNA, which all contain the same number of protons, neutrons and electrons, the number of electrons measured by

ptychography is precisely half the number of Daltons of mass. For example, the longest chromosomes, 1, has a mass of DNA of 0.27 pg containing 8.2×10^{10} electrons. The smallest chromosome, 21, has a mass of 0.05 pg. In this fashion, we calculated the mass all 46 chromosomes from known human genomic size. Henceforth, masses calculated from the known base pairs used as a reference to karyotype the measured masses of chromosomes obtained from the summation of phase shift across each the chromosome (Als-Nielsen and McMorrow, 2011).

4.2. Karyotype of human chromosomes with a M-FISH technique

For identification of any chromosomal aberrations, the karyotype was first performed on non-irradiated chromosomes obtained from both the T and B-lymphocytes with the help of chromosome identification technique known as M-FISH. The chromosomes were stained with a 24XCyte probe kit (see chapter-2, Materials and Methods) which labels all 24 chromosomes with a 5 different fluorochromes arranged in a combinatorial manner. This helps to visualise the structural rearrangements (eg. translocation) of chromosomes and numerical aberrations (Anderson, Stevens and Goodhead, 2002) (Balajee *et al.*, 2014).

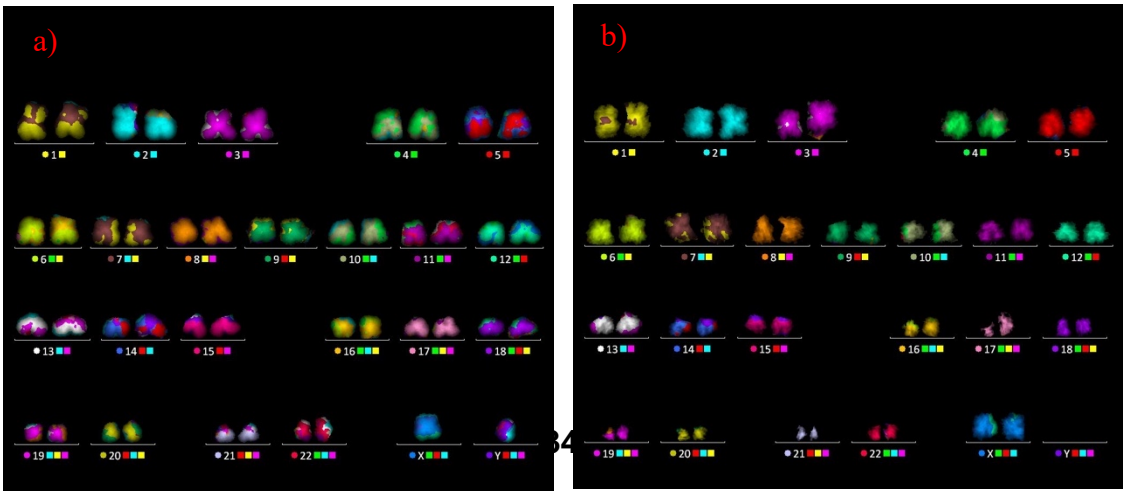

Figure 4.2: M-FISH karyotype performed on non-irradiated chromosomes obtained from a) B-lymphocytes, a male cell line (1-22, XY chromosomes) and b) Primary T-lymphocytes from a female donor (1-22, XX chromosomes).

The M-FISH karyotype in Figure 4.2 shows a set of 22 pairs of autosome chromosomes and one pair of sex chromosomes in each, depending upon the gender. The chromosome numbers are allocated the same colour as coded by computerised-colour-code scheme of MetaSystem and placed above the number assigned to each colour (Speicher, Ballard and Ward, 1996)(Anderson, 2010). The karyotype helps to identify the stability and the quality of the chromosomes obtained from B and T-lymphocytes. After validation, the same preparation of chromosomes (see chapter-2, Materials and Methods) were used for X-ray ptychography imaging, to generate masses of the each chromosome from the phase shift reconstructions.

4.3. Hard X-ray imaging of stained chromosomes

Investigation of biological samples with electron microscopy and hard X-ray imaging is very challenging because of the weak scattering property of its light atoms. In our experiment, we therefore stained the chromosomes mounted on the Si_3N_4 membrane with 1% uranyl acetate and 6 mM platinum blue in an attempt to increase the phase contrast (see chapter-2 Materials and Methods). Staining deposits a thin layer of additional electron density on the top of the chromosome samples to increase the scattering intensity of the beam. Chromosome-specific staining could also help to visualise and segment each chromosomes from nuclei and other debris, with an ImageJ software, to facilitate mass calculation of each chromosomes. The reconstructed image of each spread has gone through 50 iterations of the ptychography algorithms.

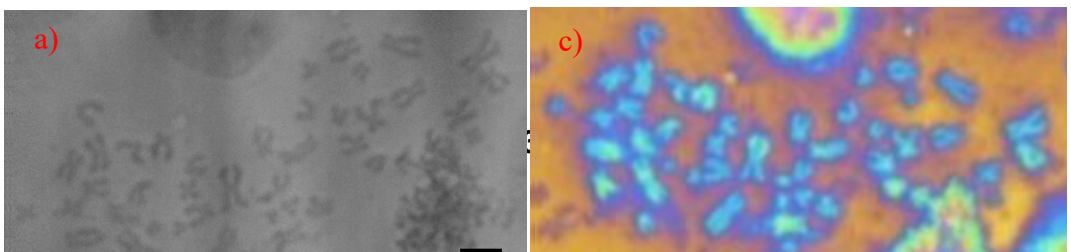

Figure 4.3: Ptychographic reconstructed phase-retrieval images of chromosome spreads measured in the air, FoV: 64 μm × 64 μm a) 1% Uranyl Acetate stained chromosomes with 1.0 sec exposure of X-rays, b) 6 mM Pt-blue stained chromosomes with 1.0 sec exposure. It also contains residues of Pt-blue aggregates (black spots in the image). The chromosomes appeared with a high intensity of grey-level separated from the even background. Image c and d are the optical images of respective spreads with the stains. The blue objects are the stained chromosomes. Scale bar = 5 μm.

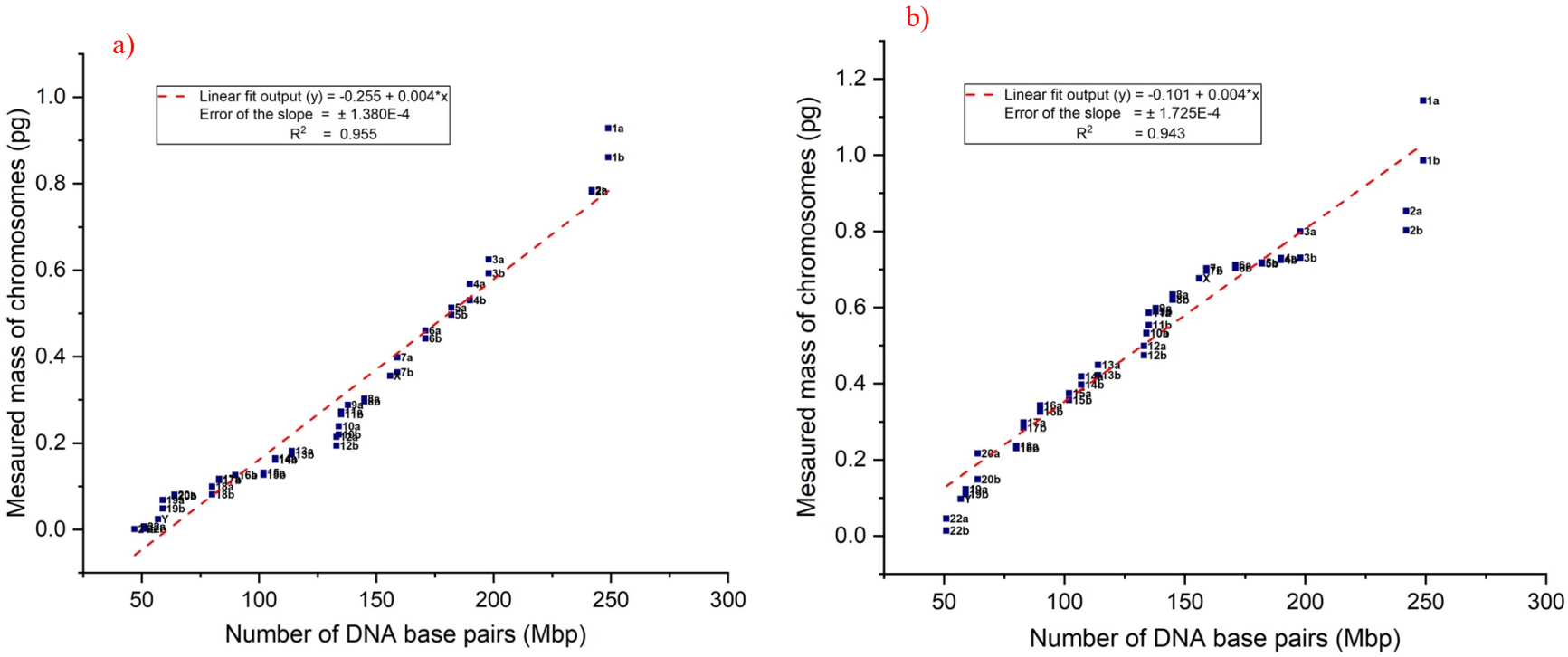

Figure 4.4: Quantitative analysis of phase image of chromosome spread obtained from B-lymphocyte cell line to produce an X-ray karyotype, accompanied with a best-linear-fit. a) Measured mass of 45 out of 46 chromosomes against the mass of known from the base pair length of each chromosomes from 1% Uranyl Acetate stained chromosomes. b) Measured mass of 44 out of 46 chromosomes against the mass of known base pair length of each chromosomes from a 6 mM platinum blue stained chromosomes. Mass of chromosomes falls within a range of picograms for both examples.

X-ray phase contrast is a quantitative way to measure the masses of heavy stained chromosome sample. Each individual reconstruction has been run through 50 iterations of the ptychographic algorithms to get a well-converged image. Subsequently, the reconstructed images were segmented with a free hand tool in ImageJ to obtain the raw integer density (RawIntDen) value. The background pixel values were subtracted to obtain the pixel values within an isolated chromosome. The following obtained values were fitted into the derived equation $M = j \, \emptyset_j \, \lambda r_{0 P_x P_y}$ (4.1). Henceforth, the number of electrons present in each individual chromosome were measured and later multiplied with the mass of the two nucleons (2 Da = 3.35×10^{-27} kg) present in an atom to generate the observed masses of each individual chromosome. The graphs in Figure 4.4 were plotted *versus* the known number of DNA base pairs of each individual chromosome to produce an X-ray karyotype from each individual stained spread. As with other karyotype methodologies, we assume the sequence of observed masses follows the same numbering of the chromosomes.

It can be seen in both cases that the masses are found to be 3-4 times the calculated mass of the DNA alone. A factor of 2 is due to the two genome copies present in the chromosomes at metaphase and the rest is attributed to the protein complement and to the stain. We note the mass calculations are slightly underestimating the mass of the stain because the heavy elements (Uranyl Acetate and platinum blue) contain additional neutrons to the simple 1:1, proton: neutron ratio of light elements. The potential benefit of heavy metal stain is to improve the contrast of the weak scattering biological sample and it has been observed for both the stains used. It appears that we have missed one chromosome in UA stained and two chromosomes in platinum blue stained (Figure 4.3 and Figure 4.4). The sum of the measured masses of 45 out of 46 chromosomes is 13.18 pg for UA stain and 22.18 pg for platinum stain with 44 out of 46 chromosomes. Both the chromosome spreads were obtained from the B-lymphocyte cell line.

4.4. X-ray ptychography of unstained human chromosomes

After obtaining successful results of ptychographic reconstructions from stained chromosomes, we combined coherent and ptychography imaging technique to understand the micro-structure of chromosomes, closer to its native state, from the unstained spreads at a high resolution. We applied the same procedure to prepare chromosome spreads on the Si_3N_4 membrane (see Chapter 2, Materials and Methods) and imaged them at a room temperature. This powerful technique provides quantitative information and from these data we have extracted masses of chromosomes obtained from both the male and female cell lines, without any staining.

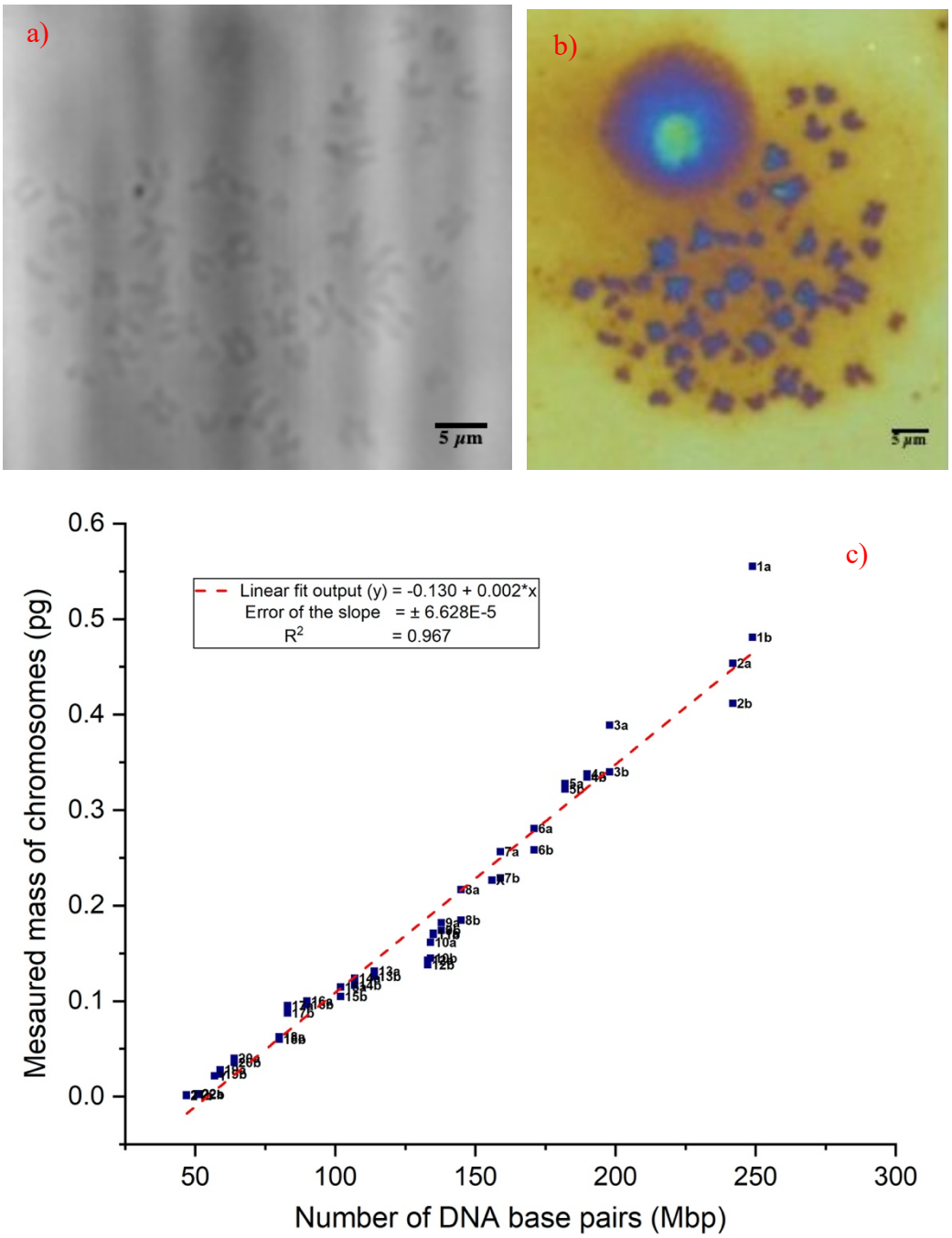

Figure 4.5: Ptychographic reconstructed unstained chromosome spread obtained from B-lymphocytes; a) phase image of B-lymphocytes (male cell line), FoV: 64 µm × 64 µm, with a 1.0 sec of exposure, b) optical microscope image of the same chromosome spread, including a big blob of nucleus, scale bar = 5 µm, cropped from a bigger FoV image. c) X-ray karyotype of the same spread.

The graph plotted between measured mass and the number of DNA base pairs of each individual, unstained chromosome from a single spread (Figure 4.5). The order of the chromosomes are aligned in the following sequence:
1>2>3>4>5>6>7>X>8>9>11>10>12>13>14>15>16>17>18>20>19>Y>22>21.
The position of sex chromosomes are as follows: chr Y falls in between chr 19 and 22 and chr X falls between chr 7 and 8. In addition, chr 11 falls before chr 10, similarly, chr 20 falls before chr 19 and chr 22 before chr 21. Chromosome 1 has the highest mass and chr 21 has the lowest mass.

We find a decrease in the measured mass of the unstained chromosomes relative to stained chromosomes in these early experiments. This indicates that the stains significantly add extra mass to the chromosomes, and this work presents the first quantitative evaluation of how much stain is apparently bound. The sum of the masses for B-lymphocytes is 8.26 pg of all 46 chromosomes. We know, from the human genome sequence, that the amount of DNA content in a male human genome is 6.54 pg per cell (Doležel *et al.*, 2003) (Piovesan *et al.*, 2019). 3.4pg of this corresponds to the four copies of the full 3.1×10^{9} base-pair complement of DNA at metaphase multiplied by 660 Da per base pair and 1.67×10^{-12} pg per Dalton.

4.5. Phase-retrieval reconstructions of irradiated unstained human chromosome spreads

With the successful experiment to image unstained human chromosomes from B-cells at a high resolution. Thereafter, in our second experiment at the I-13-1 beamline, Diamond Light Source, Didcot, UK, we performed X-ray ptychography to image unstained chromosomes obtained from primary T-lymphocytes. Metaphase human chromosomes were prepared on silicon nitride membrane (see chapter 2, Materials and Methods) and imaged at room temperature. The obtained diffraction patterns were reconstructed using ptychographic algorithms and X-ray karyotype was generated from the obtained quantitative values (Figure 2.4), as described above.

In addition, X-ray ptychography was also performed on X-ray induced chromosomes during the experiment. The aim was to observe any potential structural or numerical aberrations occurred due to the irradiation of the chromosomes. To accomplish this experiment, based on past experience, we choose three X-ray radiation doses, 0.1 Gy, 0.5 Gy and 1 Gy, to induce live cultured cells, grown for two further generations prior to extracting the chromosomes before imaging, to understand the structural rearrangement and change in the individual masses of the chromosomes. After imaging, each individual reconstruction ran for 100 iterations of the ptychographic algorithm, as described above.

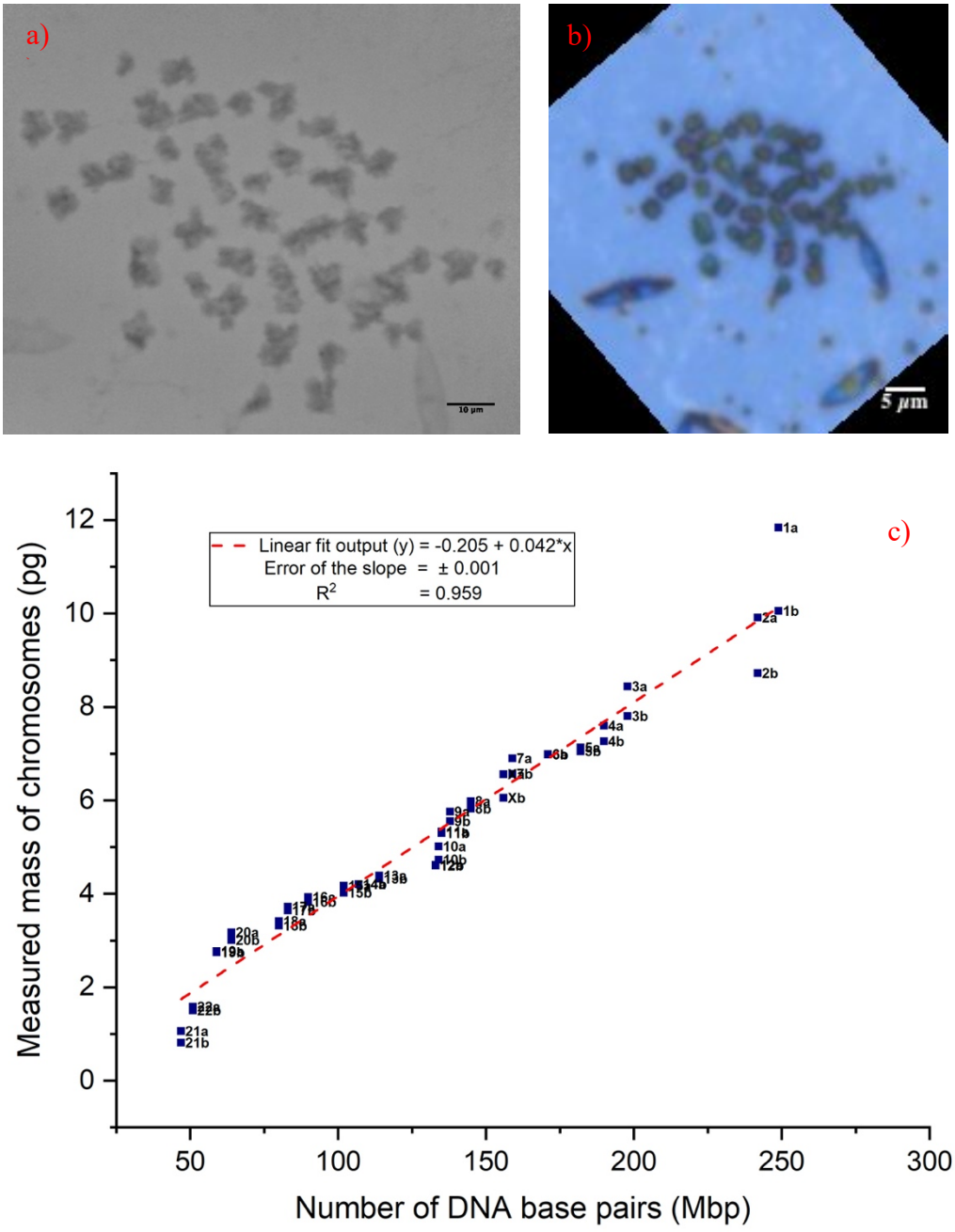

Figure 4.6: Ptychographic reconstructed unstained chromosome spread obtained from non-irradiated T-lymphocytes, as a control; a) phase image of T-lymphocytes (female cell line), FoV: 32 µm × 32 µm, with 0.3 sec of exposure, scale bar = 10 µm. The fibrous structure of the chromosomes can be seen. b) optical microscope image of the same chromosome spread, with some debris on the membrane, scale bar = 5 µm, cropped from a bigger (100 µm) FoV image, c) X-ray karyotype of the same spread, with a best-linear-fit.

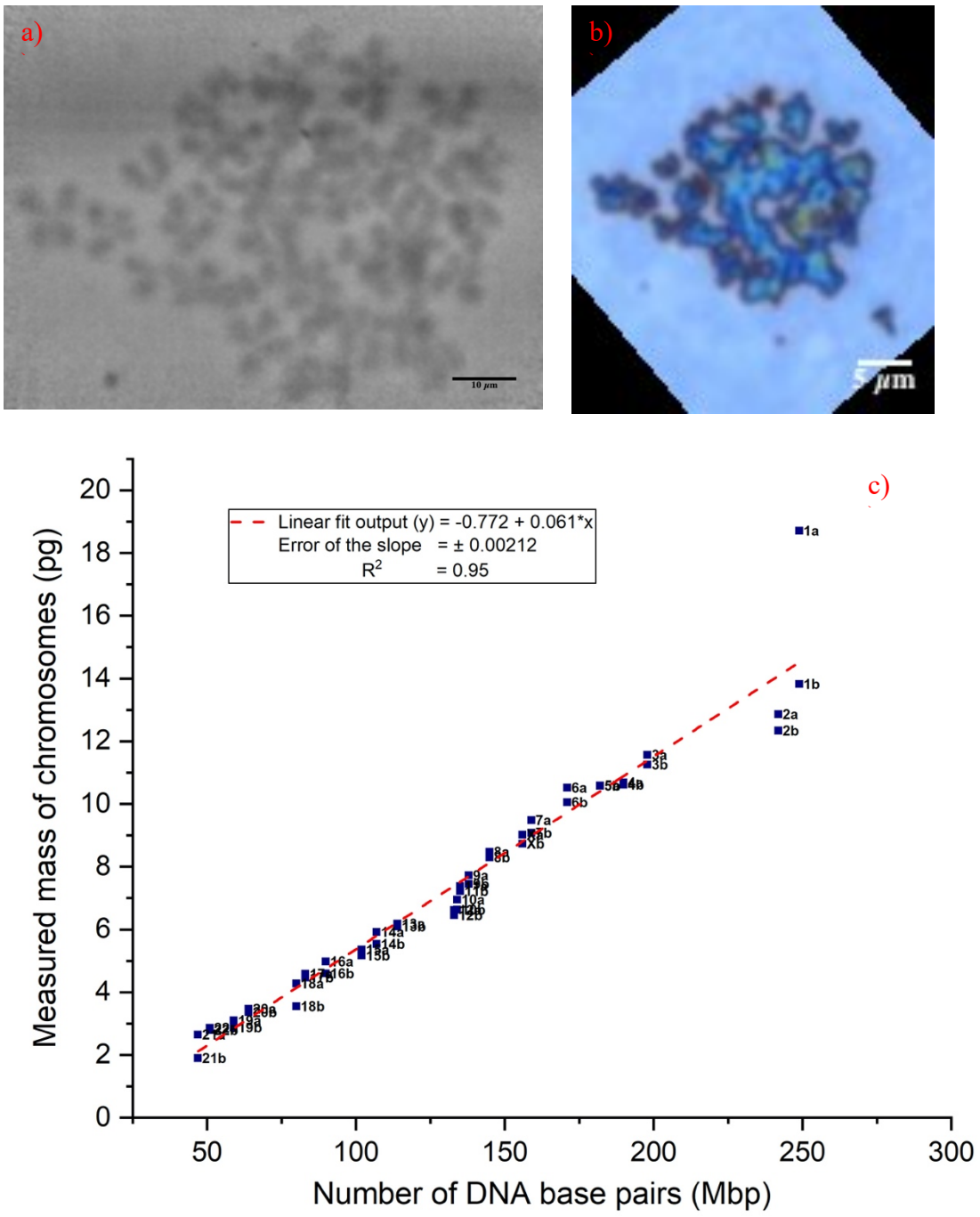

Figure 4.7: Ptychographic reconstruction of unstained chromosome spread obtained from X-ray induced T-lymphocytes cells at 0.1 Gy; a) phase image of T-lymphocytes (female cell line), FoV: 32 μm × 32 μm, with a 0.3 sec of exposure. Scale bar = 10 μm, b) optical microscope image of the same chromosome spread. Blue clustered features are chromosomes, scale bar = 5 μm, cropped from a bigger (100 μm) FoV image, c) X-ray karyotype of the same spread, with a best-linear-fit.

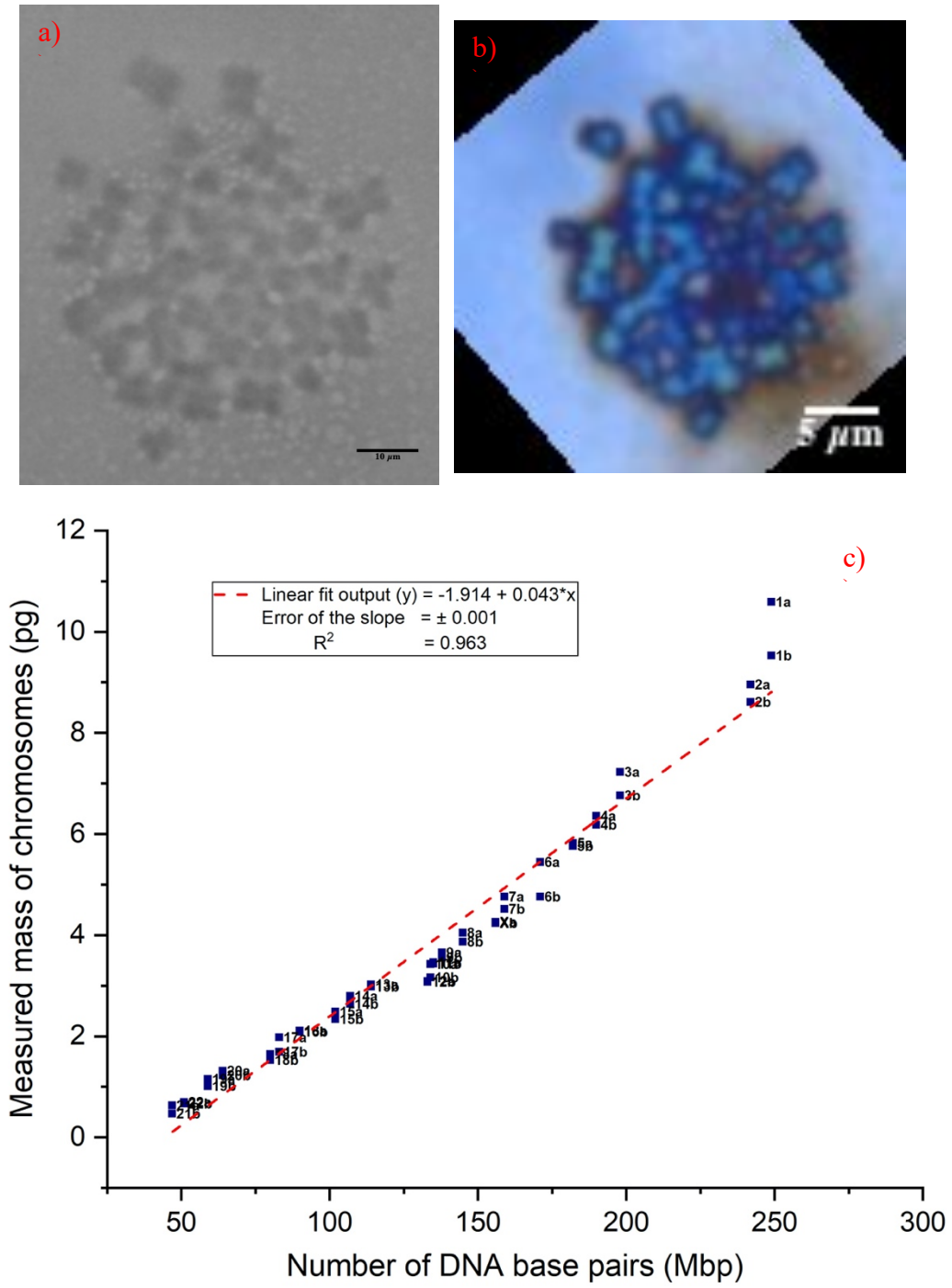

Figure 4.8: Ptychographic reconstruction of unstained chromosome spread obtained from X-ray induced T-lymphocytes cells at 0.5 Gy; a) phase image of T-lymphocytes (female cell line), FoV: 32 µm × 32 µm, with a 0.3 sec of exposure. Scale bar = 10 µm, b) optical microscope image of the same chromosome spread. Blue clustered features are chromosomes, scale bar = 5 µm, cropped from a bigger (100 µm) FoV image, c) X-ray karyotype of the same spread, with a best-linear-fit.

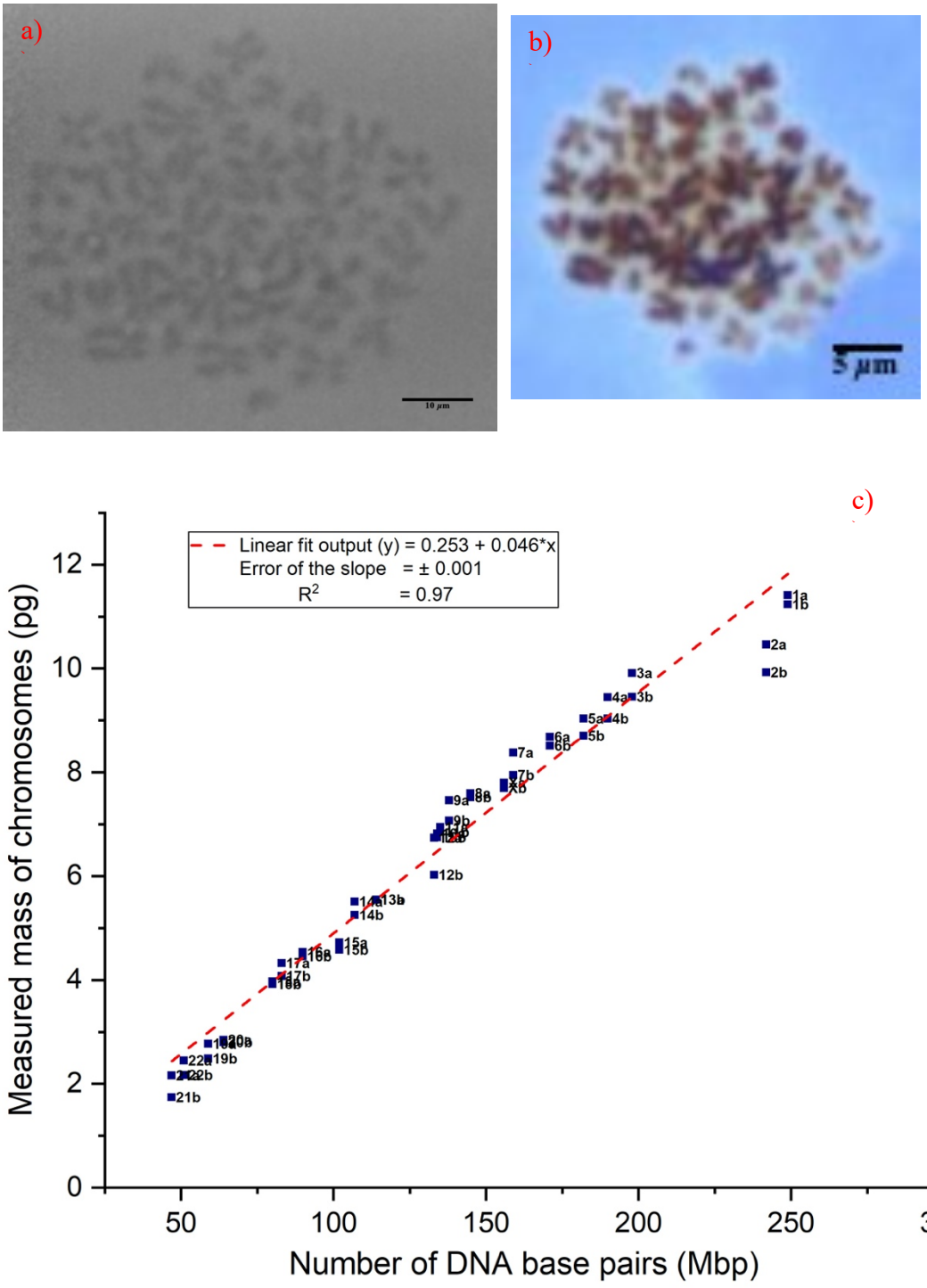

Figure 4.9: Ptychographic reconstruction of unstained chromosome spread obtained from X-ray induced T-lymphocytes cells at 1 Gy; a) phase image of T-lymphocytes (female cell line), FoV: 32 µm × 32 µm, with a 0.3 sec of exposure. Scale bar = 10 µm, b) optical microscope image of the same chromosome spread. Brown objects are chromosomes, scale bar = 5 µm, cropped from a bigger (100 µm) FoV image, c) X-ray karyotype of the same spread, with a best-linear-fit.

From each X-ray ptychography image, we measured the masses of the non-irradiated (control) and irradiated chromosomes obtained from T-lymphocytes to produce an X-ray karyotype of each. The outcome, shown in Figure 4.6, Figure 4.7, Figure 4.8 and Figure 4.9, is that the data points falls nicely on a straight line, as before, which means there is a positive relation between measured masses and the known number of DNA base pairs present in each individual chromosome. The total masses of all 46 chromosomes have been summed and they are as follows: 242.21 pg, 336.53 pg, 172.90 pg and 293.12 pg, for the control (Figure 4.6) and the radiation doses, 0.1 Gy (Figure 4.7), 0.5 Gy (Figure 4.8) and 1 Gy (Figure 4.9) respectively. Surprisingly, the total mass for 0.1 Gy is higher than the non-irradiated chromosomes (242.21 pg), then significantly decreases for 0.5 Gy and interestingly it again rises for 1 Gy. Overall, it follows the trend: 0.5 Gy<control<0.1 Gy<1Gy, with regards to "summed-masses". Moreover, it has been noticed that for each karyotype plot, the masses of chromosome 1 and 2 are much higher than the expected extrapolation from the rest of the chromosomes in the spread, irrespective of radiation doses.

It is noteworthy that the mass numbers emerging from this second experiment are an order of magnitude higher than the first experiment, reported in Sections 4.3 and 4.4. This discrepancy, which is noticed immediately in the apparent contrast of the raw ptychography images, is unexplained. The experiments were separate runs at Diamond, about a year apart and both the measurement and reconstruction method improved considerably over that time. But this would be expected to improve the only efficiency and not the phase contrast values, which should be highly quantitative. The most likely explanation was the significant delay of 5-6 months between the sample preparation, with the samples stored in 3:1 methanol acetic acid in the refrigerator, and the measurement for the first experimental run, during which time some of the chromosome mass may have been "lost" during storage. The quantitative numbers for the second batch, where the samples were freshly prepared, are therefore probably more reliable.

4.6. Protein composition determined in human metaphase chromosome

Chromosomes are composed of DNA-protein complex. From the human genome literature, the amount of DNA present in each individual human chromosome (Lander *et al.*, 2001) (Piovesan *et al.*, 2019) is reckoned to be known but the protein composition of metaphase chromosome is still somewhat less clear. We note furthermore that the human genome only records the coding part of the DNA and that the sequencing methods are unable to fully record repeated sequences. Consequently, the DNA masses based on the human genome sequence will be underestimated. This underestimation is likely to be most serious for chromosomes 1, 9, 15 and 16 with significant heterochromatic regions.

From the phase-contrast reconstructions obtained using X-ray ptychography, we would like to attempt to determine the amount of protein (histone and non-histone) present in each individual metaphase chromosome from the obtained masses. Firstly, we extracted the number and the amount of histones from the Protein Data Bank (PDB) (Table 4.1), that are known to be associated with around 166 bp of DNA, wrapped around the protein core to form each nucleosome – the fundamental structural subunit of chromatin fibre, the DNA-protein complex. A single nucleosome contains eight histones, two each of H2A, H2B, H3 and H4 (~146 DNA base pairs) and one linker histone (20 base pairs) which connects two nucleosomes to form a chain of chromatin (Harshman *et al.*, 2013). Secondly, we calculated the mass of the 166 bp of DNA, to obtain the mass of the DNA component of the nucleosome, by multiplying by the average molecular weight (660 Da) of a base pairs (bp) (Bench *et al.*, 1996). Using 1Da = 1.66×10^{-27} kg this gives the true physical mass of the nucleosome (Doležel *et al.*, 2003). From this, the mass of the nucleosome can be calculated and hence from the DNA content, the protein content can be determined for all 46 human chromosomes.

Protein	Amount (Da)
H2A histone	14, 135 x2
H2B histone	13,906 x2
H3 histone	15404 x2
H4 histone	11367 x2
H1 linker histone	32000 x1
Sum	141624 Da

Table 4.1: A list of histone proteins present in a single nucleosome (from the PDB)

Uchiyama *et. al*. (2005) measured the breakdown of all proteins involved with the metaphase chromosomes. They found a total of 48 % histone protein and 12 % of linker histone (Uchiyama *et al.*, 2005). The total histones represent 60 % of the total, so the non-histone component can be estimated to be the fraction 40/60 (non-histones/histones) = 0.67 x 141624 Da per nucleosome. The histone proteins thus make up most of the mass of the chromosomes (Uchiyama *et al.*, 2005). Consequently, the estimated mass of one nucleosome can be calculated by considering three important components:

i) DNA = 166 x 660= 109,560 Da per base pair

ii) Sum of the histone protein = 141,624 Da

iii) *Non-histone protein = 0.67 x 141,624 Da*

So, total= 346,072.08 Da per nucleosome

Therefore, the total mass of a single nucleosome is 3.5×10^5 Da. Consequently, the mass of chromosome 1 can be estimated by calculating the number of nucleosomes as 248956422/166 = 1.50×10^6, giving a total mass of $1.50 \times 10^6 \times 3.5 \times 10^5$ Da $\times 1.66 \times 10^{-27}$ kg = 0.86 pg. The DNA alone would be 0.27 pg. with the remaining 0.59 pg. being protein. Therefore, the expected mass of chromosome 1 is 0.86 pg. and further multiplied by factor of 2 to obtain mass of 4 copies of DNA content and chromosomal proteins of metaphase chromosomes and with this manner we have illustrated the expected mass of

all 46 chromosomes in a below table for both cell type (Table 4.2 and Table 4.3), along with the suspected mass loss (Table 4.2) due to radiation damage or chemical modification happened due to prolonged storage of metaphase chromosomes in methanol acetic acid (3:1) solution.

chromosome (number)	Known DNA base pairs/(M1) (pg)	Measured masses/(M2) (pg)	Expected histones/(M3) (pg)	Expected non-histones/(M4) (pg)	Expected mass/(M5) = (M1+M3+M4) (pg)	Mass loss/(M6) = (M5-M2) (pg)
1a	0.55	0.55	0.71	0.47	1.72	1.17
1b	0.55	0.48	0.71	0.47	1.72	1.24
2a	0.53	0.45	0.69	0.46	1.68	1.22
2b	0.53	0.41	0.69	0.46	1.68	1.27
3a	0.43	0.39	0.56	0.38	1.37	0.98
3b	0.43	0.34	0.56	0.38	1.37	1.03
4a	0.42	0.34	0.54	0.36	1.32	0.98
4b	0.42	0.33	0.54	0.36	1.32	0.98
5a	0.40	0.33	0.51	0.34	1.26	0.93
5b	0.40	0.32	0.51	0.34	1.26	0.94
6a	0.37	0.28	0.48	0.32	1.18	0.90
6b	0.37	0.26	0.48	0.32	1.18	0.92
7a	0.35	0.26	0.45	0.30	1.10	0.85
7b	0.35	0.23	0.45	0.30	1.10	0.87
X	0.34	0.23	0.44	0.30	1.08	0.85
8a	0.32	0.22	0.41	0.28	1.00	0.79
8b	0.32	0.18	0.41	0.28	1.00	0.82
9a	0.30	0.18	0.39	0.26	0.96	0.78
9b	0.30	0.17	0.39	0.26	0.96	0.78
11a	0.30	0.17	0.38	0.26	0.94	0.76
11b	0.30	0.17	0.38	0.26	0.94	0.77
10a	0.29	0.16	0.38	0.25	0.93	0.76
10b	0.29	0.14	0.38	0.25	0.93	0.78
12a	0.29	0.14	0.38	0.25	0.92	0.78
12b	0.29	0.14	0.38	0.25	0.92	0.78
13a	0.25	0.13	0.32	0.22	0.79	0.66
13b	0.25	0.13	0.32	0.22	0.79	0.67
14a	0.23	0.12	0.30	0.20	0.74	0.62
14b	0.23	0.12	0.30	0.20	0.74	0.62
15a	0.22	0.11	0.29	0.19	0.71	0.59
15b	0.22	0.10	0.29	0.19	0.71	0.60
16a	0.20	0.10	0.26	0.17	0.63	0.53
16b	0.20	0.10	0.26	0.17	0.63	0.53
17a	0.18	0.10	0.24	0.16	0.58	0.48
17b	0.18	0.09	0.24	0.16	0.58	0.49
18a	0.18	0.06	0.23	0.15	0.56	0.49

18b	0.18	0.06	0.23	0.15	0.56	0.50
20a	0.14	0.04	0.18	0.12	0.45	0.41
20b	0.14	0.04	0.18	0.12	0.45	0.41
19a	0.13	0.03	0.17	0.11	0.41	0.38
19b	0.13	0.02	0.17	0.11	0.41	0.38
Y	0.13	0.02	0.16	0.11	0.40	0.37
22a	0.11	0.00	0.14	0.10	0.35	0.35
22b	0.11	0.00	0.14	0.10	0.35	0.35
21a	0.10	0.00	0.13	0.09	0.32	0.32
21b	0.10	0.00	0.13	0.09	0.32	0.32

Table 4.2: Identification of all 46 chromosomes on the basis of their measured and expected masses of each individual chromosome. The assumed position of X and Y are highlighted in blue in the table. The table was generated from the phase image of unstained B-lymphocytes chromosomes shown in Figure 4.5.

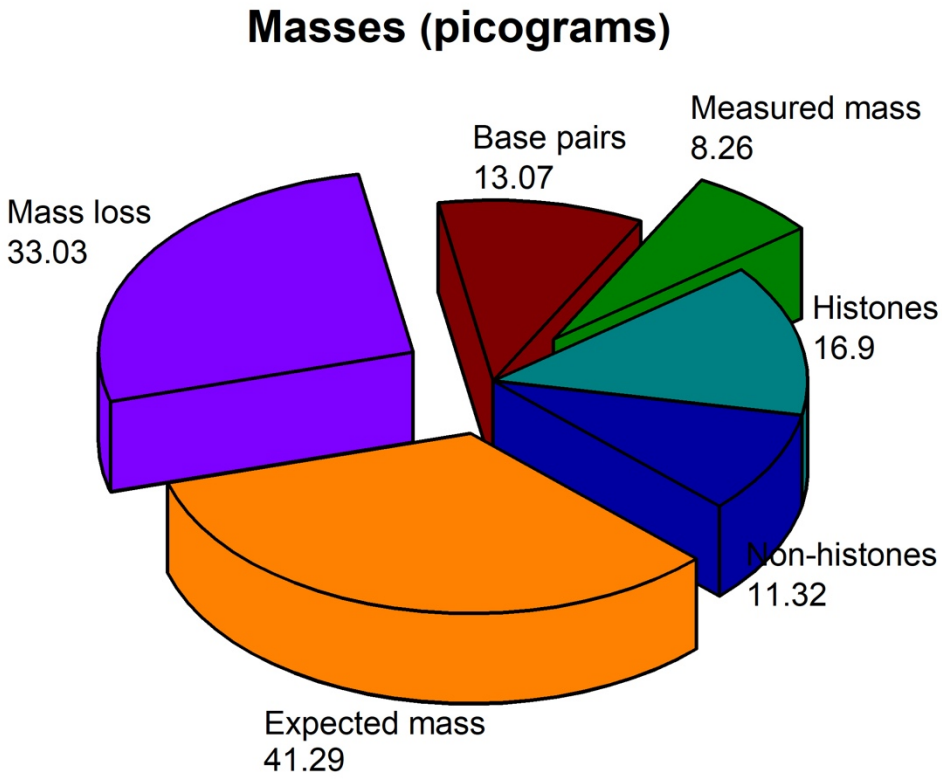

Figure 4.10: The outline of expected amount of DNA and proteins present in the human (46, XY) genome. Also shows the measured mass obtained from the phase image and the calculated expected mass. The calculated mass loss is a difference of expected mass and the measured mass (Table 4.2).

In the Table 4.2, the expected mass of histones, non-histones and an integrated mass of each individual chromosomes has been calculated from the known DNA and the histone content. Following, the pie chart (Figure 4.10) demonstrate the aggregated profile of expected and the measured masses along with the loss of mass of all 46, methanol acetic (3:1) fixed human metaphase chromosomes. The data came from an unstained spread obtained from B-cells. In addition, the particular spread has been exposed to X-ray dose for one sec while scanning to gather diffraction pattern for further processing.

The Figure 4.10, illustrates that the expected mass is 2.5 times higher than the measured mass. Therefore, the mass loss can be determined by subtracting measured mass from the expected mass for each individual chromosomes (Table 4.2). And, the expected mass is the sum of the calculated masses of histones, non-histone proteins and the known DNA mass; calculated for each individual chromosomes. The DNA content for the full set of male diploid human chromosomes is 6.54 pg (Lander *et al.*, 2001) (Doležel *et al.*, 2003) (Piovesan *et al.*, 2019).

chromosome (number)	Known DNA base pairs/(M1) (pg)	Measured masses/(M2) (pg)	Expected histones/(M3) (pg)	Expected non-histones/(M4) (pg)	Expected mass/(M5) = (M1+M3+M4) (pg)	Mass gain/(M6) = (M2-M5) (pg)
1a	0.55	11.83	0.71	0.47	1.72	10.11
1b	0.55	10.05	0.71	0.47	1.72	8.33
2a	0.53	9.91	0.69	0.46	1.68	8.23
2b	0.53	8.72	0.69	0.46	1.68	7.04
3a	0.43	8.43	0.56	0.38	1.37	7.06
3b	0.43	7.80	0.56	0.38	1.37	6.43
4a	0.42	7.60	0.54	0.36	1.32	6.28
4b	0.42	7.26	0.54	0.36	1.32	5.94
5a	0.40	7.12	0.51	0.34	1.26	5.87
5b	0.40	7.05	0.51	0.34	1.26	5.79
6a	0.37	6.99	0.48	0.32	1.18	5.80
6b	0.37	6.98	0.48	0.32	1.18	5.80
7a	0.35	6.90	0.45	0.30	1.10	5.79
7b	0.35	6.56	0.45	0.30	1.10	5.46
Xa	0.34	6.56	0.44	0.30	1.08	5.48
Xb	0.34	6.05	0.44	0.30	1.08	4.97
8a	0.32	5.98	0.41	0.28	1.00	4.97

8b	0.32	5.82	0.41	0.28	1.00	4.81
9a	0.30	5.76	0.39	0.26	0.96	4.80
9b	0.30	5.55	0.39	0.26	0.96	4.59
11a	0.30	5.32	0.38	0.26	0.94	4.39
11b	0.30	5.30	0.38	0.26	0.94	4.36
10a	0.29	5.01	0.38	0.25	0.93	4.08
10b	0.29	4.73	0.38	0.25	0.93	3.80
12a	0.29	4.62	0.38	0.25	0.92	3.69
12b	0.29	4.60	0.38	0.25	0.92	3.67
13a	0.25	4.38	0.32	0.22	0.79	3.59
13b	0.25	4.32	0.32	0.22	0.79	3.53
14a	0.23	4.20	0.30	0.20	0.74	3.46
14b	0.23	4.20	0.30	0.20	0.74	3.46
15a	0.22	4.17	0.29	0.19	0.71	3.46
15b	0.22	4.02	0.29	0.19	0.71	3.31
16a	0.20	3.93	0.26	0.17	0.63	3.30
16b	0.20	3.82	0.26	0.17	0.63	3.19
17a	0.18	3.72	0.24	0.16	0.58	3.14
17b	0.18	3.64	0.24	0.16	0.58	3.06
18a	0.18	3.41	0.23	0.15	0.56	2.85
18b	0.18	3.31	0.23	0.15	0.56	2.76
20a	0.14	3.17	0.18	0.12	0.45	2.72
20b	0.14	3.00	0.18	0.12	0.45	2.56
19a	0.13	2.77	0.17	0.11	0.41	2.36
19b	0.13	2.74	0.17	0.11	0.41	2.34
22a	0.11	1.58	0.14	0.10	0.35	1.23
22b	0.11	1.50	0.14	0.10	0.35	1.15
21a	0.10	1.05	0.13	0.09	0.32	0.73
21b	0.10	0.81	0.13	0.09	0.32	0.49

Table 4.3: Retrieved masses of all 46 chromosomes from a phase-contrast image of an unstained non-irradiated T-lymphocytes, exposed for 0.3 sec during X-ray imaging. It also shows the calculated expected masses, including the mass of DNA, histones and non-histone proteins. The assumed position of XX are highlighted in blue. The mass gain is a difference of measured mass and the expected mass.

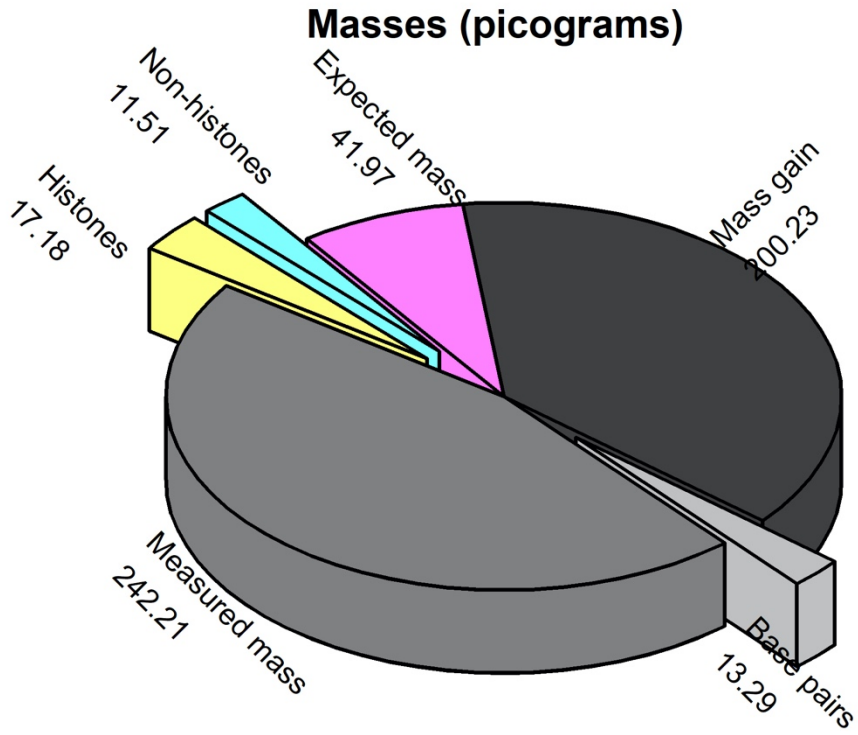

Figure 4.11: The profile shows the amount of measured and the expected masses of DNA, histones and non-histone proteins present in a human genome (46, XX). It also shows the mass gain in picograms (Table 4.3).

Similarly, from the second round of experiments, we have calculated the measured and the expected mass of a spread obtained from a female primary T-cells. Here, we have observed a mass gain since the measured mass is higher than the expected mass. Therefore, the mass gain has been calculated by subtracting the expected mass from the measured mass. Moreover, it can also be noted that the estimated expected mass of two homologous chromosome in a spread has the exactly the same mass but the measured mass differs between two homologous pairs (Table 4.3).

The mass of DNA content for the full set of female diploid human chromosomes is 6.64 pg. (Doležel *et al.*, 2003) (Piovesan *et al.*, 2019). The particular chromosome spread has been exposed to X-ray dose for 0.3 sec during scanning the silicon nitride membrane containing sample. Although, the mass gain (Table 4.3) observed could be from the additional chromosomal

proteins and trapped buffers on the surfaces of silicon nitride membrane. There is also the important question of possible DNA components which are missing from the human genome sequence .

4.7. Discussion

In this chapter, we presented our measurements of individual chromosome masses obtained from high resolution phase-contrast reconstruction using hard X-ray ptychography. The use of “spreads” in which all chromosomes from a given cell are measured together allowed us to create “X-ray karyotypes” of fixed human metaphase chromosomes. The chosen biological sample is human chromosome obtained from B and T-cells and the karyotype has been performed on both stained and unstained chromosome spreads. In addition, the X-ray karyotype also been implemented on the X-ray radiation-induced chromosomes at relevant doses of 0.1 Gy, 0.5 Gy and 1 Gy, to investigate the gain or loss of DNA-protein complex. Moreover, the karyotype was also done on chromosome spreads with different exposure time intervals during scanning, 0.3 sec, 0.6 sec and 0.9 sec, one after the other.

In the literature the chromosomes are karyotyped on the basis of morphology, volume and the DNA content using techniques such as M-FISH (Yusuf *et al.*, 2011) (Anderson, Stevens and Goodhead, 2002), SBFSEM (Chen *et al.*, 2017) and flow cytometry (Harris *et al.*, 1986), respectively. Following this, we decided to introduce the X-ray karyotype method using mass ranking for both radiation-induced and non-irradiated chromosomes. The plotted mass karyotype graphs shows a linear relation between measured mass and the known DNA content present in each individual chromosome. The X-ray phase contrast imaging is a very direct way to measure their masses because it counts electrons. Once segmented in the image, the 2D integral of the phase shift over the isolated object is a direct measure of the amount of matter present.

4.7.1. Mass quantification of stained and unstained metaphase chromosomes

Our first approach was to karyotype fixed human metaphase chromosomes stained with heavy atom elements to obtain better phase-contrast images. The 1 % Uranyl Acetate and the 6 mM platinum blue stain enhances the phase-contrast upon presence of electron density map which prevails scattering (Cao, Xu and Mao, 2011) (Carlo and Harris, 2012) (Yusuf, Millas, *et al.*, 2014). Although the UA is radioactive and toxic to the biological specimen, in addition, it disturbs the protein-protein/DNA-protein interactions and induces conformational changes (Lin, 2020). Moreover, it can form microcrystals once dried on the substrate (Carlo and Harris, 2012). Consequently, the less toxic platinum blue stain is a preferred substitute for Uranyl Acetate in TEM and SEM imaging (Inaga *et al.*, 2007), (Wanner and Formanek, 1995). One purpose of staining is to precipitate a thin layer deposit of electron density on the sample to enhance photon/electron scattering of the X-ray/electron beam (Wanner and Formanek, 1995).

The staining of a full set of weak scattering chromosome spreads at high resolution served to calibrate the hard X-ray ptychography imaging technique at room temperature. We later applied the same technique to image unstained chromosome spreads and built a karyotype of a full chromosome spread ranked according to their component masses. The total mass for 1 % UA, 6 mM platinum stain and unstained chromosomes were, 13.18 pg, 22.18 pg and 8.26 pg respectively, obtained in the first experiment.

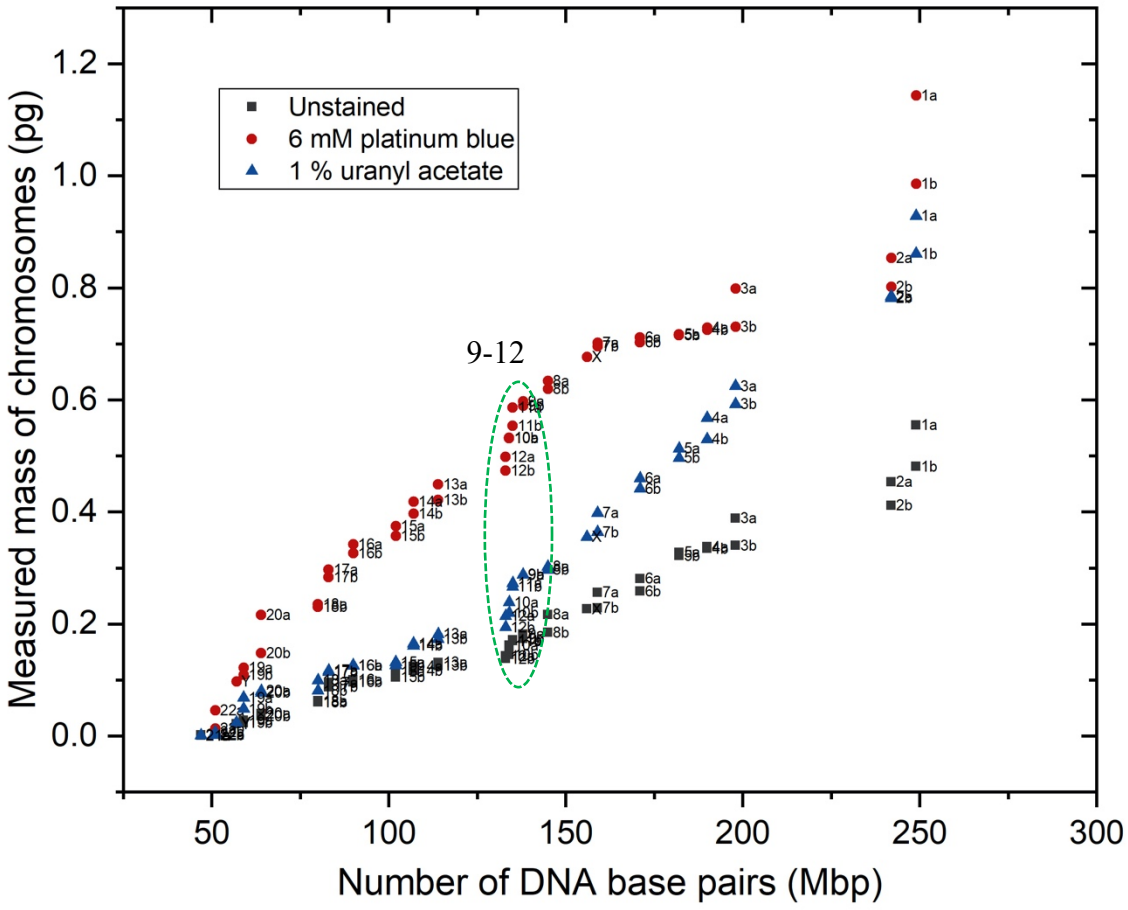

Figure 4.12: The X-ray karyotype shows the differences in the measured masses of individual chromosomes, stained with a heavy metal and unstained. The masses were retrived from the phase images of B-lymphocytes cells which were exposed for 1.00 sec during imaging. The green oval shows the chromosomes 9-12, from each spread.

In the X-ray mass karyotypes from both stained and unstained chromosome spreads (Figure 4.12) it is observed that the larger chromosomes, 1-2 have the highest variability among their homologs, followed by chromosomes 3-6, perhaps due to their enormous base pair ratio and for smaller chromosomes the variability of base pair ratio decreases. Apparently, the similar phenomena observed in all 24-chromosomes, labelled with quinacrine and its brightness, observed by autoradiography (Korenberg and Engels, 1978). The brightness indicates the amount of AT base pairs present in each individual chromosomes and the Y-chromosome shows the highest base pair ratio than the other chromosomes (Korenberg and Engels, 1978). Moreover, the base ratios also differs between the segments of a chromosome

and among a full set of chromosomes (Korenberg and Engels, 1978). The other quantitative karyotyping techniques including bivariate flow cytometry approaches do not resolve chromosomes 9-12 perhaps because of their similar DNA content and the base pair compositions (Mendelsohn *et al.*, 1973) (Korenberg and Engels, 1978) (Langlois *et al.*, 1982) (Boschman *et al.*, 1991). Two-colour flow cytometry with different dyes allow separations of these chromosomes.

Nevertheless, the phase-contrast imaging technique is adequately sensitive to resolve the relative masses of chromosomes 9-12 in a linear regression karyotypes (Figure 4.12), as this method gives the total mass of DNA content and chromosomal proteins present. Apparently, this could be the reason that the chromosomes 9-12 show a significant difference in their masses and can be easily identified in a linear regression. The green oval (Figure 4.12) indicates the concentrated data points of chromosomes 9-12, where the measured masses are well-separated in contrast to their similar genome lengths.

In Figure 4.12, it is clearly visible that unstained chromosomes have approximately 50 % decrease in their measured masses, relative to the stained examples. We can conclude that the heavy atom staining can add on up to ~ 50% extra mass to the stained chromosomes. In the second round of experiments, following improvements of the reconstruction algorithms (Batey, 2014) and the use of more freshly prepared samples, we had enough sensitivity to be able to drop the need for of staining and performed the whole radiation dose experiment with unstained chromosome spreads. The quantitative conclusions drawn below required the use of unmodified mass data.

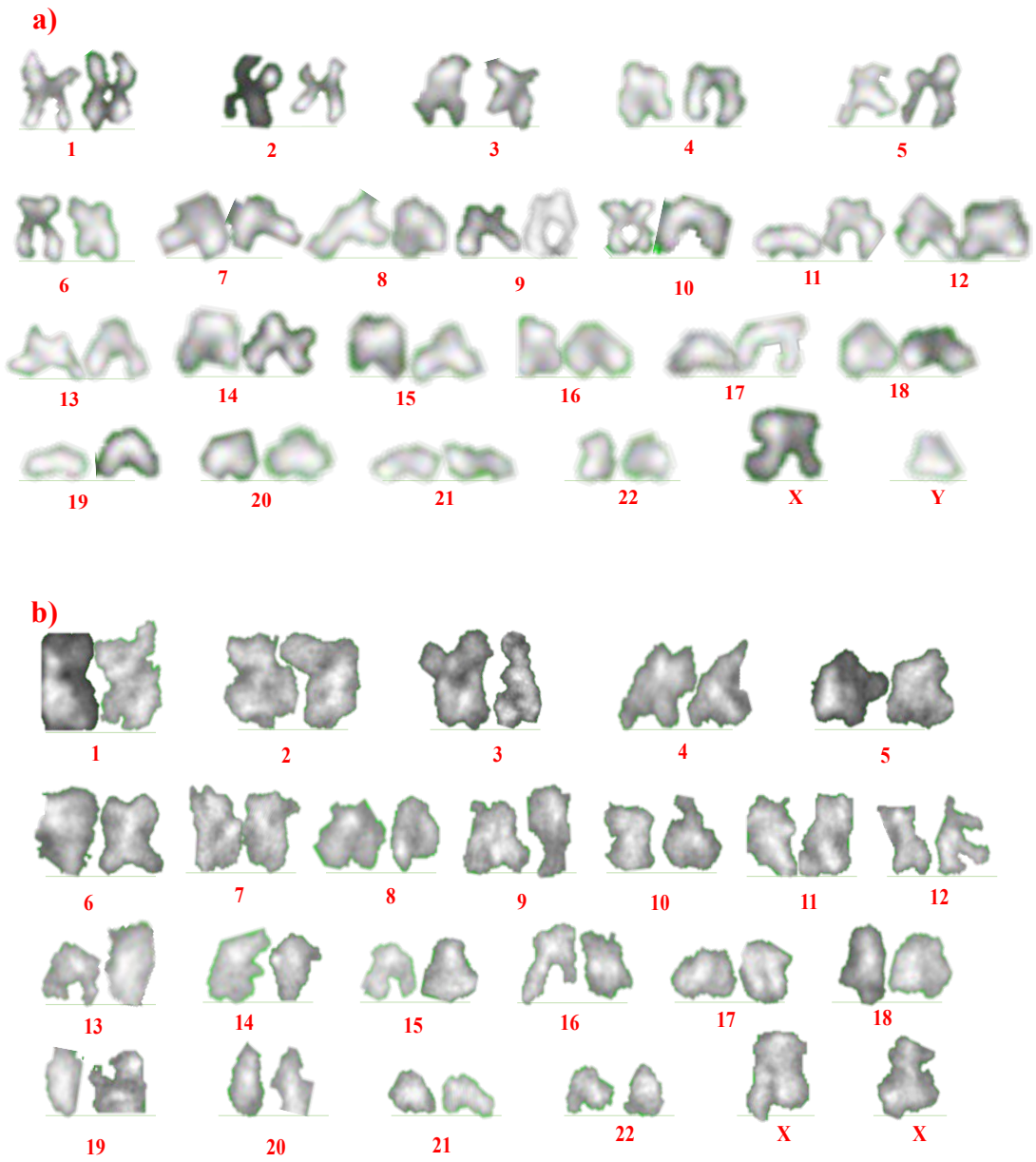

Figure 4.13: X-ray karyotyped, segmented chromosomes from a single spread, arranged on the bases of their individual masses; the numbers shown below indicates the position of each homologous pair of chromosomes. The following chromosomes were extracted from unstained non-irradiated a) B-cells, exposed to X-ray for 1.00 sec during scanning and b) T-cells, exposed to X-ray for 0.3 sec during scanning.

The knowledge of the weights allows, a fully quantitative X-ray karyotype to be generated since the number of DNA base pairs is known for each of the chromosomes in the human genome sequence. Furthermore, to test the accuracy of the method (hard X-ray ptychography imaging), the 2D integral of the phase shift over the isolated objects were segmented individually in the ImageJ software. And, once the chromosomes were segmented in the image, then the following segmented images were processed in the software using following tools: i) converted into a 16 bits image, ii) subtracted the background, iii) adjusted the threshold and iv) inverted the pixel values by using a tool called “invert LUT”. Eventually, by arranging into a descending order according to the obtained measured masses, the X-ray karyotypes of both the B and T-lymphocytes cells as shown in Figure 4.13.

Afterwards, we can reliably karyotype the chromosomes from group A (chromosomes 1-3) and B (chromosomes 4 and 5), similar to the conventional methods (**Error! Reference source not found.**) of chromosomes karyotypes. However, for the smaller chromosomes we can observe some shuffling among them, by visualising morphologically (Figure 4.13). According to our hypothesis, the alterations in the karyotype differs from a conventional fashion, this is probably due to presence of different concentration of chromosomal proteins in each individual chromosomes and their homologs as the phase shift gives a direct measure of the amount of matter present (Shemilt *et al.*, 2015), which has not been elucidated so far according to our knowledge.

Although, we are aware that amount of histones, non-histones and other chromosomal proteins are illustrated by Uchiyama et al, (2005) but that has been performed on the aggregates of metaphase human chromosomes (Uchiyama *et al.*, 2005). Moreover, we should also consider 2 % to 3 % of extra phase shift pixel values that occurs while manually segmenting individual chromosomes using free hand tool in the ImageJ software. In future, correlative imaging can be perform by accompanying immunolabelling and M-FISH technique on fixed human metaphase chromosomes (Shemilt *et al.*, 2015), followed by coherent X-ray scanning on the same spread to independently

verify the X-ray karyotype of chromosomes, including larger to smaller chromosomes.

In our investigation, we came across with a huge difference in the masses of the non-irradiated B and T- lymphocytes, the quantitively masses are 8.26 pg for B-cells and 242.21 pg for T-cells. The following could be the reasons: firstly, the chromosomes obtained from B-lymphocytes were stored cell line, whereas, the T-cells were from primary T-lymphocytes. In addition, the B-cells were long-term propagated subculture with passage 15, on the other hand, T-cells were only short-term propagated subculture with passage 3. However, the former subculture undergoes genomic instability and probably imbalance the DNA content comparative to latter (Hiorns *et al.*, 2004). Moreover, prepared chromosomes acquired from B-cells were stored in methanol acetic acid, with the ratio of 3:1 for 5-6 months in the fridge. It is reported that the methanol : acetic acid (3:1) fixation degrades histones and other relative chromosomal proteins and increases the length of the chromosomes. Prolonged fixation has a higher effect (Ronne, Andersen and Erlandsen, 1979). In addition, H1 histone protein is the most effected one in the methanol acetic acid fixation and apparently changes its conformation due to protonated of phosphate groups of DNA (Duijn, Prooijen-Knegt and Ploeg, 1985).

Secondly, the chromosomes obtained from B-cells and T-cells are from two different experiments performed separately at a different time intervals in the same beamline line (I-13-1, DLS, Oxford, UK) at room temperature. We observed a mass difference between the two separate experiments. The masses obtained from T-cells are ~30x higher than the B-cells. It is noted that the X-ray scanning while collecting diffraction pattern for the quantitative analysis, the B-cells and T-cells chromosome spreads were exposed for 1.00 sec and 0.3 sec, respectively, while scanning and lastly the radiosensitivity of B-cells to the aberrations compared to T-cells with direct X-ray scanning while imaging (Heylmann *et al.*, 2014), even after the chemical fixation.

4.7.2. Ionising radiation effects on the mass content of metaphase chromosome.

The X-ray ptychography technology gives us a powerful way to connect between known human genome sequence and the measured masses of the obtained chromosomes. Following the X-ray karyotype of fixed human metaphase chromosomes of heavy atom stained (Figure 4.4) and non-irradiated chromosomes (Figure 4.5 and Figure 4.6), we carried out a second series of experiments to X-ray karyotype the X-ray induced chromosomes at different radiation doses, 0.1 Gy (Figure 4.7), 0.5 Gy (Figure 4.8) and 1 Gy (Figure 4.9), irradiated at a dose rate of 0.5 Gy/min (see chapter 2, Materials and Methods). To distinguish the mass difference between non-irradiated and irradiated chromosomes, if the content of DNA and chromosomal proteins alters and can be identify by the quantitative X-ray karyotype.

In a typical human cell cycle, before, the DNA synthesis in S-phase, a nucleus will consist of 46 chromatids and after that it will replicate to 92 chromatids prior to separation at anaphase to form a two daughter cells (**Error! Reference source not found.**). On the other hand, the protein content differs at different stages of the cell cycle (Gookin *et al.*, 2017) such as protein from minichromosome maintenance (MCM) family, that binds to the replicating point of the DNA at the G1-phase and then it disappears once the replication starts (Forsburg, 2004), similarly condensin and topoisomerase II**α** proteins are involved in the condensation and decatenation of chromosomes which appears at the S-phase after DNA replication and disintegrate once the chromosomes are segregated properly at anaphase (Charbin, Bouchoux and Uhlmann, 2014). Above all, the core histone proteins are always present which forms DNA-protein complex (Maeshima and Eltsov, 2008). Moreover, 209 interphase proteins and 107 metaphase proteins were identified in human depending upon their localisation and function, respectively (Uchiyama *et al.*, 2005).

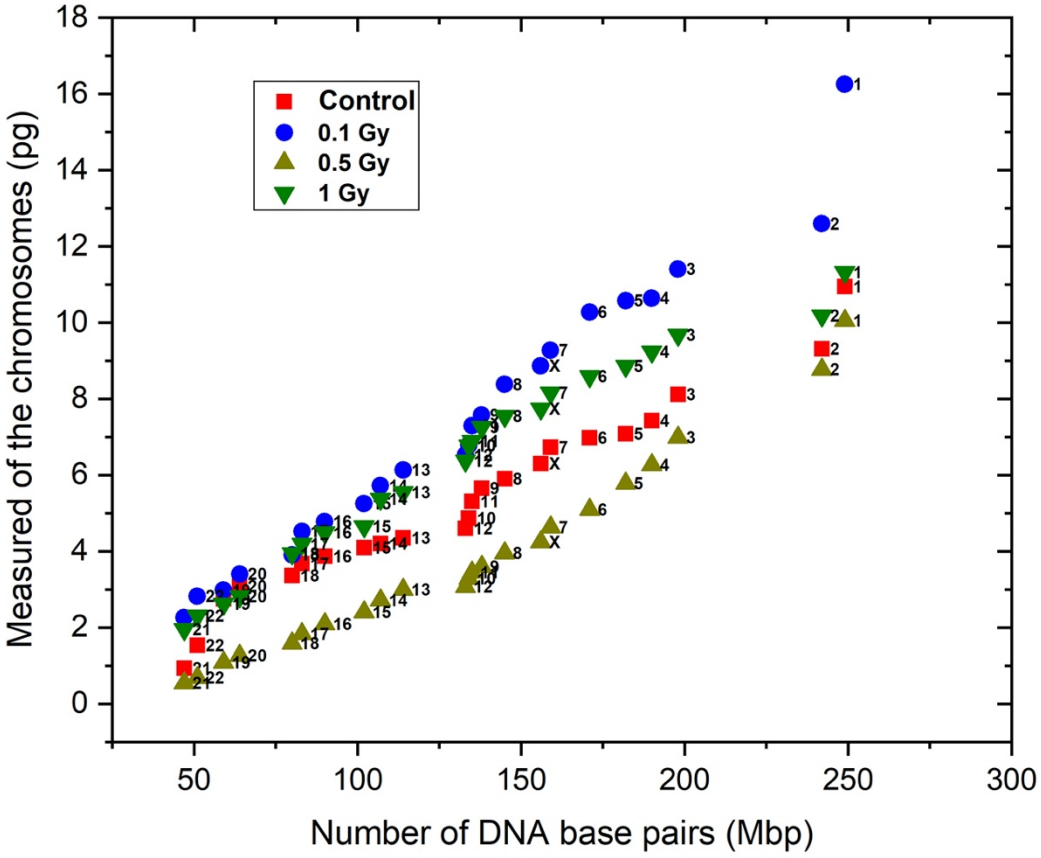

Figure 4.14: Average mass of each homologous pair of chromosomes segmented from the phase image of unstained chromosomes of irradiated chromosome in comparison with non-irradiated chromosomes. Chromosomes were obtained from T-lymphocytes and the spreads shown were exposed for 0.3 sec while X-ray scanning.

The

Figure 4.14, indicates the effect of ionising radiation on the acquired measured masses of a full set of chromosomes. According to our hypothesis, decrease in mass should occur upon irradiation and the masses should decrease with increased induced X-ray irradiation doses, possibly due to varied DNA lesions (Borrego-Soto, Ortiz-López and Rojas-Martínez, 2015) and protein modifications upon X-ray doses (Reisz *et al.*, 2014) (Lowe *et al.*, 2020). With 0.1 Gy and 1 Gy, the total obtained quantitative masses are 336.53 pg and 293.12 pg, respectively, a noticeable increase in mass can be spotted, relative to non-irradiated chromosome spread which is 242.21 pg, whereas, at 0.5 Gy dose, the measured mass decrease to 172.90 pg.

Upon irradiation various stress responsive enzymes and proteins come into an action including, DNA-PKs, 53BP1, Ku70/Ku80 (Biau *et al.*, 2019) and DNA damage response signalling pathway activates NHEJ and HRR mechanism to repair the DNA lesions (Mahaney, Meek and Lees-Miller, 2009). Immediately after radiation exposure, the cell cycle check points response with inclusion of related proteins, comes into play (Mahaney, Meek and Lees-Miller, 2009). It has been observed in the male germ cells, that with increase doses of ionising radiation the DSB number increases, on the other hand, the repair mechanism activates and repairs the lesions within 4 to 16 hours (Singh *et al.*, 2018). Therefore, we can postulate that the extra mass added to the irradiated chromosome spreads could be because of the proteins and enzymes coming into play to initiate the repair mechanism of the various DNA lesions happened straight after the irradiation at low doses. However, we cannot describe the decreased masses acquired at exposure of 0.5 Gy dose, because, interestingly, it has relatively low mass compared to non-irradiated chromosomes and other chosen X-ray doses.

Furthermore, in the literature, the radiosensitivity of the immune cells have been studied from a low-dose radiotherapy (LDRT) to high-dose radiotherapy (HDRT) and have shown that the viability of the cells decreases after 1 Gy exposure and the aberration increases, consequently, the apoptosis and cell death occurs at the doses above 10 Gy (Falcke *et al.*, 2018). Nevertheless, at continuous exposure to ionising radiation leads to histone protein degradation up to 40 % , after irradiating with the dose rate of 6 mGy/hr to 20 mGy/hr for 7 days (Lowe *et al.*, 2020).

4.7.3. Effect of radiation upon longer exposure

As a follow-up investigation, we measured the quantitative masses at a discrete intervals of exposure time used in the ptychography measurement. The same, methanol : acetic acid (3:1) fixed human metaphase chromosome spread was scanned for three different image exposure times in sequence, 0.3 sec, 0.6 sec and 0.9 sec. We collected the diffraction patterns from both irradiated (0.1 Gy,

0.5 Gy and 1 Gy) and non-irradiated (control) chromosomes. In Figure 4.15, 22 pairs of autosome and one pair of sex chromosomes (XX) are listed, and the masses of each chromosome is the averaged mass of two homologous chromosomes obtained from primary T-lymphocytes.

In Figure 4.15, the box plot depicts the following information; the big box shows the distribution of 50 % of the data points, the upper and lower whiskers defines the maxima and minima respectively, the median line and the small box, inside the big box are the median and the average value of the distribution, respectively. The data points are the acquired measured masses of fixed human metaphase chromosomes from T-lymphocytes.

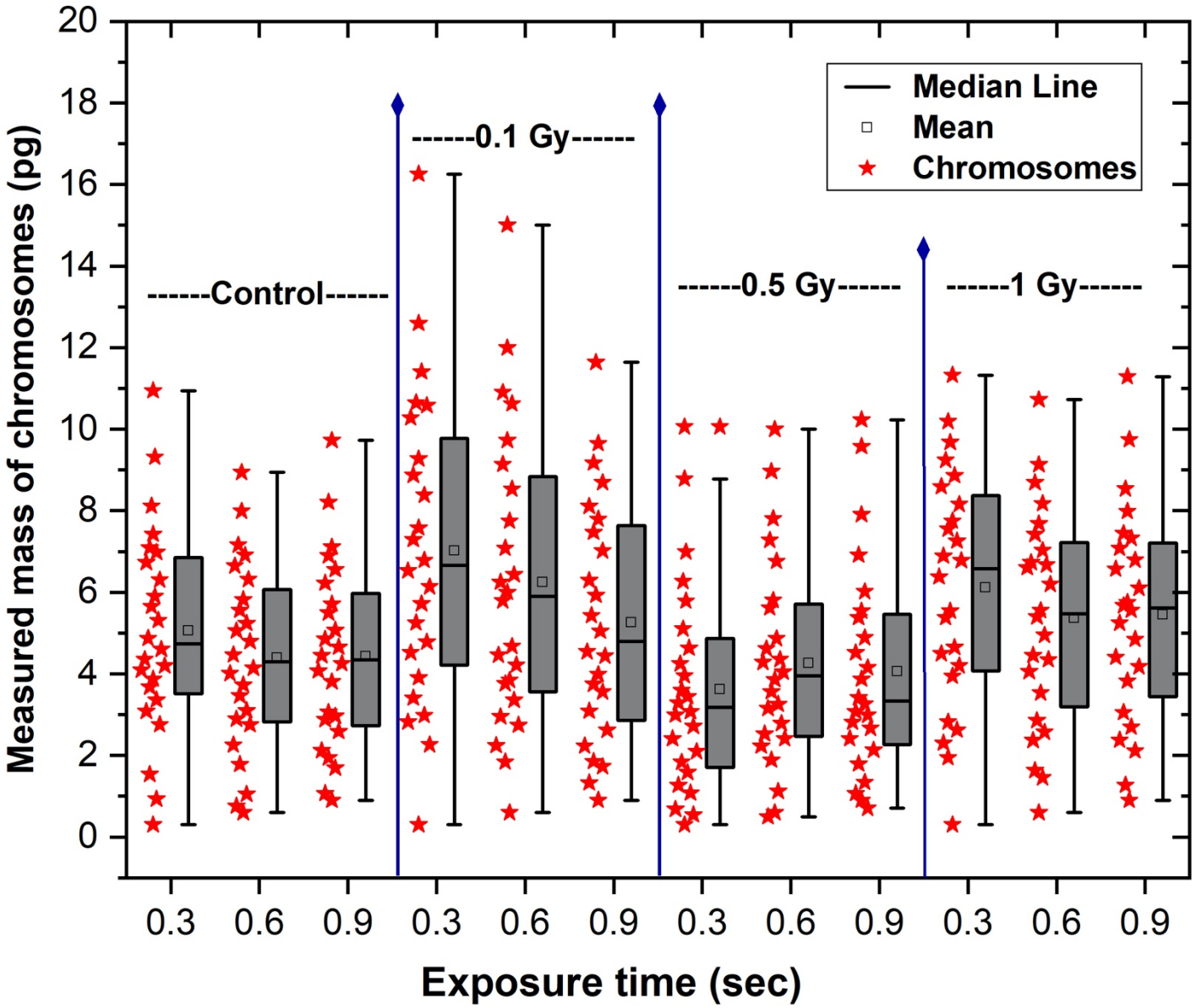

Figure 4.15: Measured mass of chromosomes from reconstructed phase images of non-irradiated and irradiated chromosomes spreads (n=1). The x-axis represents the exposure time to each sample during imaging. The red stars show the averaged masses of homologous pairs (22, XX) chromosomes from different spreads of different sample. The boxes alongside of red stars represents the maximum and minimum values of each spread. The mean and the median lines are also shown inside the boxes of a figure.

Acquired high-resolution images, <100 nm, of a fixed human metaphase chromosomes, to observe the ultrastructure, along with acquiring the measured mass of each segmented chromosomes from a single spread to build X-ray karyotype. Chromosome spreads laid on the silicon nitride membrane were scanned at room temperature and with a direct exposure to the X-ray radiation, leads to mass loss at every scan for both irradiated and non-irradiated (control) samples. For control sample, the summed masses (of all 46 chromosomes at metaphase stage) at a different intervals are: 242.21 pg, 209.68 pg and 210.84 pg for 0.3 sec, 0.6 sec and 0.9 sec, respectively. Thus, ~1.2-fold decrease in mass has been observed for 0.6 sec and 0.9 sec. Although, longer exposure to the ionising radiation leads to destruction of the biological samples (Reisz *et al.*, 2014) (Lowe *et al.*, 2020) while scanning at room temperature without any cryoprotectant. Henceforth, cryo-imaging is the future of the biological imaging (Yusuf *et al.*, 2017) (Yusuf *et al.*, 2019).

Furthermore, in case of X-ray induced chromosomes there are two factors of mass modification to be considered. Firstly, we have observed increase in the masses with increase in radiation doses (

Figure 4.14), which was induced to the T-cells prior to the chromosomal preparation (see chapter 2, Materials and Methods), except for 0.5 Gy, which acts vice-versa (

Figure 4.14 and Figure 4.15). Secondly, the decrease in the measured masses with longer exposure while X-ray scanning, expect at 0.5 Gy dose, because, a significant increase in the masses were observed with longer exposure, considering the 50 % distribution of the data points (Figure 4.15). For example, the summed masses at 0.5 Gy dose are 172.90 pg, 203.35 pg and 193.35 pg at 0.3 sec, 0.6 sec and 0.9 sec respectively, in addition, contains less DNA content when compared to the non-irradiated control sample (Figure 4.15). Apparently, we observed mass gain of ~1.1-fold for 0.6 sec and 0.9 sec relative to 0.3 sec.

Moreover, the T-cells exposed to 0.1 Gy and 1 Gy, behave roughly as expected, because, the mass reduction can be observed with a longer exposure time but on the other hand, increase in masses observed with higher radiation

doses in chromosomes induced with higher irradiation doses prior to X-ray imaging (Figure 4.15). The summed masses for 0.1 Gy irradiation are 336.53 pg, 298.67 pg, and 250.74 pg at 0.3 sec, 0.6 sec and 0.9 sec, respectively. The mass loss for 0.1 Gy irradiation for 0.6 sec and 0.9 sec relative to 0.3 sec are change of ~1.1-fold and ~1.3-fold respectively.

Similarly, at 1 Gy the summed masses are 293.12 pg, 256.46 pg, and 259.73 pg at 0.3 sec, 0.6 sec and 0.9 sec, respectively (Figure 4.15). Thus, ~1.1-fold decrease in mass has been observed for 0.6 sec and 0.9 sec relative to 0.3 sec. The increase in measured masses were observed at 0.1 Gy and 1 Gy relatively to the non-irradiated control sample are verified to be statistically significant at all exposure times, and according to our hypothesis the immediate initiation of cell cycle checkpoints responses and the activation of DNA damage repair protein signalling pathway comes to play, which probably adds extra mass to the irradiated chromosomes (Huang and Zhou, 2020).

Typically, the amount of radiation doses are directly proportional to the number of DSB lesions. Nevertheless, in this study, it has been observed that damage occurring in DNA/chromosomes are independent of exposure time at each of the irradiation doses. In the study of Neumaier *et al.*, (2012), it has been shown that “Radiation-induced foci” (RIF) were more at 0.1 Gy (64 RIF/Gy) dose compared to 1 Gy (23 RIF/Gy) dose, which means the number of DSBs is independent of irradiation doses in human cells. Apparently relative DNA repair proteins starts the repair mechanism after IR exposure.

4.8. Summary

This work demonstrates the ability to extract the individual masses of complete metaphase human chromosome spreads using two-dimensional phase-contrast images and hence built the X-ray Karyotype. The successful combination of scanning X-ray ptychography technologies allow us to measure the masses of stained and unstained metaphase human chromosomes at room temperature and gives a strong correlation between known genome sequence

and the measured mass of the chromosomes obtained using X-ray ptychography.

X-ray ptychography is a useful technique to determine the total genome mass of a species; including DNA and the related chromosomal proteins present at the different stages of the cell cycle without invasive staining.

The obtained quantitative information allowed us to measure the masses from Uranyl Acetate and platinum stained chromosome spreads obtained from B-lymphocytes and build an X-ray karyotype. The same procedure was applied to extract the masses from unstained X-ray induced chromosome spreads obtained from T-lymphocytes. Moreover, the X-ray karyotype was also generated from chromosome spreads with different exposure during X-ray scanning giving consistent results.

The individual measured masses of isolated chromosomes provides information of their DNA content along with the relative chromosomal proteins divided into histones and non-histones. Henceforth, measured and expected masses of each individual chromosome can be determined. Furthermore, with X-ray ptychography, the difference in masses of all 46 human chromosomes can be visualised in linear regression plot, including chromosomes 9-12, which is not possible in two colour flow cytometry, because of their very similar DNA content.

Chapter 5

5. General discussions and conclusions

X-ray irradiation is a common diagnostic tool for the treatment of severe diseases such as killing cancer cells (Borrego-Soto, Ortiz-López and Rojas-Martínez, 2015) (Falcke *et al.*, 2018) (Shimura and Kojima, 2018). In addition, computed tomography (CT) scanning instrumentation uses millisievert (mSv) doses is used for routine check-ups in the hospitals for the identification of unusual characteristics of human cells (Linet *et al.*, 2012). Although, after decade of investigation, the effect of ionising radiation on the structure of chromosomes is still not fully understood. This thesis has examined the structure of human chromosomes using advanced and emerging microscopy methods, namely FLIM and X-ray ptychography.

This thesis has demonstrated both the method; providing sufficient information into the possible chromatin compaction along the length of chromosomes using FLIM with multiphoton microscopy and mass measurement using negative phase-contrast X-ray ptychography of fixed human metaphase chromosomes. Studies on DNA oligo nucleotides indicates that base sequence effects leading to difference in lifetime seen by FLIM cannot be ruled out. In the X-ray ptychography experiment, it was critical to have the full karyotype present so that we could identify the entire genome. Furthermore, the effect of X-ray induced chromosome on the genome was also examined. FLIM is a useful method for providing information on the heteromorphic regions of the fixed human metaphase chromosomes showing lifetime difference with low-level X-ray irradiation. Also, the lifetime variation observed in different generations of the cell cycle in both heteromorphic as well as all 46 fixed human metaphase chromosomes. This indicates that the X-ray induced chromosomes

at different generation may be undergoing some chemical alterations which is observed by FLIM.

The lifetime variations and the mass measurement did not show continuous trend which means the effect of irradiation is independent of radiation doses. Although chromosomal breaks such as DSBs number increases with increasing irradiation doses. The effect of low-level irradiation doses observed in the fixed human metaphase chromosomes that can be assumed to be from chemical perturbations in the chromosomes. The DAPI lifetime variation and the difference in the masses of all 46 chromosomes present in the chromosome spreads were also observed in the X-ray induced chromosomes. In addition,, M-FISH aids in identifying each individual chromosome in a spread on which FLIM was already performed. The purpose of the correlative imaging was to detect any intra or inter-chromosomal aberrations occurred upon irradiation as well as to observe fluorescence decay maps of all 46 chromosomes to investigate the structural aberrations at nanosecond time scale of fluorescence decay upon excitation.

Time domain FLIM or FLIM-FRET are very useful tool to investigate the molecular environment of the chromosomes under environmental stress, for example, lifetime variation observed due to histone loss (Sherrard *et al.*, 2018), calcium ion regulation in chromatin (Phengchat *et al.*, 2016), physical change in the chromatin (Estandarte *et al.*, 2016) and effect of irradiation at higher X-ray dose (Abdollahi, Taucher-Scholz and Jakob, 2018). In this work, in chapter 3, ionising radiation is introduced to understand the nature of the high-order structure of mitotic chromosomes under oxidative stress condition. The FLIM and the mass measurement were performed on the X-ray induced chromosomes at radiation doses of 0.1 Gy, 0.5 Gy and 1 Gy. Typically, the number of chromosomal aberration increases with increasing dose but in our case we have observe the averaged (pooled from a five independent chromosome spreads) lowest lifetime with 0.5 Gy dose which increases with 0.1 Gy, followed by 1 Gy which is observed in heteromorphic chromosomes.

The average lifetime of all 46 chromosomes from five independent chromosome spreads was measured and the DAPI lifetime follows a sequence of; 0.5 Gy>0.1 Gy>1 Gy obtained from non-irradiated chromosomes. It can be assumed that the chromosome under chemical or molecular stress behaves differently at different low-level irradiation doses. The same pattern of lifetime variation has been observed with heterochromatin and non-heterochromatin regions of the chromosomes when all 46 chromosomes was considered.

The evolutionary conservation of heteromorphic DNA sequence, the pericentric location and the unusual hydrogen bonds. Beside this, high energy wave particles of ionising radiation disturbs the chemistry of DNA ultimately effects the sub-regions of the chromosomes. The high energy molecule of ionising radiation is strong enough to vibrate the DNA molecule and produces ions and free radicals ultimately leads to mutation.

In chapter 3, the reduced lifetime was maintained in heteromorphic chromosomes in different cell lines also in cancerous cells (Estandarte *et al.*, 2016). In addition, it was also observed in X-ray induced chromosomes at low-level doses. Average ionising radiation effect is noticed but the doses effect disappeared. Irradiation causes changes in the DNA, possibly due to the ionisation of guanine being lower than the other DNA bases for example as shown by pentanucleotide (GGAAT) present in the heteromorphic chromosomes (Melvin *et al.*, 1998).

With the information that the heteromorphic chromosomes shows variation in DAPI lifetime along the length of the chromosomes, depending upon the compactness of chromatins in the local regions of the chromosomes (Estandarte *et al.*, 2016). In addition, decompaction of chromatin observed at 10 Gy dose of X-ray irradiation when measured by FLIM (Abdollahi, Taucher-Scholz and Jakob, 2018). In this work, methanol: acetic acid fixed metaphase chromosome induced with low-level of X-ray doses prior to extraction of chromosomes. Nevertheless, it was observed that the DAPI lifetime values measured by FLIM decreases upon irradiation but it is independent of doses.

The difference of ~290 ps was observed between non-irradiated and irradiated chromosomes.

In chapter 4, X-ray ptychography has been used to measure the masses of chromosomes induced with X-ray doses (i:e. 0.1 Gy, 0.5 Gy and 1 Gy). It has been observed that the summed mass of all 46 chromosomes with 0.5 Gy dose has the lowest mass and then the masses increases for control sample followed by 1 Gy and 0.1 Gy doses. This technique is useful as it give accurate mass: including amount of chromosomal proteins and amount of DNA-content present in the entire genome in both non-irradiated and irradiated chromosomes and further build X-ray karyotype. The chromosomes are ranked according to their respective masses *versus* known human genome DNA sequence length.

According to our knowledge the mass of the entire genome has not been measured yet; that includes amount of chromosomal protein and expected DNA-content present in each individual chromosomes, available in a single chromosome spread. This helped to calculate the expected and the measured masses of the chromosome, along with the expected histones and non-histones present. Furthermore, mass gain or mass loss occurred due to irradiation can also be determine. We have measured an accurate masses of a full set of chromosomes for the first time; including known and unknown chromosomal proteins and DNA content (also the tightly packed DNA sequences which has not been discovered during the HGP). In the future, this can be useful to identify the genome affected with disease such as cancer by measuring the masses of each individual chromosomes from a spread and rank them according to their masses and compare with the control sample.

We have also measured masses of stained and unstained fixed metaphase chromosomes and can assume that up to 50 % of masses added to the chromosomes when stained. Therefore, the use of staining is discouraged and only imaged unstained metaphase chromosomes at room temperature. The X-ray karyotype ranked according to their masses, obtained from unstained B and T-cells were further segmented and placed on their respective positions in the karyogarm. In addition, the same fixed metaphase

chromosome spreads imaged at three different time interval (i.e. 0.3 sec, 0.6 sec and 0.9 sec). The obtained masses from the control sample, 0.1 Gy and 1 Gy show decreased summed masses with increasing amount of dose at every scan. Moreover, differences in decrease mass observed with 0.1 Gy and 1 Gy. Nevertheless, with 0.5 Gy irradiation dose, the masses increase with increasing dose at every intervals.

Overall this study is useful to further explore the chemical modification and the mechanism involved in the damage and the repair signalling that occurred upon low-level irradiation within the chromatin. More repeats are needed to obtain better results on the cytochemistry and the biochemical reaction occurring in the chromosomes upon low-level X-ray induction.

Chapter 6

6. Future outlooks

The study has demonstrated two promising imaging techniques towards DNA structural studies. Firstly, to identify early onset of chromosomal aberrations using combined FLIM and multiphoton microscopy. The effect of low-level X-ray irradiation can be observed in heteromorphic regions and the rest of the chromosome in chromosome spreads. Irradiation effects were observed in both the heterochromatin and non-heterochromatin regions of a chromosome, moreover, the effect was also observed in different generations of the cell cycle.

Secondly, the obtained masses of a human genome using X-ray ptychography was used to build an X-ray karyotype, ranked according to their masses. The advantage of this method of karyotyping is that it takes into account the contribution from both the DNA and the chromosomal proteins present in the chromosomes and can be achieved without using invasive staining methods. Hard-X-rays phase contrast imaging of heavy metal stained and unstained “spreads” (a full set of 46 chromosomes captured in one frame) was also achieved.

In the future FLIM measurement can be performed on ultraviolet (UV) irradiated fixed metaphase chromosomes. Immunofluorescence labelling of metaphase chromosomes (Terrenoire, Halsall and Turner, 2015) would be helpful to identify the chromosomal aberrations which occurred due to low-level ionising radiation. For example labelling *γ*-H2AX with antibodies to identify DSBs in the DNA (Dickey *et al.*, 2009) (Nair *et al.*, 2019) following FLIM imaging. It may be helpful tool to diagnose genomic instability in healthy and diseased cells.

The condensation and de-condensation occurred due to ionising radiation in chromosomes could be studied in polyamine prepared chromosomes in the real time, as an alternative to the methanol-acetic acid preparations we used. The FLIM-FRET technique can be utilized to unravel the intermediate 11 nm while single molecule and super resolution imaging techniques may be useful to determine structure around 150 nm structure of chromatin.

X-ray ptychography of unstained metaphase chromosomes at room temperature achieved at I-13-coherence branch, Diamond, UK, provides the basis of future 2D and 3D imaging of biological samples in a cryo-environment, for example to elucidate fine ultra-structure of chromatin. It would be advantageous to observe the full set of human chromosomes along with visualization of chromosome bands and internal details. However there are a number of technical issues to overcome as mentioned in (Yusuf *et al.*, 2017). The prime problem is to avoid ice formation throughout the cryo-imaging procedure of imaging.

Another approach is to perform M-FISH on the retrieved silicon nitride membranes to corelate with X-ray karyotype (ranked according to individual masses versus known DNA sequences) with standard cytogenetic staining patterns (M-FISH hybridisation karyotype). This can be achieved with some optimised protocols.

7. References

Abdollahi, E., Taucher-Scholz, G. and Jakob, B. (2018) 'Application of fluorescence lifetime imaging microscopy of DNA binding dyes to assess radiation-induced chromatin compaction changes', *International Journal of Molecular Sciences*, 19(2399), pp. 1–15. doi: 10.3390/ijms19082399.

AbdulSalam, S. F., Thowfeik, F. S. and Merino, E. J. (2017) 'Excessive Reactive Oxygen Species and Exotic DNA Lesions as an Exploitable Liability', *Biochemistry*, 55(38), pp. 5341–5352. doi: 10.1021/acs.biochem.6b00703.

Akbas, E., Senli, H., Hallioglu, O., Batmaz, S. and Erdogan, N. E. (2010) 'Association of pericentric inversion of chromosome 9 (inv[9][p11q13]) and genetic diseases: Case report', *Laboratory Medicine*, 41(2), pp. 96–98. doi: 10.1309/LM9ESUC9O8QKZOYO.

Allshire, R. C. and Madhani, H. D. (2018) 'Ten principles of heterochromatin formation and function', *Nature Reviews Molecular Cell Biology*, 19(4), pp. 229–244. doi: 10.1038/nrm.2017.119.

Als-Nielsen, J. and McMorrow, D. (2011) *Elements of Modern X-ray Physics*. 2nd edn. West Sussex: John Wiley & Sons, Ltd. doi: 10.1002/9781119998365.

Anderson, R. (2010) 'Multiplex Fluorescence in situ Hybridization (M-FISH)', in Bridger, J. M. and Volpi, E. V (eds) *Fluorescence in situ Hybridization (FISH) Protocols and Applications*. Totowa NJ: Humana Press, pp. 83–97.

Anderson, R. M., Stevens, D. L. and Goodhead, D. T. (2002) 'M-FISH analysis shows that complex chromosome aberrations induced by alpha-particle tracks are cumulative products of localized rearrangements', *Proceedings of the National Academy of Sciences of the United States of America*, 99(19), pp. 12167–12172. doi: 10.1073/pnas.182426799.

Anderson, R. M., Sumption, N. D., Papworth, D. G. and Goodhead, D. T. (2006) 'Chromosome breakpoint distribution of damage induced in peripheral blood lymphocytes by densely ionizing radiation', *International Journal of Radiation Biology*, 82(1), pp. 49–58. doi: 10.1080/09553000600579231.

Anthony, N., Guo, P. and Berland, K. (2009) 'Principles of Fluorescence for Quantitative Fluorescence Microscopy', in Periasamy, A. and Clegg, R. M. (eds) *FLIM Microscopy in Biology and Medicine*. 1st edn. New York: Taylor & Francis Group, LLC, pp. 35–59. doi: https://doi.org/10.1201/9781420078916.

Aparicio, T., Baer, R. and Gautier, J. (2015) 'DNA double-strand break repair pathway choice and cancer', *DNA Repair (Amst)*, 19, pp. 169–175. doi: 10.1016/j.dnarep.2014.03.014.

Azzam, E. Jay-Gerin, J. Pain, D. (2012) 'Ionizing radiation-induced metabolic oxidative stress and prolonged cell injury', *Cancer Letters*, 327(1–2), pp. 48–60. doi: 10.1016/j.canlet.2011.12.012.

Bachtrog, D. (2014) 'Y chromosome evolution: emerging insights into processes of Y chromosome degeneration', *Nature Reviews Genetics*, 14(2), pp. 113–124. doi: 10.1038/nrg3366.

Balajee, A. S., Bertucci, A., Taveras, M. and Brenner, D. J. (2014) 'Multicolour FISH analysis of ionising radiation induced micronucleus formation in human lymphocytes', *Mutagenesis*, 29(6), pp. 447–455. doi: 10.1093/mutage/geu041.

Bannister, A. J., Zegerman, P., Partridge, J. F., Miska, E. A., Thomas, J. O., Allshire, R. C. and Kouzarides, T. (2001) 'Selective recognition of methylated lysine 9 on histone H3 by the HP1 chromo domain', *Nature*, 410(6824), pp. 120–124. doi: 10.1038/35065138.

Barcellona, M. L. and Gratton, E. (1990) 'The fluorescence properties of a DNA probe - 4???-6-Diamidino-2-phenylindole (DAPI)', *European Biophysics Journal*, 17(6), pp. 315–323. doi: 10.1007/BF00258380.

Barke, I., Hartmann, H., Rupp, D., Flückiger, L., Sauppe, M., Adolph, M., Schorb, S., Bostedt, C., Treusch, R., Peltz, C., Bartling, S., Fennel, T., Meiwes-Broer, K. H. and Möller, T. (2015) 'The 3D-architecture of individual free silver nanoparticles captured by X-ray scattering', *Nature Communications*, 6, pp. 1–7. doi: 10.1038/ncomms7187.

Batey, D. J. (2014) *Ptychographic Imaging of Mixed States*. University of Sheffield. Available at: http://etheses.whiterose.ac.uk/8524/ (Accessed: 25 October 2020) .

Batey, D. J., Cipiccia, S., Van Assche, F., Vanheule, S., Vanmechelen, J., Boone, M. N. and Rau, C. (2019) 'Spectroscopic imaging with single acquisition ptychography and a hyperspectral detector', *Scientific Reports*. Springer US, 9(1), pp. 1–7. doi: 10.1038/s41598-019-48642-y.

Becker, W. (2012) 'Fluorescence lifetime imaging - techniques and applications', *Journal of Microscopy*, 247(2), pp. 119–136. doi: 10.1111/j.1365-2818.2012.03618.x.

Beckers, M., Senkbeil, T., Gorniak, T., Reese, M., Giewekemeyer, K., Gleber, S. C., Salditt, T. and Rosenhahn, A. (2011) 'Chemical contrast in soft X-ray ptychography', *Physical Review Letters*, 107(20), pp. 1–4. doi: 10.1103/PhysRevLett.107.208101.

Bench, G. S., Friz, A. M., Corzett, M. H., Morse, D. H. and Balhorn, R. (1996) 'DNA and Total Protamine Masses in Individual Sperm From Fertile Mammalian Subjects', *Cytometry*, 23, pp. 263–271.

Berger, F. (2019) 'Emil Heitz, a true epigenetics pioneer', *Nature Reviews Molecular Cell Biology*, 20, p. 572. doi: 10.1038/s41580-019-0161-z.

Beroukhim, R., Getz, G., Nghiemphu, L., Barretina, J., Hsueh, T., Linhart, D., Vivanco, I., Soto, H., Perner, S., Prensner, J., Debiasi, R. M., Demichelis, F., Hatton, C., Meyerson, M., Golub, T. A., Lander, E. S., Mellinghoff, I. K. and Sellers, W. R. (2007) 'Assessing the significance of chromosomal aberrations in cancer : Methodology and application to glioma', *Proceedings of the National Academy of Sciences of the United States of America*, 104(50), pp. 20007–20012.

Bhatnagar, M. C. and Bansal, G. (2009) 'The Chromosomes', in *Cell Biology and Genetics*. 3rd edn. Meerut: Krishna Prakashan Media (P) Ltd., pp. 131–134.

Biau, J., Chautard, E., Verrelle, P. and Dutreix, M. (2019) 'Altering DNA repair to improve radiation therapy: Specific and multiple pathway targeting', *Frontiers in Oncology*, 9: 1009, pp. 1–10. doi: 10.3389/fonc.2019.01009.

Bishop, R. (2010) 'Review Applications of fluorescence in situ hybridization (FISH) in detecting genetic aberrations of medical significance', *Bioscience Horizons*, 3(1), pp. 85–95.

Blanpain, C., Mohrin, M., Sotiropoulou, P. A. and Passegue, E. (2011) 'Review DNA-Damage Response in Tissue-Specific and Cancer Stem Cells', *Cell Stem Cell*, 8, pp. 16–29. doi: 10.1016/j.stem.2010.12.012.

Bloomer, W. D. and Adelstein, S. J. (1982) 'The Mammalian Radiation Survival Curve', *Journal of Nuclear Medicine*, 23(3), pp. 259–265.

Borràs-fresneda, M., Barquinero, J., Gomolka, M. and Hornhardt, S. (2016) 'Differences in DNA Repair Capacity , Cell Death and Transcriptional Response after Irradiation between a Radiosensitive and a Radioresistant Cell Line', *Scientific reports*, 6:27043, pp. 1–11. doi: 10.1038/srep27043.

Borrego-Soto, G., Ortiz-López, R. and Rojas-Martínez, A. (2015) 'Ionizing radiation-induced DNA injury and damage detection in patients with breast cancer', *Genetics and Molecular Biology*, 38(4), pp. 420–432. doi: 10.1590/S1415-475738420150019.

Boschman, G. A., Rens, W., van Oven, C. H., Manders, E. M. M. and Aten, J. A. (1991) 'Bivariate flow karyotyping of human chromosomes: Evaluation of variation in Hoechst 33258 fluorescence, chromomycin A3 fluorescence, and relative chromosomal DNA content', *Cytometry*, 12(6), pp. 559–569. doi: 10.1002/cyto.990120613.

Brothman, A. R., Schneider, N. R., Saikevych, I., Cooley, L. D., Butler, M. G., Patil, S., Mascarello, J. T., Rao, K. W., Dewald, G. W., Park, J. P., Persons, D. L., Wolff, D. J. and Vance, G. H. (2006) 'Cytogenetic heteromorphisms: Survey results and reporting practices of Giemsa-band regions that we have pondered for years', *Archives of Pathology and Laboratory Medicine*, 130(7), pp. 947–949. doi: 10.1043/1543-2165(2006)130[947:CHSRAR]2.0.CO;2.

Brown., T. A. (2002) *Genomes*. 2nd edn. Oxford: Wiley-Liss: Graland Science.

Cannan, W. J. and Pederson, D. S. (2016) 'Mechanisms and Consequences of Double-strand DNA Break Formation in Chromatin', *Journal of Cellular Physiology*, 231(1), pp. 3–14. doi: 0.1002/jcp.25048.

Cao, B., Xu, H. and Mao, C. (2011) 'Transmission electron microscopy as a tool to image bioinorganic nanohybrids: The case of phage-gold nanocomposites', *Microscopy Research and Technique*, 74(7), pp. 627–635. doi: 10.1002/jemt.21030.

Carlo, S. De and Harris, J. R. (2012) 'Negative staining and Cryo-negative Staining of Macromolecules and Viruses for TEM', *Micron*, 42(2), pp. 117–131. doi: 10.1385/1-59259-201-5.

Chapman, Henry N., Barty, A., Bogan, M. J., Boutet, S., Frank, M., Hau-Riege, S. P., Marchesini, S., Woods, B. W., Bajt, S., Benner, W. H., London, R. A., Plönjes, E., Kuhlmann, M., Treusch, R., Düsterer, S., Tschentscher, T., Schneider, J. R., Spiller, E., Möller, T., Bostedt, C., Hoener, M., Shapiro, D. A., Hodgson, K. O., van der Spoel, D., Burmeister, F., Bergh, M., Caleman, C., Huldt, G., Seibert, M. M., Maia, F. R. N. C., Lee, R. W., Szöke, A., Timneanu, N. and Hajdu, J. (2006) 'Femtosecond diffractive imaging with a soft-X-ray free-electron laser', *Nature Physics*, 2(12), pp. 839–843. doi: 10.1038/nphys461.

Chapman, Henry N, Barty, A., Marchesini, S., Noy, A., Cui, C., Howells, M., Rosen, R., He, H., Spence, J. C., Beetz, T., Jacobsen, C., Shapiro, D. and Hau-riege, S. P. (2006) 'High-resolution ab initio three-dimensional x-ray diffraction microscopy', *Journal of the Optical Society of America A.*, 23(5), p. 1179.

Chapman, H. N. and Nugent, K. A. (2010) 'Coherent lensless X-ray imaging', *Nature Photonics*, 4(12), pp. 833–839. doi: 10.1038/nphoton.2010.240.

Charbin, A., Bouchoux, C. and Uhlmann, F. (2014) 'Condensin aids sister chromatid decatenation by topoisomerase II', *Nucleic Acids Research*, 42(1), pp. 340–348. doi: 10.1093/nar/gkt882.

Charlesworth, B. (2003) 'The organization and evolution of the human Y chromosome', *Genome Biology*, 4(9), pp. 9–11. doi: 10.1186/gb-2003-4-9-226.

Charlesworth, B. and Charlesworth, D. (2000) 'The degeneration of Y chromosomes', *Philosophical Transactions of the Royal Society B: Biological Sciences*, 355(1403), pp. 1563–1572. doi: 10.1098/rstb.2000.0717.

Chen, B., Yusuf, M., Hashimoto, T., Estandarte, A. K., Thompson, G. and Robinson, I. (2017) 'Three-dimensional positioning and structure of chromosomes in a human prophase nucleus', *Science Advances*, 3(7), pp. 1–9. doi: 10.1126/sciadv.1602231.

Chen, T. R., Kao, M. L., Marks, J. and Chen, Y. Y. (1981) 'Polymorphic variants in human chromosome 15', *American Journal of Medical Genetics*,

9(1), pp. 61–66. doi: 10.1002/ajmg.1320090111.

Cho, Y., Kim, S., Woo, H., Kim, Y., Ha, S. and Chung, H. (2015) 'Delayed Numerical Chromosome Aberrations in Human Fibroblasts by Low Dose of Radiation', *International Journal of Environmental Research and Public Health*, 12(12), pp. 15162–15172. doi: 10.3390/ijerph121214979.

Choo, A. K. H. (1997) 'Anomalies of the human centromere', in *The Centromere*. Melbourne: Oxford University Press, pp. 255–265.

Cooper, Geoffrey. M (2000) *The cell: A Molecular Approach.* 2nd edn. Sunderland (MA): Sinauer Associates.

Cooper, Geoffrey M. (2000) *The Cell: A Molecular Approach*. 2nd edn. ASM Press.

Cram, L. S., Bartholdi, M. F., Ray, F. A., Meyne, J., Moyzis, R. K., Schwarzacher-Robinson, T. and Kraemer, P. M. (1988) 'Overview of flow cytogenetics for clinical applications', *Cytometry*, 9(3 S), pp. 94–100. doi: 10.1002/cyto.990090819.

Cremer, T. and Cremer, M. (2010) 'Chromosome territories.', *Cold Spring Harbor perspectives in biology*, 2(3), pp. 1–22. doi: 10.1101/cshperspect.a003889.

Deng, J., Chen, S., Jin, Q., Vacek, E., Jacobsen, C., Lai, B. and Vogt, S. (2019) 'Correlative X-ray Ptychographic and Fluorescence Imaging at the Advanced Photon Source', *Microscopy and Microanalysis*, 25(S2), pp. 1030–1031. doi: 10.1017/s1431927619005889.

Deng J., Vine D. J., Chen, S., Nashed, Y. S. G., Jin, Q., Peterka, T., Vogt, S. and Jacobsen, C. (2015) 'Advances and challenges in cryo ptychography at the Advanced Photon Source', *Proceedings of the National Academy of Sciences of the United States of America.*, 112, pp. 2314–9. doi: 10.1016/j.physbeh.2017.03.040.

Derksen, J. and Meekes, H. (1984) 'Selective staining of nucleic acid containing structures by uranyl acetate-lead citrate', *Micron and Microscopica Acta*, 15(1), pp. 55–58.

Desouky, O., Ding, N. and Zhou, G. (2015) 'ScienceDirect Targeted and non-targeted effects of ionizing radiation', *Journal of Radiation Research and Applied Sciences*, 8(2), pp. 247–254. doi: 10.1016/j.jrras.2015.03.003.

Dickey, J. S., Redon, C. E., Nakamura, A. J., Baird, B. J., Sedelnikova, O. A. and Bonner, W. M. (2009) 'H2AX: Functional roles and potential applications', *Chromosoma*, 118(6), pp. 683–692. doi: 10.1007/s00412-009-0234-4.

Dierolf, M., Menzel, A., Thibault, P., Schneider, P., Kewish, C. M., Wepf, R., Bunk, O. and Pfeiffer, F. (2010) 'Ptychographic X-ray computed tomography at the nanoscale', *Nature*, 467(7314), pp. 436–439. doi: 10.1038/nature09419.

Dillard, R. S., Hampton, C. M., Strauss, J. D., Ke, Z., Altomara, D., Ferreira, R. C. G., Kiss, G. and Wright, E. R. (2018) 'Biological Applications at the Cutting Edge of Cryo-Electron Microscopy', *Microscopy and Microanalysis*, 24(4), pp. 406–419. doi: 10.1017/S1431927618012382.

Doležel, J., Bartoš, J., Voglmayr, H. and Greilhuber, J. (2003) 'Nuclear DNA content and genome size of trout and human', *Cytometry Part A*, 51A(2), pp. 127–128. doi: 10.1002/cyto.a.10013.

Duijn, P. Van, Prooijen-Knegt, A. C. van and Ploeg, M. van der (1985) 'The involvement of nucleosomes in Giemsa staining of chromosomes: A new hypothesis on the banding mechanism', *Histochemistry: Springer-Verlag*, 82, pp. 363–376.

Durante, M. and Formenti, S. C. (2018) 'Radiation-induced chromosomal aberrations and immunotherapy: Micronuclei, cytosolic DNA, and interferon-production pathway', *Frontiers in Oncology*, 8:192, pp. 1–9. doi: 10.3389/fonc.2018.00192.

El-Saghire, H., Michaux, A., Thierens, H. and Baatout, S. (2013) 'Low doses of ionizing radiation induce immune-stimulatory responses in isolated human primary monocytes', *International Journal of Molecular Medicine*, 32(6), pp. 1407–1414. doi: 10.3892/ijmm.2013.1514.

Estandarte, A. K., Botchway, S., Lynch, C., Yusuf, M. and Robinson, I. (2016) 'The use of DAPI fluorescence lifetime imaging for investigating chromatin condensation in human chromosomes', *Scientific Reports*, 6(31417), pp. 1–12. doi: 10.1038/srep31417.

Falcke, S. E., Rühle, P. F., Deloch, L., Fietkau, R., Frey, B. and Gaipl, U. S. (2018) 'Clinically relevant radiation exposure differentially impacts forms of cell death in human cells of the innate and adaptive immune system', *International Journal of Molecular Sciences*, 19(11), pp. 3–6. doi: 10.3390/ijms19113574.

Forsburg, S. L. (2004) 'Eukaryotic MCM Proteins : Beyond Replication Initiation', *American Society for Microbiology*, 68(1), pp. 109–131. doi: 10.1128/MMBR.68.1.109.

Friedrich, U., Caprani, M., Niebuhr, E., Therkelsen, A. J. and Jørgensen, A. L. (1996) 'Extreme variant of the short arm of chromosome 15', *Human Genetics*, 97(6), pp. 710–713. doi: 10.1007/BF02346177.

Gagula-Palalic, S. and Can, M. (2013) 'Denver Groups Classification of Human Chromosomes Using CANN Teams', *Southeast Europe Journal of Soft Computing*, 2(2). doi: 10.21533/scjournal.v2i2.22.

Goldfeder, R. L., Wall, D. P., Khoury, M. J., Ioannidis, J. P. A. and Ashley, E. A. (2017) 'Human Genome Sequencing at the Population Scale: A Primer on High-Throughput DNA Sequencing and Analysis', *American Journal of Epidemiology*, 186(8), pp. 1000–1001. doi: 10.1093/aje/kww224.

Gookin, S., Min, M., Phadke, H., Chung, M., Moser, J., Miller, I., Carter, D.

and Spencer, S. L. (2017) ‘A map of protein dynamics during cell-cycle progression and cell-cycle exit’, *Public Library of Science: Biology*, 15(9), pp. 1–25.

Gospodinov, A. and Herceg, Z. (2013) ‘Chromatin structure in double strand break repair’, *DNA Repair*, 12(10), pp. 800–810. doi: 10.1016/j.dnarep.2013.07.006.

Grady, D. L., Ratliff, R. L., Robinson, D. L., Mccanlies, E. C., Meyne, J. and Moyzis, R. K. (1992) ‘Highly conserved repetitive DNA sequences are present at human centromeres’, *Proceedings of the National Academy of Sciences of the United States of America*, 89(5), pp. 1695–1699. doi: 10.1073/pnas.89.5.1695.

Grimwade, D., Hills, R. K., Moorman, A. V., Walker, H., Chatters, S., Goldstone, A. H., Wheatley, K., Harrison, C. J. and Burnett, A. K. (2010) ‘Refinement of cytogenetic classification in acute myeloid leukemia: Determination of prognostic significance of rare recurring chromosomal abnormalities among 5876 younger adult patients treated in the United Kingdom Medical Research Council trials’, *Blood*, 116(3), pp. 354–365. doi: 10.1182/blood-2009-11-254441.

Guk, B. K., Yae, J. Y., Tae, J. S., Hwa, S. Y., Yong, S. G. and Sang, J. L. (2008) ‘X-ray imaging of various biological samples using a phase-contrast hard X-ray microscope’, *Microscopy Research and Technique*, 71(9), pp. 639–643. doi: 10.1002/jemt.20601.

Harris, P., Boyd, E., Young, B. D. and Ferguson-Smith, M. A. (1986) ‘Determination of the DNA content of human chromosomes by flow cytometry’, *Cytogenetics and Cell Genetics*, 41, pp. 14–21.

Harshman, S. W., Young, N. L., Parthun, M. R. and Freitas, M. A. (2013) ‘H1 histones: Current perspectives and challenges’, *Nucleic Acids Research*, 41(21), pp. 9593–9609. doi: 10.1093/nar/gkt700.

Hauer, M. H., Seeber, A., Singh, V., Thierry, R., Sack, R., Amitai, A., Kryzhanovska, M., Eglinger, J., Holcman, D., Owen-Hughes, T. and Gasser, S. M. (2017) ‘Histone degradation in response to DNA damage enhances chromatin dynamics and recombination rates’, *Nature Structural and Molecular Biology*, 24(2), pp. 99–107. doi: 10.1038/nsmb.3347.

Hayat, M. A. and Miller, S. E. (1990) *Negative Staining*. New York: McGraw-Hill Publishing Company.

Hémonnot, C. Y. J. and Köster, S. (2017) ‘Imaging of Biological Materials and Cells by X-ray Scattering and Diffraction’, *American Chemical Society: Nanoscience, Nanotechnology*, 11(9), pp. 8542–8559. doi: 10.1021/acsnano.7b03447.

Henderson, A. S., Warburton, D. and Atwood, K. C. (1972) ‘Location of ribosomal DNA in the human chromosome complement.’, *Proceedings of the*

National Academy of Sciences of the United States of America, 69(11), pp. 3394–3398. doi: 10.1073/pnas.69.11.3394.

Heylmann, D., Rödel, F., Kindler, T. and Kaina, B. (2014) 'Radiation sensitivity of human and murine peripheral blood lymphocytes, stem and progenitor cells', *Biochimica et Biophysica Acta - Reviews on Cancer*, 1846(1), pp. 121–129. doi: 10.1016/j.bbcan.2014.04.009.

Hiorns, L. R., Bradshaw, T. D., Skelton, L. A., Yu, Q., Kelland, L. R. and Leyland-Jones, B. (2004) 'Variation in RNA expression and genomic DNA content acquired during cell culture', *British Journal of Cancer*, 90(2), pp. 476–482. doi: 10.1038/sj.bjc.6601405.

Hockings, C., Poudel, C., Feeney, K., Novo, C., Hamouda, M., Mela, I., Fernandez-Antoran, D., Vallejo-Ramirez, P., Rugg-Gunn, P., Chalut, K., Kaminski, C. and Kaminski-Schierle, G. (2020) 'Illuminating chromatin compaction in live cells and fixed tissues using SiR-DNA fluorescence lifetime', *BioRxiv- the preprint server for Biology*, pp. 1–11. doi: 10.1101/2020.05.02.073536.

Howells, M., Jacobsen, C., Warwick, T. and Van den Bos, A. (2006) 'Principles and Applications of Zone Plate X-Ray Microscopes', in Hawkes P.W. and Spence, J. C. H. (eds) *Science of Microscopy*. New York (NY): Springer, pp. 835–926. doi: 10.1016/s1369-7021(06)71581-4.

Howells, M. R., Beetz, T., Chapman, H. N., Cui, C., Holton, J. M., Jacobsen, C. J., Kirz, J., Lima, E., Marchesini, S., Miao, H., Sayre, D., Shapiro, D. A., Spence, J. C. H. and Starodub, D. (2009) 'An assessment of the resolution limitation due to radiation-damage in X-ray diffraction microscopy', *Journal of Electron Spectroscopy and Related Phenomena*, 170(1–3), pp. 4–12. doi: 10.1016/j.elspec.2008.10.008.

Hozier, J. C., Furcht, L. T. and Wendelshafer-grabb, G. (1981) 'Structure of Human Chromosomes Visualized at the Electron Microscopic Level', *Chromosoma*, 64, pp. 55–64. doi: https://doi.org/10.1007/BF00285749.

Huang, R. X. and Zhou, P. K. (2020) 'DNA damage response signaling pathways and targets for radiotherapy sensitization in cancer', *Signal Transduction and Targeted Therapy*, 5(1). doi: 10.1038/s41392-020-0150-x.

Huang, X., Nelson, J., Kirz, J., Lima, E., Marchesini, S., Miao, H., Neiman, A. M., Shapiro, D., Steinbrener, J., Stewart, A., Turner, J. J. and Jacobsen, C. (2009) 'Soft X-Ray Diffraction Microscopy of a Frozen Hydrated Yeast Cell', *Physical Review Letters*, 103(19). doi: 10.1103/PhysRevLett.103.198101.

Huang, X. shuang, Li, X., Tan, C., Xiao, L., Jiang, H. ou, Zhang, S. fang, Wang, D. mei and Zhang, J. xiang (2010) 'Genome-wide scanning reveals complex etiology of oculo-auriculo-vertebral spectrum', *Tohoku Journal of Experimental Medicine*, 222(4), pp. 311–318. doi: 10.1620/tjem.222.311.

Humphray, S. J., Oliver, K., Hunt, A. R., Plumb, R. W., Loveland, J. E., Howe,

K. L., Andrews, T. D., Searle, S., Hunt, S. E., Scott, C. E., Jones, M. C., Ainscough, R., Almeida, J. P., Ambrose, K. D., Ashwell, R. I. S., Babbage, A. K., Babbage, S., Bagguley, C. L., Bailey, J., Banerjee, R., Barker, D. J., Barlow, K. F., Bates, K., Beasley, H., Beasley, O., Bird, C. P., Bray-Allen, S., Brown, A. J., Brown, J. Y., Burford, D., Burrill, W., Burton, J., Carder, C., Carter, N. P., Chapman, J. C., Chen, Y., Clarke, G., Clark, S. Y., Clee, C. M., Clegg, S., Collier, R. E., Corby, N., Crosier, M., Cummings, A. T., Davies, J., Dhami, P., Dunn, M., Dutta, I., Dyer, L. W., Earthrowl, M. E., Faulkner, L., Fleming, C. J., Frankish, A., Frankland, J. A., French, L., Fricker, D. G., Garner, P., Garnett, J., Ghori, J., Gilbert, J. G. R., Glison, C., Grafham, D. V., Gribble, S., Griffiths, C., Griffiths-Jones, S., Grocock, R., Guy, J., Hall, R. E., Hammond, S., Harley, J. L., Harrison, E. S. I., Hart, E. A., Heath, P. D., Henderson, C. D., Hopkins, B. L., Howard, P. J., Howden, P. J., Huckle, E., Johnson, C., Johnson, D., Joy, A. A., Kay, M., Keenan, S., Kershaw, J. K., Kimberley, A. M., King, A., Knights, A., Laird, G. K., Langford, C., Lawlor, S., Leongamornlert, D. A., Leversha, M., Lloyd, C., Lloyd, D. M., Lovell, J., Martin, S., Mashreghi-Mohammadi, M., Matthews, L., McLaren, S., McLay, K. E., McMurray, A., Milne, S., Nickerson, T., Nisbett, J., Nordsiek, G., Pearce, A. V., Peck, A. I., Porter, K. M., Pandian, R., Pelan, S., Phillimore, B., Povey, S., Ramsey, Y., Rand, V., Scharfe, M., Sehra, H. K., Shownkeen, R., Sims, S. K., Skuce, C. D., Smith, M., Steward, C. A., Swarbreck, D., Sycamore, N., Tester, J., Thorpe, A., Tracey, A., Tromans, A., Thomas, D. W., Wall, M., Wallis, J. M., West, A. P., Whitehead, S. L., Willey, D. L., Williams, S. A., Wilming, L., Wray, P. W., Young, L., Ashurst, J. L., Coulson, A., Blöcker, H., Durbin, R., Sulston, J. E., Hubbard, T., Jackson, M. J., Bentley, D. R., Beck, S., Rogers, J. and Dunham, I. (2004) ‘DNA sequence and analysis of human chromosome 9’, *Nature*, 429(6990), pp. 369–374. doi: 10.1038/nature02465.

Inaga, S., Katsumoto, T., Tanaka, K., Kameie, T., Nakane, H. and Naguro, T. (2007) ‘Platinum blue as an alternative to uranyl acetate for staining in transmission electron microscopy’, *Archives of Histology and Cytology*, 70(1), pp. 43–49. doi: 10.1679/aohc.70.43.

Jackson, M. S., Rocchi, M., Thompson, G., Hearn, T., Crosier, M., Guy, J., Kirk, D., Mulligan, L., Ricco, A., Piccininni, S., Marzella, R., Viggiano, L. and Archidiacono, N. (1999) ‘Sequences flanking the centromere of human chromosome 10 are a complex patchwork of arm-specific sequences, stable duplications and unstable sequences with homologies to telomeric and other centromeric locations’, *Human Molecular Genetics*, 8(2), pp. 205–215. doi: 10.1093/hmg/8.2.205.

Jain, A. K., Singh, D., Dubey, K., Maurya, R. and Pandey, A. K. (2017) ‘Chromosomal Aberrations’, in Kumar, A., Dobrovolsky, V., Dhawan, A., and Shanker, R. (eds) *Mutagenicity:Assays and Applications*. 1st edn. Ahemdabad, India: Academic Press, pp. 69–83.

Jalal, S. M. and Law, M. E. (1999) ‘Utility of multicolor fluorescent in situ hybridization in clinical cytogenetics’, *Genetics in Medicine*, 1(5), pp. 181–186. doi: 10.1097/00125817-199907000-00003.

Joti, Y., Hikima, T., Nishino, Y., Kamda, F., Hihara, S., Takata, H., Ishikawa,

T. and Maeshima, K. (2012) ‘Chromosomes without a 30-nm chromatin fiber’, *Nucleus*, pp. 1–7. doi: 10.4161/nucl.21222.

Kaddour, A., Colicchio, B., Buron, D., Maalouf, E. El, Laplagne, E., Ricoul, M., Lenain, A., Hempel, W. M., Morat, L., Jawhari, M. Al, Cuceu, C., Heidingsfelder, L., Jeandidier, E., Deschênes, G., May, M. El, Girinsky, T. and Bennaceur-griscelli, A. (2017) ‘Transmission of Induced Chromosomal Aberrations through Successive Mitotic Divisions in Human Lymphocytes after In Vitro and In Vivo Radiation’, *Scientific reports*, 7: 3291, pp. 1–11. doi: 10.1038/s41598-017-03198-7.

Kapuscinski, J. (1995) ‘DAPI: A DMA-Specific fluorescent probe’, *Biotechnic and Histochemistry*, 70(5), pp. 220–233. doi: 10.3109/10520299509108199.

Karg, T. J. and Golic, K. G. (2018) ‘Photoconversion of DAPI and Hoechst dyes to green and red emitting forms after exposure to UV excitation’, *Chromosoma*, 127(2), pp. 235–245. doi: 10.1007/s00412-017-0654-5.

Kielkopf, C. L., White, S., Szewczyk, J. W., Turner, J. M., Baird, E. E., Dervan, P. B. and Rees, D. C. (1998) ‘A structural basis for recognition of A.T and T.A base pairs in the minor groove of B-DNA.’, *Proceedings of the National Academy of Sciences of the United States of America*, 282(5386), pp. 111–115. doi: 10.1126/science.282.5386.111.

Kirz, J., Jacobsen, C. and Howell, M. (1995) ‘Soft X-ray microscopes and their biological applications’, *Quarterly Reviews of Biophysics*, 28(1), pp. 33–130. doi: 10.1017/S0033583500003139.

Korenberg, J. R. and Engels, W. R. (1978) ‘Base ratio, DNA content, and quinacrine-brightness of human chromosomes’, *Proceedings of the National Academy of Sciences of the United States of America*, 75(7), pp. 3382–3386.

Kosyakova, N., Grigorian, A., Liehr, T., Manvelyan, M., Simonyan, I., Mkrtchyan, H., Aroutiounian, R., Polityko, A. D., Kulpanovich, A. I., Egorova, T., Jaroshevich, E., Frolova, A., Shorokh, N., Naumchik, I. V., Volleth, M., Schreyer, I., Nelle, H., Stumm, M., Wegner, R. D., Reising-Ackermann, G., Merkas, M., Brecevic, L., Martin, T., Rodríguez, L., Bhatt, S., Ziegler, M., Kreskowski, K., Weise, A., Sazci, A., Vorsanova, S., Cioffi, M. D. B. and Ergul, E. (2013) ‘Heteromorphic variants of chromosome 9’, *Molecular Cytogenetics*, 6(1), pp. 1–11. doi: 10.1186/1755-8166-6-14.

Lakowicz, J. R. (2006a) ‘Fluorescence Lifetime Imaging Microscopy’, in *Principles of Fluorescence Spectroscopy*. 3rd edn. Boston, MA: Springer, pp. 741–755.

Lakowicz, J. R. (2006b) ‘Introduction to Fluorescence’, in *Principles of Fluorescence Spectroscopy*. 3rd edn. Boston, MA: Springer, pp. 1–26.

Lakowicza, J. R., Chereka, H., Gryczynskia, I., Joshia, N. and Johnson, M. L. (1987) ‘Analysis of fluorescence decay kinetics measured in the frequency domain using distributions of decay times’, *Biophysical Chemistry*, 28(1), pp.

35–50. doi: 10.1016/j.physbeh.2017.03.040.

Lander ES, Linton LM, Birren B, Nusbaum C, Zody MC, Baldwin J, Devon K, Dewar K, Doyle M, FitzHugh W, Funke R, Gage D, Harris K, Heaford A, Howland J, Kann L, Lehoczky J, LeVine R, McEwan P, McKernan K, Meldrim J, Mesirov JP, Miranda C, Morris W, Naylor J, S. J. I. H. G. S. C. (2001) 'Initial sequencing and analysis of the human genome', *Nature*, 409(6822), pp. 860–921.

Langlois, R. G., Yu, L. C., Gray, J. W. and Carrano, A. V. (1982) 'Quantitative karyotyping of human chromosomes by dual beam flow cytometry', *Proceedings of the National Academy of Sciences of the United States of America*, 79, pp. 7876–7880. doi: 10.1073/pnas.79.24.7876.

Laptenok, S., Mullen, K. M., Borst, J. W., Stokkum, I. H. M. va., Apanasovich, V. V and Visser, A. J. W. . (2007) 'Fluorescence Lifetime Imaging Microscopy (FLIM) Data Analysis with TIMP', *Journal Of Statistical Software*, 18(8), pp. 1–20. doi: 10.18637/jss.v069.i12.

Larabell, C. A. and Nugent, K. A. (2010) 'Imaging Cellular Architecture with X-rays', *Current Opinion in Structural Biology*, 20(5), pp. 623–31. doi: 10.1038/jid.2014.371.

Levan, A., Fredga, K. and Sandberg, A. A. (1964) 'Nomenclature for Centromeric Position on Chromosomes', *Hereditas*, 52(2), pp. 201–220. doi: 10.1111/j.1601-5223.1964.tb01953.x.

Lin, C. C., Wu, L. S. H. and Lee, K. F. (2019) 'The Potential Effect of Different Doses of Ionizing Radiation on Genes and Disease', *Dose-Response*, 17(2), pp. 1–10. doi: 10.1177/1559325819843375.

Lin, Y. W. (2020) 'Uranyl binding to proteins and structural-functional impacts', *Biomolecules*, 10(3), pp. 1–16. doi: 10.3390/biom10030457.

Linet, M. S., Slovis, T. L., Miller, D. L., Kleinerman, R., Lee, C., Rajaraman, P. and Gonzalez, A. B. De (2012) 'Cancer Risks Associated With External Radiation From Diagnostic Imaging Procedures', *CA: A Cancer Journal for Clinicians*, 62(2), pp. 75–100. doi: 10.3322/caac.21132.

Llères, D., James, J., Swift, S., Norman, D. G. and Lamond, A. I. (2009) 'Quantitative analysis of chromatin compaction in living cells using FLIM–FRET', *The Journal of Cell Biology*, 187(4), pp. 481–496. doi: 10.1083/jcb.200907029.

Lomax, M. E., Folkes, L. K. and Neill, P. O. (2013) 'Biological Consequences of Radiation-induced DNA Damage : Relevance to Radiotherapy', *Clinical Oncology*, 25(10), pp. 578–585. doi: 10.1016/j.clon.2013.06.007.

Lowe, D. J., Herzog, M., Mosler, T., Cohen, H., Felton, S., Beli, P., Raj, K., Galanty, Y. and Jackson, S. P. (2020) 'Chronic irradiation of human cells reduces histone levels and deregulates gene expression', *Scientific Reports*, 10(1), pp. 1–16. doi: 10.1038/s41598-020-59163-4.

Madian, N. and Jayanthi, K. B. (2014) 'Analysis of human chromosome classification using centromere position', *Measurement: Journal of the International Measurement Confederation*, 47(1), pp. 287–295. doi: 10.1016/j.measurement.2013.08.033.

Madon, P. F., Athalye, A. S. and Parikh, F. R. (2005) 'Polymorphic variants on chromosomes probably play a significant role in infertility', *Reproductive BioMedicine Online*. Reproductive Healthcare Ltd, Duck End Farm, Dry Drayton, Cambridge CB23 8DB, UK, 11(6), pp. 726–732. doi: 10.1016/S1472-6483(10)61691-4.

Maeshima, K. and Eltsov, M. (2008) 'Packaging the genome: The structure of mitotic chromosomes', *Journal of Biochemistry*, 143(2), pp. 145–153. doi: 10.1093/jb/mvm214.

Maeshima, K., Imai, R., Tamura, S. and Nozaki, T. (2014) 'Chromatin as dynamic 10-nm fibers', *Chromosoma*, 123(3), pp. 225–237. doi: 10.1007/s00412-014-0460-2.

Mahaney, B. L., Meek, K. and Lees-Miller, S. P. (2009) 'Repair of ionizing radiation-induced DNA double strand breaks by non-homologous end-joining', *Biochemistry*, 417(3), pp. 639–650. doi: 10.1038/jid.2014.371.

Maiden, A., Johnson, D. and Li, P. (2017) 'Further improvements to the ptychographical iterative engine', *Optica*, 4(7), pp. 736–745. doi: 10.1364/optica.4.000736.

Maiden, A. M. and Rodenburg, J. M. (2009) 'An improved ptychographical phase retrieval algorithm for diffractive imaging', *Ultramicroscopy*, 109(10), pp. 1256–1262. doi: 10.1016/j.ultramic.2009.05.012.

Maraschio, P., Zuffardi, O., Dalla Fior, T. and Tiepolo, L. (1988) 'Immunodeficiency, centromeric heterochromatin instability of chromosomes 1, 9, and 16, and facial anomalies: The ICF syndrome', *Journal of Medical Genetics*, 25(3), pp. 173–180. doi: 10.1136/jmg.25.3.173.

Marchal, J., Horswell, I., Willis, B., Plackett, R., Gimenez, E. N., Spiers, J., Ballard, D., Booker, P., Thompson, J. A., Gibbons, P., Burge, S. R., Nicholls, T., Lipp, J. and Tartoni, N. (2013) 'EXCALIBUR: A small-pixel photon counting area detector for coherent X-ray diffraction - Front-end design, fabrication and characterisation', *Journal of Physics: Conference Series*, 425(PART 6), pp. 9–14. doi: 10.1088/1742-6596/425/6/062003.

Maser, J., Osanna, A., Wang, Y., Jacobsen, C., Kirz, J., Spector, S., Winn, B. and Tennant, D. (2000) 'Soft X-ray microscopy with a cryo scanning transmission X-ray microscope : I . Instrumentation, imaging and spectroscopy', *Journal of Microscopy*, 197, pp. 68–79.

Mayall, B. H., Carrano, A. V., Moore, D. H., Ashworth, L. K., Bennett, D. E. and Mendelsohn, M. L. (1984) 'The DNA-based human karyotype', *Cytometry*, 5(4), pp. 376–385. doi: 10.1002/cyto.990050414.

Melvin, T., Cunniffe, S. M. T., O'Neill, P., Parker, A. W. and Roldan-Arjona, T. (1998) 'Guanine is the target for direct ionisation damage in DNA, as detected using excision enzymes', *Nucleic Acids Research*, 26(21), pp. 4935–4942. doi: 10.1093/nar/26.21.4935.

Mendelsohn, M. L., Mayall, B. H., Bogart, E., Moore II, D. H. and Perry, B. H. (1973) 'DNA Content and DNA-Based Centromeric Index of the 24 Human Chromosomes', *Science*, 179(4078), pp. 1126–1129.

Meyne, J., Bartholdi, M. F., Travis, G. and Cram, L. S. (1984) 'Counterstaining human chromosomes for flow karyology', *Cytometry*, 5, pp. 580–583.

Miao, J., Sandberg, R. R. L. and Song, C. (2012) 'Coherent X-Ray Diffraction Imaging', *IEEE Journal Of Selected Topics In Quantum Electronics*, 18(1), pp. 399–410. doi: 10.1109/JSTQE.2011.2157306.

Miao, J., Sayre, D. and Chapman, H. N. (1998) 'Phase retrieval from the magnitude of the Fourier transforms of nonperiodic objects', *Journal of the Optical Society of America A*, 15(6), pp. 1662–1669. doi: 10.1364/JOSAA.15.001662.

Moralli, D., Yusuf, M., Mandegar, M. A., Khoja, S., Monaco, Z. L. and Volpi, E. V. (2011) 'An Improved Technique for Chromosomal Analysis of Human ES and iPS Cells', *Stem Cell Reviews and Reports*, 7(2), pp. 471–477. doi: 10.1007/s12015-010-9224-4.

Morgan, David O. (2007) *The Cell Cycle: Principles of Control*. Oxford: New Science Press Ltd.

Muehlbauer, P. A. and Schuler, M. J. (2005) 'Detection of numerical chromosomal aberrations by flow cytometry : A novel process for identifying aneugenic agents', *Mutation Research*, 585, pp. 156–169. doi: 10.1016/j.mrgentox.2005.05.002.

Nair, S., Engelbrecht, M., Miles, X., Ndimba, R., Fisher, R., du Plessis, P., Bolcaen, J., Nieto-Camero, J., de Kock, E. and Vandevoorde, C. (2019) 'The impact of dose rate on DNA double-strand break formation and repair in human lymphocytes exposed to fast neutron irradiation', *International Journal of Molecular Sciences*, 20(21). doi: 10.3390/ijms20215350.

Newman, H. C., Prise, K. M., Folkard, M. and Michael, B. D. (1997) 'DNA double-strand break distributions in X-ray and α-particle irradiated V79 cells: Evidence for non-random breakage', *International Journal of Radiation Biology*, 71(4), pp. 347–363. doi: 10.1080/095530097143978.

Nicetto, D. and Zaret, K. (2019) 'Role of H3K9me3 Heterochromatin in Cell Identity Establishment and Maintenance', *Current Opinion in Genetics & Development*, 55(2), pp. 1–10. doi: 10.1016/j.gde.2019.04.013.

Nishibuchi, G. and Déjardin, J. (2017) 'The molecular basis of the organization of repetitive DNA-containing constitutive heterochromatin in mammals', *Chromosome Research*, 25(1), pp. 77–87. doi: 10.1007/s10577-016-9547-3.

Nishino, Y., Takahashi, Y., Imamoto, N., Ishikawa, T. and Maeshima, K. (2009) 'Three-dimensional visualization of a human chromosome using coherent X-ray diffraction', *Physical Review Letters*, 102(1), pp. 8–11. doi: 10.1103/PhysRevLett.102.018101.

Ojima, M., Ito, M., Suzuki, K. and Kai, M. (2015) 'Unstable Chromosome Aberrations Do Not Accumulate in Normal Human Fibroblast after Fractionated X-Irradiation', *PLoS ONE*, 10(2), pp. 1–13. doi: 10.1371/journal.pone.0116645.

Ou, H. D., Phan, S., Deerinck, T. J., Thor, A., Ellisman, M. H. and O'Shea, C. C. (2017) 'ChromEMT: Visualizing 3D chromatin structure and compaction in interphase and mitotic cells', *Science*, 357(6349). doi: 10.1126/science.aag0025.

Ouchi, N. B. (2015) 'On the Dynamical Approach of Quantitative Radiation Biology', in Nenoi, M. (ed.) *Evolution of Ionizing Radiation Research*. IntechOpen, pp. 41–62.

Palmer, C. G. and Funderburk, S. (1965) 'Secondary constrictions in human chromosomes.', *Cytogenetics*, 4(4), pp. 261–276. doi: 10.1159/000129863.

Park, Y., Peoples, A. R., Madugundu, G. S., Sanche, L. and Wagner, J. R. (2013) 'Side-by-side comparison of DNA damage induced by low-energy electrons and high-energy photons with solid TpTpT trinucleotide', *Journal of Physical Chemistry B*, 117(35), pp. 10122–10131. doi: 10.1021/jp405397m.

Pfeiffer, P., Goedecke, W. and Obe, G. (2000) 'Mechanisms of DNA double-strand break repair and their potential to induce chromosomal aberrations', *Mutagenesis*, 15(4), pp. 289–302. doi: 10.1093/mutage/15.4.289.

Phengchat, R., Takata, H., Morii, K., Inada, N., Murakoshi, H., Uchiyama, S. and Fukui, K. (2016) 'Calcium ions function as a booster of chromosome condensation', *Scientific Reports*, 6(1), p. 38281. doi: 10.1038/srep38281.

Piovesan, A., Pelleri, M. C., Antonaros, F., Strippoli, P., Caracausi, M. and Vitale, L. (2019) 'On the length, weight and GC content of the human genome', *BMC Research Notes*, 12(1), pp. 1–7. doi: 10.1186/s13104-019-4137-z.

Pita, M., Gosálvez, J., Gosálvez, A., Nieddu, M., López-Fernández, C. and Mezzanotte, R. (2010) 'A highly conserved pericentromeric domain in human and gorilla chromosomes', *Cytogenetic and Genome Research*, 126(3), pp. 253–258. doi: 10.1159/000251962.

Prosser, J., Frommer, M., Paul, C. and Vincent, P. C. (1986) 'Sequence relationships of three human satellite DNAs', *Journal of Molecular Biology*, 187(2), pp. 145–155. doi: 10.1016/0022-2836(86)90224-X.

Rau, C., Batey, D., Cipiccia, S., Shi, X., Marathe, S., Storm, M., Bodey, A. J. and Zdora, M.-C. (2019) 'New imaging opportunities at the DIAMOND beamline I13L', in X-Ray Nanoimaging: Instruments and Methods IV (ed.)

Proceedings of Spie 11112. California, United States. doi: 10.1117/12.2543799.

Rau, C., Wagner, U. H., Vila-Comamala, J., Bodey, A., Parson, A., García-Fernández, M., De Fanis, A., Pešić, Z., Zanette, I. and Zdora, M. (2016) 'Micro- and nano-imaging at the diamond beamline I13L-imaging and coherence', in *AIP Conference Proceedings*. New York (NY), United States: AIP Publishing, pp. 030008–1–030008–5. doi: 10.1063/1.4952831.

Reisz, J. A., Bansal, N., Qian, J., Zhao, W. and Furdui, C. M. (2014) 'Effects of ionizing radiation on biological molecules - mechanisms of damage and emerging methods of detection', *Antioxidants and Redox Signaling*, 21(2), pp. 260–292. doi: 10.1089/ars.2013.5489.

Ried, T., Schröck, E., Ning, Y. and Wienberg, J. (1998) 'Chromosome painting: A useful art', *Human Molecular Genetics*, 7(10), pp. 1619–1626. doi: 10.1093/hmg/7.10.1619.

Robinson, I. (2015) 'Coherent three-dimensional X-ray cryo-imaging', *International Union of Crystallography (IUCr) Journal*, 2(1976), pp. 477–478. doi: 10.1107/S2052252515015109.

Robinson, I., Yang, Y., Zhang, F., Lynch, C., Yusuf, M. and Cloetens, P. (2016) 'Nuclear incorporation of iron during the eukaryotic cell cycle', *Journal of Synchrotron Radiation*, 23(6), pp. 1490–1497. doi: 10.1107/S1600577516012807.

Robinson, I., Yusuf, M., Schwenke, J., Estandarte, A., Zhang, F., Bhella, G., Parmar, N., Clark, J., Song, C., Nam, D., Ratnasari, G., Kaneyoshi, K., Takata, H. and Fukui, K. (2015) 'Damage-free imaging of human chromosomes', *Chromosome Science*, 18, pp. 69–72.

Rodenburg, J. M., Hurst, A. C., Cullis, A. G., Dobson, B. R., Pfeiffer, F., Bunk, O., David, C., Jefimovs, K. and Johnson, I. (2007) 'Hard-X-ray lensless imaging of extended objects', *Physical Review Letters*, 98(3), pp. 1–4. doi: 10.1103/PhysRevLett.98.034801.

Ronne, M., Andersen, O. and Erlandsen, M. (1979) 'Effect of colcemid exposure and methanol acetic acid fixation on human metaphase chromosome structure', *Hereditas*, 90(2), pp. 195–201. doi: 10.1111/j.1601-5223.1979.tb01306.x.

Rozgaj, R., Kašuba, V., Šentija, K. and Prlić, I. (1999) 'Radiation-induced chromosomal aberrations and haematological alterations in hospital workers', *Occupational Medicine*, 49(6), pp. 353–360. doi: 10.1093/occmed/49.6.353.

Ryan, T. L., Pantelias, A. G., Terzoudi, G. I., Pantelias, G. E. and Balajee, A. S. (2019) 'Use of human lymphocyte G0 PCCs to detect intra- And inter-chromosomal aberrations for early radiation biodosimetry and retrospective assessment of radiation-induced effects', *PLoS ONE*, 14(5), pp. 1–18. doi: 10.1371/journal.pone.0216081.

Ryu, T. H., Kim, J. H. and Kim, J. K. (2016) 'Chromosomal Aberrations in Human Peripheral Blood Lymphocytes after Exposure to Ionizing Radiation', *Genome Integrity*, 7: 5, pp. 3–5. doi: 10.4103/2041-9414.197172.

Sahin, F. I., Yilmaz, Z., Yuregir, O. O., Bulakbasi, T., Ozer, O. and Zeyneloglu, H. B. (2008) 'Chromosome heteromorphisms: An impact on infertility', *Journal of Assisted Reproduction and Genetics*, 25(5), pp. 191–195. doi: 10.1007/s10815-008-9216-3.

Saksouk, N., Simboeck, E. and Déjardin, J. (2015) 'Constitutive heterochromatin formation and transcription in mammals', *Epigenetics and Chromatin*, 8(1), pp. 1–17. doi: 10.1186/1756-8935-8-3.

Sanchez, L., Martinez, P. and Goyanes, V. (1991) 'Analysis of centromere size in human chromosomes 1, 9, 15, and 16 by electron microscopy', *Genome*, 34(5), pp. 710–713. doi: 10.1139/g91-109.

Sanders, J., Freeman, T., Xu, Y., Golloshi, R., Stallard, M., Martin, R. S., Balajee, A. and McCord, R. P. (2019) 'Radiation-Induced DNA Damage and Repair Effects on 3D Genome Organization', *BioRxiv- the preprint server for Biology*. doi: https://doi.org/10.1101/740704.

Schnerch, D., Yalcintepe, J., Schmidts, A., Becker, H., Follo, M., Engelhardt, M. and Wäsch, R. (2012) 'Cell cycle control in acute myeloid leukemia.', *American journal of cancer research*, 2(5), pp. 508–528.

Schröder, A., Kriesen, S., Hildebrandt, G. and Manda, K. (2019) 'First insights into the effect of low-dose X-ray irradiation in adipose-derived stem cells', *International Journal of Molecular Sciences*, 20(23), pp. 1–13. doi: 10.3390/ijms20236075.

Schroer, C. G., Kuhlmann, M., Hunger, M. D., Günzler, T. F., Kurapova, O., Feste, S., Frehse, F., Drakopoulos, M., Somogyi, H. R., Simionovici, A. S., Snigirev, A., Snigireva, I., Schug, C. and Schröder, W. H. (2003) 'Nanofocusing parabolic refractive X-ray lenses', *Applied Physics Letters*, 82(9), pp. 1485–1487. doi: 10.1063/1.1556960.

Schwenke, J., Shemilt, L. A., Wagner, U., Morrison, G. R., Zhang, F., Yusuf, M., Rau, C. and Robinson, I. K. (no date) 'Quantitative phase measurements of human cell nuclei using X-ray ptychography', pp. 1–14.

Schwer, B., Wei, P., Chang, A. N. and Kao, J. (2016) 'Transcription-associated processes cause DNA double-strand breaks and translocations in neural stem / progenitor cells', *Proceedings of the National Academy of Sciences of the United States of America*, 113(8), pp. 2258–2263. doi: 10.1073/pnas.1525564113.

Seidel, C. A. M., Schulz, A. and Sauer, M. H. M. (1996) 'Nucleobase-specific quenching of fluorescent dyes. 1. Nucleobase one-electron redox potentials and their Correlation with static and dynamic quenching efficiencies', *Journal of Physical Chemistry*, 100(13), pp. 5541–5553. doi: 10.1021/jp951507c.

Shapiro, D., Thibault, P., Beetz, T., Elser, V., Howells, M., Jacobsen, C., Kirz, J., Lima, E., Miao, H., Neiman, A. M. and Sayre, D. (2005) 'Biological imaging by soft x-ray diffraction microscopy', *Proceedings of the National Academy of Sciences of the United States of America*, 102(43), pp. 15343–15346. doi: 10.1073/pnas.0503305102.

Shaw, M. W. (1973) 'Uses of banding techniques for the identification of human disease of cytogenetic origin', *Environmental Health Perspectives*, 6, pp. 151–156. doi: 10.1289/ehp.7306151.

Shemilt, L. A., Estandarte, A. K. C., Yusuf, M. and Robinson, I. K. (2014) 'Scanning electron microscope studies of human metaphase chromosomes.', *Philosophical transactions. Series A, Mathematical, physical, and engineering sciences*, 372(2010), p. 20130144. doi: 10.1098/rsta.2013.0144.

Shemilt, L., Verbanis, E., Schwenke, J., Estandarte, A. K., Xiong, G., Harder, R., Parmar, N., Yusuf, M., Zhang, F. and Robinson, I. K. (2015) 'Karyotyping human chromosomes by optical and X-ray ptychography methods', *Biophysical Journal*, 108(3), pp. 706–713. doi: 10.1016/j.bpj.2014.11.3456.

Sherrard, A., Bishop, P., Panagi, M., Villagomez, M. B., Alibhai, D. and Kaidi, A. (2018) 'Streamlined histone-based fluorescence lifetime imaging microscopy (FLIM) for studying chromatin organisation', *Biology Open*, 7(3), pp. 1–8. doi: 10.1242/bio.031476.

Shimura, N. and Kojima, S. (2018) 'The Lowest Radiation Dose Having Molecular Changes in the Living Body', *Dose-Response*, 16(2), pp. 1–17. doi: 10.1177/1559325818777326.

Sidorenko, P. and Cohen, O. (2016) 'Single-shot ptychography', *Optica*, 3(1), pp. 9–14.

Singh, P., Aggarwal, L. M., Parry, S. A. and Raman, M. J. (2018) 'Radiation dosimetry and repair kinetics of DNA damage foci in mouse pachytene spermatocyte and round spermatid stages', *Mutagenesis*, 33(3), pp. 231–239. doi: 10.1093/mutage/gey007.

Smith, E. A., McDermott, G., Do, M., Leung, K., Panning, B., Le Gros, M. A. and Larabell, C. A. (2014) 'Quantitatively imaging chromosomes by correlated cryo-fluorescence and soft X-ray tomographies', *Biophysical Journal*, 107(8), pp. 1988–1996. doi: 10.1016/j.bpj.2014.09.011.

Sotnik, N. V, Osovets, S. V, Scherthan, H. and Azizova, T. V (2014) 'mFISH analysis of chromosome aberrations in workers occupationally exposed to mixed radiation', *Radiation and Environmental Biophysics*, 53(2), pp. 347–354. doi: 10.1007/s00411-014-0536-7.

Spagnol, S. T. and Dahl, K. N. (2016) 'Spatially Resolved Quantification of Chromatin Condensation through Differential Local Rheology in Cell Nuclei Fluorescence Lifetime Imaging', *PLoS ONE*, 11(1), pp. 1–19. doi: 10.1371/journal.pone.0146244.

Speicher, M. R., Ballard, S. G. and Ward, D. C. (1996) 'Karyotyping human chromosomes by combinatorial multi-fluor FISH', *Nature Genetics*, 12, pp. 368–375.

Stachnik, K. (2012) *Ptychographical measurements of biological specimen*. Poland.

Strachan, T. and Read, Andrew P. (2004) 'Chromosome structure and function', in *Human Molecular Genetics*. 3rd edn. London and New York: Garland Science: Taylor & Francis Group, pp. 34–36.

Suhling, K., Hirvonen, L. M., Levitt, J. A., Chung, P.-H., Tregidgo, C., Le Marois, A., Rusakov, D. A., Zheng, K., Ameer-Beg, S., Poland, S., Coelho, S., Henderson, R. and Krstajic, N. (2015) 'Fluorescence lifetime imaging (FLIM): Basic concepts and some recent developments', *Medical Photonics*, 27, pp. 3–40. doi: 10.1016/j.medpho.2014.12.001.

Suhling, K., Levitt, J. A., Chung, P.-H., Kuimova, M. K. and Yahioglu, G. (2012) 'Fluorescence Lifetime Imaging of Molecular Rotors in Living Cells', *Journal of Visualized Experiments*, (60), pp. 1–5. doi: 10.3791/2925.

Sullivan, L. L., Chew, K. and Sullivan, B. A. (2017) 'α satellite DNA variation and function of the human centromere', *Nucleus*. Taylor & Francis, 8(4), pp. 331–339. doi: 10.1080/19491034.2017.1308989.

Sumner, A. T. (1982) 'The nature and mechanisms of chromosome banding', *Cancer Genetics and Cytogenetics*, 6(1), pp. 59–87. doi: 10.1016/0165-4608(82)90022-X.

Tagarro, I., Fernández-Peralta, A. M. and González-Aguilera, J. J. (1994) 'Chromosomal localization of human satellites 2 and 3 by a FISH method using oligonucleotides as probes', *Human Genetics*, 93(4), pp. 383–388. doi: 10.1007/BF00201662.

Takata, H., Uchiyama, S., Nakamura, N., Nakashima, S., Kobayashi, S., Sone, T., Kimura, S., Lahmers, S., Granzier, H., Labeit, S., Matsunaga, S. and Fukui, K. (2007) 'A comparative proteome analysis of human metaphase chromosomes isolated from two different cell lines reveals a set of conserved chromosome-associated proteins', *Genes to Cells*, 12(3), pp. 269–284. doi: 10.1111/j.1365-2443.2007.01051.x.

Terrenoire, E., Halsall, J. A. and Turner, B. M. (2015) 'Immunolabelling of human metaphase chromosomes reveals the same banded distribution of histone H3 isoforms methylated at lysine 4 in primary lymphocytes and cultured cell lines', *BMC Genetics*, 16(1), pp. 1–7. doi: 10.1186/s12863-015-0200-5.

Therman, E. (2012) 'Structure of the Eukaryotic Chromosome and the Karyotype', in *Human Chromosomes: Structure, Behavior, Effects*. 2nd edn. Berlin Heidelberg: Springer-Verlag, pp. 11–23.

Tobias, E. (2011) 'Chromosome aberrations', in *Essential Medical Genetics*.

6th edn. Singapore: Wiley-Blackwell, pp. 89–111.

Travers, A. (2014) ‘Structural biology. The 30-nm fiber redux.’, *Science (New York, NY)*, 344(6182), pp. 370–372. doi: 10.1126/science.1253852.

Tremethick, D. J. (2007) ‘Higher-Order Structures of Chromatin: The Elusive 30 nm Fiber David’, *Cell*, 128, pp. 651–654. doi: 10.1016/j.cell.2007.02.008.

Truong, K., Bradley, S., Baginski, B., Wilson, J. R., Medlin, D., Zheng, L., Wilson, R. K., Rusin, M., Takacs, E. and Dean, D. (2018) ‘The effect of well-characterized, very low-dose x-ray radiation on fibroblasts’, *PLoS ONE*, 13(1), pp. 1–16. doi: 10.1371/journal.pone.0190330.

Tubbs, A. and Nussenzweig, A. (2017) ‘Endogenous DNA Damage as a Source of Genomic Instability in Cancer’, *Cell*, 168(4), pp. 644–656. doi: 10.1016/j.cell.2017.01.002.

Uchiyama, S., Kobayashi, S., Takata, H., Ishihara, T., Hori, N., Higashi, T., Hayashihara, K., Sone, T., Higo, D., Nirasawa, T., Takao, T., Matsunaga, S. and Fukui, K. (2005) ‘Proteome analysis of human metaphase chromosomes’, *Journal of Biological Chemistry*, 280(17), pp. 16994–17004. doi: 10.1074/jbc.M412774200.

Wako, T., Yoshida, A., Kato, J., Otsuka, Y., Ogawa, S., Kaneyoshi, K., Takata, H. and Fukui, K. (2020) ‘Human metaphase chromosome consists of randomly arranged chromatin fibres with up to 30-nm diameter’, *Scientific Reports*, 10(1), pp. 1–6. doi: 10.1038/s41598-020-65842-z.

Wall, W. J. (2016) ‘Tissue Culture and the Cell Cycle: The Answer Is Revealed.’, in *The Search for Human Chromosomes*. 1st edn. Switzerland: Springer International Publishing, pp. 85–102.

Wang, C. and Bai, C. (2006) ‘Single Molecule Fluorescence Imaging and Spectrocopy: Far-Field studies’, in *Single Molecule Chemistry and Physics-An Introduction*. 1st edn. Beijing, China: Springer-Verlag Berlin Heidelberg, pp. 183–190.

Wanner, G. and Formanek, H. (1995) ‘Imaging of DNA in human and plant chromosomes by high-resolution scanning electron microscopy’, *Chromosome Research*, 3(6), pp. 368–374. doi: 10.1007/BF00710018.

Woodcock, C. L. and Ghosh, R. P. (2010) ‘Chromatin Higher-order Structure and Dynamics’, pp. 1–25.

Xu, X. and Wu, M. (1983) ‘Electron microscopy of G-banded human mitotic chromosomes’, *Chromosoma*, 88(3), pp. 237–240. doi: 10.1007/BF00285626.

Yahav, G., Hirshberg, A., Salomon, O., Amariglio, N., Trakhtenbrot, L. and Fixler, D. (2016) ‘Fluorescence Lifetime Imaging of DAPI- Stained Nuclei As a Novel Diagnostic Tool for the Detection and Classification of B-Cell Chronic Lymphocytic Leukemia’, *Cytometry Part A*, 89A(6), pp. 644–652. doi: 10.1002/cyto.a.22890.

Yamamoto, Y. and Shinohara, K. (2002) 'Application of X-ray microscopy in analysis of living hydrated cells', *Anatomical Record*, 269(5), pp. 217–223. doi: 10.1002/ar.10166.

Yan, H., Nazaretski, E., Lauer, K., Huang, X., Wagner, U., Rau, C., Yusuf, M., Robinson, I., Kalbfleisch, S., Li, L., Bouet, N., Zhou, J., Conley, R. and Chu, Y. S. (2016) 'Multimodality hard-x-ray imaging of a chromosome with nanoscale spatial resolution', *Scientific Reports*, 6, pp. 1–7. doi: 10.1038/srep20112.

Yusuf, M., Bauer, D. L. V., Lipinski, D. M., MacLaren, R. E., Wade-Martins, R., Mir, K. U. and Volpi, E. V. (2011) 'Combining M-FISH and Quantum Dot technology for fast chromosomal assignment of transgenic insertions', *BMC Biotechnology*, 11:121, pp. 1–10. doi: 10.1186/1472-6750-11-121.

Yusuf, M., Chen, B., Hashimoto, T., Estandarte, A. K., Thompson, G. and Robinson, I. (2014) 'Staining and embedding of human chromosomes for 3-D serial block-face scanning electron microscopy', *BioTechniques*, 57(6), pp. 302–307. doi: 10.2144/000114236.

Yusuf, M., Kaneyoshi, K., Fukui, K. and Robinson, I. (2019) 'Use of 3D imaging for providing insights into high-order structure of mitotic chromosomes', *Chromosoma*, 128(1), pp. 7–13. doi: 10.1007/s00412-018-0678-5.

Yusuf, M., Leung, K., Morris, K. J. and Volpi, E. V. (2013) 'Comprehensive cytogenomic profile of the in vitro neuronal model SH-SY5Y', *Neurogenetics*, 14(1), pp. 63–70. doi: 10.1007/s10048-012-0350-9.

Yusuf, M., Millas, A. L. G., Estandarte, A. K. C., Bhella, G. K., McKean, R., Bittencourt, E. and Robinson, I. K. (2014) 'Platinum blue staining of cells grown in electrospun scaffolds', *BioTechniques*, 57(3). doi: 10.2144/000114206.

Yusuf, M., Zhang, F., Chen, B., Bhartiya, A., Cunnea, K., Wagner, U., Schwenke, J. and Robinson, I. K. (2017) 'Procedures for cryogenic X-ray ptychographic imaging of biological samples', *International Union of Crystallography (IUCr) Journal*, 4, pp. 147–151. doi: 10.1107/S2052252516020029.

Zhang, F., Vila-Comamala, J., Diaz, A., Berenguer, F., Bean, R., Chen, B., Menzel, A., Robinson, I. K. and Rodenburg, J. M. (2013) 'Translation position determination in ptychographic coherent diffraction imaging', *Optics Express*, 21(11), p. 13592. doi: 10.1364/OE.21.013592.